Active Extraordinary Optical Transmission Metasurfaces Using Phase-Change Materials

Submitted by Euan Humphreys

to the University of Exeter as a thesis for the degree of

PhD Physics/Engineering (CDT)

May 2023

This thesis is available for Library use on the understanding that it is copyright material and that no quotation from the thesis may be published without proper acknowledgement.

I certify that all material in this thesis which is not my own work has been identified and that any material that has previously been submitted and approved for the award of a degree by this or any other University has been acknowledged.

To Charles Barclay and Clive Stell, two wonderful mentors without whom I might not have followed this path.

Abstract

The key question that this thesis aims to answer is "Can a tuneable bandpass optical filter for the mid-infrared regime be made by combining extraordinary optical transmission (EOT) arrays and phase-change materials (PCMs)?".

It is proposed that such devices may be useful for a wide range of applications where the ability to dynamically change the transmissive (or reflective) properties of a filter is required, include multispectral sensing/imaging and signal modulation amongst others. Current multispectral imaging systems are mainly dependant on either multiple sets of lenses and sensors, or multiple mechanically-exchanged filters exposed through in-sequence; the use of a single, dynamically tuneable phase-change EOT-based filter opens avenues to reducing systems' size, cost and complexity.

The EOT effect is observed with arrays of sub-wavelength-sized holes in thin plasmonic metal (e.g. gold) films, with the transmission peak position dependent on the array geometry and surrounding materials' optical properties: a PCM layer on top of the array allows shifting of the transmission peak position by switching the PCM phase (and its refractive index) via heat pulses.

Specific areas studied in this thesis include the use of different fabrication methods to make phase-change EOT transmission filters for the mid-infrared regime, including electron-beam lithography-based techniques and a novel (and much faster) approach of direct patterning via laser ablation. Tuneable filters for use in various parts of the optical spectrum, especially the mid and long-wave infrared range, were designed, simulated, fabricated and characterised. Good performance was obtained for phase-change EOT filters over a wide range of array pitch sizes. EOT arrays designed for the mid-infrared range and fabricated via wet-etching and measured with FTIR spectroscopy produced very similar spectra to those of finite-element simulations with peak transmittance of Q-factors between 5-6 and a peak transmittance of ~0.8. Laser-ablated arrays showed a similar (though not quite so good) performance, due mainly to slight irregularities in the positioning of holes in the array.

The addition of a phase-change layer, specifically $Ge_2Sb_2Te_5$, to the EOT arrays resulted in a shift in the wavelength of the peak transmission, with the amount of shift depending on the phase-state (crystalline, amorphous, or mixed-state) of the phase-change layer, so demonstrating the ability for dynamic tuning of the filter response by switching of the phase-change layer. An important requirement for proper and prolonged operation of the filter devices was found to be the use of a thin dielectric barrier layer (here Si_3N_4, between the plasmonic film and the phase-change layer, to prevent inter-diffusion between the two: reflection cavities of $Ge_2Sb_2Te_5$ on unpatterned gold layers were created to investigate this effect, with resonance features of a 20 nm layer being destroyed without a barrier layer present and the complete assimilation of gold and phase-change layers evident with cross-section TEM imaging.

1. Preamble

1.1. Table of Contents

1. Preamble 5

1.1. Table of Contents 5

1.2. List of Figures 9

1.3. List of Tables 19

1.4. Abbreviations 22

1.5. Conferences Contributions 23

1.6. Journal Publications 23

1.7. Acknowledgements 24

1.8. External Research Collaborators 25

2. Introduction 26

2.1. Outline 27

2.2. Objectives 28

3. Background and Theory 30

3.1. Metasurfaces 30

3.2. Extraordinary Optical Transmission 30

3.2.1. Overview 30

3.2.2. Types of Extraordinary Optical Transmission Mechanisms 32

3.2.2.1. Surface Enhanced Optical Transmission 33

3.2.2.2. Localised Enhanced Optical Transmission 36

3.2.2.3. Absorption-Induced Transparency 36

3.2.2.4. Quasi-Cylindrical Waves 38

3.2.3. EOT Array Variations 39

3.3. Phase-Change Materials 40

3.3.1. Overview 40

3.3.2. Switching 43

3.4. Multispectral Imaging and Sensing ... 45
3.4.1. Overview ... 45
3.4.2. Existing Types of Multispectral Imaging Systems ... 46
3.4.3. Tuneable Filter via Phase-Change EOT ... 48
4. Methods ... 50
4.1. Simulation ... 50
4.1.1. Electromagnetic Modelling ... 50
4.1.2. Electro-Thermal Modelling ... 55
4.2. Fabrication ... 58
4.2.1. Substrate Shapes ... 58
4.2.2. Deposition Techniques ... 59
4.2.2.1. Thermal Evaporation ... 59
4.2.2.2. Magnetron Sputtering ... 61
4.2.3. Device Patterning ... 63
4.2.3.1. Electron Beam Lithography ... 63
4.2.3.2. Lift-Off ... 64
4.2.3.3. Wet-Etching ... 66
4.2.3.4. Focused Ion Beam Milling ... 67
4.2.3.5. Laser Ablation ... 68
4.2.4. Characterisation ... 73
4.2.4.1. Optical Microscopy ... 73
4.2.4.2. Ellipsometry ... 73
4.2.4.3. Scanning Electron Microscopy ... 75
4.2.4.4. Surface Profiler Scanning ... 76
4.2.4.5. Atomic Force Microscopy ... 76
4.2.4.6. Energy Dispersive (X-ray) Spectroscopy ... 78
4.2.4.7. Fourier Transform Infrared Spectroscopy ... 79
4.2.4.8. Ultraviolet to Near-Infrared Micro-Spectrophotometry ... 80

5. Modelling and Device Design 82

5.1. Analytical Modelling............ 82

5.1.1. Calculating EOT Minima Positions............ 82

5.1.2. Optical Properties with Crystallisation Fraction............ 85

5.2. Mid-Infrared EOT Array Simulations............ 91

5.2.1. Use of Square vs Hexagonal Arrays............ 91

5.2.2. Rectangular Arrays............ 93

5.2.3. Changing Array Pitch............ 97

5.2.4. Changing Fill Factor............ 98

5.2.5. Changing Incident Radiation Elevation............ 98

5.2.6. Effect of Hole Mispositioning from Laser Ablation............ 101

5.2.7. Changing Substrate Material............ 103

5.2.8. Changing EOT Film Material............ 105

5.2.9. Changing EOT Film Thickness............ 106

5.3. UV – Near-Infrared EOT Array Simulations............ 108

5.4. Simulations of EOT Arrays with PCM Layers............ 110

5.4.1. Material Type............ 110

5.4.2. PCM Thickness............ 112

5.4.3. PCM Layer Deposition Schemes............ 114

5.4.3. Visible-NIR EOT-PCM arrays............ 119

5.4.4. THz Modulator Arrays............ 125

5.5. Thermal Modelling............ 126

5.5.1. Cooling Rates............ 127

5.5.2. Peak Temperatures Reached............ 135

5.6. Chapter Summary............ 141

6. Phase-Change EOT Devices Experimental Results............ 143

6.1. Gold EOT Arrays............ 143

6.1.1. Arrays Fabricated via E-beam Lithography............ 143

6.1.2. Mid-Infrared Arrays Fabricated via Laser Ablation 148

6.1.2.1. Comparisons between Laser Ablation and Wet-Etching 148

6.1.2.2. Non-Square Arrays 150

6.2. Phase-Change EOT Devices 154

6.2.1. PCM Optical Data Obtained Through Ellipsometry 154

6.2.2. Mid/Long-IR Tuneable Filters 160

6.2.3. Visible-NIR Tuneable Filters 163

6.2.4. Laser-Processed Devices 164

6.3. Investigation of Au/PCM Diffusion Effects 166

6.3.1. Investigation of Diffusion in Phase-Change EOT Devices 166

6.3.2. TEM imaging of Diffusing Layers in Reflection Cavities 168

6.3.3. Optical Response of Reflection Cavities 177

6.4. Chapter Summary 179

7. Conclusions and Future Work 181

8. Appendices 186

8.1. Simulation Mesh Configuration 186

8.2. Fabrication Process Notes 187

8.2.1. Metal Deposition with HHV Auto 306 Thermal Evaporator 187

8.2.2. Thickness-Check Sample Preparation 189

8.2.3. Lithography and Wet-Etching 189

8.2.4. Laser-Ablation 190

8.2.5. Sputtering with NanoPVD 191

9. References 193

1.2. List of Figures

Figure 1: (a) Experimental zero-order light transmittance, lattice period=750 nm, hole diameter of 280 nm in a freestanding 320 nm Ag film (inset: electron micrograph of the perforated metal film) taken from [23]) 31
Figure 2: Transmission spectra of a 250 nm period array with 100 nm diameter holes in a 200 nm-thick silver film on a glass substrate [31]. The black line represents transmission without the of red-absorbing dye layer and the red line the transmission with it, the latter showing the induced transmission peak starting at a wavelength of 685 nm. 37
Figure 3: (a) Array used to test for effect of QCWs and (b) normalised transmission measurements vs model-only based on surface plasmons, from [30] 38
Figure 4: (a) refractive index and (b) extinction coefficient data for different measurements of GST-225 PCM from different published cources, [55] (Source 1), [32] (Source 2) and [56] (Source 3) 42
Figure 5: Plots showing phase transition temperatures of GST-326, taken from [58], data from [60] 43
Figure 6: Schematic of an embedded microheater switching phase-change metasurface, as featured in [63] 44
Figure 7: Example uses of multispectral imaging of (a) a lung tissue sample [75] and (b) a crop field [76] 46
Figure 8: Example configurations of multispectral imaging systems, multiple interchangeable filters [77] (left) and multiple filter/lens/sensor units [78] (right) 47
Figure 9: Schematic of the operation of a tuneable filter with single sensor setup, switching through configurations (clockwise from top-left) then resetting 48
Figure 10: PCM-enhanced EOT devices displaying shift in peak wavelength, simulated (broken curves) vs measured spectra with peaks normalised to 1 (adapted from [27]) 49
Figure 11: Illustrative theoretical transmission spectra (not derived from measurements or simulations) of a phase-change EOT-based band-pass filter for a multispectral imaging system in the mid-long IR regime. Plotted various “settings”, the transmission band position depending on the PCM crystallisation. 49

Figure 12: COMSOL unit cell for a square-array EOT metasurface, with different components highlighted and enlarged in insets... 52
Figure 13: (a) Perfectly-matched layers of a COMSOL unit cell (b) FPBCs along x and y axes of a square COMSOL unit cell.. 53
Figure 14: Example COMSOL unit cell swept meshes from different perspectives (a) side-on for a square array and (b) top-down for square and hexagonal arrays, with identical array pitch, fill factor and mesh fineness settings........................ 55
Figure 15: Gold electrical resistivity and conductivity against temperature (adapted from [80])... 57
Figure 16: Components of an EOT array unit cell in COMSOL Multiphysics for electro-thermal modelling 58
Figure 17: Schematic diagram of thermal evaporation process, 22 cm between boat and substrates on block.. 61
Figure 18: Schematic diagram of magnetron sputtering process, 22 cm distance between target and substrates. 63
Figure 19: Optical microscope images of MWIR EOT arrays showing potential issues, (a) holes not clearing (b) film destruction due to over-sonication 65
Figure 20: 3D AFM scan of the surface of an EOT array fabricated via lift-off, showing unwanted build-up of metal around the hole edges........................... 65
Figure 21: 3D AFM scan of the surface of an EOT array fabricated via wet-etching, showing no unwanted build-up of metal around the hole edges, z-axis kept at the same scale as for Figure 20 66
Figure 22: Examples of how holes of different intended sizes (1, 2 and 3 μm diameters shown) have different percentage undercuts for a given etching time, with a written mask hole diameter here smaller than the final etched hole by 200 nm in every case 67
Figure 23: Segment extracted from film via FIB milling for TEM imaging 68
Figure 24: Schematic of laser-writing setup, from [4], red lines for laser-processing beam and green lines for the LED-illuminated in-situ observation path 70
Figure 25: (a) Laser-written hole diameter vs. pulse energy and (b) array period vs.scanning velocity with 1 kHz repetition rate) for NA 0.25, from [4], insets of microscope images of written arrays 70
Figure 26: Schematic diagrams of different array fabrication methods used in the work of this thesis.. 72

Figure 27: Wet-etched device at different stages of fabrication as seen through optical microscope, showing PMMA mask hole outlines and metal layers 73
Figure 28: Schematic of basic ellipsometry measurement setup...................... 74
Figure 29: FIB/SEM setup, the tiltable stage allowing the SEM imaging of vertical features of the sample as shown in the inset.. 75
Figure 30: (a) Schematic of AFM operation with (b) photographs of the sample and probe head suspended above from the front (topt) and above (bottom) ... 77
Figure 31: (a) SEM image of an example AFM probe tip [84] (and (b) schematic showing the representation of the accuracy limitations of AFM scanning 77
Figure 32: (a) Schematic of basic FTIR instrument layout [86], aperture plate (b) with and (c) without sample in place, and (d) aperture plate in Thermo-Fisher Nicolet iS5 FTIR bay 80
Figure 33: Schematic of micro-spectrophotometer optical componentry, adapted from [16], [19] 81
Figure 34: Experimental transmission intensity of a 600 nm-pitch array in 200 nm thick Ag film with 150 nm hole diameter adapted from [43]. Surface plasmon energy dispersion bands (solid lines) overlaid show positions of spectral minima against component of incident photon momentum, k_x=0 indicates beam normal to the array plane. 83
Figure 35: Dispersion relations (of square arrays in Au film on CaF_2 substrates) against beam angle for varied SP orders, e.g. “(1,0)±” meaning ±1 i and 0 j, section marked out on 4 μm-pitch array plot expanded on in Figure 36........... 84
Figure 36: Modelled 4 μm-pitch array in 40 nm Au film on CaF_2, fill-factor of 0.5 and incident radiation 30° from the array normal along the same plane as the array polarisation (see Figure 48), minima from resonance modes labelled. ... 85
Figure 37: Models of crystalline growth, adapted from [87] 86
Figure 38: calculated n values against PCM volume crystallised (fraction of crystallisation f) using the different models, for (a) 2.5 μm and (b) 5 μm incident light wavelengths... 88
Figure 39: Calculated optical data values for partially crystalline PCMs, crystallisation fraction intervals of 20% between amorphous (solid lines) and crystalline (dashed lines) states. 89
Figure 40: Calculated reflectivity values against volume crystallised (fraction of crystallisation f) using different models, at 2.5 um (left) and 5 um (right) 90

Figure 41: Simulated transmittance spectrum of a crystalline silicon etalon (ignoring Si absorption), with peaks indicated by Equation (56) marked out .. 91
Figure 42: Demonstration of polarisation (in)sensitivity of a 4 μm pitch square array (a) with fill factor of 0.5, vs its hex' (b) equivalent (array pitch adjusted to ~4.62 μm to provide peak at same wavelength, holes resized to fill factor of 0.4653 (~93% of square array fill factor) to cover same proportional area), with unit cell schematics inset 92
Figure 43: Simulated spectra demonstrating (a) the different spectra generated for square vs hex' arrays with a fill factor of 0.5 but different pitches and (b) the effect of equating the relative hole areas, square array with p=4 μm and hex' array with p=4.62 μm 93
Figure 44: Simulated transmittance spectra of a rectangular EOT array with $p_y=1.25p_x$, with incident E-field linear polarisation at different angles, 0° representing polarised along the short (x) axis and 90° along the long (y) axis 94
Figure 45: Simulated transmittance spectra of rectangular EOT arrays with $p_x=4$ μm for (a) $p_y=1.25p_x$ and (b) $p_y=1.5p$. E-field is linearly polarised along the short axis (blue) and long axis (red), fill factor relative to short axis is kept constant at ff=0.5 (solid lines) and adjusted so that the holes cover an equivalent area of the rectangular unit cell as a ff=0.5 hole in a square array (dashed lines). 96
Figure 46: Simulated transmission spectra of square EOT arrays with varied pitches, in 40 nm Au film on CaF2 substrate and hole fill-factor of 0.5 97
Figure 47: (a) Simulated spectra 4 μm pitch square EOT arrays in 40 nm Au film on CaF_2, altering hole fill factor and (b) plots of peak T and Q-factor against hole fill factor for simulated 2, 4 and 6 μm pitch square arrays in 40 nm Au film on CaF_2 98
Figure 48: Simulated transmittance spectra of a 4 μm pitch square array in 40 nm Au film on CaF_2 with the incident beam at a range of elevation angles in the same plane as the E-field polarisation, showing full wavelength range with inset beam orientation schematic (top) and a smaller section (bottom) with peaks highlighted in bold in Table 5 marked. 99
Figure 49: Simulated transmittance spectra of a 4 μm pitch square array in 40 nm Au film on CaF_2 with the incident beam at a range of elevation angles in the opposite plane as the E-field polarisation, with inset beam orientation schematic. 100

Figure 50: 4×4 hole array cell for COMSOL derived from laser-fabricated device, sample slightly rotated anti-clockwise in image so cell compensated. Laser scanning direction is along horizontal axis. 101
Figure 51: Simulation plots of 4×4 array shown in Figure 50 compared to a perfect array, 6.6 µm pitch imperfect square array in 40 nm Au film on CaF_2 substrate, hole fill factor of 0.6. 102
Figure 52: (a) Transmittance of 1 mm MgF_2 [88], CaF_2 [82] and BaF_2 [81] substrates and (b) simulated transmittance spectra of 4 µm-pitch EOT devices in 40 nm Au films on different substrate materials... 103
Figure 53: (a) Substrate refractive index derived from dispersion relation equations for MgF_2, CaF_2 and BaF_2 [89] and (b) their reflectivity in air with incident radiation at normal to surface calculated using Equation (61)......... 104
Figure 54: Comparisons of devices with and without Si_3N_4 barrier layers, in simulations with (a) PCM layers and (b) on a plain array fabricated device ... 105
Figure 55: (a) Real component of the relative permittivity/dielectric constant of various film materials derived from refractive index data and (b) simulated 4 µm pitch EOT arrays on CaF_2 substrate with fill-factor of 0.5, using different metals for the 40 nm film.. 106
Figure 56: Simulated transmission spectra for a 4 µm pitch EOT arrays on CaF_2 substrate with fill-factor of 0.5, varying the thickness of the Au film................ 107
Figure 57: (a) Transmission and (b) reflection spectra of visible to NIR EOT arrays in 40 nm Au film on CaF_2 substrates, fill factor of 0.5, varying array pitch...... 108
Figure 58: (a) Transmission and (b) reflection spectra of visible/NIR EOT arrays in 40 nm Au film on CaF2 substrates, array pitch p=400 nm with varied fill factor 109
Figure 59: Simulations of 4 um pitch EOT arrays with a 100 nm layer of notional PCM material, (a) varying n and keeping k=0 and (b) keeping n=6 and varying k 111
Figure 60: Simulated transmittance spectra of a 4 µm pitch EOT array in 40 nm Au film on CaF_2 substrate with GST-225 PCM layers of varied thicknesses, using (a) measured n and k values from [55] and (b) same measured n values with k=0 112
Figure 61: Simulated transmission spectra of (a) 2 µm and (b) 4 µm pitch EOT arrays in 40 nm Au film on CaF_2 substrates with 100 nm layers of amorphous (solid lines) and crystalline (dashed lines) PCM of different types (GST-225, GST-

326 and GSST-2241). Plots of crystalline PCM with 5% thickness reductions are also shown (dotted lines).. 114
Figure 62: Schematics of different potential structures of combining PCM layers with EOT arrays. Note that option 5 has the same total PCM film thickness as the other cases but is split across the two layers. 115
Figure 63: Simulated 4 μm pitch EOT arrays on CaF_2 substrate with fill-factor of 0.5 and 100 nm Au film, with 100 nm GST-225 PCM layers in the covering schemes shown in Figure 58 (50 nm each on top of and below the film for 5.) 117
Figure 64: E-field plots of a simulated EOT array for deposition scheme 3 (as shown in Figure 63) for amorphous GST-225 PCM, z-plane in xy plots at the film (and PCM)/substrate interface, white-dashed lines on xz and yz plots marking out film and PCM layers 118
Figure 65: H-field plots of a simulated EOT array for deposition scheme 3 (as shown in Figure 63) for amorphous GST-225 PCM, z-plane in xy plots at the film (and PCM)/substrate interface, white-dashed lines on xz and yz plots marking out film and PCM layers. 119
Figure 66: In-house ellipsometry-obtained optical data of GST-225, GST-326 and GSST-2241 PCMs (a) refractive index n (b) extinction coefficient k............... 120
Figure 67: Simulated 400 nm pitch square arrays with ff=0.5 circular holes in 40 nm Au film on CaF_2, with GST-225 layers of varied thicknesses, (a) transmittance and (b) reflectance 121
Figure 68: Simulated 400 nm pitch square arrays with ff=0.5 circular holes in 40 nm Au film on CaF_2, with GST-326 layers of varied thicknesses, (a) transmittance and (b) reflectance 121
Figure 69: Simulated 400 nm pitch square arrays with ff=0.5 circular holes in 40 nm Au film on CaF_2, with GSST-2241 layers of varied thicknesses, (a) transmittance and (b) reflectance 122
Figure 70: Modulation depths of simulated SWIR EOT arrays featuring (a) GST-225 and (b) GSST-2241 for PCM layers of various thicknesses 122
Figure 71: Optical data of Sb_2S_3 and Sb_2Se_3 PCMs, (a) refractive index n and (b) extinction coefficient k 123
Figure 72: Simulated (a) transmitted and (b) reflectance spectra of a 400 nm pitch square array with coatings of Sb_2S_3 PCM 124

Figure 73: Simulated (a) transmitted and (b) reflectance spectra of a 400 nm pitch square array with coatings of Sb_2Se_3 PCM 124
Figure 74: GST-225 n & k data in THz regime, crystallised at 300°C (from [98]) 125
Figure 75: Simulated phase-change EOT modulator (a) transmittance and (b) modulation depths for fill factors of 0.3 and 0.4, using 100 nm Au film with 175 µm pitch, on quartz substrate with 100 nm GST-225 126
Figure 76: 3D temperature plot of 400 nm pitch Joule-heating device unit cell, showing (a) the centre of the hole being coolest and (b) temperature plot of larger section of device, including more of the substrate 128
Figure 77: (a) Temperatures and (b) cooling rates at the centre of a PCM filled hole in the EOT array, while varying pulse duration (ns) 129
Figure 78: (a) Temperatures and (b) cooling rates at the centre of a PCM filled hole in the EOT array, while varying PCM thermal conductivity κ ($W\ m^{-1}\ K^{-1}$) 130
Figure 79: (a) Temperatures and (b) cooling rates at the centre of a PCM filled hole in the EOT array, while varying PCM heat capacity C ($MJ\ kg^{-1}\ K^{-1}$)........ 130
Figure 80: (a) Temperatures and (b) cooling rates at the centre of a PCM filled hole in the EOT array, while varying substrate thermal conductivity κ ($W\ m^{-1}\ K^{-1}$) 131
Figure 81: (a) Temperatures and (b) cooling rates at the centre of a PCM filled hole in the EOT array, while varying substrate heat capacity C ($J\ kg^{-1}\ K^{-1}$).... 132
Figure 82: (a) Temperatures and (b) cooling rates at the centre of a PCM filled hole in the EOT array, while varying the array pitch (nm) and keeping a constant fill factor of 0.5 133
Figure 83: (a) Temperatures and (b) cooling rates at the centre of a PCM filled hole in the EOT array, while varying the array fill factor and keeping a constant pitch of 400 nm 133
Figure 84: (a) Temperatures and (b) cooling rates at the centre of a PCM filled hole in the EOT array, while varying PCM thickness (nm), using 40 nm Au film 134
Figure 85: (a) Temperatures and (b) cooling rates at the centre of a PCM filled hole in the EOT array, while varying PCM thickness (nm), using 100 nm Au film 135
Figure 86: Schematic of temperature distribution across a unit cell during resistance/Joule heating, showing dependence on current flow direction 136

Figure 87: (a) Maximum film temperature against time and (b) peak temperatures reached in the EOT metal film for 5-50 ns re-amorphisation pulse durations. 136
Figure 88: Peak temperatures reached in the EOT metal film when varying (a) PCM thermal conductivity and (b) heat capacity 137
Figure 89: Peak temperatures reached in the EOT metal film when varying (a) substrate thermal conductivity and (b) heat capacity..................................... 137
Figure 90: Peak temperatures reached in the EOT metal film when maintaining a constant fill factor of 0.5 and varying (a) array pitch and (b) keeping a 400 nm pitch while changing fill factor... 138
Figure 91: Peak temperatures reached in the EOT metal film when altering PCM thickness, with (a) 40 nm and (b) 100 nm Au films.. 138
Figure 92: Plots of simulated (a) current and (b) cumulative energy expended of a single cell (400 nm array pitch, ff=0.5, 40 nm Au film and 20 nm PCM layer on 500 µm MgF_2 substrate) throughout pulses of 5-50 ns duration (runs shown in Figure 77/Table 21) 139
Figure 93: Plots of simulated (a) current and (b) cumulative energy expended of a single cell (200-600 nm array pitch, ff=0.5, 40 nm Au film and 20 nm PCM layer on 500 µm MgF_2 substrate) throughout the 20 ns pulse, (runs shown in Figure 82/Table 26) 139
Figure 94: Optical microscope image of the corner of an EOT array in an Au film on a CaF2 substrate, wet-etched holes with a 6.6 µm pitch 145
Figure 95: Transmission spectra for EOT arrays made in 3/40 nm Cr/Au film on calcium fluoride and with a constant fill-factor (hole diameter proportional to array period) of 0.6. Experimental (FTIR measured) results shown as solid lines, with COMSOL simulations as dotted lines... 145
Figure 96: SEM image of a 300 nm pitch inverse-design disc/meta-atom array on an oxidised silicon substrate... 146
Figure 97: Example experimental reflectance spectra of disc arrays on oxidised silicon, (a) maintaining a constant designed relative disc diameter to array period of 0.45 and (b) with a constant array pitch of 350 nm..................................... 147
Figure 98: Example measured transmission spectra of disc arrays fabricated via lift-off on calcium fluoride (a) maintaining a constant relative disc diameter to array period of 0.25 and (b) with a constant array pitch of 350 nm.......................... 147

Figure 99: Transmission spectra of laser-ablated EOT (dotted lines) arrays vs wet-etched (solid lines), constant fill-factor of 0.6, 3/40 nm Cr/Au film on calcium fluoride, transmittance normalised to the substrate 148
Figure 100: Scanning-electron microscope image of a typical laser fabricated EOT array, showing stitching errors between adjacent rows 150
Figure 101: SEM images of hexagonal arrays fabricated via laser ablation, with low and high pulse intensities respectively giving (a) smaller and (b) larger holes 150
Figure 102: SEM images of rectangular arrays (with p_x=3 μm and p_y=6 μm) fabricated via laser ablation, with (a) identical holes and (b) alternating hole sizes along the rows. Note that issues of stitching errors had been resolved by the time these arrays had been fabricated. 151
Figure 103: FTIR spectra of hexagonal arrays without linear polariser and under various incident polarisation conditions 151
Figure 104: FTIR spectra of rectangular arrays without linear polariser and under various incident polarisation conditions (also including mean of E_x and E_y) ... 152
Figure 105: Transmittance of linear polariser used, orientations corresponding to those used for the array measurements 153
Figure 106: FTIR spectra of hexagonal arrays, all measurements normalised to the substrate alone 153
Figure 107: FTIR spectra of rectangular arrays, all measurements normalised to the substrate alone 154
Figure 108: Measured GST PCM (a) n and (b) k in visible-NIR range 155
Figure 109: GST PCM (a) n and (b) k in visible-SWIR range, from [72] 155
Figure 110: Psi and delta values obtained via mid-long infrared range ellipsometry of PCM samples, with example model fittings overlaid. 156
Figure 111: Measured GST PCM (a) n and (b) k in mid-long infrared range .. 157
Figure 112: GST PCM (a) n and (b) k in mid-long infrared range, from [55]... 157
Figure 113: (a) SEM image of GST-225 target area measured via EDS, (b) EDS data plot and (c) samples mounted for EDS measurements in machine. 158
Figure 114: Schematic cross-section of a phase-change EOT device, showing (a) a schematic of how the PCM layer covers the metal film and fills the array holes and (b) a cross-section SEM image of a fabricated device, trench etched out with focused ion beam milling. 160

Figure 115: Transmission spectra of measurements vs simulations (using optical data from [55]) of wet-etched phase-change EOT devices in 40 nm Au films on CaF_2, with (a) 70 nm GST-225 (crystallised by heating for 3 minutes on 150°C hotplate, using 1 minute intervals) and (b) 100 nm GST-326 (crystallised by heating for 5 minutes on 300°C hotplate, shortest time tested and no change observed after further heating) 161
Figure 116: Transmission spectra of measurements vs simulations (using optical data obtained by ellipsometry) of wet-etched phase-change EOT devices in 40 nm Au films on CaF_2, with (a) 70 nm GST-225 and (b) 100 nm GST-326...... 162
Figure 117: Exemplar reflection and transmission spectra for 'inverse-design' visible-NIR disc arrays with 15 nm of GST-225 PCM and 8 nm barrier and capping layers. (a) Reflectance spectra of a 400 nm pitch disc array with d=0.5p on oxidised silicon and (b) transmittance spectra of 350 nm pitch disc array with d=0.25p on calcium fluoride 164
Figure 118: Measured and simulated transmission spectra (simulated using optical data obtained by ellipsometry) of laser-ablated phase-change EOT device in 40 nm Au film on CaF_2, with 100 nm GST-326 layer, simulated fill factor of 0.61 165
Figure 119: Transmission spectrum of 4 um-pitch EOT array in 3/40 nm Cr/Au film with a 70 nm GST-225 layer. There was no barrier layer between the gold and the GST (though there was an 8 nm Si_3N_4 capping layer). The transmission peak almost completely degraded upon heating. 167
Figure 120: Optical microscope images of phase-change EOT arrays (a) before and (b) after heating, showing evidence of gold diffusion.............................. 167
Figure 121: Transmission spectra of 4 um-pitch EOT device in 5/90 nm Cr/Au film on CaF_2 substrate both before (grey line) and after (yellow) line the deposition of an 8 nm Si_3N_4 layer on top of the gold layer.. 168
Figure 122: Cross-section TEM images of diffusion test samples using 20 nm GST-225 PCM both (a) without and (b) with S_3iN_4 barrier layers, alongside schematic diagrams illustrating the layer structure... 169
Figure 123: EDS maps of 20 nm-thick GST diffusion test samples, with (a) no barrier layer and (b) 8 nm Si_3N_4 barrier, with position "zero" points (where the deposited layers meet the substrate) indicated 170
Figure 124: EDS scans of 20 nm PCM diffusion sample without a barrier layer 171

Figure 125: EDS scans of 20 nm PCM diffusion sample with a barrier layer.. 172
Figure 126: Cross-sectional TEM images of diffusion test samples using 220 nm GST-225 PCM both (a) without and (b) with barrier layers, alongside schematic diagrams illustrating layer composition.. 173
Figure 127: EDS maps of 220 nm-thick PCM diffusion test samples, with (a) no barrier layer and (b) 8 nm Si_3N_4 barrier, with position “zero” points (where the deposited layers meet the substrate) indicated 174
Figure 128: EDS scans of 220 nm PCM diffusion sample without a barrier layer 175
Figure 129: EDS scans of 220 nm PCM diffusion sample with a barrier layer 176
Figure 130: Microspectrometer measurements of reflection cavities with 20 nm GST-225 PCM layers (solid lines) and simulations of equivalent devices (without factoring in PCM diffusion for no-barrier structure) in COMSOL (dashed lines) 178
Figure 131: FTIR reflectance measurements of reflection cavities with 220 nm GST-225 PCM layers (solid lines) and simulations of equivalent devices (without factoring in PCM diffusion for no-barrier structure) in COMSOL (dashed lines) 179
Figure 132: Device fabricated to test electrical properties, red circle in the centre of strip 2 marking out an array.. 185
Figure 133: COMSOL swept mesh cross sections with fineness settings (4 μm array pitch with ff=0.5 in 40 nm Au on CaF_2) with comparative run durations, alongside the models’ corresponding simulated transmittance spectra.......... 186
Figure 134: Transmission spectra for COMSOL simulations of same basic model shown in Figure 133 (with “Fine” mesh setting) altering the height of the cell between transmitting and receiving ports (given as a multiple of the array period), small range inset to show anomalous peak at 4 μm in more detail). 187

1.3. List of Tables

Table 1: Peak data for simulated arrays shown in Figure 44............................ 95
Table 2: Peak data for simulated arrays with $p_y=1.25*p_x$ shown in Figure 45... 96
Table 3: Peak data for simulated arrays with $p_y=1.5*p_x$ shown in Figure 42..... 96
Table 4: Changes in main EOT peak properties with array pitch...................... 98

Table 5: Calculated positions of peak minima (to nearest 0.05 μm) for 4 μm pitch EOT array in Au on CaF_2 substrate, for range of incident beam angles, points marked out on table in bold are shown on Figure 48....................................... 99
Table 6: Peak transmittance and Q-factor of simulated arrays in Figure 49... 100
Table 7: Displacement of holes along horizontal axis (rightwards positive) as fractions of the array period. Cell "zeroed" on row 1, column 1, marked in **bold**. 102
Table 8: Peak transmittance and Q-factor of simulated arrays in Figure 56... 107
Table 9: Tabulated results of transmission simulations shown in Figure 57... 109
Table 10: Tabulated results of transmission simulations shown in Figure 58. 110
Table 11: Tabulated results of simulations shown in Figure 59 (a)................. 111
Table 12: Tabulated results of simulations shown in Figure 59 (b)................. 111
Table 13: Effect of increasing PCM layer thickness for amorphous PCM from Figure 60 (k=0).. 112
Table 14: Effect of increasing PCM layer thickness for crystalline PCM from Figure 60 (a).. 113
Table 15 Effect of increasing PCM layer thickness for crystalline PCM (with k=0) from Figure 60 (b).. 113
Table 16: Effect of increasing PCM layer thickness on shift characteristics as seen in Figure 60 (left) 113
Table 17: Plot data from NIR EOT simulations shown in Figure 70................ 123
Table 18: Visible-NIR EOT simulation data using low-loss (in this range) PCMs 125
Table 19: Comparison of simulated modulator properties, “Peak T” given for filter as a whole in its most transmissive state 126
Table 20: Thermal properties of materials used in simulations, amorphous GSST-2241 from [63]*, gold from standard values used in the built-in COMSOL materials, MgF_2 from* [88]... 127
Table 21: Pulse voltage and peak current applied to devices in Figure 77..... 129
Table 22: Pulse voltage and peak current applied to devices in Figure 78..... 130
Table 23: Pulse voltage and peak current applied to devices in Figure 79..... 131
Table 24: Pulse voltage and peak current applied to devices in Figure 80..... 131
Table 25: Pulse voltage and peak current applied to devices in Figure 81..... 132
Table 26: Pulse voltage and peak current applied to devices in Figure 82..... 133
Table 27: Pulse voltage and peak current applied to devices in Figure 83..... 134

Table 28: Pulse voltage and peak current applied to devices in Figure 84..... 134
Table 29: Pulse voltage and peak current applied to devices in Figure 85..... 135
Table 30: Effects of changing device and material properties on phase-change EOT bandpass filter performance.. 141
Table 31: Comparison of peak properties for EOT arrays made with different fabrication methods, wet-etching (WE) and laser ablation (LA)...................... 149
Table 32: Positions of element emission peak observed for in-house EDS measurements of GST PCM samples [105]. 158
Table 33: Expected compositions of GST PCMs.. 159
Table 34: Calculated percentages of GST PCM elements in sputtering targets deposited films. Any elements not featured in the PCM (e.g. from substrate, barrier and capping layers) are not included in the total. 159
Table 35: Performance metrics of wet-etched phase-change EOT device with 70 nm GST-225 layer shown in Figure 115 and Figure 116................................ 162
Table 36: Peak shift properties of wet-etched phase-change EOT device with 70 nm GST-225 layer shown in Figure 115 and Figure 116................................ 163
Table 37: Performance metrics of wet-etched phase-change EOT device with 100 nm GST-326 layer shown in Figure 115 and Figure 116................................ 163
Table 38: Peak shift properties of wet-etched phase-change EOT device with 100 nm GST-326 layer shown in Figure 115 and Figure 116................................ 163
Table 39: Key performance metrics of laser-ablated phase-change EOT device with 100 nm GST-326 layer, extracted from Figure 118................................. 165
Table 40: Peak shift properties of laser-ablated phase-change EOT device with 100 nm GST-326 layer, extracted from Figure 118 166
Table 41: Laser-ablation setup configuration details 191

1.4. Abbreviations

AFM	Atomic force microscope/microscopy
AIT	Absorption-induced transparency
am	Amorphous
AR	Aspect ratio
CMYK	Cyan, magenta, yellow and black
cr	Crystalline
EBL	Electron-beam lithography
EDS	Energy dispersive x-ray spectroscopy
E-field	Electromagnetic field
EOT	Extraordinary optical transmission
FPBC	Floquet periodic boundary conditions
FF	Fill factor
FIR	Far-infrared
FTIR	Fourier transform infrared spectroscopy
FWHM	Full-width half-maximum
GSST-2241	$Ge_2Sb_2Se_4Te_1$ alloy
GST-225	$Ge_2Sb_2Te_5$ alloy
GST-326	$Ge_3Sb_2Te_6$ alloy
IR	Infrared
LEOT	Localised extraordinary optical transmission
LSP	Localised surface plasmon
MIR	Mid-infrared
NIR	Near-infrared
PCM	Phase-change material
PML	Perfectly-matched layer
QCW	Quasi-cylindrical waves
Q-factor	Quality factor
RGB	Red, green and blue
SEM	Scanning electron microscope/microscopy
SEOT	Surface extraordinary optical transmission
SP	Surface plasmon
SPP	Surface plasmon polariton
TEM	Transmission electron microscope/microscopy

1.5. Conferences Contributions

- E. Humphreys, J. Bertolotti and C. D. Wright, "Phase-Change Extraordinary Optical Transmission Metasurfaces for Active Filtering and Modulation from the Visible to Terahertz Regimes" in *12th International Conference on Metamaterials, Photonic Crystals and Plasmonics (META 2022 Torremolinos - Spain)*, Torremolinos, 19 – 22 July 2022, pp. 949-950, [Online]. Available: https://metaconferences.org/META/index.php/META2022/proceeding [Accessed: 20-Apr-2023] [1]

- E. Humphreys, J. Bertolotti, C. D. Wright, "Filtering and Modulation from Visible to Terahertz using Phase-Change Extraordinary Optical Transmission Metasurfaces" in *European Phase-Change and Ovonic Symposium (E\PCOS 2022)*, Wolfson College, Oxford, 18 – 21 September 2022, pp. 4-5. [2]

1.6. Journal Publications

- C. Ruiz de Galarreta, S. G. Carrillo, Y-Y Au, E. Gemo, L. Trimby, J. Shields, E. Humphreys, J. Faneca, L. Cai, A. Baldycheva, "Tunable optical metasurfaces enabled by chalcogenide phase-change materials: from the visible to the THz" *Journal of Optics*, vol. 22, no. 11, pp. 114001-114001, 2020, doi:10.1088/2040-8986/abbb5b [3]

- C. Ruiz de Galarreta Fanjul, N. Casquero, E. Humphreys, J. Bertolotti, J. Solis, C. D. Wright and J. Siegel, "Single-Step Fabrication of High-Performance Extraordinary Transmission Plasmonic Metasurfaces Employing Ultrafast Lasers" *ACS Applied Material Interfaces*, vol. 14, no. 2, pp. 3446-3454, 2022, 10.1021/acsami.1c19935 [4]

- E. Humphreys, J, Bertolotti, C. Ruiz de Galarreta Fanjul, N. Casquero, J. Siegel and C. D. Wright, "Filtering and Modulation from the Infrared to the Terahertz using Phase-Change Extraordinary Optical Transmission Metasurfaces" *physica status solidi (RRL)–Rapid Research Letters*, 2023, doi: 10.1002/pssr.202200474 [5]

1.7. Acknowledgements

There are a multitude of people who I wish to thank for all of the support that made this work possible.

First of all are my PhD supervisors, C. David Wright and Jacopo Bertolotti, for the incomparable efforts in guiding and supporting me during my PhD.

From within my research group, I wish to thank Liam Trimby, Carlota Ruiz de Galarreta Fanjul, Santiago Garcia Cuevas Carrillo, Joe Shields, Joe Pady, Emanuele Gemo and Yat-Yin Au, who were always ready to share their knowledge, data and experience. Among the other researchers at the University of Exeter there is Philip Thomas for performing UV-NIR ellipsometry measurements and also Hannah Barnard, Prarthana Dakappa and Huanling Zou for kindly giving their time and expertise to provide additional FTIR measurements on equipment kindly provided courtesy of Geoff Nash.

Thanks to Mark Heath and Hong Chang, respective Experimental Officers for the Physics Building cleanroom and Harrison Building Imaging Suite facilities, for providing both the equipment and training necessary to make and test the fabricated devices, and thanks too to Heather Ford, Emily Wong, Cameron Clark, Anna Bate, Charlotte Lopez, Tyree Hook and Lesley Rigby of the Biosciences Teaching Laboratory for making their FTIR equipment and facilities available for my use.

Others at the University of Exeter to whom I wish to extend my gratitude include my pastoral tutor Ian Hooper, Anja Roeding of the CRMI, Lesley Van Der Merwe of Procurement and Jade Hayes, the UoE TEAM-A Programme Support Officer. Also of the TEAM-A collaboration is Chris Lawrence, of QinetiQ.

And finally, I would like to acknowledge all of my family and friends, who have never ceased to encourage me in my journey to become a research scientist.

1.8. External Research Collaborators

- Jan Siegel, Noemi Casquero Maroto and Carlota Ruiz de Galarreta Fanjul at the CSIC Instituto de Optica in Madrid, who developed techniques of laser ablation of thin films and performed the laser patterning work on EOT devices fabricated using this process that are featured in this thesis.

- Geoff West of the University of Warwick, who performed TEM imaging and EDS characterisation of samples prepared for investigation of gold/phase-change layer inter-diffusion effects.

- Lou Deguzman of the University of North Carolina at Charlotte as part of the EPSRC AMETA project (grant no. EP/W003341/1), who provided mid-IR ellipsometry measurements of various GeSbTe compositions used in this thesis.

2. Introduction

This thesis covers a specific area in the broad field of light filtration, how can a device be made to output light with certain properties different to that inputted? This can take the form of restricting polarisations compared to the source; reducing transmitted/reflected intensity overall (such as neutral density filters for photography) and reducing the output intensity of specific “colours” (energies, wavelengths, frequencies etc.) to create bandpass or bandstop filters, respectively absorbing and transmitting/reflecting little/none of the incident light but for within a relatively small defined region. The ability to control colour (and radiation wavelength in general) is important in so many aspects of life, not just for aesthetic reasons in the visible (~400-700 nm wavelength) regime, but for enabling modern systems of communication; shielding people and technology alike from harm and enabling new discoveries to made in a myriad of scientific fields.

The “traditional” method of controlling colour (within the visible regime at least) has often been to use various absorbing pigments/dyes, with additive (RGB) and subtractive (CMYK) systems serving different purposes. In more recent times though, it has been understood that other properties can also contribute to colour control, from differing refractive indices allowing refraction via a prism to separate out the spectrum of a white light source to the brilliant blue hue emanating from the naturally occurring structures of diffraction gratings in the wings of a blue morpho butterfly.

The method on which almost all the work in this thesis is based is the phenomenon of extraordinary optical transmission (EOT), selectively allowing the transmission of incident light energies by patterning arrays of holes in thin films of plasmonic materials to create a metasurface. The EOT effect has only been studied for a relatively short time (the first publications dating from just twenty-five years ago) but it has been investigated extensively since it was first identified and observed to occur from the UV to THz regimes, opening new possibilities in the field of filtration. It is hypothesised here that one of these possibilities is being able to create tuneable filters via the addition of phase-change materials (PCMs) to the EOT array, potentially enabling the transmissive/reflective properties of

these metasurfaces to be repeatedly non-destructively altered by switching the phase-state of the PCM layer and in turn changing the PCM layer's refractive index. Other methods exist for tuning metasurfaces to alter their electromagnetic response, including: from mechanical actuation (whether deforming a structure [6], moving separate elements in relation to each other to change their interaction [7] or acting independently [8]); using water or some other liquid as an active element to effectively alter the device structure [9], [10]; using sandwiches of metasurfaces around an liquid-crystal layer [11], [12] and the electrically-tunable properties (e.g. chemical potential) of graphene [13], [14].

The primary figures of merit used to evaluate performance are peak transmittance *T*, the percentage of light allowed through the filter at the most transmitting wavelength, and the quality-factor (also called Q-factor) of the main transmission peak, how wide a range of wavelengths are significantly transmitted. Other factors include the degree of peak wavelength shift and the transmittance contrast ratios, with different characteristics required by different types of devices.

2.1. Outline

The general aim of the work presented here was to investigate how the transmissive/reflective properties of extraordinary optical transmission metasurfaces can be altered by the introduction of phase-change materials to create tuneable bandpass filters. This section will provide an overview of the content of the following chapters.

Chapter 3 contains the relevant background information regarding the science involved in this work, including: metasurfaces and their applications in general; the extraordinary optical transmission (EOT) effect and the significance of phase-change materials (PCMs) and how they can be implemented in EOT devices to add tuneability.

Chapter 4 describes the different methods used in this thesis, both for computational and experimental processes. The former covers modelling and simulation techniques used to simulate electromagnetic device characteristics in order to establish the necessary design parameters to achieve the desired

performance and provide a basis for comparison with the fabricated samples and devices. Additional modelling was performed to investigate device electro-thermal characteristics during in-situ Joule heating. Experimental methods concern the different processes involved in sample and device fabrication and characterisation, including the methods used to ascertain the properties of the device materials, the techniques used to deposit and pattern them, and the ways in which device performance was assessed.

Chapter 5 features modelling and simulation results, both electromagnetic and electro-thermal, conducted to evaluate how altering device characteristics affects performance and to determine suitable design parameters for fabricated devices. These properties include both geometric dimensions and material data (for optical simulations the refractive index *n* and extinction coefficient *k*, for thermal simulations the thermal conductivity and heat capacity). Material properties are modelled both simplistically (e.g. *n* is fixed for all wavelengths and *k* varied alone to investigate how it alone effects performance) and realistically (actual material data is used, *n* and *k* varying with wavelength).

Chapter 6 covers experimental results of devices made practically, including the effect of differing device dimensions on device performance; the use and comparison of $Ge_2Sb_2Te_5$ (GST-225) and $Ge_3Sb_2Te_6$ (GST-326) PCMs; array fabrication with wet-etching and laser-ablation techniques; the efficacy of silicon nitride barrier layers to prevent metal/PCM diffusion, using reflection cavities of GST-225 on gold films with and without barriers.

Chapter 7 provides some general conclusions and suggestions for future work.

2.2. Objectives

The overall objectives of the work of this thesis can be concisely summarised as follows:

- Study how different aspects of EOT device design and fabrication affect optical performance, in both models/simulations and in practice:
  - Varying device geometric parameters

    - Varying materials used
    - Exploring different array fabrication techniques and how their characteristics factor into how devices can be constructed

- Assess the addition of PCMs to add tuneability to EOT devices:
    - Identifying desired optical properties for different filter applications, matching the PCM type to arrays with appropriate properties at the desired working wavelength ranges
    - Studying the effects of PCM layer geometry, both thickness and the different structures resulting from different array fabrication methods
    - How diffusion of PCMs and metal layers affects phase-change EOT device performance and how this can be mitigated with barrier layers
    - How PCM layers might be switched between states using Joule heating of the EOT film, and how their thickness and thermal properties affect heating and cooling rates

3. Background and Theory

This chapter will cover the conceptual ideas on which the research in this thesis is founded, the topics broadly being: metasurfaces and extraordinary optical transmission (EOT); phase-change materials (PCMs); multispectral imaging and how a filter for multispectral imaging using EOT and PCMs could be constructed.

Some types of metasurfaces are described with emphasis being placed on the phenomenon of extraordinary optical transmission (EOT), a core concept on which the light filters being developed in this project are based on. Phase-change materials (PCMs) are then described, with discussion of their properties, applications and how they are manipulated. The specific topic of multispectral imaging is then focused on, with its uses and current technologies explored. Design, fabrication and modelling techniques for a tuneable filter combining EOT and PCM technologies are then described.

3.1. Metasurfaces

The development of metasurfaces started in the early 1970s [15], but has become more prevalent with the advancement and ubiquity of nanofabrication techniques. Metasurfaces are essentially flat metamaterials, periodically structured artificial materials designed to provide properties not found in nature. These properties are obtained by careful selection of the metasurface geometry and material so as to manipulate the way they will interact with the incident radiation. These capabilities include band-pass/stop filtration [16]; reflective and transmissive lensing [17], beam steering [18], [19], and various forms of polarisation control [20], [21] (e.g. creating a linear polariser with greater transmission efficiency than the ~20-25% seen later in Figure 105).

3.2. Extraordinary Optical Transmission

3.2.1. Overview

Light will easily propagate through apertures in opaque materials when the incident wavelength is much smaller than the hole diameter, with the percentage

transmitted being equal to the proportional area of the hole to area that the light is falling on. In 1944 Bethe et al. [22] showed that when the hole size (radius r) approaches the wavelength (λ), the transmission efficiency η_B of far-field radiation reduced dramatically as shown in Equation (1).

$$\eta_B = \frac{1024\pi^2}{27}\left({}^{r}/_{\lambda}\right)^4 \qquad (1)$$

This theory was accepted to apply in all cases until Ebbesen et al. demonstrated the effect of extraordinary optical transmission (EOT) in 1998 [23]; as shown in Figure 1, an array of sub-wavelength holes in a thin silver film demonstrated transmission many orders of magnitude greater than the Bethe theory would seem to suggest.

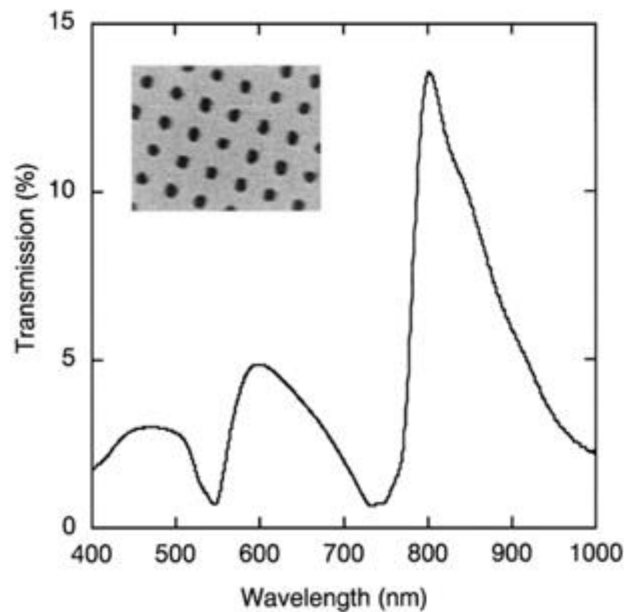

Figure 1: (a) Experimental zero-order light transmittance, lattice period=750 nm, hole diameter of 280 nm in a freestanding 320 nm Ag film (inset: electron micrograph of the perforated metal film) taken from [23]*)*

In fact, when normalising the proportional area of the holes to that of the whole array, the peak transmission values can be greater than 100% (example in Figure 1 is 125%), indicating that light incident on the film itself, rather than just the hole, is being transmitted. The effect is allowed because in certain materials, particularly the noble metals such as silver and gold [24], the apertures modify the film's EM fields with many different phenomena believed to contribute

including surface enhanced optical transmission (SEOT), localised enhanced optical transmission (LEOT) and quasi-cylindrical waves (QCWs). Transmission has been observed in many different scenarios with variations including hole size, hole shape, hole distribution and film patterning, each of which will be further discussed. These geometric factors allow the spectra to be modified to suit the device requirements during the design stages, with more flexibility than simpler structures such as Fabry–Pérot cavities/etalons (which, as seen in Figure 41, also produce peaks of comparable height rather than a single sharp one with the others suppressed),

The EOT effect used in the devices described in this thesis is to provide the initial bandpass filter, with tuneability provided by additional elements. Focus will be placed on the mid/long infrared regimes as this is particularly useful for thermal imaging, but investigations were also conducted regarding EOT in the THz regime. Despite the effect being titled extraordinary **optical** transmission, it applies to a wide range of EM regimes including ultraviolet [25], visible [23], [26], infrared [27] and THz [28] & [29].

3.2.2. Types of Extraordinary Optical Transmission Mechanisms

The initial theories explaining EOT focused on surface plasmons/surface plasmon polaritons (SPs/SPPs), oscillations of free electrons occurring at the interfaces of the metal film and surrounding dielectrics. The presence of holes modifies the momentum characteristics of the SPs; incident light couples to them on one surface and they in turn couple to SPs on the other surface so the light can be re-radiated on the opposite side. More recently, the contribution of quasi-cylindrical waves (QWCs) has been demonstrated [30] and, in certain circumstances, absorption-induced transparency (AIT) [31].

In this thesis, EOT effects will mainly concern periodic square arrays of holes, the most common arrangement, with period (centre to centre separation) p, but it is noted that other publications have demonstrated the effect with hexagonal lattice arrays [27], [32]. The effect has also been observed in single holes [33]–[36], random arrays [37], [38], and quasiperiodic arrays [39].

3.2.2.1. Surface Enhanced Optical Transmission

Surface enhanced optical transmission (SEOT) is considered as one of the main mechanisms behind EOT, describing the coupling of incident light to surface plasmons in the metal film. For a flat and unpatterned metal-dielectric interface, it is difficult for the incident radiation to couple to the surface plasmons because of a lack of conservation of energy and momentum [40]; a periodic array allows coupling by modifying the characteristics of the surface modes and relaxing momentum conservation. The large local density of the EM states associated with surface modes gives a highly efficient coupling; light that would otherwise be reflected remains at the interface and is instead transmitted. Individual transmittance of each hole is still small, but it is effectively constantly being re-illuminated by the surface modes [41]. The mechanism should occur when two localised modes are weakly coupled between themselves (through the holes) and to a continuum, thus SEOT can also be expressed as a Fano resonance [42].

Equation (2) describes momentum conservation in a square/rectangular array with rows and columns along the x and y axes and an E_x linear polarised incident beam. When coupling occurs, momentum is conserved by allowing the coupling of the SP wavevector $\boldsymbol{k_{SP}}$ to that of the incident light $\boldsymbol{k_x}$ [43] ($\boldsymbol{k_x}$ represents the component of the momentum along the x-axis).

$$\overrightarrow{k_{SP}} = \overrightarrow{k_x} \pm i\overrightarrow{G_x} \pm j\overrightarrow{G_y} = (k_x \pm i|G_x|)\hat{x} \pm j|G_y|\hat{y} \qquad (2)$$

with $\boldsymbol{G_x}$ and $\boldsymbol{G_y}$ representing the array's reciprocal lattice vectors and *i* and *j* being integers representing the different reciprocal lattice orders. The relationship between the reciprocal lattice vectors and array period *p* for a square array (p_x=p_y) is given by Equation (3)

$$\left|\overrightarrow{G_x}\right| = \left|\overrightarrow{G_y}\right| = \frac{2\pi}{p} \qquad (3)$$

For a beam that is angled by θ to the surface normal along the xz plane, the component of incident momentum k_x along the x direction is related to the total

momentum k by Equation (4) and so equals zero when the beam is at normal to the surface. k is related to light wavelength λ by Equation (5).

$$k_x = k \sin\theta \qquad (4) \qquad\qquad k = \frac{2\pi}{\lambda} \qquad (5)$$

All this means that Equation (2) can be rewritten in terms of more convenient variables, as shown in Equation (6)

$$\overrightarrow{k_{SP}} = \frac{2\pi}{p}\left(\frac{p \sin\theta}{\lambda} \pm i\right)\hat{x} \pm j\hat{y} \qquad (6)$$

with the total magnitude of momentum being given by Equation (7)

$$\left|\overrightarrow{k_{SP}}\right| = \frac{2\pi}{p}\sqrt{\left(\frac{p \sin\theta}{\lambda} \pm i\right)^2 + j^2} \qquad (7)$$

The magnitude of surface plasmon momentum can also be given in terms of relative permittivity (sometimes called the dielectric constant, despite being wavelength-dependent) of the film ε_f and substrate/superstrate ε_s as shown in Equation (8)

$$\left|\overrightarrow{k_{SP}}\right| = \frac{\omega}{c}\sqrt{\frac{\varepsilon_f \varepsilon_s}{\varepsilon_f + \varepsilon_s}} = \frac{2\pi}{\lambda_{SP}}\sqrt{\frac{\varepsilon_f \varepsilon_s}{\varepsilon_f + \varepsilon_s}} \qquad (8)$$

Equating Equations (7) and (8) gives Equation (9)

$$\frac{1}{\lambda_{SP}}\sqrt{\frac{\varepsilon_f \varepsilon_s}{\varepsilon_f + \varepsilon_s}} = \frac{1}{p}\sqrt{\left(\frac{p \sin\theta}{\lambda} \pm i\right)^2 + j^2} \qquad (9)$$

which rearranged gives the positions of the transmission spectrum minima (wavelengths where the incident light momentum resonates perfectly with that of an SPP mode, giving a transmission of zero) in Equation (10)

$$\lambda_{SP} = \frac{\sqrt{\frac{\varepsilon_f \varepsilon_s}{\varepsilon_f + \varepsilon_s}}}{\sqrt{\left(\frac{p \sin\theta}{\lambda} \pm i\right)^2 + j^2}} p \qquad (10)$$

All fabricated devices in this thesis involved measuring with the array surface normal to the path between the light source and detector (θ equals zero) giving the simplified relation in Equation (11) of

$$\lambda_{SP} = \frac{\sqrt{\frac{\varepsilon_f \varepsilon_s}{\varepsilon_f + \varepsilon_s}}}{\sqrt{i^2 + j^2}} p \qquad (11)$$

For the first-order modes (when i=1 and j=0 or vice-versa), Equation (11) is further reduced to Equation (12)

$$\lambda_{SP} = \sqrt{\frac{\varepsilon_f \varepsilon_s}{\varepsilon_f + \varepsilon_s}} p \qquad (12)$$

giving the longest wavelength minimum featured in the transmission spectrum, which precedes the main peak. When $\varepsilon_f >> \varepsilon_s$, this simplifies to Equation (13)

$$\lambda_{SP} = \sqrt{\varepsilon_s} p = n_s p \qquad (13)$$

giving the essential basic relation showing the dependence of the main transmission peak position on the array pitch p and refractive index of the surrounding material n_s in an EOT device. This is approximately equal to the Rayleigh wavelength λ_R, the minimum wavelength for which incident radiation is transmitted as a single diffraction order, with all other diffraction orders being evanescent [44]).

The factors shown in Equation (13) are what mainly determine the behaviour of an EOT array, with other factors such as hole size, depth and shape affecting the shape of transmission peaks, but not the resonance positions. If materials with different refractive indices are used for the substrate and superstrate (e.g. a glass

disc substrate underneath with air on top), each SP mode will produce a separate set of minima for each value of n_s (i.e. that of the substrate and that of the superstrate). The main peak position is then determined by the material with the highest n_s. Transmission is most enhanced when the substrate and superstrate have the same refractive index [45], however in many cases this is not practical.

To change the position of the main transmission peak Equation (13) presents two potential options, either change the array period or the refractive index of the surrounding materials. The former approach might be realised by using some kind of flexible/stretchable metasurface (an example using resonators can be seen in [6]), but this is not explored in this thesis. The latter approach, i.e. changing the refractive index of surrounding materials, is explored and can be achieved by use of phase-change materials (PCMs) whose refractive index differs markedly in value dramatically between its crystalline and amorphous states, and which can be switched readily between these states (see Section 3.3. for more details on PCMs).

3.2.2.2. Localised Enhanced Optical Transmission

This is the EOT effect that occurs with a single hole in a film, and for random arrays and distributions where the holes are far enough apart to be considered isolated. The operating wavelength regime depends on the material properties as for SEOT, but also on the hole shape and size (including film thickness) rather than hole spacing [37]. SP modes can also be enhanced by the presence of structures such as corrugations around the holes to reflect and contain the modes [34], as well as by filling the hole(s) with a high refractive index material [46]. Since none of these localised effects were exploited in the work of this thesis, the reader is referred to the literature cited for further information on this topic.

3.2.2.3. Absorption-Induced Transparency

The transmission spectra of a hole array in a film can sometimes be non-intuitively modified by the addition of an absorbing material [31], [47]. It is thus known as absorption-induced transparency (AIT), though the effect is not

necessarily linked to surface plasmons thus limited to regular arrays or dependent on hole positioning.

In the example shown in Figure 2 (from [31]), a 30 nm layer of red-absorbing dye (cyanine J-aggregate) is applied to a 250 nm-pitch array in a silver film induces a red transmission peak in a region that is non-transmissive in the dye's absence.

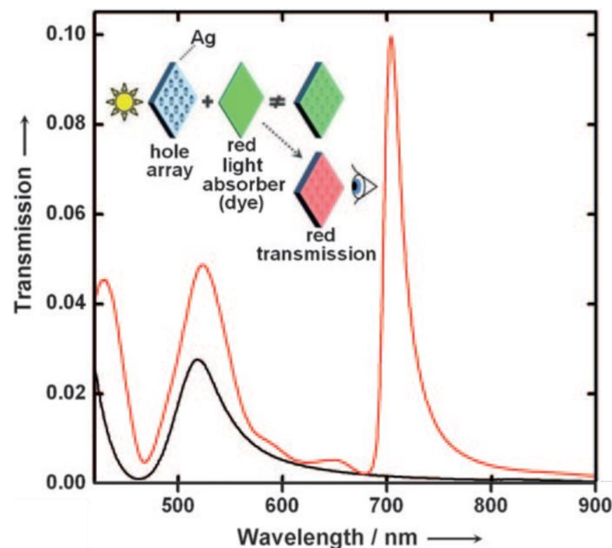

Figure 2: Transmission spectra of a 250 nm period array with 100 nm diameter holes in a 200 nm-thick silver film on a glass substrate [31]. *The black line represents transmission without the of red-absorbing dye layer and the red line the transmission with it, the latter showing the induced transmission peak starting at a wavelength of 685 nm.*

This works due to the interaction of dye molecules in close proximity to the interface (within 20 nm) with free electrons in the metal via dipole coupling. A frequency region is forced into existence by Kramers-Kronig relations where the real and imaginary dielectric constants of the dye are relatively large and small, which can allow a propagating waveguide mode to open or a weakly-bound surface mode becoming more strongly-bound [44]. Since this area was not explored in the work of this thesis, the reader is referred to the literature cited for further information on this topic.

3.2.2.4. Quasi-Cylindrical Waves

The quasi-cylindrical wave (QCW) field is described as the field diffracted by a subwavelength indentation/hole in a surface. In a perfect electrical conductor, the QCW is a cylindrical wave in free space decaying as $1/x^{1/2}$ (with x being the distance from the hole/scatterer): for metals (with finite conductivity at the incident wavelength) the QCW is only seen over a short range (only a few wavelengths), the decay rate being $1/x^{3/2}$ at large distances from the scatterer. As the distance between the holes increases the field coupling them weakens, with the significance of the QCWs being greatest when the holes are close together and becoming less significant when they are far apart. The contributions of QCWs was proposed by van Beijnum in 2012, by comparing predictions with a purely SPP analytical model against measured spectra [30] in 150 nm Au films on glass (with a 20 nm Cr layer to dampen SPPs at the metal/air interface), where arrays were made with chains of holes with a constant array period along the y-axis (a_y= a_0=450 nm) and varied spacing between the chains a_x=qa_0, where q=1, 2…7.

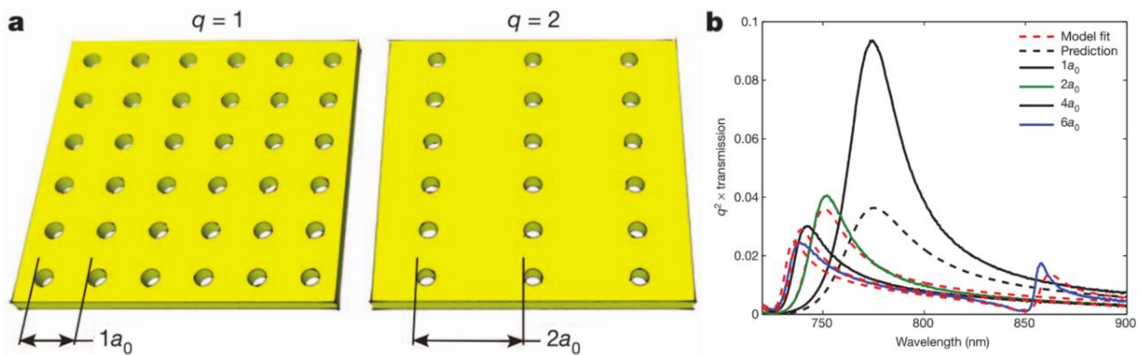

Figure 3: (a) Array used to test for effect of QCWs and (b) normalised transmission measurements vs model-only based on surface plasmons, from [30]

The incident light has its E-field polarised along the x-axis to produce negligible SPP propagation along the y-axis. As shown in Figure 3, if surface plasmons are the only contribution to the EOT effect, the separation between the columns of holes in the x-direction should scale the transmission by hole density (increased separation giving fewer holes per surface area) as per *Equation (14)*, with t_f being the transmission coefficient of a single hole chain.

$$T \propto q^{-2}\left|t_f\right|^2 \quad (14)$$

This was not observed by van Beijnum et al., instead the transmission is greatly enhanced when the x and y-axis hole separation distances are equal (close together), but all other configurations' (with the more-rectangular arrays) transmission approximately scaling as expected. This corresponds to the QCWs having a damping length of around one wavelength, effects at longer scales being negligible. Note that although QCW effects were not explicitly explored in the work of this thesis, their contributions, if any, to EOT effects of samples and devices designed in this work would be appropriately accounted for in COMSOL simulations of sample/device operation (though it would require additional input parameters to account for QCWs in analytical models such as those discussed in Section 3.2.2.1.

3.2.3. EOT Array Variations

The use of holes in EOT arrays with non-regular shapes can provide an additional means of modifying the peaks: for example, annular rings have been shown to support additional resonances, enhancing transmission despite reducing the total hole area [48]. Other interesting variations include array geometries that can create peaks in different positions depending on the polarisation angle of the incident light.

One approach to do this would be to use rectangular lattices, with a different period for each axis giving two sets of resonances (spectral minima) and main peaks [49]. For unpolarised light the positions are given by a modification of Equation (11).

$$\lambda_{min} \approx \frac{n_s}{\sqrt{\frac{i^2}{{p_x}^2} + \frac{j^2}{{p_y}^2}}} \quad (15)$$

If the holes keep the same size/shape as for a normal (square) lattice then the relative area of the holes to the entire film would be reduced, decreasing peak

transmission efficiency. As mentioned above, the quasi-cylindrical waves theory also proposes another reason that rectangular arrays (compared to square arrays) would experience reduced transmission.

As previously mentioned, another way of peak shaping is to use of holes with non-square aspect ratios [26], [50]–[52]. When using a linearly polarised light source, the polarisation angle of the incident light will have a significant effect on the transmission spectrum by exciting different localised modes. With an incident linearly polarised beam with the E-field aligned parallel to the holes' short axis (H-field aligned to long axis) the peak position is redshifted compared to that of an array identical but instead using circular holes, blueshifting occurring when the E-field is aligned parallel to the hole's long axis. Since the array period remains the same the spectral minima do not move but the peak maxima positions are shifted. Some of these effects are explored experimentally in Section 6.1.2.2, using laser-fabricated EOT arrays.

3.3. Phase-Change Materials

3.3.1. Overview

Phase-change materials (PCMs) are materials that are typically non-volatile (stable at room temperature) but whose structures can be repeatably changed between non-volatile amorphous (no long-range order) and crystalline states by heating, thus giving dramatically different optical and electrical properties with a wide variety of applications.

Technological applications of such materials were first proposed by Stanford Ovshinsky in 1968 [53], who demonstrated a form of non-volatile electrical memory using PCMs, but the most well-known use is probably rewritable optical discs (e.g. CD-RW, DVD±RW, BD-RE), commercialised in the 1980s. Rather than having "pits" hard-written into a metal film, these use a PCM layer on top of the film with the laser (normally used for reading data) switching the PCM state to changing its reflectance and allowing new data to be written and re-written.

Chalcogenide phase-change materials contain one or more elements from the chalcogen group (16) of the periodic table, usually selenium (Se), tellurium (Te) or sulphur (S), with the most well-known composition, often called the “archetypal PCM”, being the alloy $Ge_2Sb_2Te_5$ (also written here as GST-225).

The combination of PCMs with EOT arrays is the basis on which this work aspires to create a tuneable filter. By referring to Equation (13), if the refractive index of the array’s surrounding material can be changed, the spectral positions of the transmission peak(s) will shift. This is achieved by depositing a PCM layer on top of the EOT array, and as long as the PCM has a higher refractive index (in either state) than the substrate, shifting the PCM state will also shift the spectral position of the main transmission peak [27], [32]. Other areas of interest in this work include signal modulators (potentially working up to the THz regime), where a change in PCM extinction coefficient will modify the transmission peak amplitude.

The required PCM characteristics depends on the purposes that the devices are designed for. In general, desirable properties include:

- The ability to be heated and cooled/quenched fast and easily, reducing energy required to switch the PCM and transitioning time.

- Stability at room temperature whether in amorphous, partially crystalline or fully crystalline phases. For imaging this could for a fraction of a second, for memory applications this could be years. This property is desirable in many situations to avoid power being continuously applied to maintain a particular state, devices that would benefit from using a volatile PCM may use a material such as vanadium dioxide (VO_2),

- Long-term durability. The device should continue to function over a great many switching cycles, this means that the properties for each state should remain constant.

A tuneable filter for multispectral imaging would want the largest possible shift in refractive index *n* when switching the PCM from fully amorphous to fully crystalline states, to give the largest possible operating wavelength range. It

would also require the smallest possible extinction coefficient *k* in any state, to maximise filter transmission efficiency by reducing absorption in the PCM layer. GST-225 is good for such an application in the infrared, as are other GST variants. PCMs using different compositions can also be used to address other regions of the optical spectrum (e.g. Sb_2Se_3 or Sb_2S_3 for visible wavelengths).

Having accurate optical material properties is vital for selecting the right PCM, characterising the devices and running models and simulations. The parameters required are normally the refractive index *n* and extinction coefficient *k*; if required these can be derived from the dielectric functions. Published *n* and *k* data for PCMs does tend to vary from source to source (see Figure 4), probably due to differences in the methods and/or process conditions used for sample deposition (e.g. materials being deposited at different rates during sputtering), along with possible variations in composition for notionally identical products. Due to such variations in literature values, ideally one should try to obtain *n* and *k* data for one's own films by standard methods, such as ellipsometry [54]. This is however dependent on the available equipment and its wavelength range capabilities.

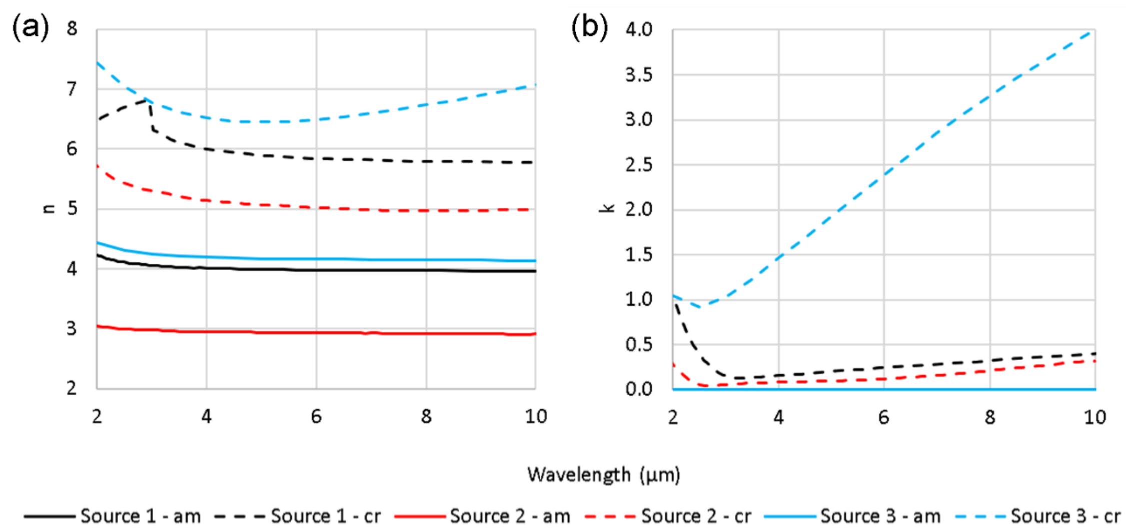

Figure 4: (a) refractive index and (b) extinction coefficient data for different measurements of GST-225 PCM from different published cources, [55] *(Source 1),* [32] *(Source 2) and* [56] *(Source 3)*

3.3.2. Switching

The PCM phase is changed by heating, rearranging the bonds in the amorphous phase into a crystalline structure and vice versa. For GST-225, the temperature at which shifting rapidly ensues is in the region of 150°C under “static” heating conditions (where the temperature is constant as opposed to ramped up and down), but PCMs can also shift over longer periods at lower temperatures (e.g. if left in direct sunlight). The crystallisation temperature has also been noted to vary with the heating rate, variation across a range of 180°C-350°C shown in [57].

To re-amorphise, the PCM must be melted to break the crystalline bonds (~600°C) then quickly quenched so they do not reform as the temperature decreases, freezing it in the amorphous state [58]. For GST-225 the minimum cooling rate to quench is difficult to measure experimentally, but is generally thought to be of the order of 5 K/ns [59]. It is therefore important to have device components made from materials with high thermal conductivities that can act as a heat-sinks to facilitate such fast cooling. Figure 5 provides a representation of the temperatures and qualitative comparative cooling rates required for both crystallisation and amorphisation.

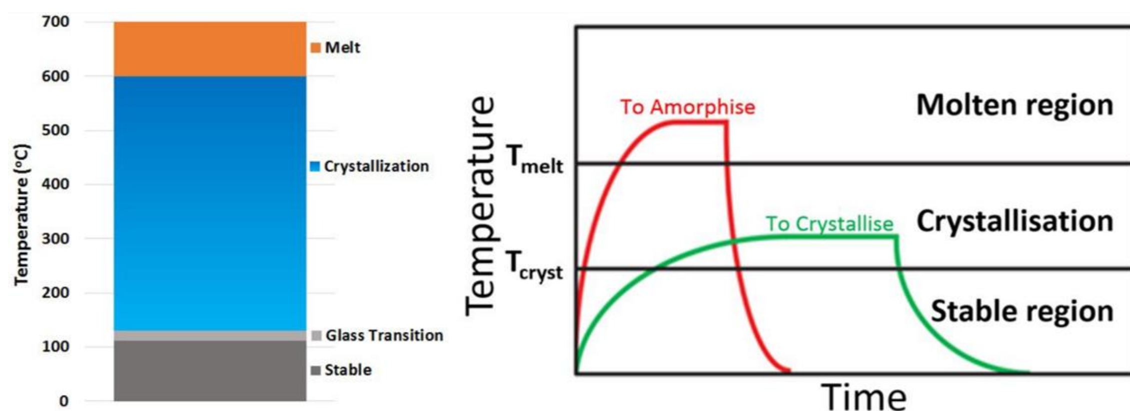

Figure 5: Plots showing phase transition temperatures of GST-326, taken from [58]*, data from* [60]

Methods of switching devices include:

- Thermal annealing – crystallising the sample’s PCM by heating with a hot plate or oven. This will heat up the entire device, meaning it cannot be

used to re-amorphise the PCM as the surrounding environment remains too hot to support rapid quenching.

- Optical switching – an intense light source (normally a laser) shines on the PCM material, which absorbs the light energy, generating heat [61]. Already commonly used in for rewritable optical discs, most of the device stays comparatively cool thus the rapid quenching needed for re-amorphisation is supported.

- Embedded micro-heater – a heating element is built into the device, possibly, in our case, even the EOT film itself. This approach has already been experimented with for applications related to PCM-based optical metasurfaces (as shown for example in Figure 6) and integrated PCM-based photonic memories [62]. Careful design, considering both material and geometric properties, is needed to ensure that sufficiently high cooling rates can be achieved for successful amorphisation using this approach.

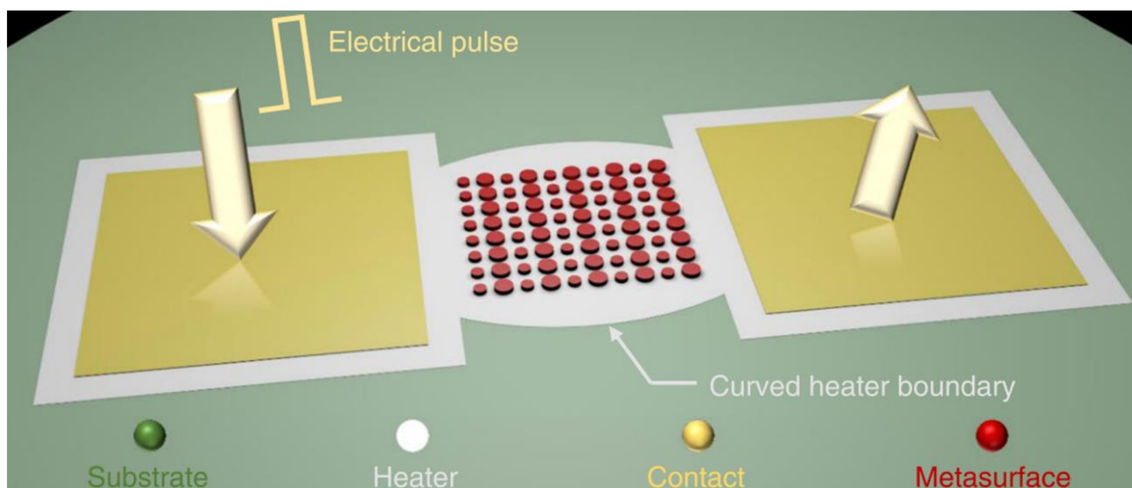

Figure 6: Schematic of an embedded microheater switching phase-change metasurface, as featured in [63]

- Direct heating – here electrical current is driven directly through the phase-change material itself, in turn causing heating via the Joule heating effect. Materials containing the chalcogenide elements that make up many PCMs can exhibit a phenomenon called Ovonic threshold switching [53], where increasing the voltage across it can show comparatively gradual increases in current up to a certain threshold voltage, at which point the resistivity

drops significantly. This can allow a higher current to pass through the highly-resistive amorphous phase of PCMs such as GST, helping to enable switching.

This method requires electrodes to be placed on either side of the PCM, which for optical applications, such as the EOT-PCM filters, require finding transparent and conductive capping materials. As with the embedded micro-heater approach, the design would have to be optimised to give consistent switching across the entire filter surface area, which could be up to several square centimetres.

3.4. Multispectral Imaging and Sensing

3.4.1. Overview

Multispectral sensing normally involves obtaining optical information from a subject over a range of narrow wavelength bands, conventionally via multiple exposures. A typical approach uses a panchromatic sensor (sensitive to all wavelengths within a given range), with a set of bandpass filters then isolating a narrow set of wavelengths. This can help in identifying light emitting in a restricted wavelength range, which may be otherwise obscured by a background of similar wavelength but higher intensity. When multispectral sensing is combined with a camera sensor to also provide spatial information, you have multispectral imaging.

A further extension is the principle of hyperspectral imaging, combining imaging with spectroscopy by using a greatly increased number of wavebands to produce a full spectrum for every pixel. Uses for such multispectral and hyperspectral technology are widespread, including archaeology [64] and art conservation [65], agriculture [66]–[69], medical diagnosis [70], colour night vision [71], recycling sorting [72], [73] and missile tracking [74], with examples shown in Figure 7.

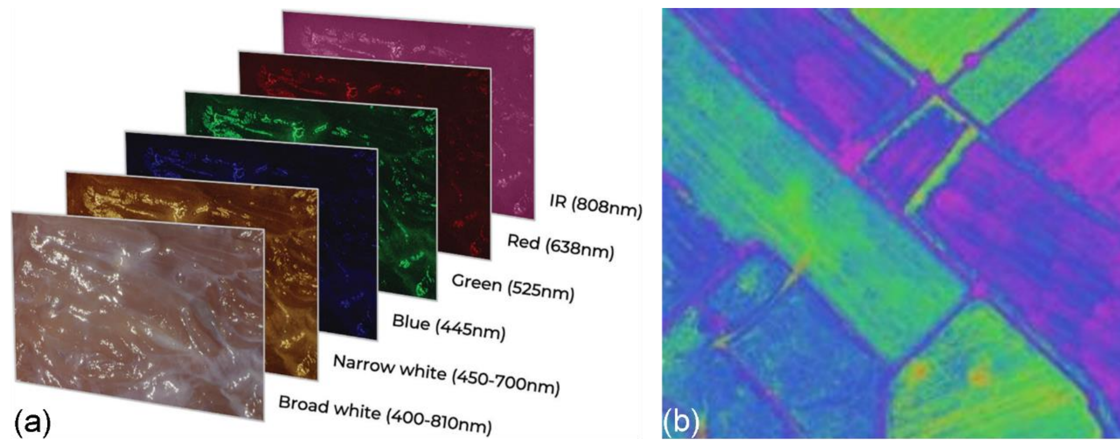

Figure 7: Example uses of multispectral imaging of (a) a lung tissue sample [75] *and (b) a crop field* [76]

3.4.2. Existing Types of Multispectral Imaging Systems

A number of methods currently exist to enable multispectral imaging. Perhaps the most common involves the use of multiple interchangeable filters placed before the sensor, sometimes mounted in a rotating wheel, as illustrated in Figure 8. The multiple exposures are performed sequentially, with the wheel stopping then advancing to the next wavelength band each time. Every pixel is sensitive to the entire wavelength range, thus the maximum potential spatial resolution is achieved. Disadvantages include the physical size of the multiple filters, the mechanical complexity necessitated by the need to move parts along with the added cost and fragility that this would entail. There is also a marked time delay between each exposure as the filters are advanced. Depending on the application's exposure time this may greatly increase the time necessary to produce each image and result in motion smearing (where a moving subject appears in a different position for each exposure).

Figure 8: Example configurations of multispectral imaging systems, multiple interchangeable filters [77] *(left) and multiple filter/lens/sensor units* [78] *(right)*

An alternative approach is instead to use multiple sets of detectors, e.g. separate units of lenses, filters and sensors each tailored to a specific wavelength band. While this would produce all exposures simultaneously, it also inherits the issues of size, cost and complexity, making it impractical for systems required to be small, lightweight and inexpensive. An additional downside may include parallax issues, spatial displacement of the optics giving slightly different images.

An undoubted improvement on the above described approaches would be a multispectral system of the type as shown in Figure 9, using a single sensor, one set of optics and a solid-state filter that can be quickly (sub frame rate) modified to allow a range of different transmission bands. This in effect replicates the operation of a filter wheel without the added size and complexity and a much-reduced delay time between the individual exposures.

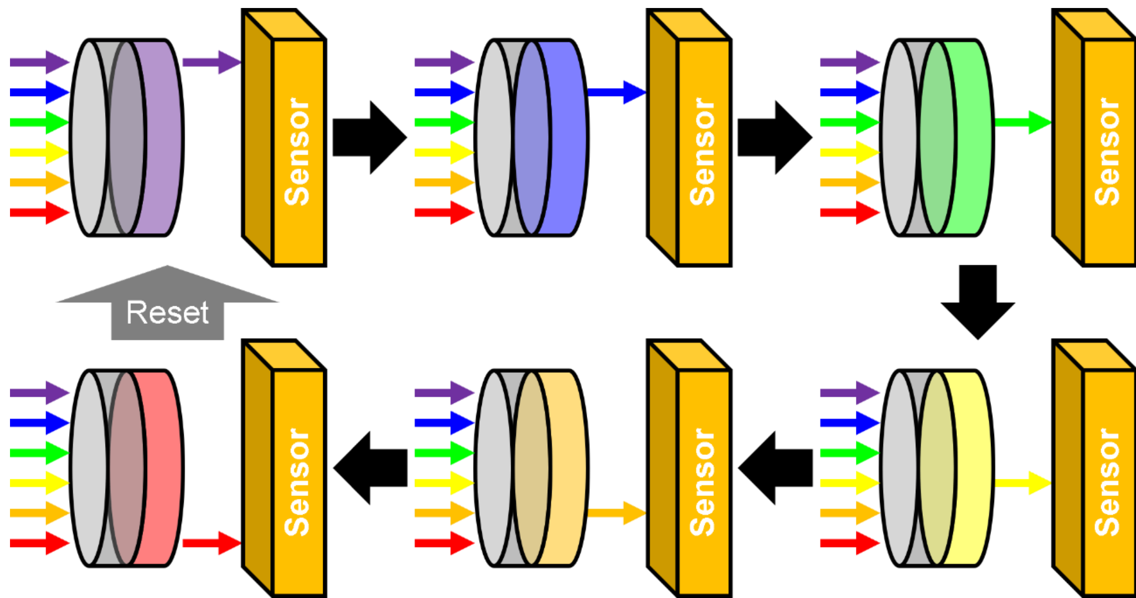

Figure 9: Schematic of the operation of a tuneable filter with single sensor setup, switching through configurations (clockwise from top-left) then resetting

3.4.3. Tuneable Filter via Phase-Change EOT

A potential method of achieving a single tuneable filter is by combining the phenomenon of extraordinary optical transmission (EOT) with phase-change materials (PCMs) since, as previously discussed in Section 3.2.2.1, changing the refractive index *n* of the material surrounding the hole array (by switching the phase-state of the PCM) shifts the spectral features, thus transmission peak position. Exposures can be taken between the upper and lower peak-shifted positions, by using a PCM that can be shifted into partially-crystallised states.

The basic principle of shifting the peak transmission of an EOT array was first shown by Rudé et al. [27] in the visible and near infra-red regime (see Figure 10). One of the main aims of the work of this thesis is to explore the potential of such an approach in the mid and long-wave infrared wavelengths (particularly useful for thermal imaging) with the aim, ultimately, of achieving relatively high transmission efficiency over a useful wavelength range as the PCM is progressively crystallised, as shown for example in in Figure 11. The use of PCM-enhanced EOT arrays in the THz spectral range will also be explored (at least in simulation).

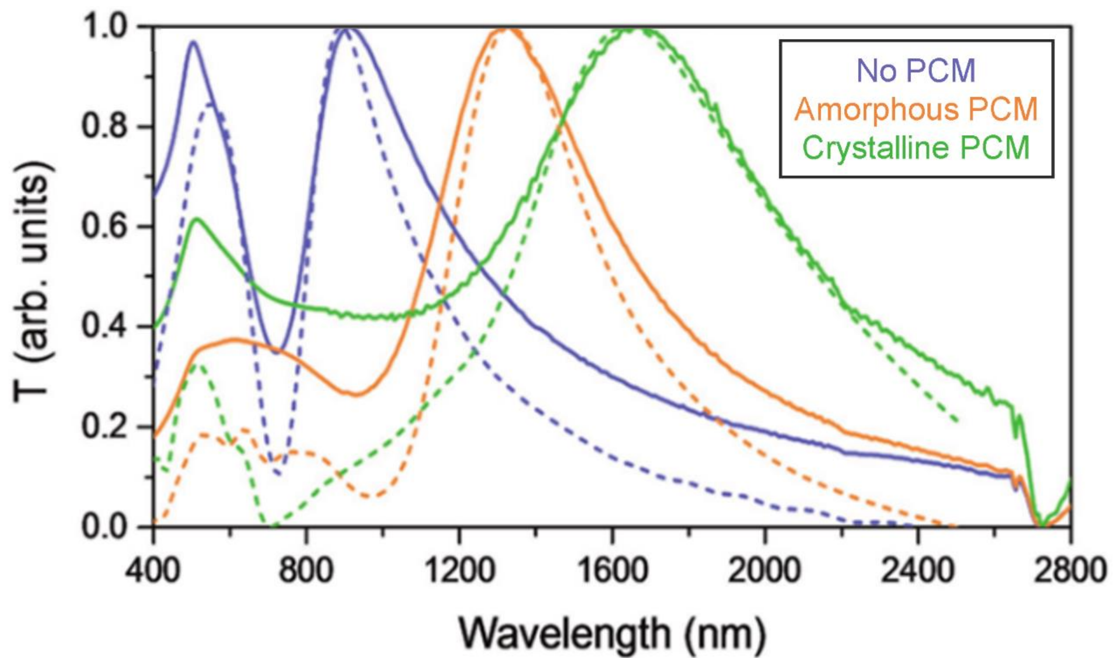

Figure 10: PCM-enhanced EOT devices displaying shift in peak wavelength, simulated (broken curves) vs measured spectra with peaks normalised to 1 (adapted from [27]*)*

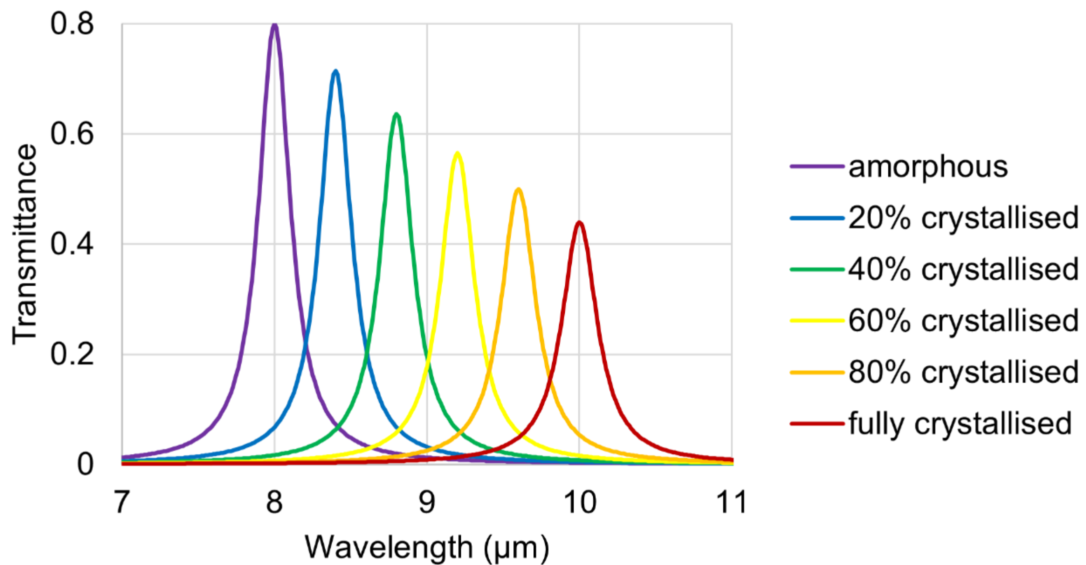

Figure 11: Illustrative theoretical transmission spectra (not derived from measurements or simulations) of a phase-change EOT-based band-pass filter for a multispectral imaging system in the mid-long IR regime. Plotted various "settings", the transmission band position depending on the PCM crystallisation.

4. Methods

This chapter covers the different processes used in the design, construction and characterisation of the devices studied in this thesis in the following chapters. They involve both computational and experimental techniques, for purposes of designing/optimisation, fabrication and characterisation.

4.1. Simulation

COMSOL Multiphysics was the software used exclusively here for performing finite element modelling, mainly involving electromagnetic simulations but also thermal simulations too. Material data (both from published sources and self-obtained) was applied to three-dimensional geometric shapes replicating those of devices to be built, in order to evaluate and optimise designs prior to fabrication.

4.1.1. Electromagnetic Modelling

The majority of modelling concerned was that of the optical performance of EOT devices in the mid and long-wave infrared, and (to a lesser extent), in the THz regime. Specifically of interest was the optical transmission and reflection response as a function of the wavelength/frequency of the various EOT arrays and EOT-PCM filters explored. The electric field distribution within devices at different wavelengths is also a feature of interest, and other devices examined include meta-atom arrays and reflection cavities/etalons.

A virtual device in COMSOL is constructed by forming distinct regions/domains, in this case exclusively 3D structures. These domains can be constructed either by combining individual shapes (e.g. a cylinder within a cuboid to represent a hole in a film), or by taking a 2D surface with the shapes drawn on it (e.g. a circle within a square) and extruding/sweeping it with layers of set thicknesses.

In a general sense, the domains are subdivided to form a (finite) mesh of elements within which Maxwell's equations in matter (equations (16) - (19)) are solved, given in terms of the electric field vector ***(E),*** electric vector (***D***), free

electrical charge density (ρ), magnetic induction ***(B)***, magnetic vector (***H***) and current (***j***) [79].

$$\vec{\nabla}.\vec{D} = \rho \quad (16) \qquad \vec{\nabla}.\vec{B} = 0 \quad (17)$$

$$\vec{\nabla} \times \vec{E} = -\frac{\partial \vec{B}}{\partial t} \quad (18) \qquad \vec{\nabla} \times \vec{H} = \vec{j} + \frac{\partial \vec{D}}{\partial t} \quad (19)$$

The "Electromagnetic Waves, Frequency Domain (emw)" solver within the Radio Frequency COMSOL module was used since the E-field and H-field behaviour must be modelled across a range of specified frequencies/wavelengths (the independent variable when the model is run) and there was no need for any modelling with consideration for time dependence. Field distributions were derived by solving the Helmholtz wave equation (20).

$$\frac{1}{\mu_r}\vec{\nabla} \times \left(\vec{\nabla} \times \vec{E}\right) - {k_0}^2\left(\varepsilon_r - \frac{j\sigma}{\omega\varepsilon_0}\right)\vec{E} = 0 \quad (20)$$

Scattering parameters (also called S-parameters) are used to derive transmittance and reflectance values from the electric fields, across solid angle Ω for the input (1) and output (2) ports (equations (21) – (22))

$$S1x = \frac{\int_{\partial\Omega}(\vec{E} - \overrightarrow{E_1}).\overrightarrow{E_1}}{\int_{\partial\Omega}\overrightarrow{E_1}.\overrightarrow{E_1}} \quad (21) \qquad S2x = \frac{\int_{\partial\Omega}\vec{E}.\overrightarrow{E_2}}{\int_{\partial\Omega}\overrightarrow{E_2}.\overrightarrow{E_2}} \quad (22)$$

with transmittance and reflectance calculated by

$$T = abs(S21)^2 \quad (23) \qquad R = abs(S11)^2 \quad (24)$$

Each domain in the simulation is assigned a material, defined by refractive index *n* and extinction coefficient *k*. It is important to note that these material properties are often wavelength dependant with potential for great variation, so the datasets used for the simulation should ideally encompass the wavelength range being simulated. It is also important to ensure that, when applicable, the dataset is not

just of the same material type but for the correct structure (e.g. similar film thicknesses) being simulated as this can also affect the optical properties.

EOT arrays were simulated (i.e. thin plasmonic metal films with arrays of sub-wavelength holes arranged in a grid) by creating a cuboid cell representing a single hole and the surrounding material, with base side lengths equal to the array period (or periods, if simulating rectangular arrays). As seen in Figure 12, the film/metasurface level is in the middle of the cell, with the excitation port radiating down from the top (in the air) and the listening port below (in the substrate). With the scales of the devices involved, it was not always possible to use realistic layer thickness for the substrate and air (on the orders of millimetres), since these would dwarf those of the film/PCM/barrier/cap layers (on the orders of nanometres). PCM birefringence is also ignored.

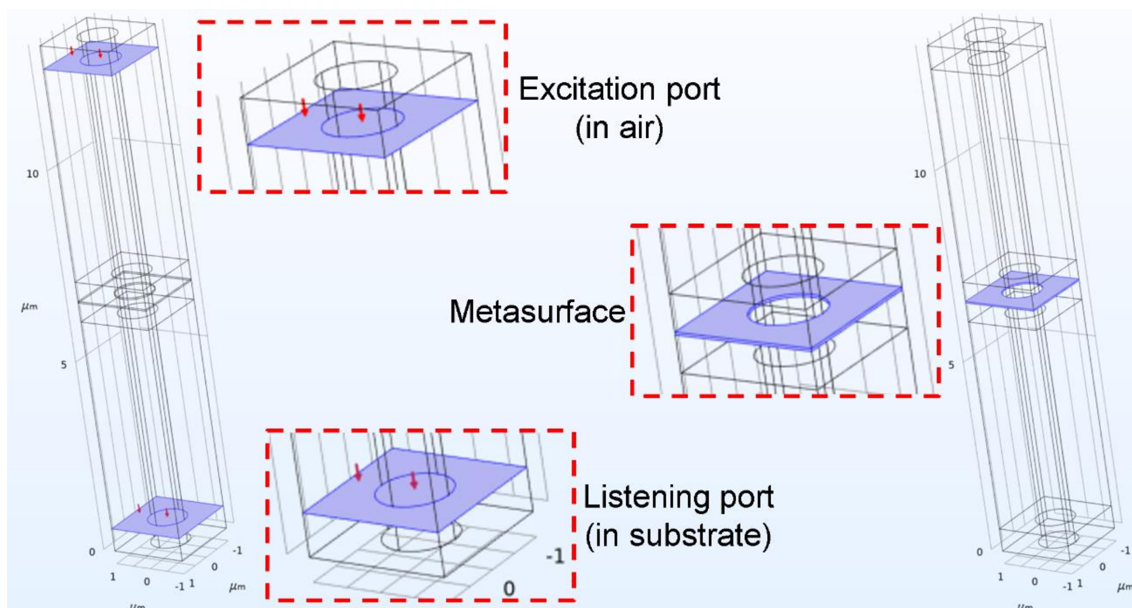

Figure 12: COMSOL unit cell for a square-array EOT metasurface, with different components highlighted and enlarged in insets

Radiation was provided by the excitation port positioned above the film surface with the (unexcited) listening port below required for transmittance measurements: this is not so for reflectance simulations, the single port above the film serving both functions. The wavelength range, direction, intensity (1 W excitation power used universally) and linear polarisation of the emitted radiation can be altered, but it was not possible to simulate unpolarised light in the

simulation setup used here. The COMSOL module uses frequency values for each calculation; if evenly spaced a plot of transmittance against wavelength would give smaller intervals between points at the shorter wavelength end of the spectrum compared to the longer. For each simulation setup, a set of wavelength points evenly distributed across the desired range would be plotted in a spreadsheet and converted to the equivalent frequency for inputting into COMSOL. If any particularly sharp spectra features were noted, point density could be increased across a specific region rather than setting small intervals universally, reducing computation time.

As shown in Figure 13, the ports are defined as the interfaces between the air/substrate domains and their enveloping perfectly matched layers (PMLs). PMLs are domains that replicate the effect of free space, absorbing radiation to prevent reflections from the edges of the cell and causing interference, and are defined by Equation (25), with ***n*** being the domain surface vector.

$$\vec{n} \times \vec{E} = 0 \qquad (25)$$

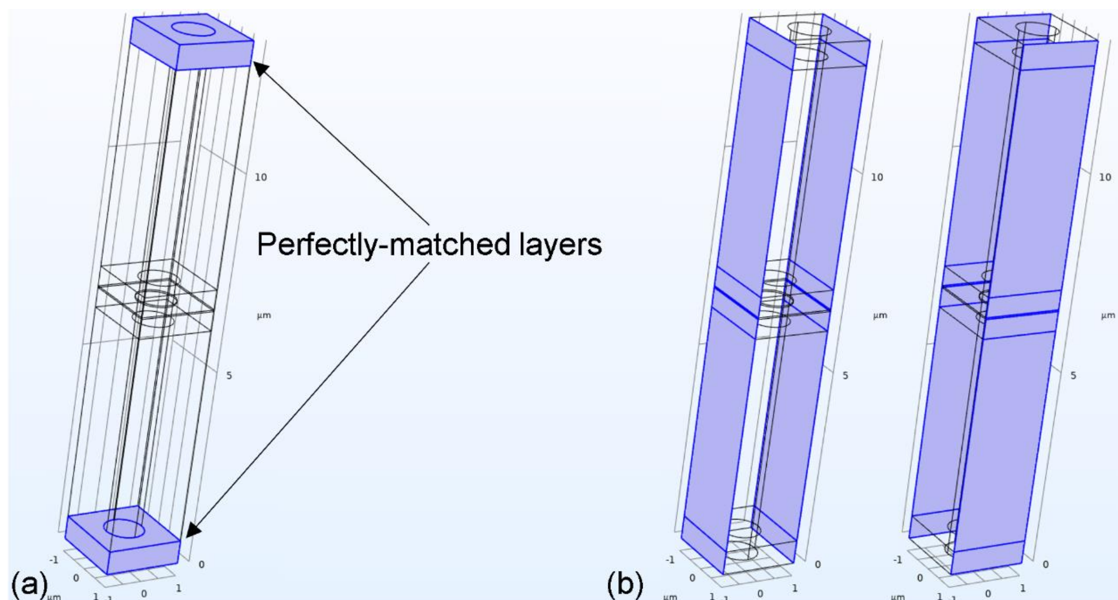

Figure 13: (a) Perfectly-matched layers of a COMSOL unit cell (b) FPBCs along x and y axes of a square COMSOL unit cell

The periodic structure was attained by setting infinitely repeating Floquet periodic boundary conditions (FPBCs) to match the faces that shared (x or y) axes, also

shown in Figure 13. Using a repeated unit cell was a far more computationally efficient process than trying to simulate an entire array, which could consist of more than a million holes on a practical fabricated device. These boundary conditions are defined in Equations (26) and (27), and describe radiation travelling from a source point $\boldsymbol{r_{src}}$ at one boundary to a destination point $\boldsymbol{r_{dst}}$ on the opposite one, $\boldsymbol{E_{src/dst}}$ being the electric field at the source/destination and $\boldsymbol{H_{src/dst}}$ the magnetic equivalent. $\boldsymbol{k_F}$ is the Floquet wavevector which equals zero for light at normal incidence.

$$\overrightarrow{E_{dst}} = \overrightarrow{E_{src}} e^{-i\overrightarrow{k_F}.(\overrightarrow{r_{dst}}-\overrightarrow{r_{src}})} \qquad (26)$$

$$\overrightarrow{H_{dst}} = \overrightarrow{H_{src}} e^{-i\overrightarrow{k_F}.(\overrightarrow{r_{dst}}-\overrightarrow{r_{src}})} \qquad (27)$$

Other considerations were also taken into account during simulations to ensure consistency between the models and as-fabricated devices. Increasing the number of mesh elements makes for a more accurate replication of reality but this naturally increases processing time, so tests were carried out to find acceptable coarseness before diverging results were observed (see Section 8.1). It is required that mesh fineness be greatest at areas where a large change in electric field is expected, normally at the interfaces between the different materials; this can be controlled by setting the number of divisions of each vertex and the maximum element size growth rate. Hexagonal arrays required two-hole unit cells (as seen in Figure 14), requiring a greater number of mesh elements (thus computing time) cf. square arrays.

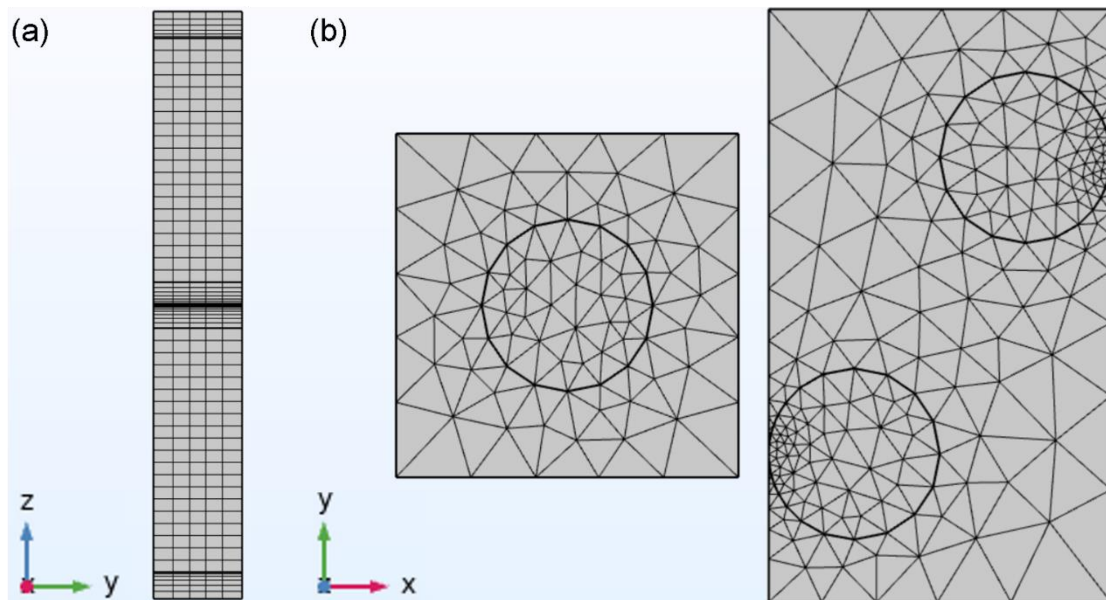

Figure 14: Example COMSOL unit cell swept meshes from different perspectives (a) side-on for a square array and (b) top-down for square and hexagonal arrays, with identical array pitch, fill factor and mesh fineness settings

Also, during application of PCM/barrier/cap layers by magnetron sputtering material not only coats the faces parallel to the plane of the substrate but those perpendicular too (specifically the walls of the array holes), slightly increasing the total material volume. Of the material on the sides, only the PCM was included in the models as this has a slight but noticeable effect on shifting (see Section 5.4.3), the 8 nm barrier/cap layers being disallowed by the software because the domains were too narrow for MWIR-scale devices.

4.1.2. Electro-Thermal Modelling

Simulations were also carried out to investigate the possibility of electrically switching phase-change material layers in an EOT devices via Joule heating, generating heat by passing current through the metal EOT array film itself. Models were constructed in COMSOL of a single cell and solved using a time dependant solver with the “Heat Transfer in Solids (ht)” and “Electric Currents (ec)” modules. An array hole was “constructed” on top the substrate and covered with a layer of PCM. Voltage pulses were then applied to the EOT film, with measurements being taken of temperatures reached at various spatial points and the current against time. From this, heating and cooling rates can be derived,

along with both instantaneous and total power (and energy) required for a switching cycle.

To model heat flow due to conduction COMSOL used Equation (28), solving for total heat transfer Q in terms of the change in temperature T; local heat transfer q; specific heat capacity C_p and density ρ.

$$Q = \rho C_p \frac{\partial T}{\partial t} + \vec{\nabla}.\vec{q} \qquad (28)$$

q is a function of the material's thermal conductivity κ as seen in Equation (29), and heat capacity was sometimes provided in the literature as a function of volume rather than density as related in Equation (30).

$$\vec{q} = -\kappa \vec{\nabla} T \qquad (29) \qquad\qquad C_V = \rho C_p \qquad (30)$$

giving the Equation (28) in terms of the independent variables in Equations (31) and (32).

$$Q = \rho C_p \frac{\partial T}{\partial t} - \kappa \vec{\nabla} T \qquad (31) \qquad\qquad Q = C_V \frac{\partial T}{\partial t} - \kappa \vec{\nabla} T \qquad (32)$$

For the metal comprising the EOT film, the resistivity/conductivity is also required, which varies according to temperature as shown in Figure 15 for gold (the EOT metal used predominantly in the work of this thesis).

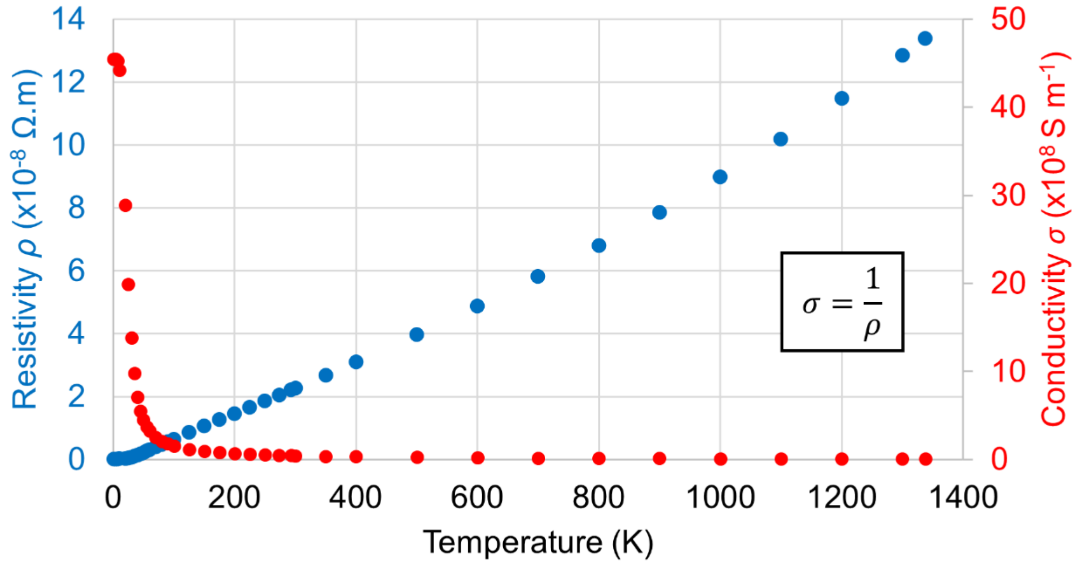

Figure 15: Gold electrical resistivity and conductivity against temperature (adapted from [80]*)*

Boundary conditions were defined for both electrical and thermal properties to best mimic reality. The model is set universally to room temperature (20°C /293.15 K) at the start of each run, with the base of the substrate kept at this temperature so it acts a heat sink and the top surface set to non-zero heat flux q_0 to mimic heat loss to air.

$$-\vec{n}.\vec{q} = q_0 \quad (33)$$

with q_0 as a function of the heat transfer coefficient h (given in Equations (34) and (35)), and here set to 10 W m^{-2} K^{-1} for air [63].

$$q_0 = h(T_{ext} - T) \quad (34) \qquad -\vec{n}.\vec{q} = h(T_{ext} - T) \quad (35)$$

As per Equation (36), the four sides of the cell are defined as thermal insulation boundaries with zero heat flux, since any surrounding cells (array holes) would be identical.

$$-\vec{n}.\vec{q} = 0 \quad (36)$$

Electrical ports (for current in and current out) are defined as opposing vertical sides of the metal film (see Figure 16).

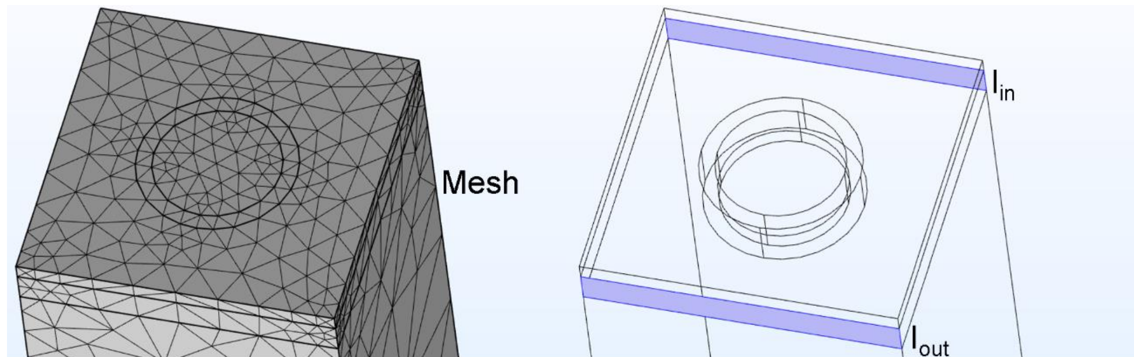

Figure 16: Components of an EOT array unit cell in COMSOL Multiphysics for electro-thermal modelling

Temperatures were measured at different positions in the cell, both as single points and cross-sectional plots along a defined plane. Areas of greatest interest are the narrowest spaces between unit cells (where electrical resistance of the array film is greatest and the highest temperatures are reached) and the centres of the array holes (the place where it takes the most time for the PCM layer to be heated up).

4.2. Fabrication

4.2.1. Substrate Shapes

The majority of optical measurements (including all in transmittance) were performed on devices using pre-shaped circular CaF_2 or BaF_2 optical blanks (provided by Crystran Ltd), cleaved on the (111) plane [81], [82]. Both CaF_2 or BaF_2 substrate materials offered very high transmittance in the mid to long-wave infrared regime, with >90% transmission up to 9 μm and 11.5 μm respectively for a 1 mm thickness. The standard thickness used was 1 mm, 0.5 mm was available and tested but while it was less absorbing it was found to be too delicate, even breaking when just being removing from a Gel-Pak©. Substrate diameters of 10-13 mm were preferred, giving a good balance between ease of handling and experimental convenience (e.g. having a few practically sized arrays per device).

For tasks that required silicon substrates, these were cut down from larger (typically 4”) wafers to typical sizes of 10×10 mm using a Loadpoint MicroAce dicer. To protect the wafer surface during the cutting process, a thick layer of 950K A6 PMMA was spun on at low speed and baked, this was then removed by soaking in warm acetone when the substrate was to be used. Wafers were processed this way both with and without additional layers of material to be used in the final device, including 3/40 nm layers of chromium/gold.

4.2.2. Deposition Techniques

This section covers the two deposition systems used to make devices for this thesis: a thermal evaporator for EOT films and adhesive layers and a magnetron sputterer for the PCM, barrier and capping layers. Samples for material characterisation/instrument calibration were made using the same processes to those for devices for optical measurements.

4.2.2.1. Thermal Evaporation

Evaporation is a physical vapour deposition (PVD) process that heats small pieces of metal in a high vacuum so it reaches liquid then gaseous form, and subsequently condenses onto the exposed surfaces of the substrates (see schematic in Figure 17). Heating may be achieved with electron or ion beams, but in this case was performed by Joule/resistance heating of tungsten using an HHV Auto 306 machine. The metals were loaded onto boats on a rotating stage, which when positioned correctly allowed electrical current to flow through the boats to and from contacts.

Gold (for the EOT films) came in the form of 1 mm diameter wire, which was cut into pieces a few mm long so it would fit in its boat (a solid strip of tungsten with a “dished” bottom). The rule of thumb for judging the required quantity for a desired layer thickness was 2 mm of wire per 10 nm of film, e.g. 8 mm for a 40 nm film. A little extra was added to provide leeway and allow for cleaning (see later). Chromium (for the EOT film adhesive layer) came in the form of pellets a few mm across, which were loaded into a basket-type boat. A single pellet would always be more than sufficient for the very thin layer of Cr required (3-5 nm).

Before loading for a new run the evaporator was thoroughly cleaned, first with a vacuum cleaner before being wiped over with acetone. Metal was loaded onto the boats and substrates onto a block which was attached to a stage at the top of the vacuum chamber, 22 cm above the level of the boats and blocked off from them by a moveable shutter. The chamber was then pumped down until a pressure of at least 2×10^{-6} Torr (~2.66 10^{-4} Pa) was reached, taking a few hours.

The first deposited layer would be chromium, but before this the pieces of gold wire needed to be melted and allowed to resolidify so they would not fall off when the stage was rotated. Sufficient voltage was applied so that the gold could be seen to liquify (through the chamber observation window) but not so that any material would be detected on the layer thickness gauge. After allowing a few minutes for the gold to be guaranteed solid the stage would be rotated so the chromium boat was positioned at the electrical contacts. Ensuring that the correct material was programmed in (to give accurate thickness readings), the voltage was very gradually increased until a positive deposition rate and a layer thickness was displayed. After a few nm of chromium had been cleaned off, the shutter was opened to expose the substrates to the vapour then closed again when the required thickness was reached. All the while as steady a deposition rate as possible was maintained, the ideal between 0.5 and 1 Å s^{-1}, with minute adjustments to the voltage sometimes being needed during the deposition to maintain such rates.

Gold deposition followed much the same pattern, often requiring voltage adjustments as the quantity of metal in the boat reduced. In addition to the machine's thickness gauge, test pieces of PMMA dots on polished silicon substrates would be positioned on the block among the optical samples. After deposition these pieces would be sonicated to remove the PMMA, expose the substrate surface where the dot had been and allow a surface profiler measurement to be taken of the step formed by the film edge. To improve metal thickness consistency across samples made in the same batch, the block was set to rotate during deposition.

The main reason for using thermal evaporation to produce metal films was that of convenience, requiring a far shorter pumping down period (matter of hours)

than those of the sputtering systems available to us (which were best left to pump down overnight), yet producing films of comparable quality. A theoretical advantage of the sputtering processes would be the ability to deposit all the device layers (targets are available for all the relevant metal, barrier, PCM and capping materials) in one session without needing to unload and expose the surfaces to air unnecessarily. However, this does not apply here since the metal film must be patterned into an EOT array before PCM application: it is also usually desirable to characterise the EOT array before application of further layers.

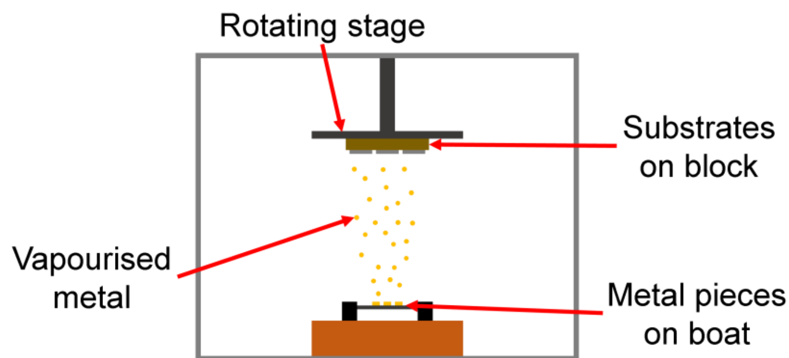

Figure 17: Schematic diagram of thermal evaporation process, 22 cm between boat and substrates on block.

4.2.2.2. Magnetron Sputtering

Sputtering is another form of PVD process, where (in our case) argon atoms are positively ionised by free electrons flowing from the target (the cathode) to the substrate plate (the anode), and are accelerated toward the target with sufficient energy to liberate tiny particles of the target material which then deposit onto the exposed area of the substrates (see schematic in Figure 18). The system we used (a Moorfield nanoPVD S10A) utilised magnetron sputtering, the target being magnetised to constrain the plasma to it and increase efficiency of the sputtering process. Radio frequency (RF) sputtering was used, as recommended by the target manufacturers for the specific materials used here.

The two factors that affect deposition rate are the applied deposition power and the gas pressure (controlled by adjusting the flow rate). Increasing the power will increase the deposition rate, but excessive power can overheat the chamber

(necessitating cooling periods that negate any speed advantage) and exceeding the target's specified limit power density could lead to it being damaged. Depending on the material, this power could range between 15-75 W (2" diameter targets used so power density of ~0.76-3.8 W cm^{-1}) in the Moorfield system used.

Increasing the chamber pressure decreases the mean free path between particles and increase the number of collisions between them, slowing the deposition. A higher pressure (flow rate) is required to ignite/strike the plasma (sometimes along with a higher-than-normal power), but it is then reduced for the deposition proper to provide a typical pressure of 5×10^{-3} mbar (0.5 Pa). This allowed for reasonable deposition rates while also giving a good degree of security; the plasma was unlikely to cut out during the middle of a run and ruin a batch of devices.

The Moorfield machine is capable of holding up to three targets at once, allowing deposition of the barrier, PCM and capping layers in a single session without exposing the sample to the atmosphere. The substrate plate is suspended above the target, protected by a moveable shutter when not depositing, and rotates to ensure even coverage.

No instantaneous (i.e. during deposition) layer thickness monitoring was available in the Moorfield system, requiring deposition rate calibration runs to be made for all materials used, and care being taken to ensure that the run settings (power and flow rate) were kept as consistent as possible between runs. Thickness-check samples of the same type for thermal evaporation runs (PMMA dots on polished silicon substrates) were also used here.

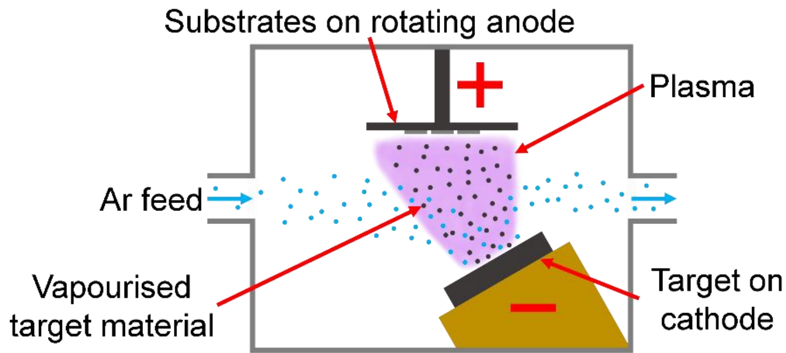

Figure 18: Schematic diagram of magnetron sputtering process, 22 cm distance between target and substrates.

4.2.3. Device Patterning

4.2.3.1. Electron Beam Lithography

The first step in patterning the majority of devices featured here was e-beam lithography (EBL), then followed by lift-off or wet-etching (described in Section 4.2.3.2). The NanoBeam nB4 machine used here provides the necessary spatial resolution for fabricating EOT devices for the mid-infrared regime, able to reliably produce feature sizes on the order of 100 nm and arrays of the required size within a reasonable time.

The first step is the application of a resist layer, in this case putting a few drops of poly(methyl methacrylate) (PMMA, from Kayaku® Advanced Materials Inc.) polymer on the substrate and spin coating to give a layer with a consistent thickness. The sample is then baked on a hotplate to harden the resist.

Additional applications of PMMA may be deposited if more is needed than a single layer allows, e.g. for lift-off with a thick metal film. Lift-off also requires an additional layer of conductive polymer to be spun on and baked when a non-conductive substrate (such as calcium fluoride) is used.

Dots of silver "paint" are placed on the corners of the substrate, which is then loaded into the EBL. The chamber is pumped down to a pressure at least below 2×10^{-6} mbar, and the machine is focused using the silver particles in the paint. The pattern is written with the electron beam into the resist, which can be either

positive (the written area being weakened) or negative (the written area being strengthened). Factors that affect the pattern include the dose (total e-beam flux applied) and the beam current (flux rate); increasing either will increase the size of the feature and thus the total written area for a given pattern. A minimum dose is required for the resist to be properly developed; a typical beam current is ~10 nA for devices for mid-infrared regime (feature size on order of 1 μm). If a finer pattern is being written (feature size on order of 100 nm) the beam current would be reduced to ~1 nA.

Following patterning in the e-beam system, the resist is "developed" using a suitable developing solution. 950K A4 PMMA resist was predominantly used in the work of this thesis, requiring a 15:5:1 mix of isopropyl alcohol (IPA), 4-methyl-2-pentanone (MKI) and methyl-ethyl ketone (MEK). The degree of developing depends on the total time submerged, the longer time the greater the degree of development; a developing time of 30 seconds was used here, after which the sample/device was submerged in IPA for 1 minute to stop any further development, a clock timer being used to monitor this. Any agitation of the device in the developer can also increase the developing rate, so samples were held as still as possible.

4.2.3.2. Lift-Off

Lift-off involves the deposition of metal layers onto a pre-written and developed mask. The masked region is subsequently removed (or lifted-off) by dissolving it in a solvent such as acetone, leaving metal in the un-masked regions. For making EOT arrays, a mask consisting of an array of pillars (where the holes will be) is required.

When using this approach, metal deposited on the hole sidewalls can make removing the unwanted material difficult (as seen in Figure 19 (a)), by preventing the solvent from reaching the mask. This can be avoided by having the mask holes give an undercut structure, the exposed spaces at the base of the film being slightly wider than those at the top, hopefully giving gaps in the metal. Using features with sharp edges (e.g. arrays with square holes rather than circular holes) can help. Gentle sonication during lift-off can also help to remove the

mask, but this can risk damaging the film as seen in Figure 19 (b), and so was avoided in this work when possible.

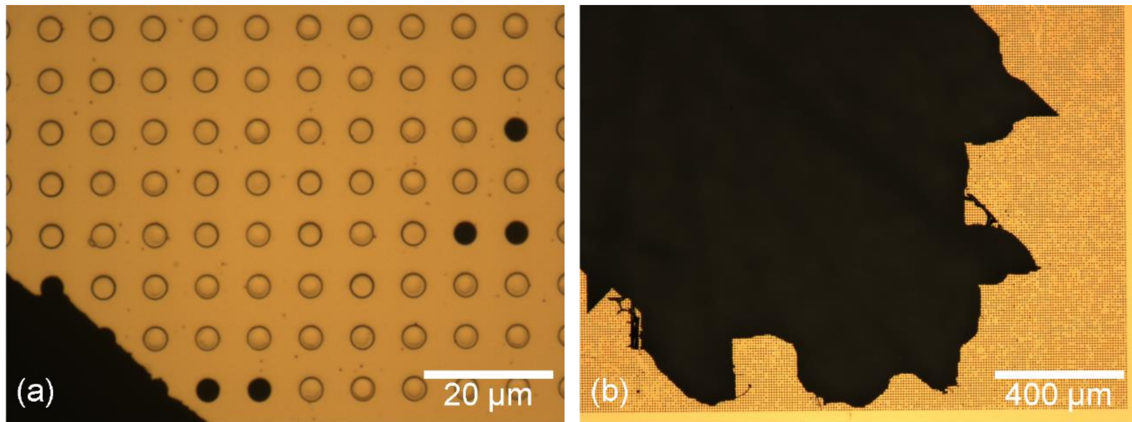

Figure 19: Optical microscope images of MWIR EOT arrays showing potential issues, (a) holes not clearing (b) film destruction due to over-sonication

Another feature of hole arrays made using lift-off can be the presence of unwanted metal at the hole edges (see Figure 20), building up around the mask pillars during deposition, their height above the plane of the film being similar to that of the film thickness.

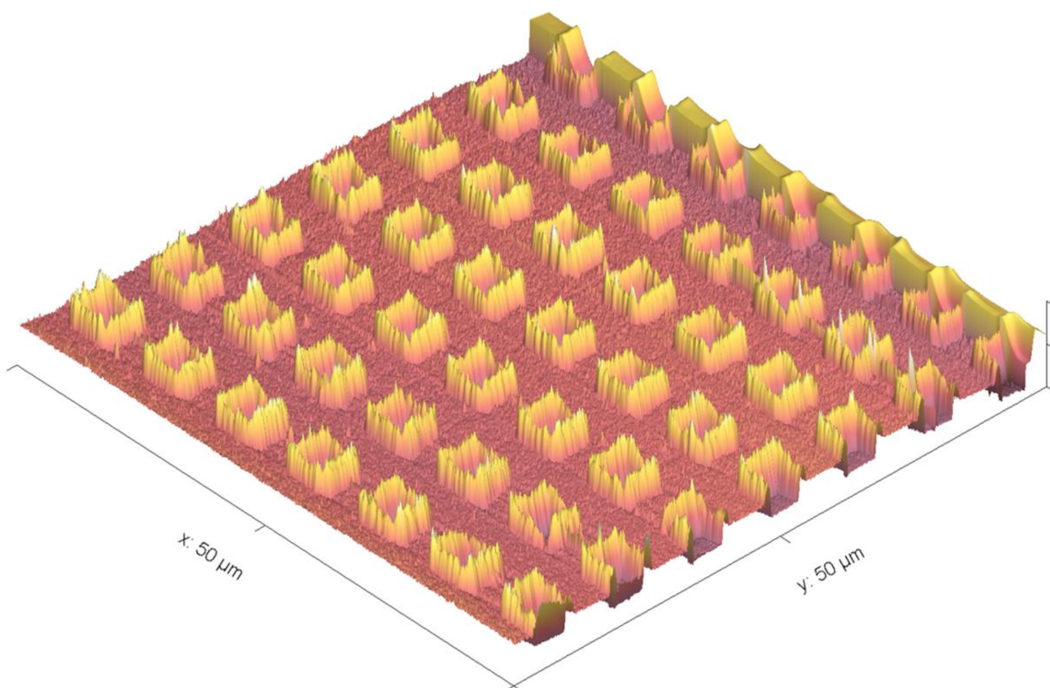

Figure 20: 3D AFM scan of the surface of an EOT array fabricated via lift-off, showing unwanted build-up of metal around the hole edges

4.2.3.3. Wet-Etching

Wet-etching has the resist mask created on top of existing metal layers then, after developing, the device is submerged in liquid etchants to remove metal in the areas where it is exposed. After etching the mask is easily dissolved in a solvent such as acetone.

Wet-etching was the preferred method for patterning EOT arrays in this thesis, primarily for the following reasons:

- Only a single layer of resist is needed, rather than the two or three for lift-off, since a smaller total mask thickness is required

- Sonication to remove excess metal (risking damaging the film) was never required, since a metal shape is not formed around the mask

- The final EOT film was found to have a very "clean" surface profile, with no build-up of metal around the hole edges as shown in Figure 21

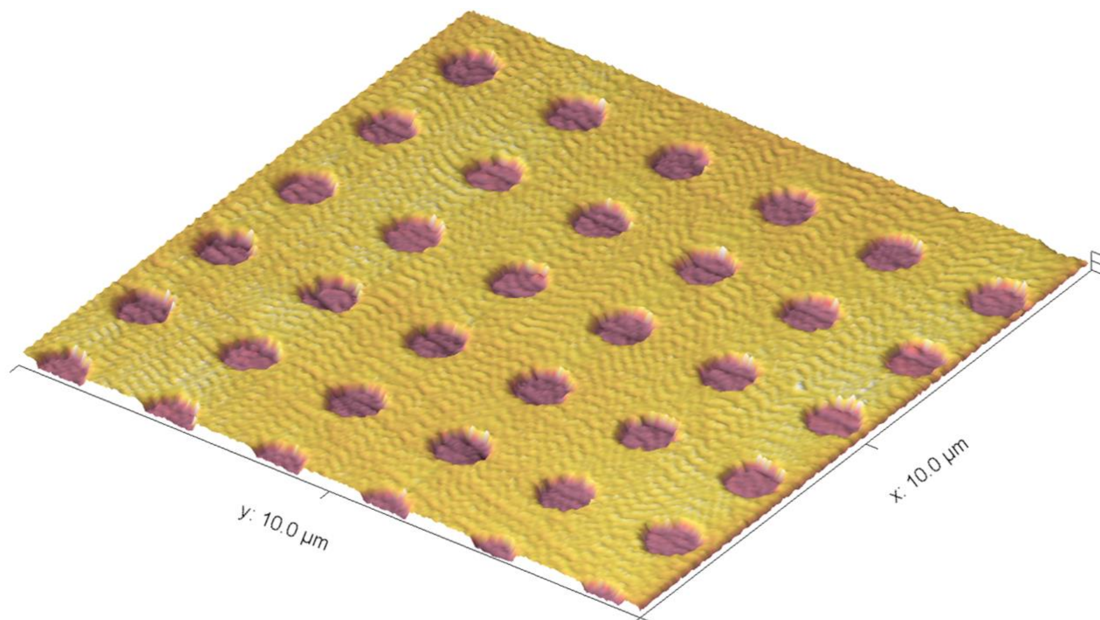

Figure 21: 3D AFM scan of the surface of an EOT array fabricated via wet-etching, showing no unwanted build-up of metal around the hole edges, z-axis kept at the same scale as for Figure 20

A potential disadvantage of the wet-etching approach is that the hole sidewalls are not quite vertical, the etchant eating away at the top of the film for longer than the bottom, so making the holes wider at the top. However, for the comparatively large feature sizes of mid-infrared EOT arrays (1 μm+) relative to the film thicknesses (40-100 nm) this was not a concern here.

Another consideration is that the etched hole is larger than that of the array mask, and this must be accounted for when designing the array patterns to be written with the e-beam. For example, if devices of different pitch but identical fill factor (relative diameter to pitch) are wanted then the pattern holes must be undersized by the same amount in each case as shown in Figure 22.

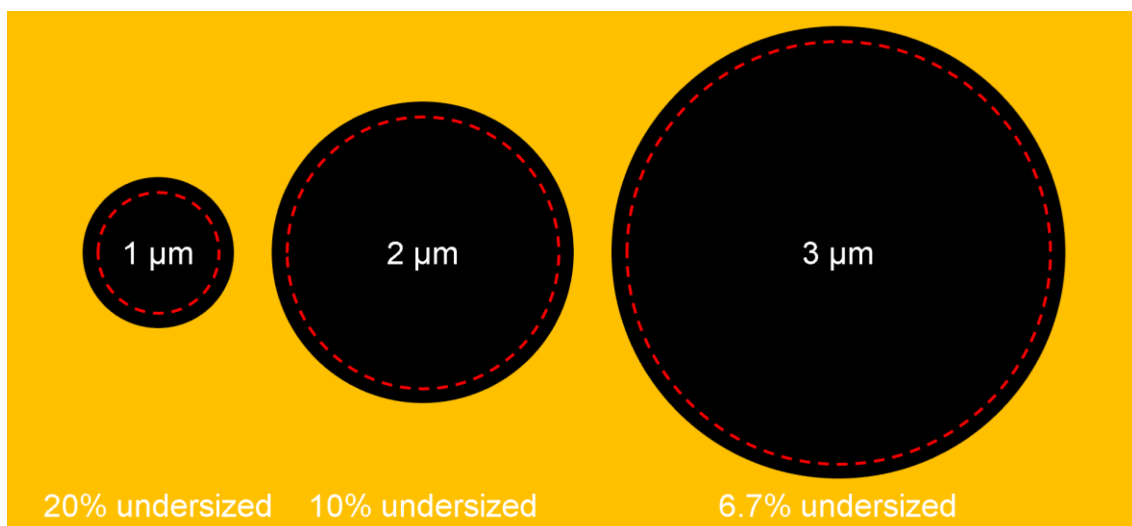

Figure 22: Examples of how holes of different intended sizes (1, 2 and 3 μm diameters shown) have different percentage undercuts for a given etching time, with a written mask hole diameter here smaller than the final etched hole by 200 nm in every case

4.2.3.4. Focused Ion Beam Milling

The focused ion beam (FIB) milling system used at the University of Exeter (an xT Nova Nanolab 600 SEM/FIB system) uses gallium, an accelerated ion beam of which, in the work of this thesis, could be used to carve out the array holes from the device film. This approach was however not seriously considered for “mainstream” EOT device fabrication, due to (i) the time and effort needed to make an array of sufficiently large area for optical testing (~2×2 mm required,

maximum of 100×100 µm achievable without manual realignment in the FIB), and (ii) the relative surface "dirtiness" of the resulting samples and the chance of gallium contamination.

FIB milling was, however, used to make holes in the devices to examine the cross-sections of the layers with subsequent SEM or TEM imaging, including the investigation of the possible effects of metal/PCM interdiffusion in Section 6.3. For the latter, segments were milled from the devices and extracted using a micromanipulator probe (see Figure 23), the processing being done by Geoff West of the University of Warwick.

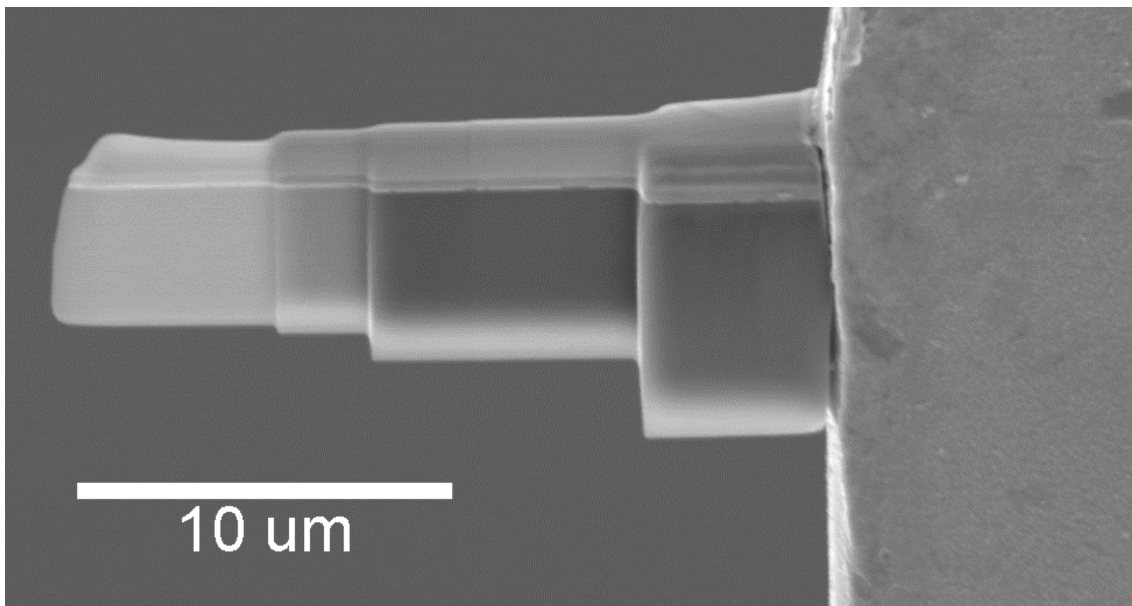

Figure 23: Segment extracted from film via FIB milling for TEM imaging

4.2.3.5. Laser Ablation

Similar in concept to FIB milling, ultrafast laser processing/laser ablation directly patterns holes into the EOT film with sub-picosecond pulses used to ablate the metal beneath the laser spot. This allows large-scale arrays to be fabricated using far fewer steps (and less demand in cleanroom facilities) much more quickly than via the e-beam lithography approach, (also being much faster than FIB milling and with no risks of gallium contamination. The laser processing techniques trialled here for the fabrication of EOT devices were carried out by

collaborators at the CSIC Instituto de Optica in Madrid, but with all material depositions and device optical characterisations carried out here in Exeter.

The laser processing system is shown schematically in Figure 24; the metalled substrates are secured to a moveable stage beneath the 1030 nm-wavelength laser, no application of photoresist or the pumping down of equipment to a vacuum is needed. The arrays are written hole-by-hole as the sample stage scans with 340 fs-long pulses, the hole size dependent on the energy of the laser pulse (distributed about the hole as a Gaussian function). Larger holes requiring higher total energies as shown in Figure 25, but this can also be achieved by using higher laser powers, leaving total write-times unaffected.

The array pitch Λ dependent on the pulse repetition rate (F_{rep}) and scanning velocity (V_{scan}), as given in Equation (37) [4] and also shown in Figure 25, F_{rep} and V_{scan} values up to 20 MHz and 20 mm s^{-1} being possible.

$$\Lambda = \frac{V_{scan}}{F_{rep}} \quad (37)$$

If keeping a constant F_{rep}, smaller-pitch arrays take longer to write because a slower V_{scan} is required. For the devices featured here this is much faster (up to 19 minutes maximum per 2×2 mm array) than for equivalent devices made using any EBL-based technique (which can take several hours).

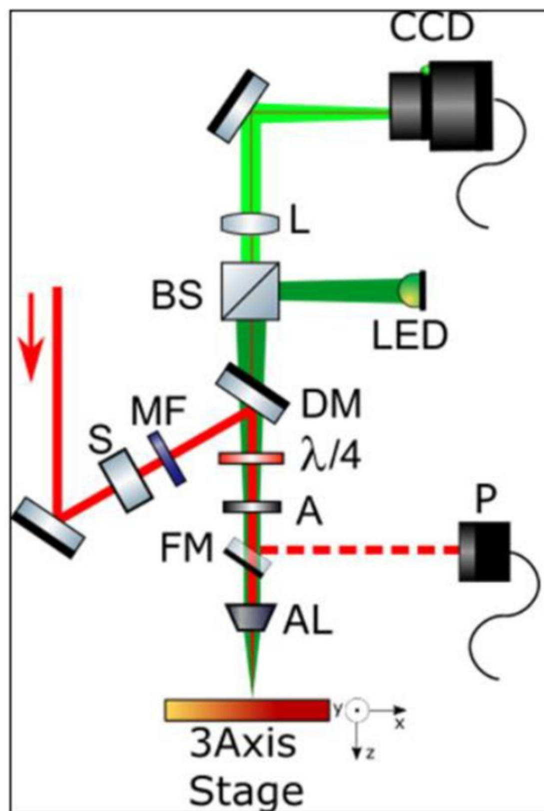

Setup components

A	aperture
AL	aspheric lens
BS	beam splitter
DM	dichroic mirror
FM	flip mirror
L	tube lens
MF	metallic filter
P	power meter
S	slit
λ/4	quarter-waveplate

Figure 24: Schematic of laser-writing setup, from [4]*, red lines for laser-processing beam and green lines for the LED-illuminated in-situ observation path*

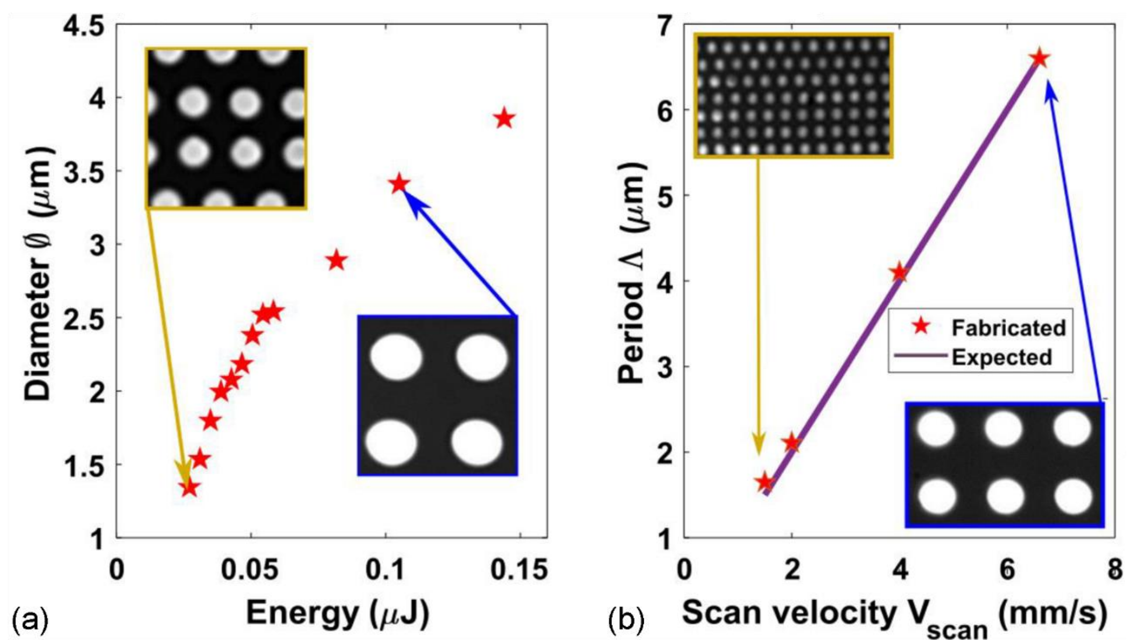

Figure 25: (a) Laser-written hole diameter vs. pulse energy and (b) array period vs.scanning velocity with 1 kHz repetition rate) for NA 0.25, from [4]*, insets of microscope images of written arrays*

Some exemplar arrays using the laser processing route are shown in Figure 25, where the dependence of hole diameter and array period on pulse energy and scan velocity can be seen. A numerical aperture (NA) of 0.47 was used for arrays with a 2 μm array pitch, changed to 0.25 for 4 μm and 6.6 μm arrays: NA=0.47 and NA=0.25 respectively correspond to 1.09 μm and 1.78 μm Gaussian peak waist widths (where local intensity of the beam has decayed to $1/e^2 \approx 0.135$ of the peak intensity) [4].

The quality of the arrays written by this method depends on large part of the quality of the setup, with some difficulties being encountered in the repositioning between rows leading to "stitching" type errors (misalignment between rows), seen later in Figure 100. This is a result of irregular delays of the motorised stage in moving after writing each row, leading to loss of synchronisation [4].

It was also found (see Section 6.1.2.1) that the laser patterning process used here tended to lead to a wider variation in hole shapes, as compared to the e-beam lithography approach. As to be expected, this is more noticeable when ablating smaller holes, but for mid-infrared EOT devices, pitches down to 2 μm pitch (with ~1 μm diameter holes) with excellent optical performance were found to be readily very achievable.

A comparison of the three methods (lift-off, wet-etching and laser ablation) used in the work of this thesis for EOT device fabrication is summarised schematically in Figure 26.

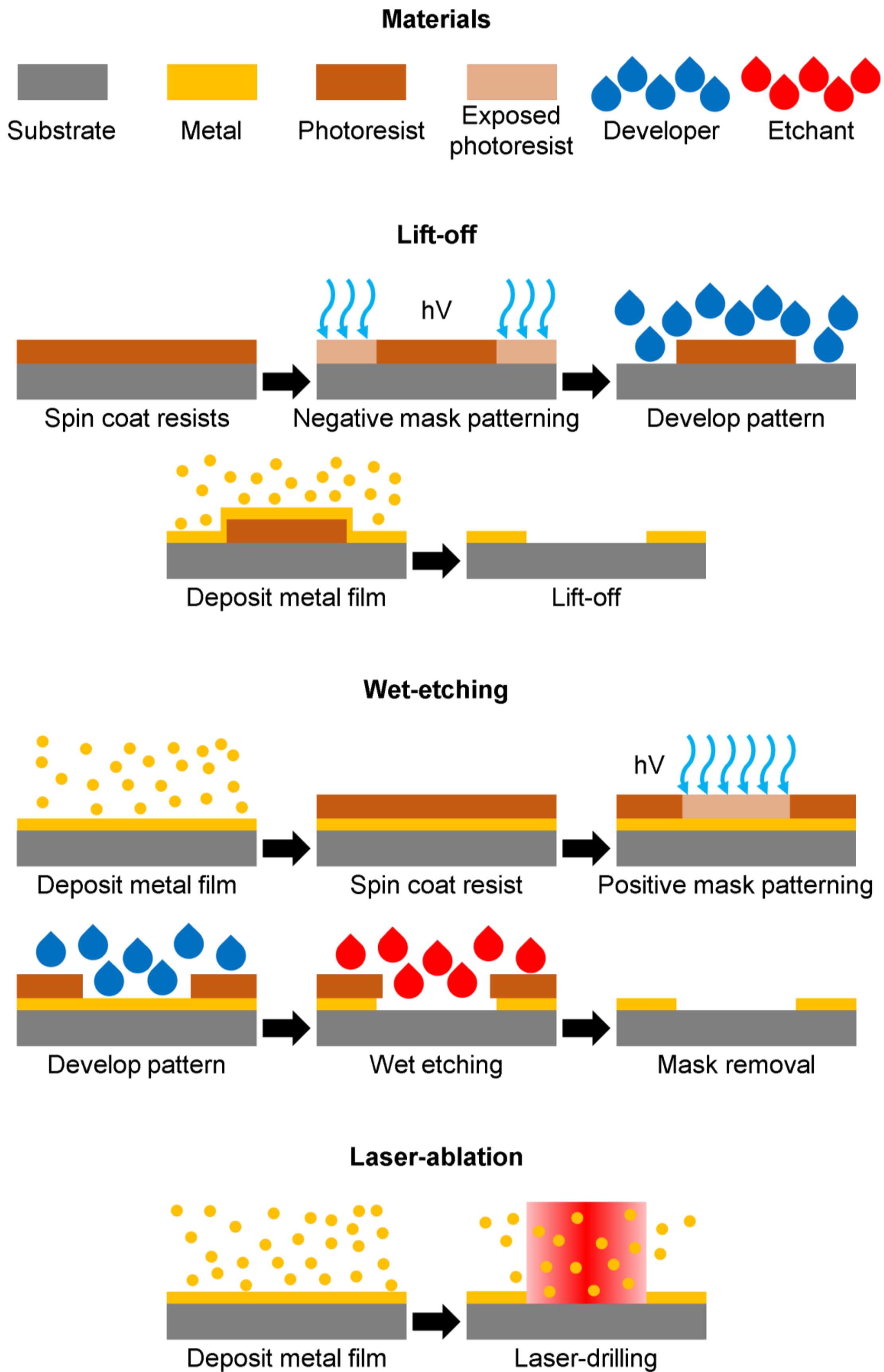

Figure 26: Schematic diagrams of different array fabrication methods used in the work of this thesis.

4.2.4. Characterisation

4.2.4.1. Optical Microscopy

Besides being used for taking images of arrays, a Nikon LV150 optical microscope (with ×5-100 objective lens magnification) was used during fabrication for device quality checks, e.g. that holes were fully formed after etching before moving removing the PMMA mask. Exemplar device images obtained at various stages of the fabrication process are shown in Figure 27.

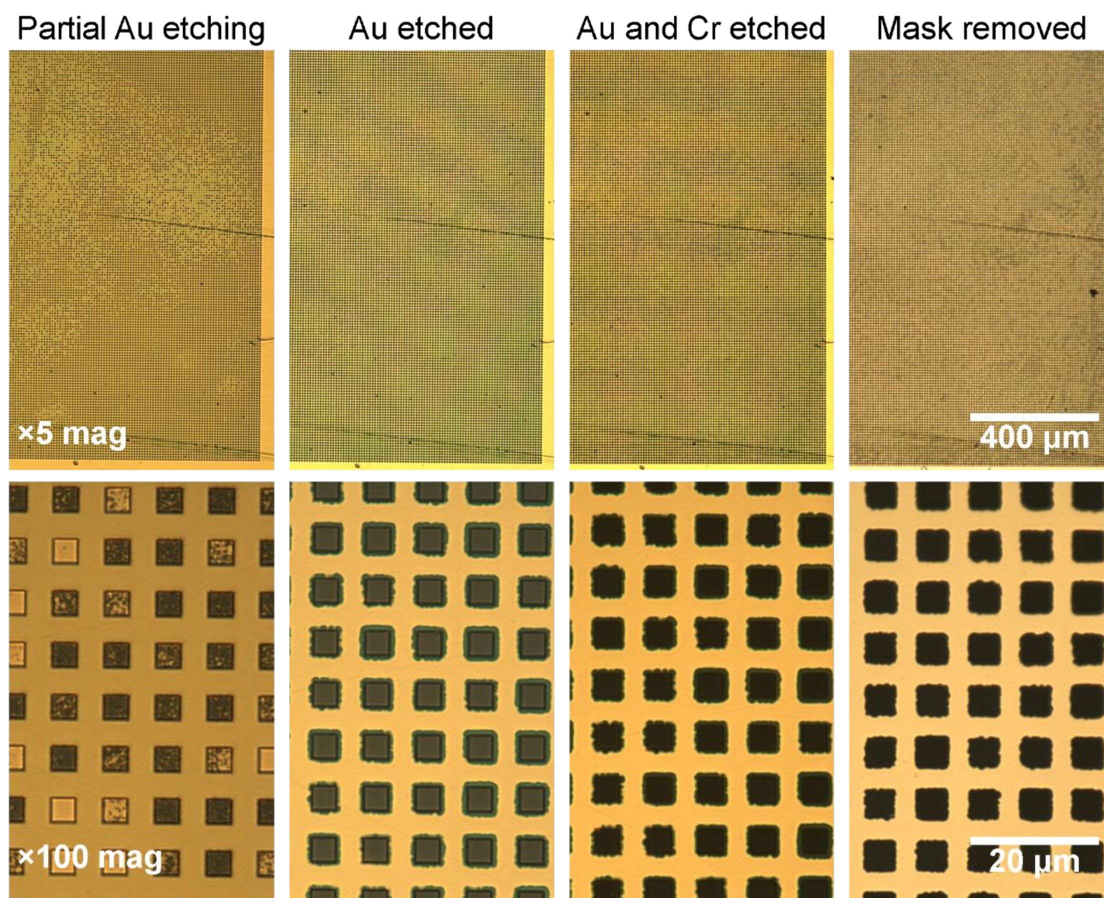

Figure 27: Wet-etched device at different stages of fabrication as seen through optical microscope, showing PMMA mask hole outlines and metal layers

4.2.4.2. Ellipsometry

Ellipsometry is a technique to obtain the optical properties *n* and *k* of thin films by measuring changes in polarisation (from linear to elliptical) after a beam is reflected off a surface at an angle as shown in Figure 28. The system used at

the University of Exeter was a J.A. Woollam Co. M-2000XI, with a working range from 400 to 1700 nm and data processing being performed in CompleteEASE 6.51. Measurements of *n* and *k* in the mid- and long-wave region, as performed externally by collaborators UNCC in the USA, were obtained using a Woollam spectroscopic ellipsometer having a range out to 20 μm.

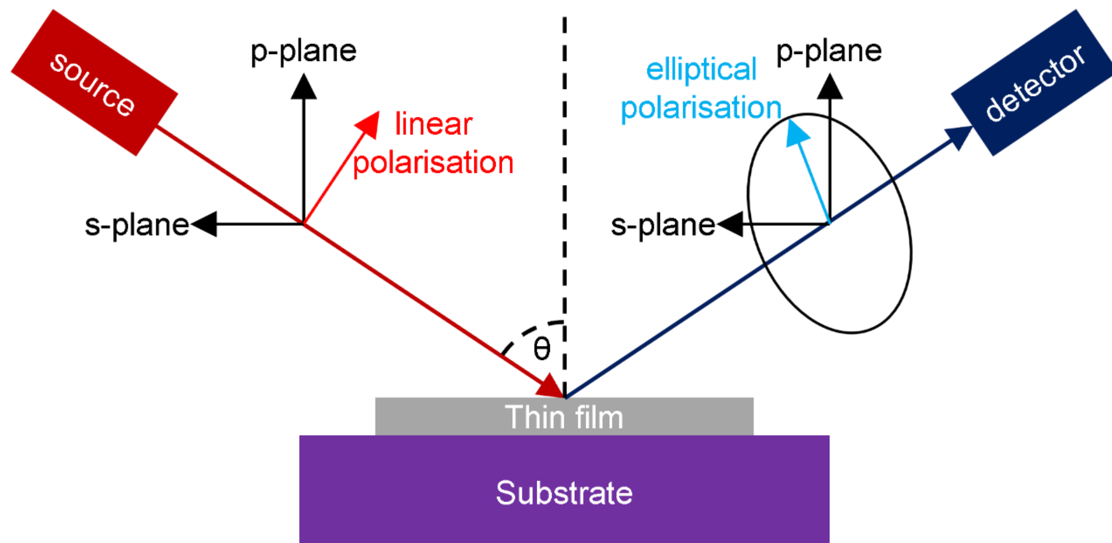

Figure 28: Schematic of basic ellipsometry measurement setup

The measured components are *ψ* (psi, amplitude component) and *Δ* (delta, phase-shift) of the detected beam, and vary depending on the film thickness and composition. When combined with the normalised reflection coefficients of the *p* and *s* polarised light (r_p and r_s) the complex reflectance ratio *ρ* in Equation (38) is obtained [83].

$$\rho = \frac{r_p}{r_s} tan\, \psi \,.\, e^{i\Delta} \quad (38)$$

The collected data is compared to an oscillator model ("Cody Lorentz + Gaussian" type used here) of the same material featuring expected film thickness (derived from AFM or surface profiler measurements) and optical property values, from which the actual values for *n* and *k* can be extracted.

Since the devices consist of multiple types of materials (e.g. the substrate and/or capping layers) measurements are also taken of each separately to account for

reflections at the different material interfaces: in these cases they would be of the blank substrates and substrates with only the capping layer material deposited.

4.2.4.3. Scanning Electron Microscopy

Scanning electron microscopy (SEM) provides much higher spatial resolution than any optical system allows, with ×10,000+ zoom allowing detail mere tens of nm across to be imaged. An accelerated beam of electrons is scanned across the device surface, the interaction with which providing several possible products (back-scattered & secondary electrons, x-rays, visible light etc.) to be detected by the appropriate sensors.

The main system utilised here was a combined xT Nova Nanolab 600 FIB/SEM with a tiltable stage as shown in Figure 29. This was useful since it allows for a trench to be milled in the sample with the ion beam and then the trench wall to be imaged with the electron beam, giving an idea as to the 3D structure of the device layers (e.g. showing how the PCM coats the array hole sidewalls).

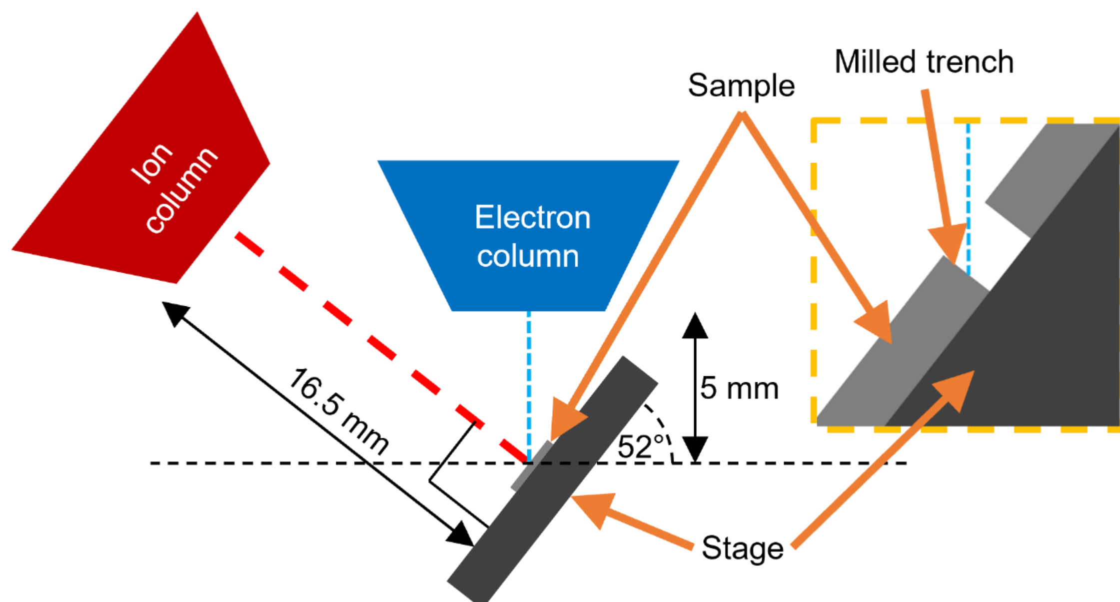

Figure 29: FIB/SEM setup, the tiltable stage allowing the SEM imaging of vertical features of the sample as shown in the inset

Transmission electron microscopy was utilised here to image cross-sections of deposited layers, with slices extracted with a probe after FIB milling. The

machine used was a FEI Talos™ F200X (based at the University of Warwick and operated by Geoff West), a 200 kV accelerating voltage set for measurements.

4.2.4.4. Surface Profiler Scanning

A sample is placed on a moveable stage and a probe is lowered onto the surface. As the sample moves beneath, the probe registers the change in height. The machine used here was a KLA Tencor D-100, with a typical scanning speed of 0.04 mm/s, meaning that a 2 mm-long scan would take less than a minute to generate, much quicker than can obtained with a typical AFM.

The Tencor profiler was used to quickly confirm the film thicknesses made after thermal evaporation or magnetron sputtering runs, only 2D (height cross-section) scans could be taken and the probe is incapable of being positioned accurately enough over ~1 μm diameter holes to measure their dimensions.

4.2.4.5. Atomic Force Microscopy

Atomic force microscopy (AFM) involves scanning a probe with an atomically-sharp tip on the end of a cantilever across the surface of a sample to provide detailed surface topology, usually derived by measuring the deflection of a laser off the reflective top of the cantilever via a split photodiode (see Figure 30). A Bruker Innova desktop AFM unit with both contact mode and tapping mode probe tips was used in this thesis.

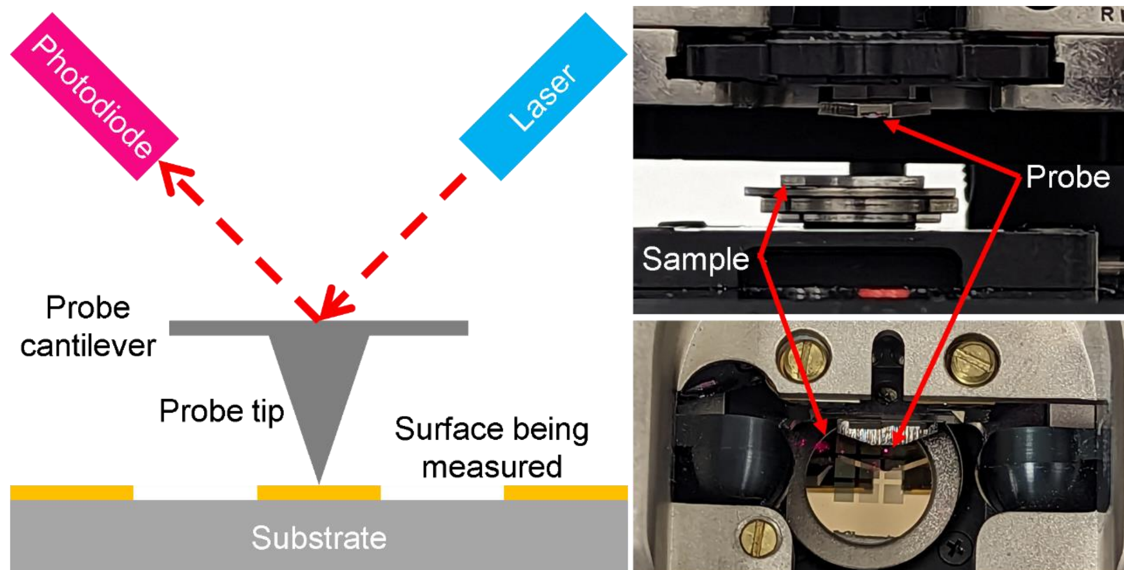

Figure 30: (a) Schematic of AFM operation with (b) photographs of the sample and probe head suspended above from the front (topt) and above (bottom)

Unlike surface profiler measurements, the AFM is capable of providing both 2D (film height for a line across the device surface) and 3D (height for a section of the plane) within a small area (on micrometer scale). The accuracy is limited though by the steepness of the vertical features and the sharpness of the probe tip, as illustrated schematically in Figure 31.

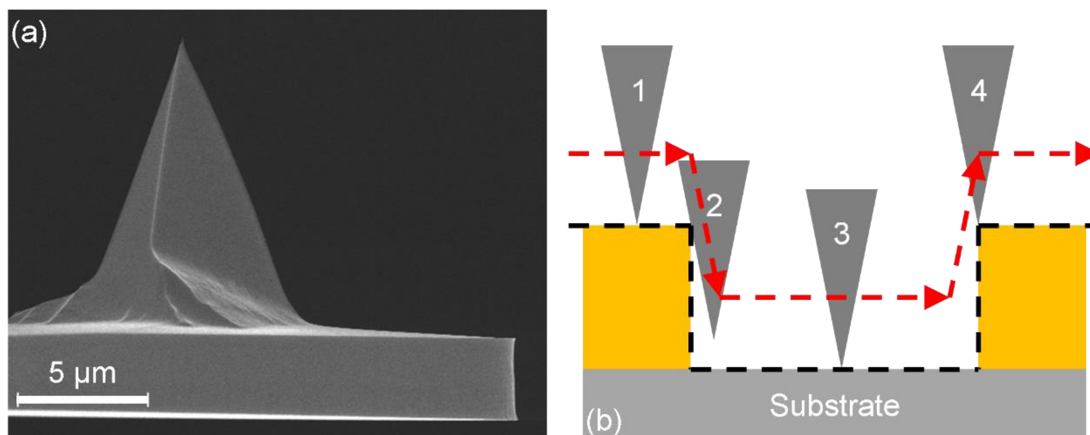

Figure 31: (a) SEM image of an example AFM probe tip [84] *(and (b) schematic showing the representation of the accuracy limitations of AFM scanning*

Other disadvantages of the AFM as compared to the surface profiler system include taking a much longer time to set up (potentially hours rather than the minutes) and probes quickly wearing out (depends on the material, but can be as

little as 5 runs), so AFM runs were mainly used here to confirm that surface profiler measurements were accurate. The AFM was also used to confirm the different topology features of devices made with different methods, showing the build-up of metal around holes as a result of lift-off (see Figure 20) and the non-vertical side walls obtained with wet-etching (see Figure 21).

4.2.4.6. Energy Dispersive (X-ray) Spectroscopy

Energy dispersive X-ray spectroscopy (EDS) is a technique used to evaluate material composition, involving measuring the emitted photon energy (at x-ray wavelengths) after excitation by an electron beam from an SEM or TEM. These energies are compared with values in a catalogue to determine the element (many having multiple energy peaks, corresponding to different electron transitions), and the emission intensity is used to work out the proportions. The process is “standardless” since it does not require use of standard reference samples of the materials to be detected.

The machine used that performed measurements at the University of Exeter was a TESCAN VEGA3 SEM with an Oxford Instruments X-MAXN EDS detector, using a working distance of 15 mm. The energy resolution was 127 eV, with a typical acceleration voltage of 20 kV (20 keV maximum beam energy).

EDS was mostly used to confirm that the compositions of alloys/compounds used/deposited was as expected (was used here for both the PCM sputtering targets and deposited films), but was also utilised here to check the effectiveness of barrier layers to prevent different materials from mixing. The thicknesses of the samples tested ranged from the order of hundreds of nm (deposited films) to several millimeters (sputtering targets), the use of "standardless” process giving on the order of 2 % accuracy [85].

4.2.4.7. Fourier Transform Infrared Spectroscopy

Fourier transform infrared (FTIR) spectroscopy was the main method of measuring device reflectance and transmittance used in this thesis. As shown in schematic in Figure 32, rather than detecting the absorbance of a monochromatic light source by a material, a moving mirror allows for selective constructive and destructive interference of light from a broadband source covering the entire wavelength range. Fourier transforms operations are performed to provide plots of transmittance/reflectance against wavenumber, which is then easily converted to wavelength.

Measurements using the Thermo-Fisher Nicolet iS5 FTIR equipment in the work of this thesis typically had a wavelength range of 1-15 μm (wavenumbers of 10,000-667 cm^{-1}). For most runs, the samples were attached to a 1 mm thick aluminium plate with a 1 mm aperture at its centre (necessitating 2×2 mm arrays to make complete coverage easy), seen in the photographs in Figure 32. Additional runs, including all those performed in reflectance and with a polariser, were conducted using a Bruker Vertex 80v FTIR system.

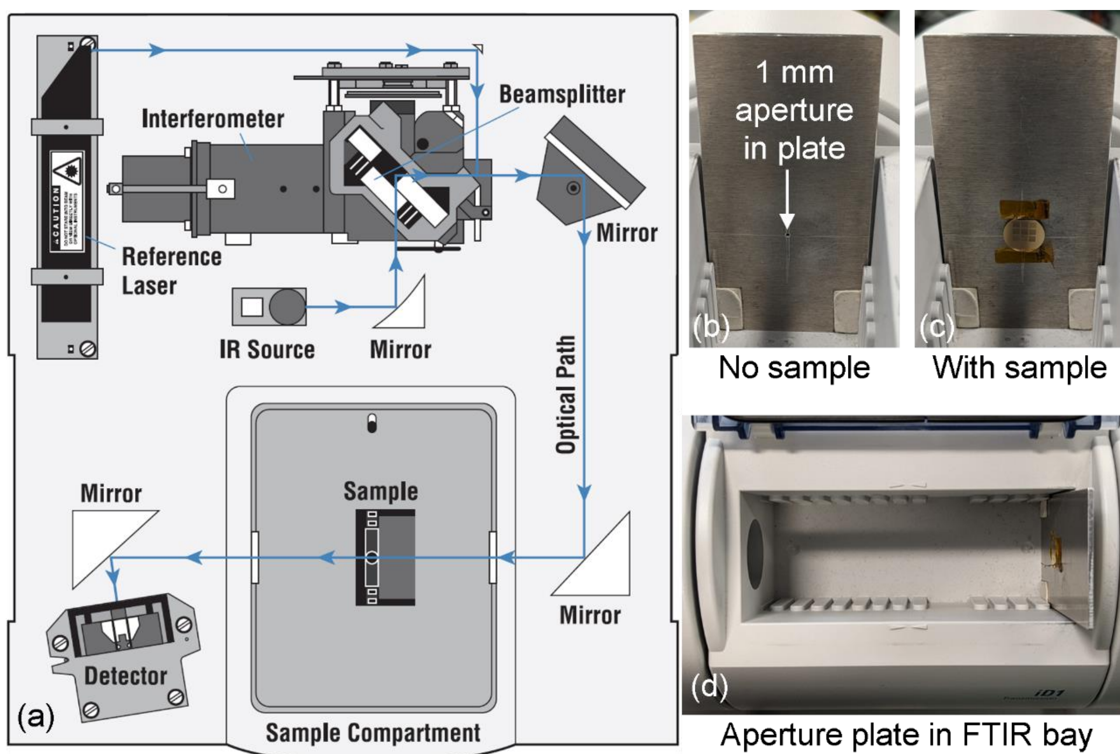

Figure 32: (a) Schematic of basic FTIR instrument layout [86], *aperture plate (b) with and (c) without sample in place, and (d) aperture plate in Thermo-Fisher Nicolet iS5 FTIR bay*

FTIR runs were taken separately with the aperture plate in-place, a blank sample substrate and then the arrays to be measured. Array spectra were then usually normalised to the substrate transmission to provide a measurement of the EOT transmission independent of substrate absorption, which is thickness dependant. Runs that were performed with a linear polariser (e.g. those with hexagonal arrays) were also normalised to account for the absorption of the polariser.

Sequential runs were conducted for each sample setup until successive spectra looked identical. This was to allow the machine to “settle” and would normally require only three runs (the latter two showing no difference).

4.2.4.8. Ultraviolet to Near-Infrared Micro-Spectrophotometry

Optical reflection and transmission spectra at shorter wavelengths than could be obtained using the FTIR approach were conducted with a Jasco MSV-5300 micro-spectrophotometer, with a range of 200-1,600 nm. Unlike the FTIRs, this used a grating to filter specific wavelengths from a broadband light source (layout

shown in Figure 33), which needed to be allowed to warm up for half an hour after switching on before starting any measurements to ensure steady output and accurate measurements.

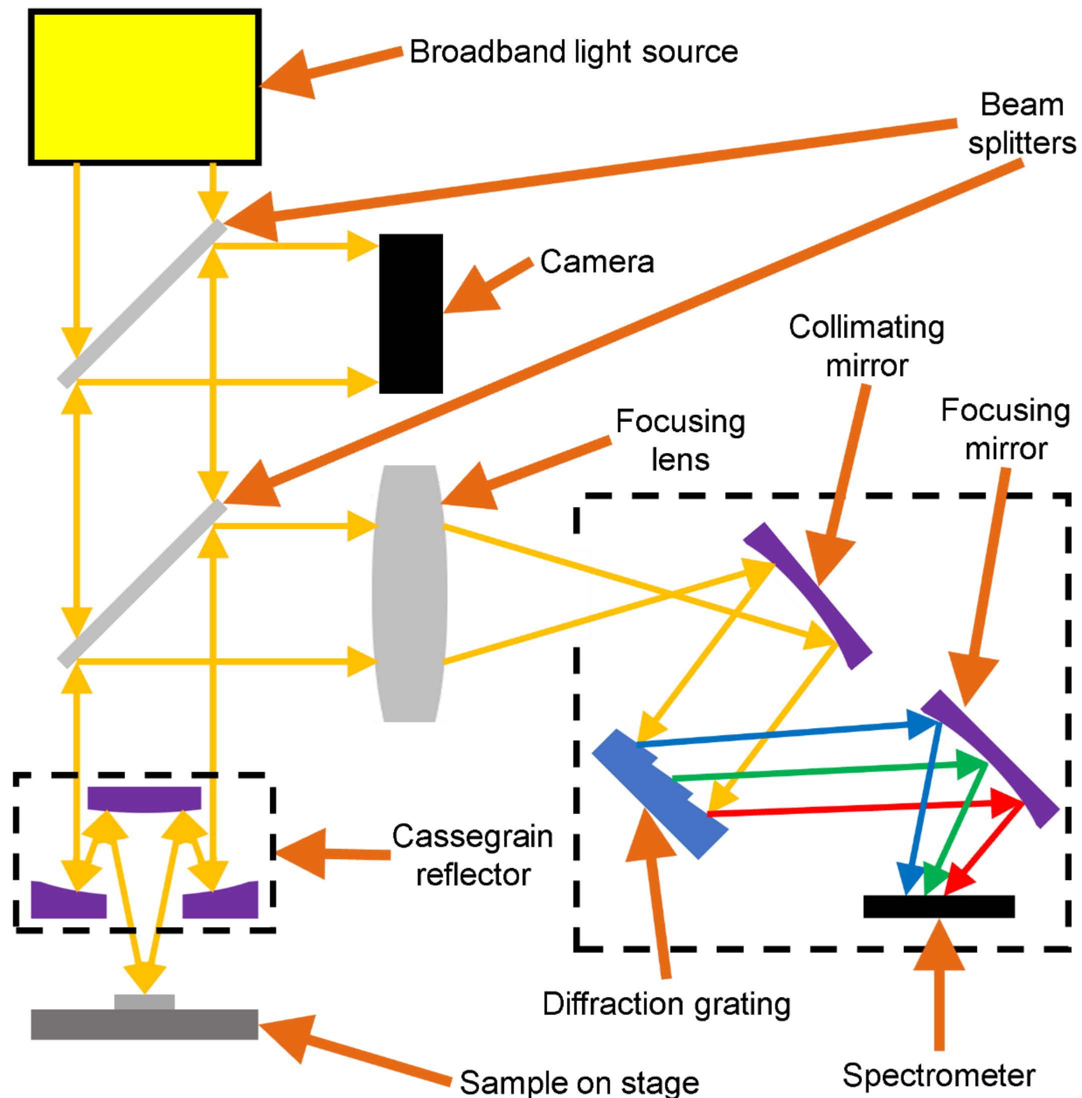

Figure 33: Schematic of micro-spectrophotometer optical componentry, adapted from [16], [19]

The setup had an inbuilt microscope with a ×32 magnification Cassegrain lens that allowed specific small regions of a device (down to a few μm) to be measured. Reflectance runs normally baselined using an aluminium mirror, issues with baselining occasionally led to some reflectance spectra apparently showing over 100% transmission. Another issue that could not be eliminated was the “bump” that occurs in every spectrum at 850 nm, where the detectors used in the system (for higher and lower wavelength sub-ranges) are changed.

5. Modelling and Device Design

The purpose of this chapter is to explore how changing the parameters of phase-change EOT devices alters their characteristics, focusing primarily on the optical performance but also looking at the viability of using Joule heating (by passing electrical current through the EOT film) to heat the PCM so it can be switched between states. Most simulations were performed by using finite-element analysis in COMSOL Multiphysics (process explained in Chapter 3), but calculations of certain spectral features were also performed using simple scripts in Octave, complementing and verifying the simulations.

The simulations involve modelling of devices using actual optical data (obtained both from prior-published external sources and from measurements performed internally and by outside academic collaborators), and simulations using arbitrary materials parameters to demonstrate the effect of changing a single parameter (e.g. allowing the value of the PCM refractive index n to vary, while keeping the extinction coefficient k constant for the entire wavelength range). Parameters varied in terms of exploring device design/performance include the device dimensions (e.g. array period, array type, hole fill-factors, layer thicknesses); incident light properties (e.g. incident light polarisation and beam orientation) and material properties (n and k for optical modelling along with electrical resistivity, thermal conductivity and specific heat capacity for thermal modelling).

5.1. Analytical Modelling

5.1.1. Calculating EOT Minima Positions

From the dispersion relation in Equation (10), the positions of the minima of an EOT film for a wide range of incident beams angles can be calculated as a function of this angle and relative permittivity of the film and substrate/superstrate.

$$\lambda_{SP} = \frac{\sqrt{\frac{\varepsilon_f(\lambda)\varepsilon_s(\lambda)}{\varepsilon_f(\lambda)+\varepsilon_s(\lambda)}}}{\sqrt{\left(\frac{p \sin\theta}{\lambda} \pm i\right)^2 + j^2}} p \qquad (39)$$

A modified form is shown in Equation (39), accounting for wavelength-dependent optical properties. Using a simple MATLAB/Octave script, plots (shown in Figure 35) can be generated for dispersion curves by iterating toward the wavelength value that best balances both sides of the equation. Here, relations for a range of array pitches and angles of the incident beam (parallel to the plane of the electric field polarisation, see Figure 48 later) were calculated, similar to the plot in Figure 34: this shows an example of the surface plasmon energy dispersion with respect to the incident light momentum k_x (rather than the incident angle but the two are related by Equation (4)), with energy bands for the different resonance modes which correspond with the transmission spectra's feature positions.

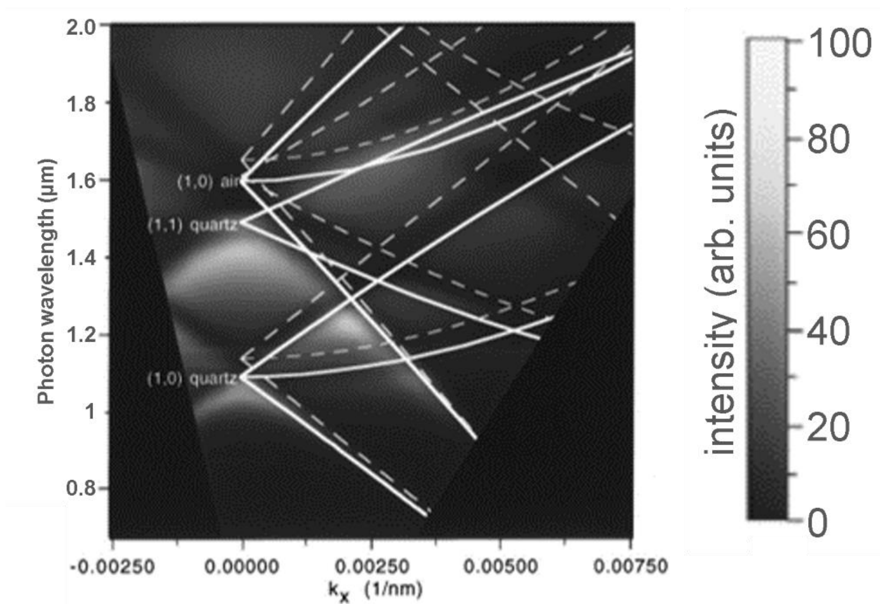

Figure 34: Experimental transmission intensity of a 600 nm-pitch array in 200 nm thick Ag film with 150 nm hole diameter adapted from [43]. *Surface plasmon energy dispersion bands (solid lines) overlaid show positions of spectral minima against component of incident photon momentum, k_x=0 indicates beam normal to the array plane.*

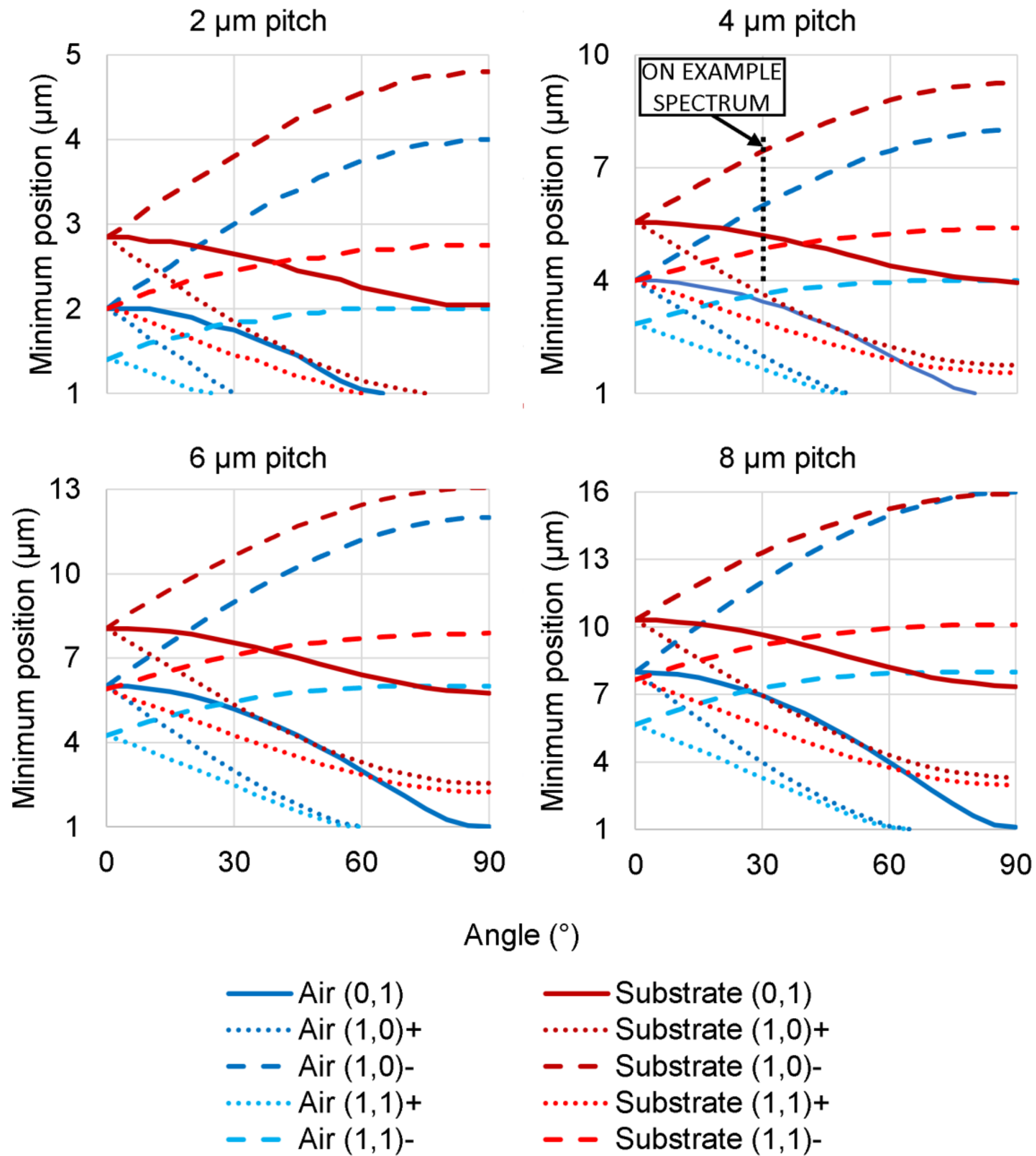

Figure 35: Dispersion relations (of square arrays in Au film on CaF_2 substrates) against beam angle for varied SP orders, e.g. "(1,0)±" meaning ±1 i and 0 j, section marked out on 4 µm-pitch array plot expanded on in Figure 36

The minima positions predicted by this analytical model correspond exactly to simulations performed in COMSOL Multiphysics, in Figure 36 a 4 µm-pitch array (equivalent to 4 µm-pitch array in Figure 34), the effect of the beam incident angle to the array plane is discussed further in Section 5.2.5.

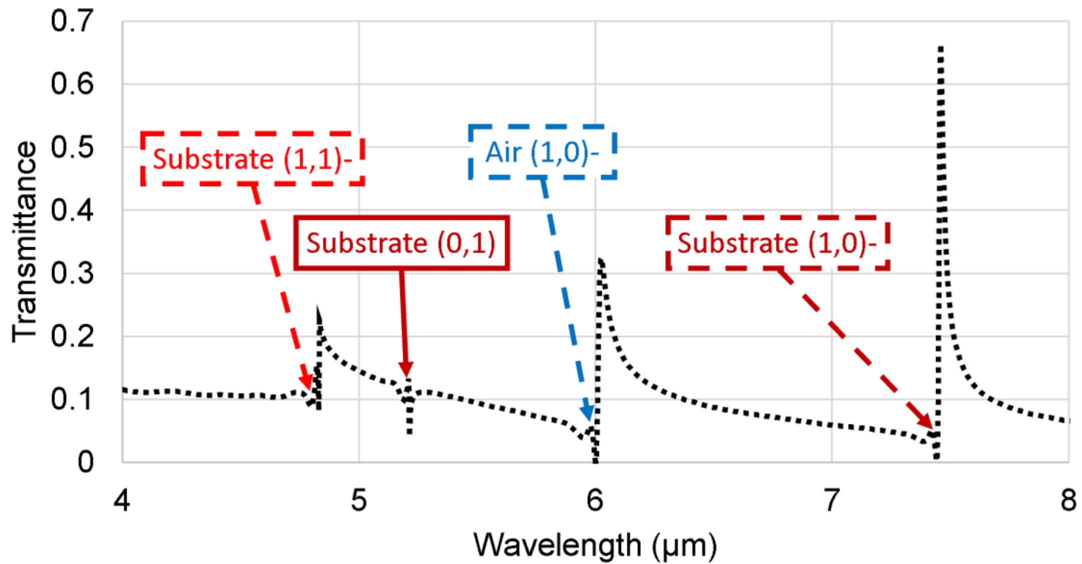

Figure 36: Modelled 4 µm-pitch array in 40 nm Au film on CaF_2, fill-factor of 0.5 and incident radiation 30° from the array normal along the same plane as the array polarisation (see Figure 48), minima from resonance modes labelled.

From Figure 35 it can be seen that angling the incident beam away from the surface normal expands out the minima corresponding to different SP orders. However, since all measurements were performed with the incident beam parallel to the surface normal, the most relevant information here is the longest wavelength minimum when this angle equals zero, in this case the "substrate (0,1)" order. This order precedes the main EOT peak, giving the wavelengths for which an array of a particular period *p* will act as a bandpass filter.

5.1.2. Optical Properties with Crystallisation Fraction

Between the fully amorphous and fully crystalline states, the variation of *n* and *k* is usually modelled using effective medium theory. Possible crystallisation mechanisms typically used in such models are shown schematically in Figure 37.

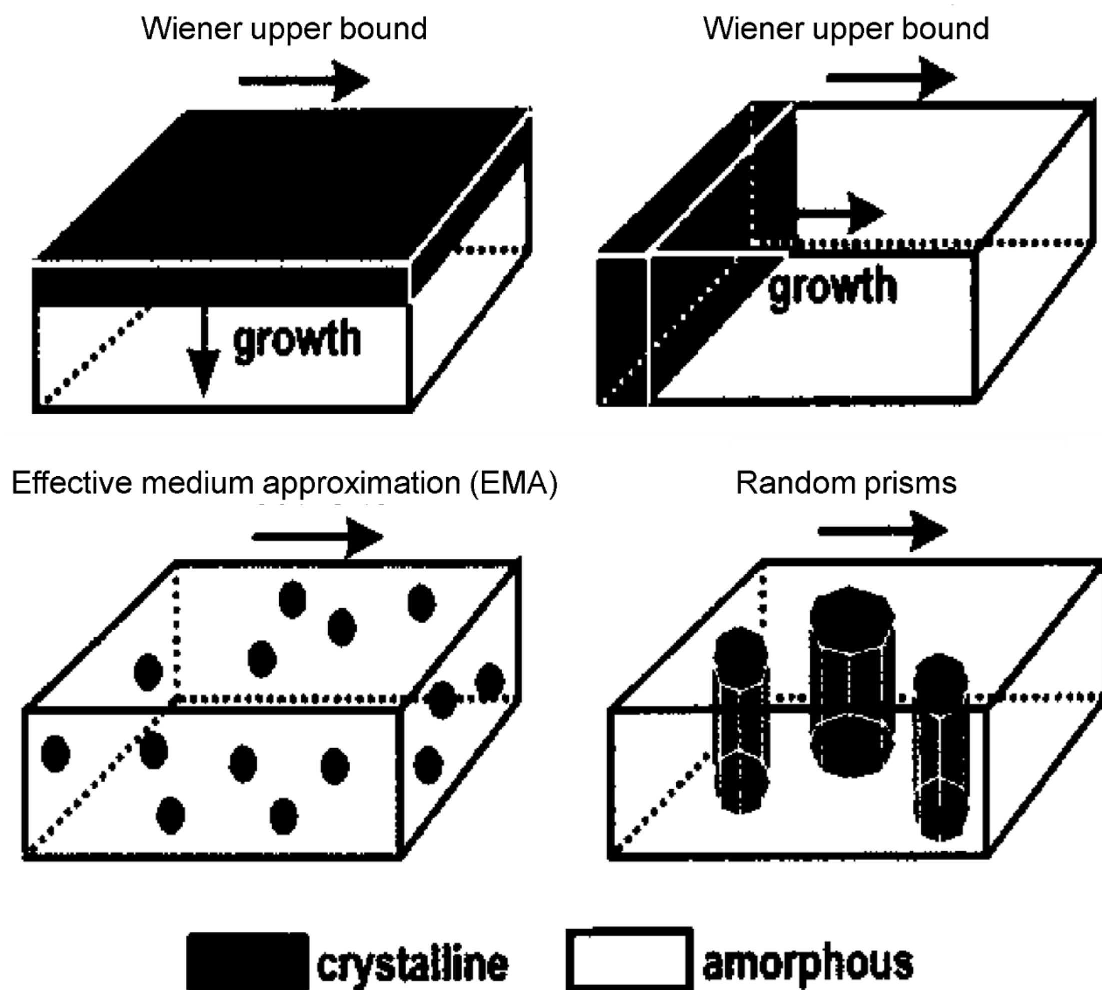

Figure 37: Models of crystalline growth, adapted from [87]

These models can be given as functions of the (real) refractive index n imaginary refractive index/extinction coefficient k, with complex refractive index $\tilde{n}$ is a function of n and k as given by Equation (40)

$$\tilde{n} = n + ik \quad (40)$$

The complex relative permittivity is a function of complex refractive index, given by Equation (41)

$$\tilde{\varepsilon_r} = \varepsilon_r' + i\varepsilon_r'' = \tilde{n}^2 = n^2 + 2ink - k^2 \quad (41)$$

where

$$\varepsilon_r' = n^2 - k^2 \quad (42) \qquad \varepsilon_r'' = 2nk \quad (43)$$

From [46], the Wiener upper bound is given by

$$\widetilde{\varepsilon_r}\left(f,\widetilde{\varepsilon}_{r_{am}},\widetilde{\varepsilon}_{r_{cr}}\right)=\left(1-f\right)\widetilde{\varepsilon}_{r_{am}}+f\widetilde{\varepsilon}_{r_{cr}}\right) \qquad (44)$$

The Wiener lower bound is

$$\widetilde{\varepsilon_r}\left(f,\widetilde{\varepsilon}_{r_{am}},\widetilde{\varepsilon}_{r_{cr}}\right)=\frac{1}{\left(\frac{1-f}{\widetilde{\varepsilon}_{r_{am}}}\right)-\frac{f}{\widetilde{\varepsilon}_{r_{cr}}}} \qquad (45)$$

The Bruggeman-type effective medium approximation (EMA) is

$$\widetilde{\varepsilon_r}\left(f,\widetilde{\varepsilon}_{r_{am}},\widetilde{\varepsilon}_{r_{cr}}\right)=\frac{1}{4}\left(2\varepsilon_p-\varepsilon_p'+\sqrt{\left(2\varepsilon_p-\varepsilon_p'\right)^2+8\widetilde{\varepsilon}_{r_{am}}\widetilde{\varepsilon}_{r_{cr}}}\right) \qquad (46)$$

with

$$\varepsilon_p=(1-f)\widetilde{\varepsilon}_{r_{am}}+f\widetilde{\varepsilon}_{r_{cr}} \qquad (47) \qquad \varepsilon'_p=f\widetilde{\varepsilon}_{r_{am}}+(1-f)\widetilde{\varepsilon}_{r_{cr}} \qquad (48)$$

For the case of random prisms, we have

$$\widetilde{\varepsilon_r}\left(f,\widetilde{\varepsilon}_{r_{am}},\widetilde{\varepsilon}_{r_{cr}}\right)=\sqrt{\widetilde{\varepsilon}_{r_{am}}\widetilde{\varepsilon}_{r_{cr}}}\,\frac{\varepsilon_p+\sqrt{\widetilde{\varepsilon}_{r_{am}}\widetilde{\varepsilon}_{r_{cr}}}}{\varepsilon_p'+\sqrt{\widetilde{\varepsilon}_{r_{am}}\widetilde{\varepsilon}_{r_{cr}}}} \qquad (49)$$

Equations (44) - (49) give optical data in terms of dielectric function *ε*, but electrical characteristics can be similarly modelled by substituting this for conductivity *σ*. To go from *ε* to *n* and *k*, Equations (50) and (51) are used.

$$n=\sqrt{\frac{1}{2}\left|\widetilde{\varepsilon_r}\right|+\varepsilon_r'} \qquad (50) \qquad k=\sqrt{\frac{1}{2}\left|\widetilde{\varepsilon_r}\right|-\varepsilon_r'} \qquad (51)$$

With

$$|\tilde{\varepsilon_r}| = \sqrt{{\varepsilon_r}'^2 + {\varepsilon_r}''^2} \tag{52}$$

so the values of *n* and *k* as functions of the fully amorphous/crystalline *n*/*k* values and the fraction of crystallisation *f* can be given as

$$n(f, n_{am}, k_{cr}) = \sqrt{\frac{1}{2}|\tilde{\varepsilon_r}(n_{am}, k_{cr})| + {\varepsilon_r}'(n_{am}, k_{cr})} \tag{53}$$

and

$$k(f, n_{am}, k_{cr}) = \sqrt{\frac{1}{2}|\tilde{\varepsilon_r}(n_{am}, k_{cr})| - {\varepsilon_r}'(n_{am}, k_{cr})} \tag{54}$$

n values with crystallisation fraction *f* are given for a couple of example wavelengths in Figure 38, using refractive index data for GST-225 from [55], showing that the EMA and random prisms models give an almost linear relation between *f* and the proportional change in *n*. EMA most accurately represents growth of crystalline regions in GST-225 (dominated by the process of nucleation) so this correlation is not unexpected.

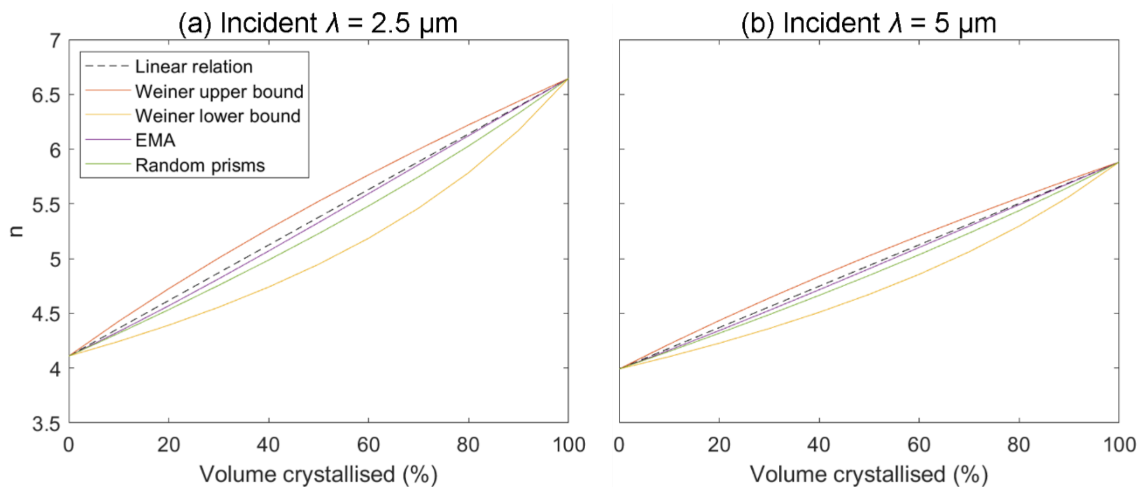

Figure 38: calculated n values against PCM volume crystallised (fraction of crystallisation f) using the different models, for (a) 2.5 µm and (b) 5 µm incident light wavelengths

Figure 38 also shows that the Wiener upper and lower bound calculations have the greatest deviation from the linear relation, acting as the limits within which the calculated dielectric functions/refractive index values occur within regardless of the filling scheme [87]. Figure 39 shows plots of *n* and *k* for the different models of partially crystalline PCM (again using GST-225 *n* values from [55] as an example) across a wide wavelength, from 0% (amorphous) to 100% (crystallised) volume crystalline *f* in intervals of 20%.

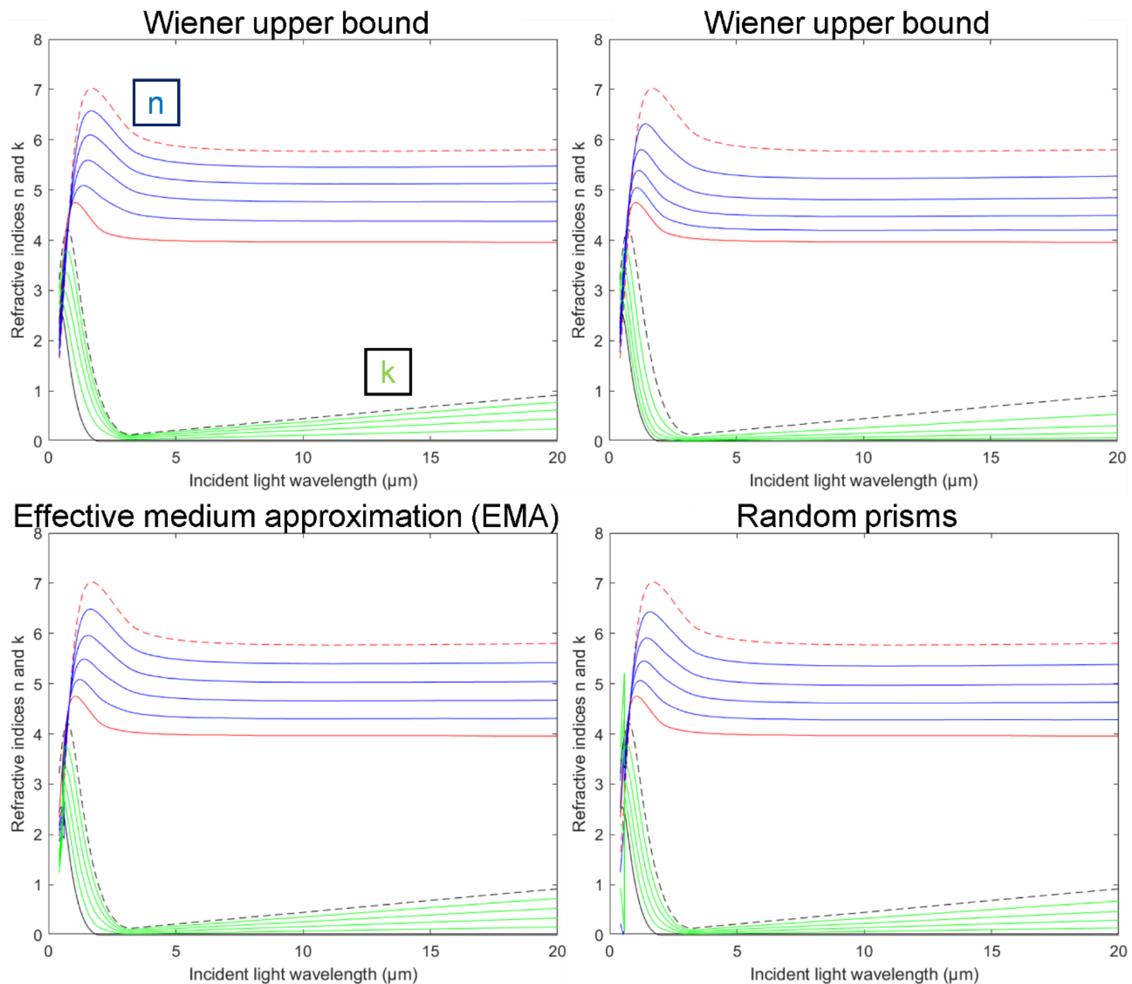

Figure 39: Calculated optical data values for partially crystalline PCMs, crystallisation fraction intervals of 20% between amorphous (solid lines) and crystalline (dashed lines) states.

For light at normal incidence, the reflectivity of a material with refractive index n_2 (in surroundings of n_1) is related by the Fresnel equation in Equation (55) and can thus be calculated as a function of *f* using these models, with examples using GST-225 *n* values from [55] shown in Figure 40.

$$Reflectivity = \left|\frac{n_1 - n_2}{n_1 + n_2}\right|^2 \qquad (55)$$

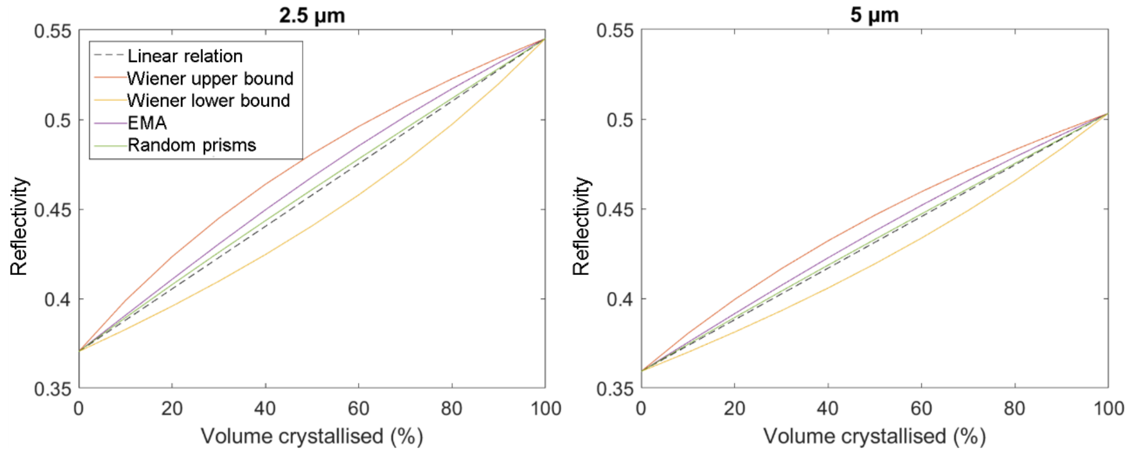

Figure 40: Calculated reflectivity values against volume crystallised (fraction of crystallisation f) using different models, at 2.5 um (left) and 5 um (right)

As a consequence, reflectivity off a PCM surface appears to be a good indication of the fraction of crystallisation, however the effect of additional layers of the device needs to be considered, as must the wavelength dependency as a result of constructive/destructive interference effects created by additional layers resulting in as an etalon/Fabry-Perot cavity. For the latter, transmittance peaks occur at the positions given by Equation (56)

$$\lambda_{peak,x} = \frac{2nt}{x} \qquad (56)$$

with a simulated example shown below in Figure 41 for a thickness t=580 nm crystalline silicon film (consistent n=~3.5 across the chosen wavelength range) suspended in air (same FPBCs with PML cell tops and bottoms as EOT models) giving a first-order peak at 4 μm and subsequent ones at $\lambda_{peak,x} = \frac{4}{x}$.

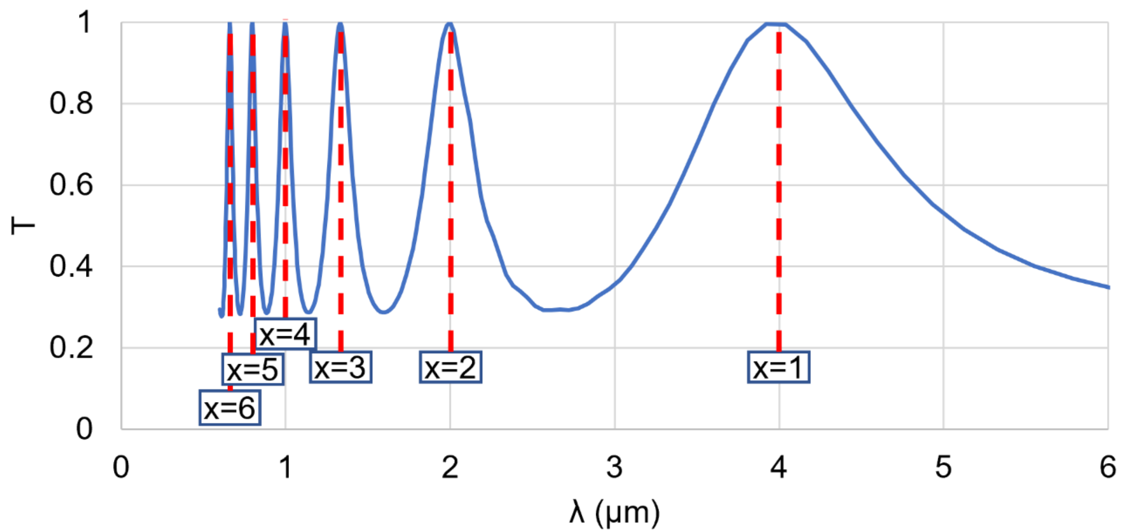

Figure 41: Simulated transmittance spectrum of a crystalline silicon etalon (ignoring Si absorption), with peaks indicated by Equation (56) marked out

5.2. Mid-Infrared EOT Array Simulations

5.2.1. Use of Square vs Hexagonal Arrays

The majority of devices featured in this thesis utilise square arrays, although one might imagine that using hexagonal (hex') arrays would give more nearest-neighbour features to any hole in an otherwise-equivalent EOT film and thus boost the EOT effect. There were several reasons for choosing to concentrate on square arrays, including:

- Facilitation of simulation
  - Square arrays have the simplest possible unit cell, a cross-section of a single circle within a square as opposed to a hex' array's two holes within a rectangle. This reduces the number of mesh elements required and thus processing time.
  - Square arrays are insensitive to changes in polarisation whereas hex' arrays are sensitive to polarisation (see Figure 42), meaning that any measured data collected experimentally must also ideally have multiple runs with different polarisation angles.
  - Hex arrays need different models for fill factors up to and above 0.5 (at ff=0.5 the holes meet the unit cell walls), making parametric sweeps when changing the hole diameter more complex.

- There is little difference in fabrication complexity when using e-beam lithography or laser-drilled processes between making square and hex' arrays, though the former is slightly simpler since only a single cell with equal periodicity in x and y axes is required.

- Simulations showed consistently higher peak transmittance values and Q-factor for square arrays.

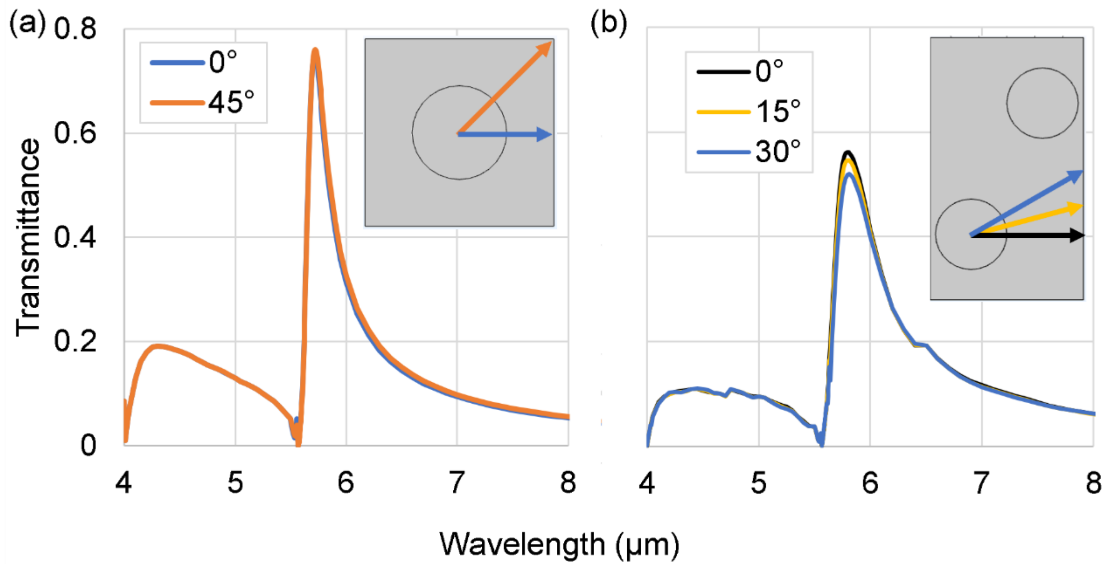

Figure 42: Demonstration of polarisation (in)sensitivity of a 4 μm pitch square array (a) with fill factor of 0.5, vs its hex' (b) equivalent (array pitch adjusted to ~4.62 μm to provide peak at same wavelength, holes resized to fill factor of 0.4653 (~93% of square array fill factor) to cover same proportional area), with unit cell schematics inset

Fill factor *ff* is the proportional size of the array holes with diameter *d* for array pitch *p*, as given by Equation (57).

$$ff = \frac{d}{p} \quad (57)$$

Use of a hex' array with the same pitch and hole size as a square one will not produce an identical spectrum, due to their differing reciprocal lattice vectors *g* for an array period *p* as given in Equations (58) and (59).

$$\left|\overrightarrow{G_{square}}\right| = \frac{2\pi}{p} \quad (58) \qquad \left|\overrightarrow{G_{hexagonal}}\right| = \frac{4\pi}{p\sqrt{3}} \quad (59)$$

The reciprocal lattice vector of a hexagonal is larger than that of a square array by a factor of 2/sqrt(3)=~1.1547, necessitating an equivalent increase in pitch to produce similarly positioned transmission spectra. Figure 43 shows simulations of 4 µm pitch square and hex' arrays, alongside a ~4.62 µm pitch hex' one.

The hole sizes may also be adjusted to account for the slightly greater coverage of a certain fill factor for a hex' array, two holes in an hex' cell of area sqrt(3)*p^2=~1.732p^2 as opposed to one hole in a square cell of area p^2. This relative size of this fill factor is sqrt(sqrt(3)/2)=~0.9306, a 2 µm diameter hole in a square array equating to 1.8612 µm in a hex' array (fill factor of ~0.4653), with an example of how this affects the spectrum also in Figure 43**.**

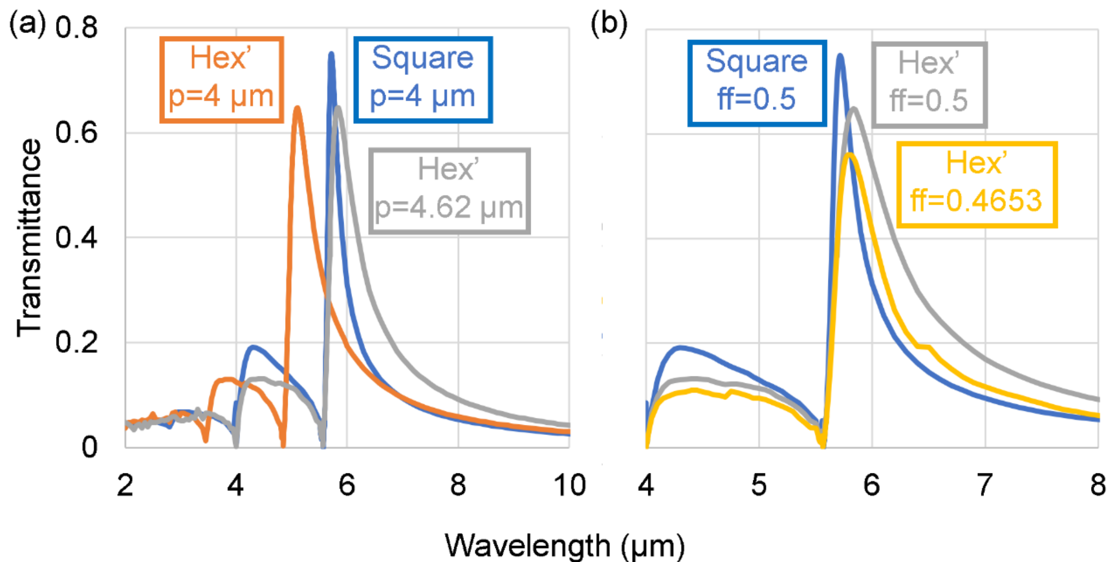

Figure 43: Simulated spectra demonstrating (a) the different spectra generated for square vs hex' arrays with a fill factor of 0.5 but different pitches and (b) the effect of equating the relative hole areas, square array with p=4 µm and hex' array with p=4.62 µm

5.2.2. Rectangular Arrays

Polarisation dependence can also be introduced by using rectangular arrays, with different array pitches for the rows and columns. This will give two major peaks

at different wavelengths, giving the possibilities of acting as polarisation-dependent signal modulator at two different frequencies simultaneously, or perhaps extending the range of a filter tuneable by other means.

Figure 44 shows simulations of an EOT array in 40 nm Au film on a CaF_2 substrate with p_x=4 μm and p_y=5 μm at varied linearly polarised E-field angles (2 μm hole diameter, ff_x=0.5 and ff_y=0.4), giving main peak separation of ~1.25 μm.

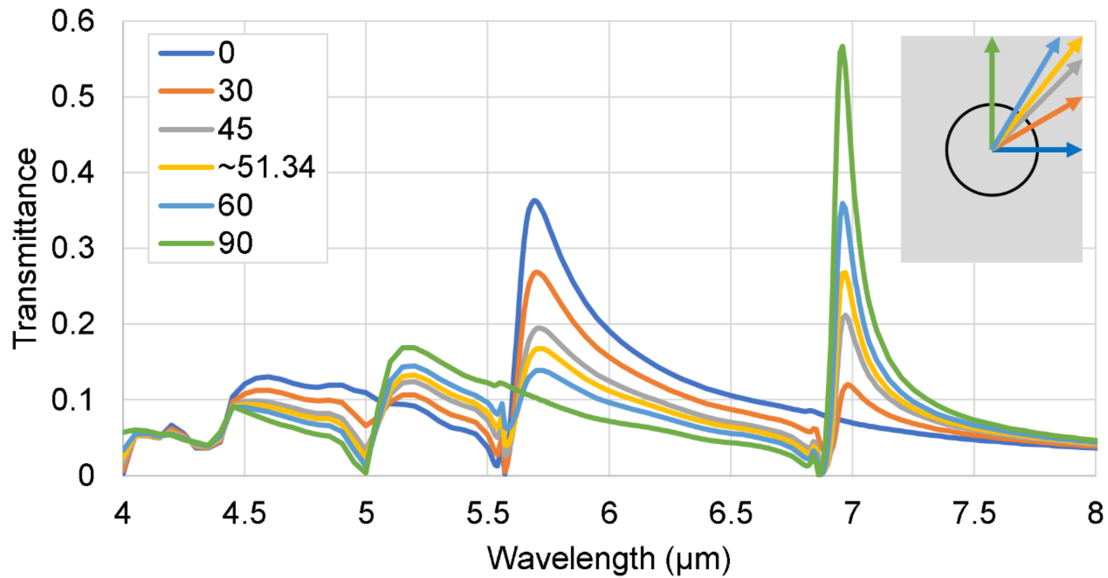

Figure 44: Simulated transmittance spectra of a rectangular EOT array with p_y=1.25p_x, with incident E-field linear polarisation at different angles, 0° representing polarised along the short (x) axis and 90° along the long (y) axis

When the incident light is not polarised exactly along an array axis, the major peaks associated with both axes are seen at the same time in a transmission spectrum, with each's prominence depending on how closely aligned the polarisation is to the relevant axis. The peak heights and widths for each incident radiation angle are given in Table 1, along with the peak sharpness, also called quality factor or Q-factor, as defined in Equation (60).

$$Q - factor = \frac{\lambda_{apex}}{\Delta\lambda_{FWHM}} \quad (60)$$

Table 1: Peak data for simulated arrays shown in Figure 44

Angle (°)	~5.7 μm (short pitch) peak			~6.9 μm (long pitch) peak		
	T	Width (μm)	Q-factor	T	Width (μm)	Q-factor
0	0.36	0.41	13.72		NA	
30	0.27	0.49	11.68	0.12	0.44	15.80
45	0.19	0.59	9.75	0.21	0.21	33.95
~51.34	0.17	0.63	9.03	0.27	0.17	41.48
60	0.14	0.70	8.15	0.36	0.14	49.58
90		NA		0.57	0.12	59.17

This shows that as the polarisation orientation becomes more aligned with the array axis associated with a particular peak, the peak's transmittance increases along with the Q-factor (as the peak width decreases). The example in Figure 44 and Table 1 shows the ~6.9 μm (long pitch) peak becoming sharper and taller as the polarisation angle increases from 0° (perpendicular to the long pitch axis) to 90° (parallel with the long pitch axis), while the ~5.7 μm (short pitch) peak diminishes until it disappears.

The lengthening of the square unit cells to rectangles reduces the relative area covered by the holes, meaning that peak transmittance drops as the aspect ratio increases if the hole diameters are kept the same. Simulations shown in Figure 45 (with data in Table 2) compare transmittance spectra for rectangular arrays of two different aspect ratios, with two different hole sizes for each. One size is the same for both arrays (fill factor relative to the short axis of 0.5), the other holes have been enlarged so they cover the same proportional area of the rectangular unit cell as a ff=0.5 hole in a square unit cell. These enlarged holes have fill factors (relative to the same-length short axes) of ff=0.559 ($\sim 0.5 * \sqrt{1.25}$) when p_y=1.25p_x and ff=0.612 ($\sim 0.5 * \sqrt{1.5}$) when p_y=1.5p_x. When the hole sizes are increased, the peak transmittance values for the different aspect ratio arrays come closer, difference in T of 0.11 (down from 0.14) between the p_y=1.25p_x and p_y=1.5p_x arrays for polarisation along the short axis and only 0.04 (down from 0.16) for polarisation along the long axis.

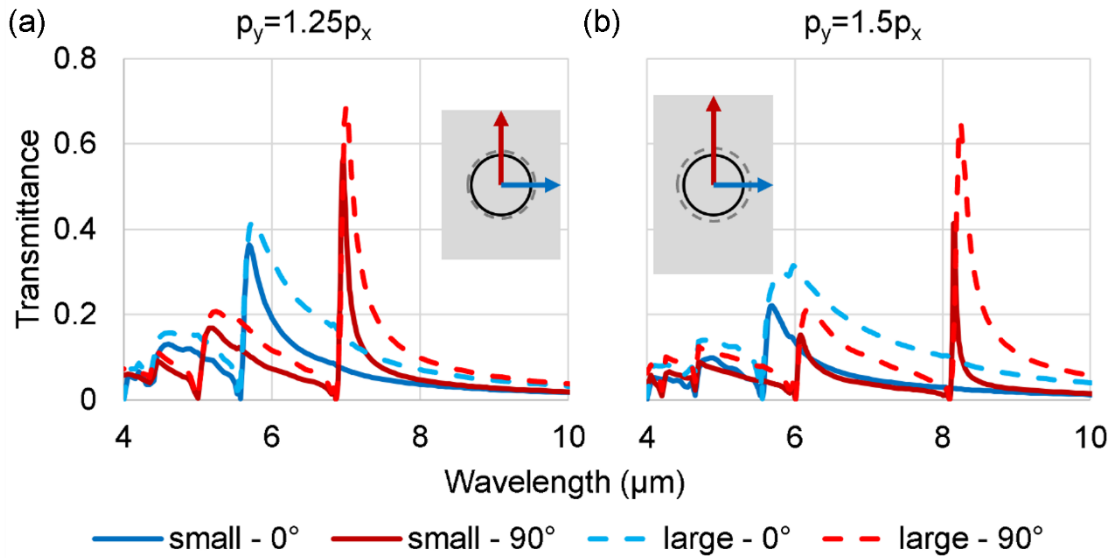

Figure 45: Simulated transmittance spectra of rectangular EOT arrays with p_x=4 µm for (a) p_y=1.25p_x and (b) p_y=1.5p. E-field is linearly polarised along the short axis (blue) and long axis (red), fill factor relative to short axis is kept constant at ff=0.5 (solid lines) and adjusted so that the holes cover an equivalent area of the rectangular unit cell as a ff=0.5 hole in a square array (dashed lines).

*Table 2: Peak data for simulated arrays with p_y=1.25*p_x shown in Figure 45*

Configuration	Peak T	Peak wavelength (µm)	Peak width (µm)	Q-factor
small - 0°	**0.36**	**5.69**	**0.41**	**13.72**
small - 90°	**0.57**	**6.96**	**0.12**	**59.17**
large - 0°	0.42	5.74	0.88	6.49
large - 90°	0.69	7.00	0.24	29.21

*Table 3: Peak data for simulated arrays with p_y=1.5*p_x shown in Figure 42*

Configuration	Peak T	Peak wavelength (µm)	Peak width (µm)	Q-factor
small - 0°	**0.22**	**5.68**	**0.52**	**11.00**
small - 90°	**0.41**	**8.15**	**0.06**	**138.30**
large - 0°	0.31	5.98	1.45	4.12
large - 90°	0.65	8.24	0.23	35.90

Increasing the unit cell aspect ratio also has the effect of widening the separation between the main peaks generated for each incident light polarisation. As also

shown in Figure 45, for the p_y=1.25*p_x device the difference between peak maxima is ~1.25 µm and for the p_y=1.5*p_x this spacing increases to ~2.3-2.4 µm (depending on the hole size chosen). The Q-factor is also affected by changing the aspect ratio, the longer-wavelength peak becoming sharper and the shorter-wavelength one broader.

5.2.3. Changing Array Pitch

Keeping all other device factors constant,
Figure 46 shows that increasing the pitch of an EOT array will redshift the position of the main peak in accordance with the approximation of the Rayleigh wavelength in Equation (13). As shown in Table 4, the peak heights remain more or less constant as the pitch changes, and while the peak widths are seen to broaden with pitch the Q-factor increases.

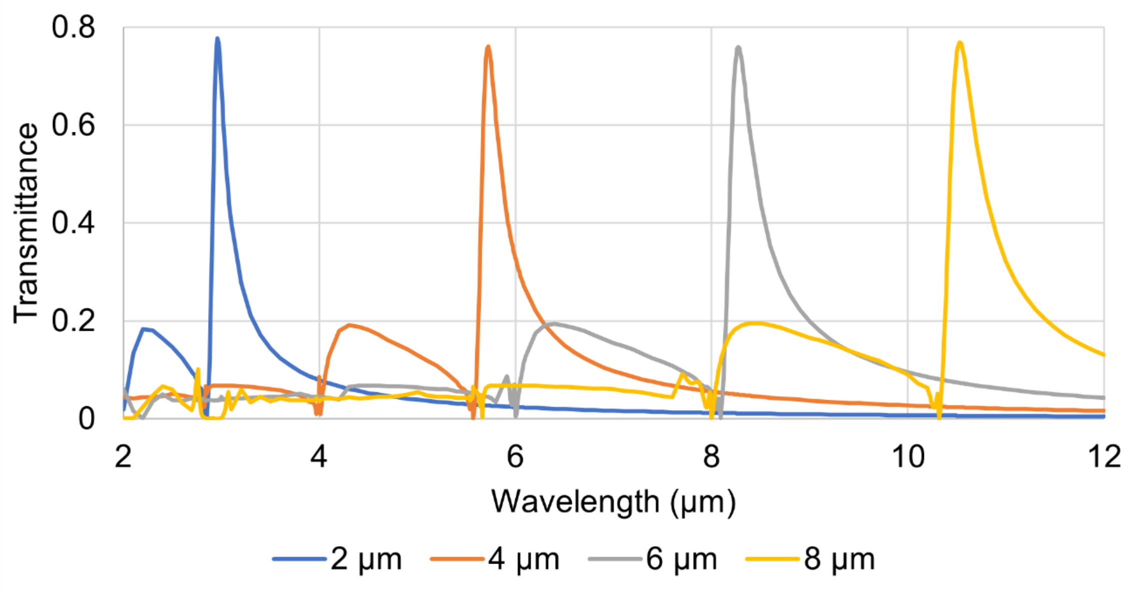

Figure 46: Simulated transmission spectra of square EOT arrays with varied pitches, in 40 nm Au film on CaF2 substrate and hole fill-factor of 0.5

Table 4: Changes in main EOT peak properties with array pitch

p (µm)	Peak T	Peak wavelength (µm)	Peak width (µm)	Q-factor
2	0.78	2.96	0.20	14.64
4	0.76	5.72	0.30	19.20
6	0.76	8.27	0.39	20.97
8	0.77	10.53	0.48	22.09

5.2.4. Changing Fill Factor

Increasing the fill-factor will increase the total amount of light transmitted thus the peak transmittance, but at the expense of the Q-factor as shown in Figure 47. For most arrays featured here, a designed fill factor of 0.5-0.6 was chosen to give a maximum transmission in the region of 80%.

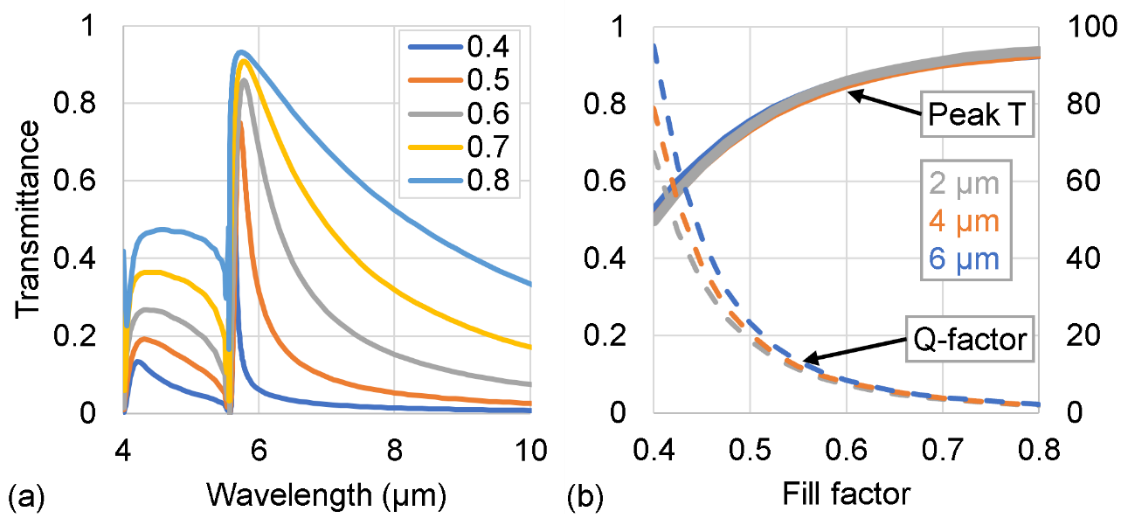

Figure 47: (a) Simulated spectra 4 µm pitch square EOT arrays in 40 nm Au film on CaF_2, altering hole fill factor and (b) plots of peak T and Q-factor against hole fill factor for simulated 2, 4 and 6 µm pitch square arrays in 40 nm Au film on CaF_2

5.2.5. Changing Incident Radiation Elevation

The dispersion relation calculations used to form the plots in Figure 35 give the spectral minima positions when the component of the incident beam momentum matches that of the EOT array. For a 4 µm pitch array example, minima are

calculated via Equation (39) to occur at wavelengths shown in Table 5 for the listed angles, and compared to simulated transmission spectra in Figure 48.

Table 5: Calculated positions of peak minima (to nearest 0.05 µm) for 4 µm pitch EOT array in Au on CaF_2 substrate, for range of incident beam angles, points marked out on table in bold are shown on Figure 48

θ (°)	Minima (µm)									
	Air (0,1)	Air (1,0)+	Air (1,0)-	Air (1,1)+	Air (1,1)-	Sub (0,1)	Sub (1,0)+	Sub (1,0)-	Sub (1,1)+	Sub (1,1)-
0		4		2.85			**5.55**		4	
15	3.85	2.95	5.05	2.25	3.3	5.45	4.55	**6.55**	3.45	4.45
30	3.45	2	**6**	1.65	3.65	5.2	3.65	**7.45**	2.9	4.85
45	2.85	1.2	**6.85**	1.05	3.85	4.85	2.85	**8.2**	2.35	**5.1**

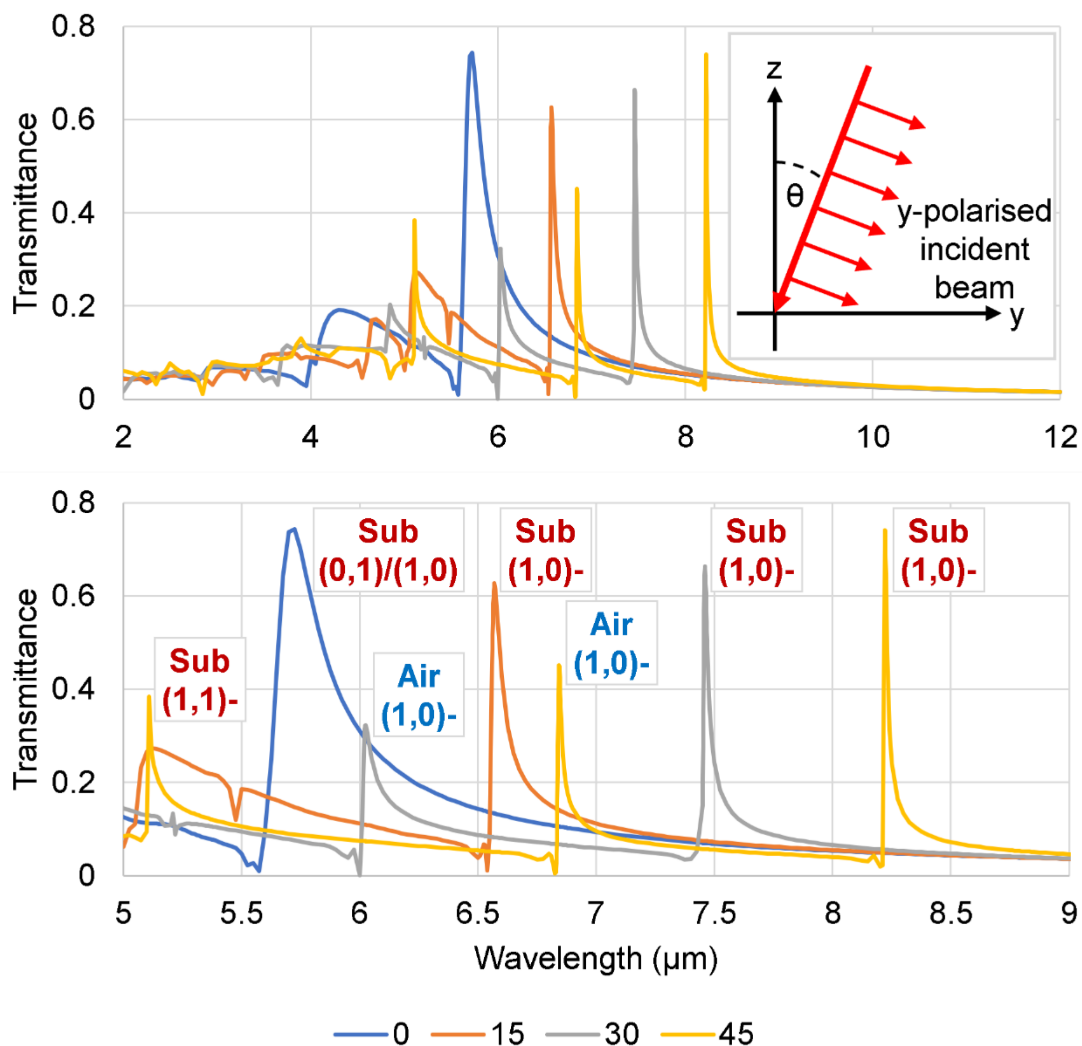

Figure 48: Simulated transmittance spectra of a 4 µm pitch square array in 40 nm Au film on CaF_2 with the incident beam at a range of elevation angles in the same

plane as the E-field polarisation, showing full wavelength range with inset beam orientation schematic (top) and a smaller section (bottom) with peaks highlighted in bold in Table 5 marked.

Altering the elevation in the opposite plane to the case of Figure 48 (i.e. perpendicular to the direction of the incident light polarisation) has the effect of reducing peak transmittance and Q-factor as shown in Figure 49 and Table 6, but with comparatively little shift in wavelength.

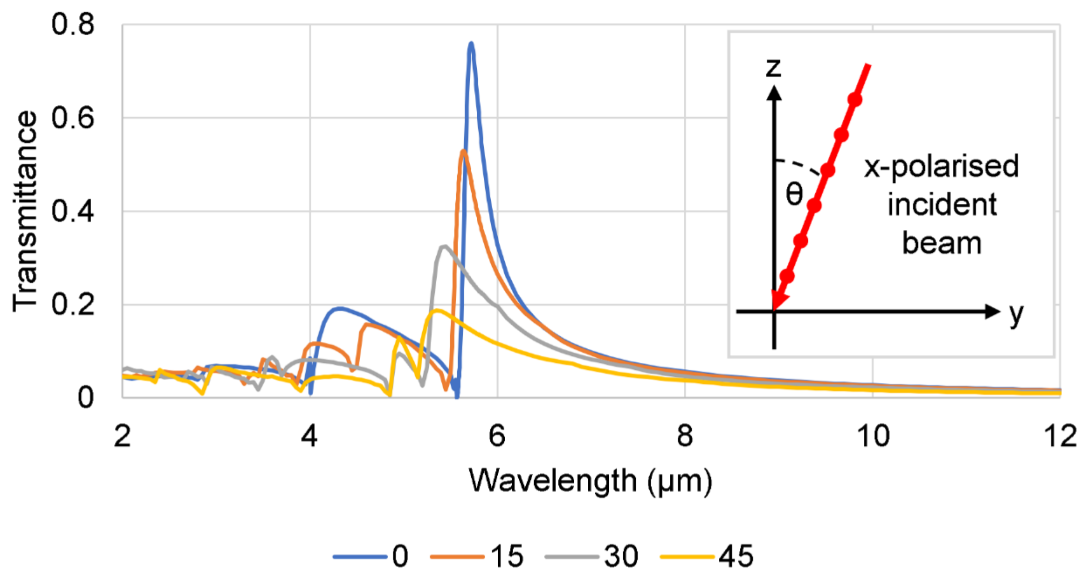

Figure 49: Simulated transmittance spectra of a 4 μm pitch square array in 40 nm Au film on CaF_2 with the incident beam at a range of elevation angles in the opposite plane as the E-field polarisation, with inset beam orientation schematic.

Table 6: Peak transmittance and Q-factor of simulated arrays in Figure 49

Elevation angle (°)	**Peak T**	**Q-factor**
0	0.76	18.75
15	0.53	12.40
30	0.32	6.65
45	0.19	4.78

5.2.6. Effect of Hole Mispositioning from Laser Ablation

Simulations were performed to investigate the effect of having non-perfect arrays, which occurred for some of the laser-ablated devices (see Sections 4.2.3.5 and 6.1.2.1). A 4×4 square array of holes with a nominal pitch of 6.6 μm and fill factor of 0.6 was configured by fitting circles over an image of a fabricated array, as shown in Figure 50, with the same periodic boundary conditions (as the single-hole simulations) set to infinitely repeat the cell along both axes.

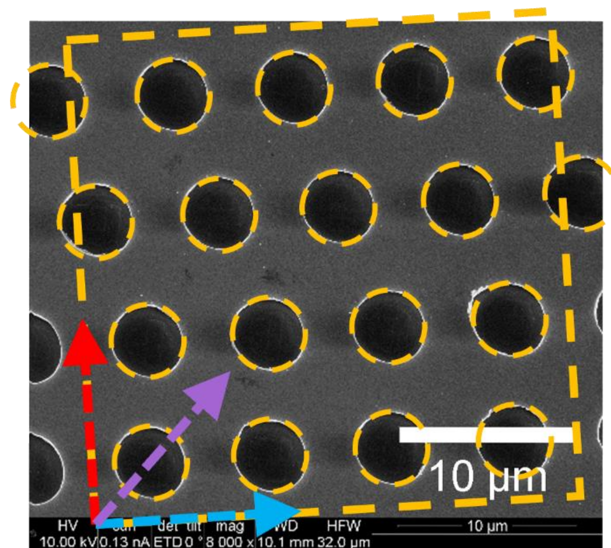

Figure 50: 4×4 hole array cell for COMSOL derived from laser-fabricated device, sample slightly rotated anti-clockwise in image so cell compensated. Laser scanning direction is along horizontal axis.

The displacements along the horizontal axis of the hole positions from the square array ideals are shown in Table 7. Note that the displacement of some of the rows is such that holes overlap the cell edge, in which case major and minor segments at the left and right edges are present for rows 3 and 4.

*Table 7: Displacement of holes along horizontal axis (rightwards positive) as fractions of the array period. Cell "zeroed" on row 1, column 1, marked in **bold**.*

	Outside (l)	Column 1	Column 2	Column 3	Column 4	Outside (r)
Row 4	+0.35	+0.375	+0.365	+0.355	+0.35	
Row 3		-0.325	-0.3	-0.325	-0.325	-0.325
Row 2		+0.05	+0.05	+0.025	+0.025	
Row 1		**0**	0	0	0	

Each row is displaced by approximately the same amount, but slight variations (within 0.025*p*) are noted. This could be attributable to errors in fitting the circles or "noise" during the fabrication process, whatever the reason a 4×4 hole cell was used for simulation rather than (e.g.) a 4×1 hole cell for greater accuracy. Modelling a larger section of the array would increase accuracy further, but this was prohibited due to limits of computing time and capabilities.

Simulated spectra are shown in Figure 51, with plot E-field polarisations matching those shown on Figure 50: in any of them, the array transmittance was lower than that of an equivalent perfect (exactly square) array.

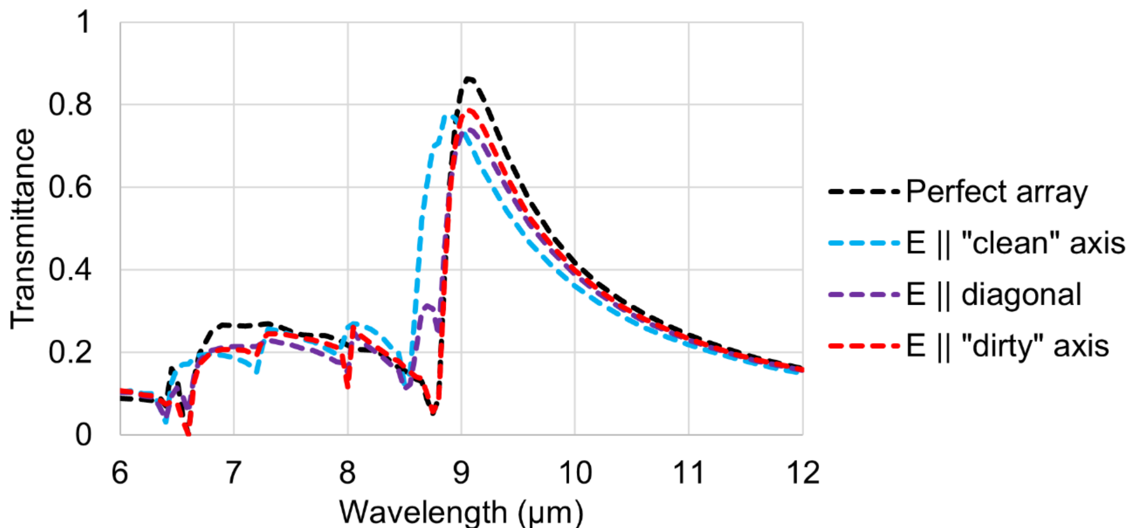

Figure 51: Simulation plots of 4×4 array shown in Figure 50 compared to a perfect array, 6.6 μm pitch imperfect square array in 40 nm Au film on CaF_2 substrate, hole fill factor of 0.6.

5.2.7. Changing Substrate Material

The substrate material ideally needs the lowest possible absorption across the working wavelength range to maximise filter transmission. Materials considered for use as substrates in the mid-infrared included various flourides, with transmittance data for 1 mm windows shown in Figure 52 (a), with barium flouride (BaF_2) giving the widest possible range. Calcium flouride (CaF_2) has slightly higher transmittance up to ~7 μm and a sufficient wavelenth range for most mid-infrared devices (from a practical standpoint it is also much cheaper to acquire). Magnesium flouride (MgF_2) has a transmittance window that is too restrictive for most mid-IR devices covered in this thesis, and is also more expensive than CaF_2, but theoretically could be more suitable for electrically switched devices due to a higher thermal conductivity and specific heat capacity than the other two materials (see Section 5.5).

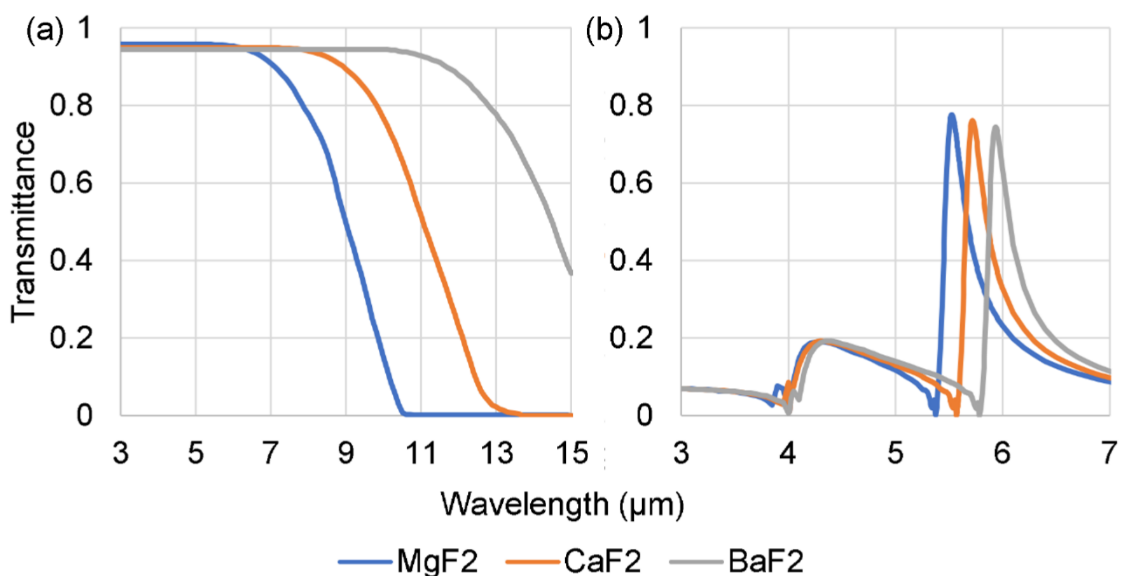

Figure 52: (a) Transmittance of 1 mm MgF_2 [88], *CaF_2* [82] and *BaF_2* [81] *substrates and (b) simulated transmittance spectra of 4 μm-pitch EOT devices in 40 nm Au films on different substrate materials*

The slightly different feature positions of the EOT transmittance spectra seen in Figure 52 (b) can be attributed to the differing substrate refractive index values for the various fluoride substrates (as shown in Figure 53 (a)). Notice in Figure 52 (b) how the minima preceding the main peaks (from the first film-substrate coupling, circa 5.5 μm) vary whereas the minima for the first film-air coupling is

constant at 4 μm (due to the 4 μm array period). The reduction in peak height can also, at least partly, be attributed to the differing refractive indices of the substrates. The relation between reflectivity *R* and material index *n* is given generally by Equation (55) and more specifically Equation (61)

$$Reflectivity = \left|\frac{n_{air} - n_{material}}{n_{air} + n_{material}}\right|^2 \quad (61)$$

The higher the substrate *n* (thus difference in *n* between it and the air above) the greater the fraction of incident radiation reflected off a surface (thus the less transmitted), and this can be seen in Figure 53 (b).

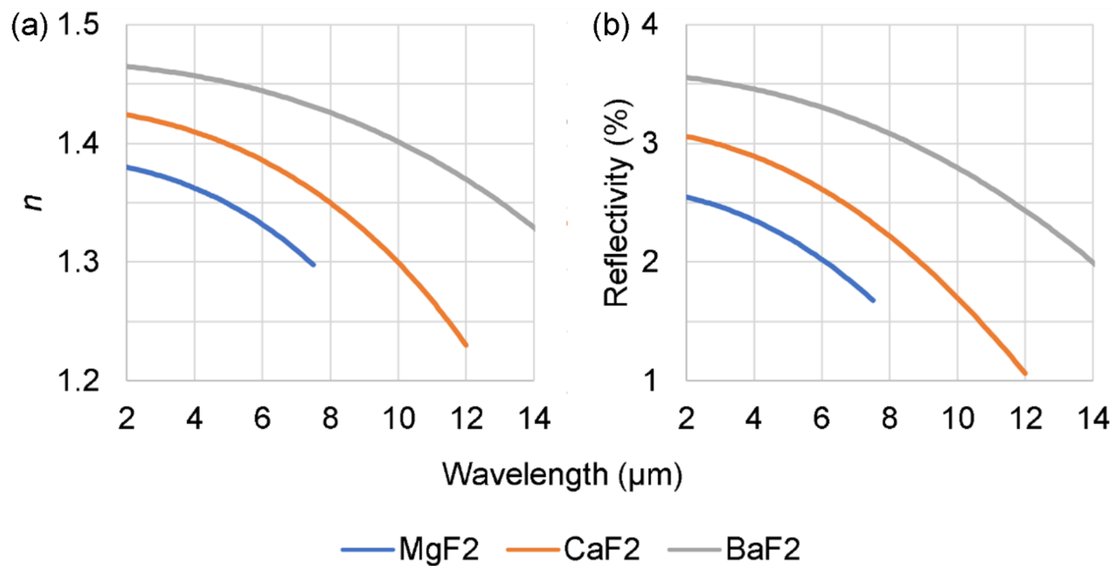

Figure 53: (a) Substrate refractive index derived from dispersion relation equations for MgF_2, CaF_2 and BaF_2 [89] *and (b) their reflectivity in air with incident radiation at normal to surface calculated using Equation (61)*

In the cases of the substrates shown here the total reflectivity is no more than a few percent. Additionally, a coating of silicon nitride (used as a protective barrier between the EOT metal film and PCMs, see Section 6.3) was observed to sometimes slightly increase total transmission after application (see Figure 54 (b)), leading to speculation that it acts as an anti-reflective coating by reducing the change in *n* at the device surface. This specific effect was not seen in simulations (see Figure 54 (a)), the only result being a slight reddening and broadening of the main transmission peak.

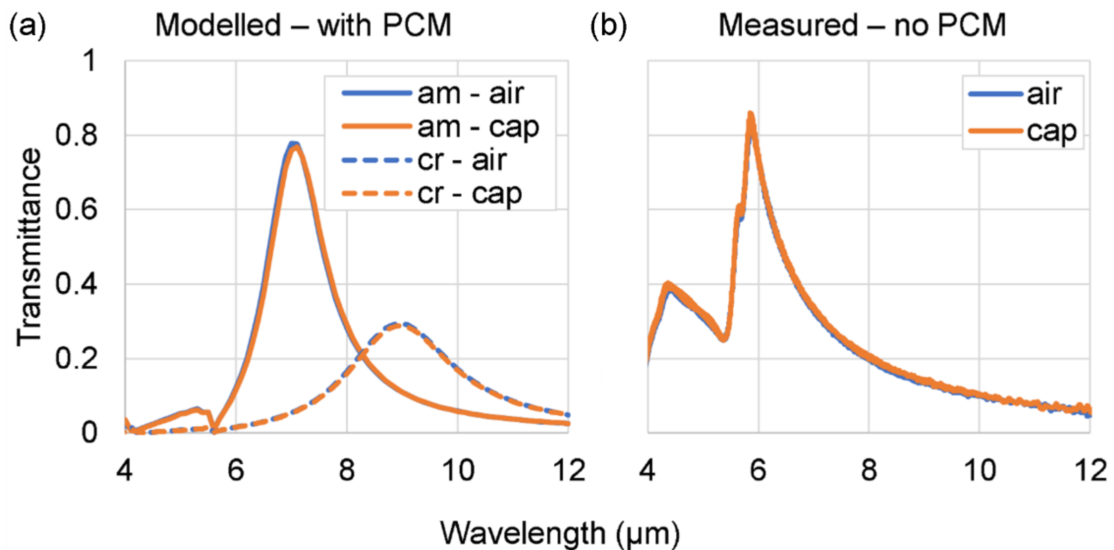

Figure 54: Comparisons of devices with and without Si_3N_4 barrier layers, in simulations with (a) PCM layers and (b) on a plain array fabricated device

Another consideration is that, for EOT devices with PCM layers functioning as tuneable filters, it is vital that the substrate refractive index be less than that of the PCM in any state in the desired wavelength range, otherwise the film-substrate coupling will dominate and reduce the PCM switching effectiveness.

5.2.8. Changing EOT Film Material

Simulations with various EOT film materials are shown in Figure 55, showing that transmission is optimised by the film having a highly negative real component of the dielectric constant. In this regard the optimum metal would appear to be aluminium [90] (with silver [91] and gold [92] not far behind) but when this data was used in simulations the gold and silver provided higher peak transmission, suggested in [93] to be the result of the aluminium's higher absorption. All other example metals shown (tungsten [94], platinum [95], iron [96] and titanium [94]) provide successively "worse" peaks in the simulations, as real permittivity increases/becomes less negative.

Gold was used exclusively for fabricated devices here, since it is stable when exposed to air, and has a relatively high melting temperature (1064°C). This latter point is important since amorphising the PCM layer requires heating it above its melting point (~ 600°C for GST-225), and any metal layers adjacent to the PCM

layer must be able to withstand such high temperatures without themselves melting. Silver, although good plasmonically tarnishes in air and has a lower melting point (962°C) than gold. Aluminium is also good plasmonically in this wavelength range, but it has an even lower melting point of only 660°C.

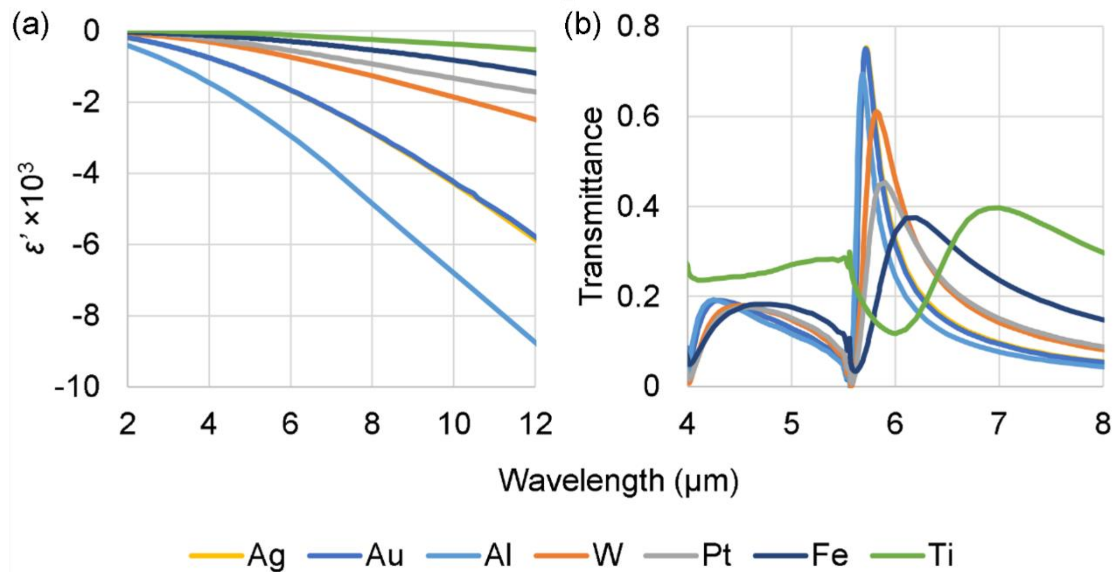

Figure 55: (a) Real component of the relative permittivity/dielectric constant of various film materials derived from refractive index data and (b) simulated 4 µm pitch EOT arrays on CaF_2 substrate with fill-factor of 0.5, using different metals for the 40 nm film

5.2.9. Changing EOT Film Thickness

Appropriate EOT film thickness is required for good device performance, simulations shown in Figure 56 and Table 8 demonstrating that increasing this from 20-120 nm tends to increase Q-factor when all other factors are kept constant. The peak transmission over this thickness range is just under 0.8, for films thicker than 60 nm.

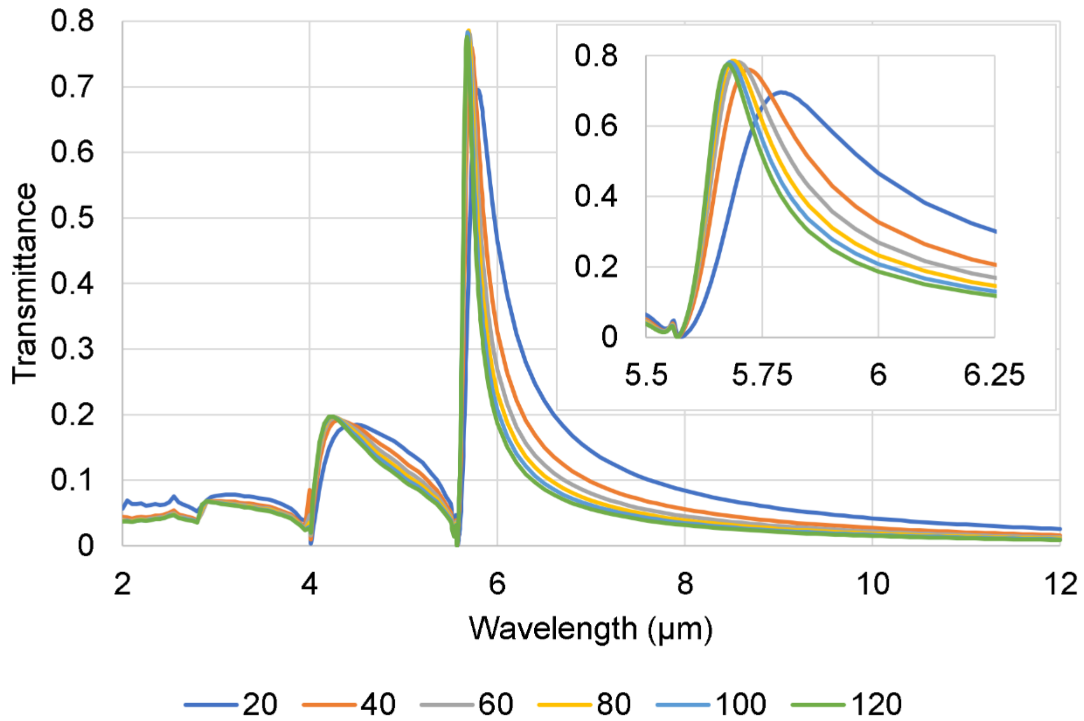

Figure 56: Simulated transmission spectra for a 4 µm pitch EOT arrays on CaF_2 substrate with fill-factor of 0.5, varying the thickness of the Au film

Table 8: Peak transmittance and Q-factor of simulated arrays in Figure 56

Film thickness (nm)	Peak T	Q-factor
20	0.70	12.05
40	0.76	19.13
60	0.78	23.66
80	0.79	27.21
100	0.78	30.46
120	0.78	33.72

For most devices fabricated in the work of this thesis, an Au film thickness of 40 nm was used, since this yields good peak transmission (as seen in Table 7) and at the same time proved easier to work with than thicker films. Devices fabricated with thicker Au layers suffered from the following process issues:

- Harder to make devices via lift-off, often requiring sonication to remove unwanted metal thus risking damaging the films

- More complicated for wet-etching, with: larger undercut beneath the mask holes; greater hole wall curvature and more “ragged” hole edges

- Thicker material more difficult to laser-drill

5.3. UV – Near-Infrared EOT Array Simulations

Additional simulations were performed of devices with similar structures to those discussed above, but much smaller array pitches, to give EOT spectral features in the visible to near-infrared (NIR) wavelength range. The JASCO micro-spectrophotometer available for measurements of practical devices has a spectral range of 0.4-1.6 μm in both reflection and transmission, so simulations were performed in this range too. Optical data (refractive index *n* and extinction coefficient *k*) for Au films deposited in-house was also available for this range and could be utilised in the simulations.

As with simulations for MIR wavelengths, devices were modelled using circular holes in 40 nm thick gold films on calcium fluoride substrates. Figure 57 shows the effect of altering the array pitch between 300 and 600 nm with a constant fill factor of 0.5, respectively for transmission and reflection.

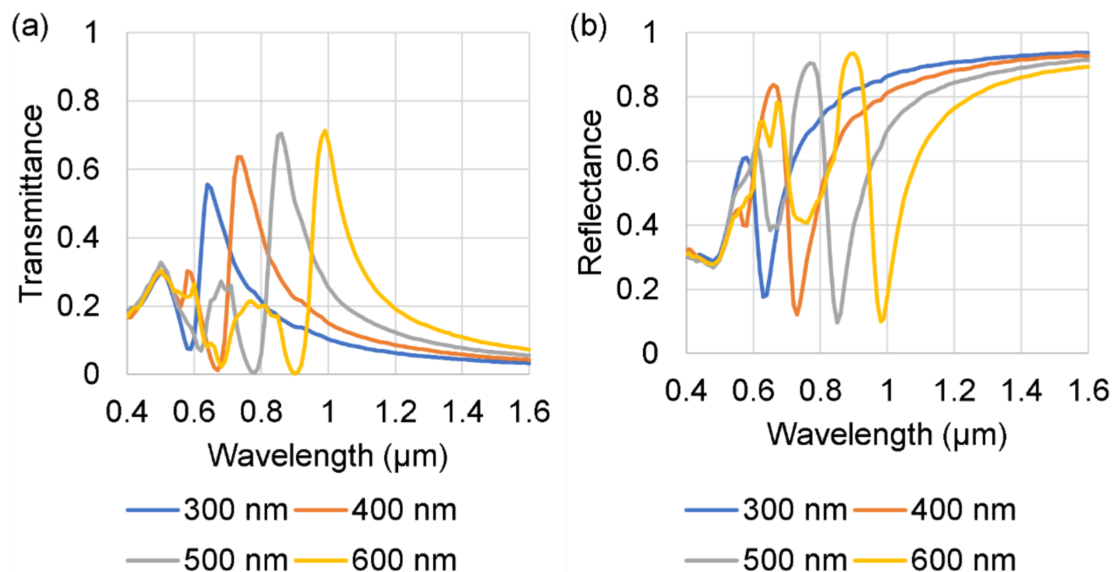

Figure 57: (a) Transmission and (b) reflection spectra of visible to NIR EOT arrays in 40 nm Au film on CaF_2 substrates, fill factor of 0.5, varying array pitch

Table 9: Tabulated results of transmission simulations shown in Figure 57

p (nm)	Peak T	Peak wavelength (nm)	Peak width (nm)	Q-factor
300	0.56	640	130	4.92
400	0.64	740	133	5.57
500	0.71	860	130	6.62
600	0.71	990	128	7.76

As with the MWIR array simulations, increasing the array pitch increases the transmission peak Q-factor, though in this case the peak transmission is reduced for the shorter pitches (300 and 400 nm) modelled.

Simulations (shown in Figure 58) were also performed to demonstrate the effect of the hole fill factor on transmittance/reflectance and peak Q-factor.

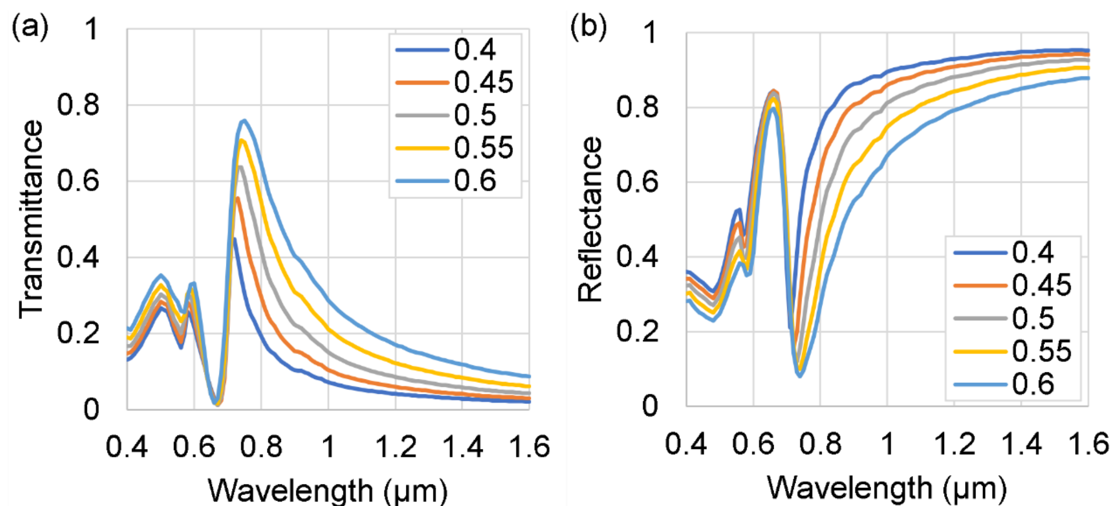

Figure 58: (a) Transmission and (b) reflection spectra of visible/NIR EOT arrays in 40 nm Au film on CaF2 substrates, array pitch p=400 nm with varied fill factor

As with the MWIR models, increasing the array hole fill factor increases transmittance and peak width at the expense of a lower Q-factor (see Table 10).

Table 10: Tabulated results of transmission simulations shown in Figure 58

fill factor	Peak T	Peak wavelength (nm)	Peak width (nm)	Q-factor
0.4	0.45	720	86	8.33
0.45	0.55	730	103	7.07
0.5	0.64	740	133	5.57
0.55	0.71	740	167	4.42
0.6	0.76	750	224	3.34

5.4. Simulations of EOT Arrays with PCM Layers

5.4.1. Material Type

Multiple PCMs exist that can be used for tuneable filter applications, including several GST-based alloys. The key factors are finding compositions with the desired optical properties for the device requirements in the working wavelength range for the target application. For multispectral imaging systems we would like as large a change in refractive index n as possible (between PCM phases), while at the same time having the lowest possible extinction coefficient k (in both phases). Examples of the effects of changing n and k properties individually (with the other kept constant) are shown in Figure 59, Table 11 and Table 12.

In addition to the expected redshift in the peak with increasing n (while keeping constant k=0), the peak transmittance is reduced with the Q-factor at first also decreasing but then increasing again despite the peak constantly broadening (Figure 54 (a)). Increasing just k slightly red-shifts the peak, but the main feature is a significantly reduced transmittance (due to higher absorption) and Q-factor (Figure 54 (b)). Why the Q-factor changes with each of these properties is worth further consideration, as one might naively think that it wouldn't change (e.g. that the curve would simply be linearly stretched or compressed).

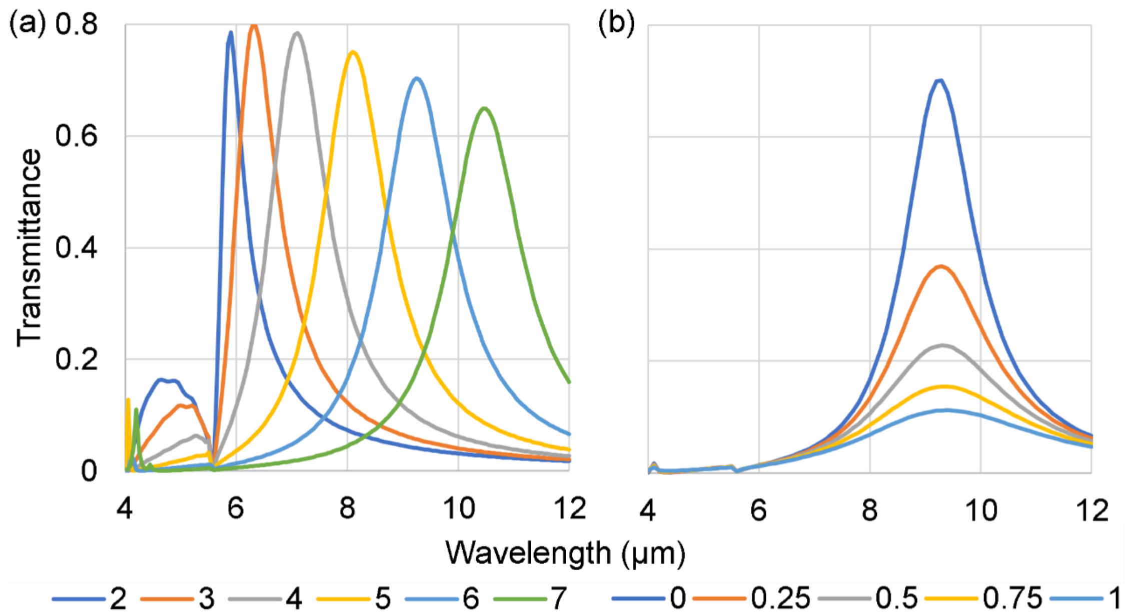

Figure 59: Simulations of 4 um pitch EOT arrays with a 100 nm layer of notional PCM material, (a) varying n and keeping k=0 and (b) keeping n=6 and varying k

Table 11: Tabulated results of simulations shown in Figure 59 (a)

PCM *n*	Peak T	Peak wavelength (μm)	Peak width (μm)	Q-factor
2	0.78	5.90	0.56	10.50
3	0.80	6.30	0.95	6.63
4	0.78	7.10	1.28	5.55
5	0.75	8.10	1.45	5.59
6	0.70	9.29	1.56	5.96
7	0.65	10.45	1.63	6.41

Table 12: Tabulated results of simulations shown in Figure 59 (b)

PCM *k*	Peak T	Peak wavelength (μm)	Peak width (μm)	Q-factor
0	0.70	9.29	1.56	5.96
0.25	0.37	9.35	2.14	4.36
0.50	0.23	9.43	2.73	3.46
0.75	0.15	9.53	3.30	2.88
1.00	0.11	9.63	3.87	2.49

5.4.2. PCM Thickness

The thickness of the PCM layer is an important contributor to a filter's properties, the thicker the layer the greater the expected shift of the peak transmission wavelength between states, but also the greater the proportional drop in peak transmission and the lower the Q-factor. Simulated examples are shown in Figure 60 of a realistic PCM (k=0 in amorphous phase and increasing throughout wavelength range in crystalline phase) and of one with k=0 universally, with key spectral data reported in Table 13, Table 14 and Table 15.

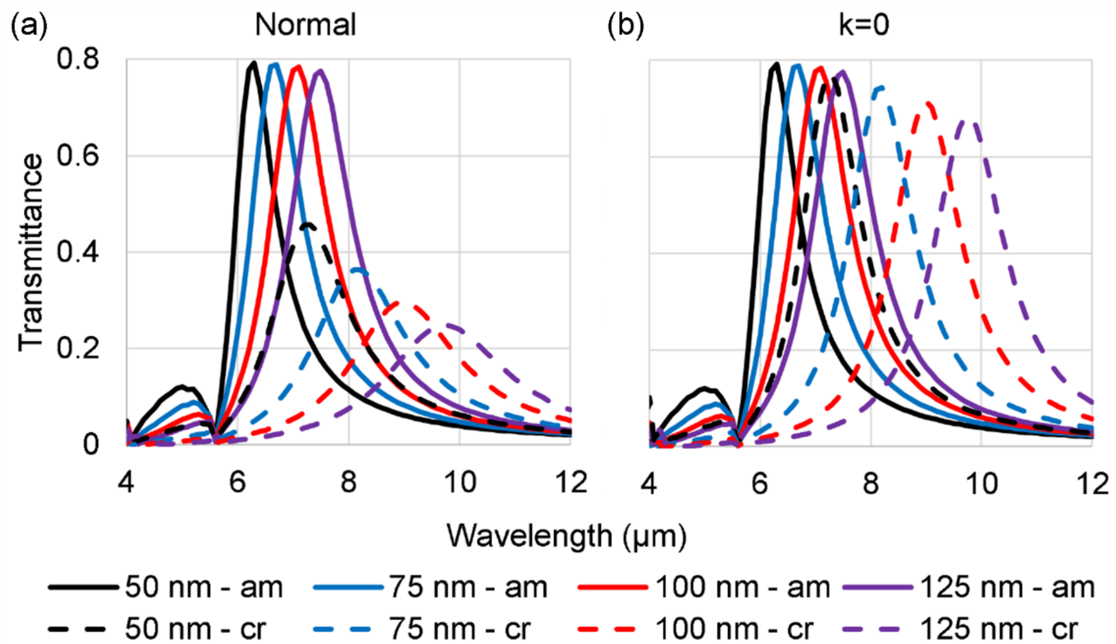

Figure 60: Simulated transmittance spectra of a 4 μm pitch EOT array in 40 nm Au film on CaF_2 substrate with GST-225 PCM layers of varied thicknesses, using (a) measured n and k values from [55] *and (b) same measured n values with k=0*

Table 13: Effect of increasing PCM layer thickness for amorphous PCM from Figure 60 (k=0)

PCM *t* (nm)	Peak T	Peak wavelength (μm)	Peak width (μm)	Q-factor
50	0.79	6.30	0.92	6.84
75	0.79	6.70	1.14	5.88
100	0.78	7.10	1.27	5.59
125	0.77	7.50	1.37	5.48

Table 14: Effect of increasing PCM layer thickness for crystalline PCM from Figure 60 (a)

PCM *t* (nm)	Peak T	Peak wavelength (μm)	Peak width (μm)	Q-factor
50	0.46	7.30	1.67	4.36
75	0.36	8.20	2.04	4.03
100	0.30	9.00	2.35	3.83
125	0.25	9.70	2.62	3.70

Table 15 Effect of increasing PCM layer thickness for crystalline PCM (with k=0) from Figure 60 (b)

PCM *t* (nm)	Peak T	Peak wavelength (μm)	Peak width (μm)	Q-factor
50	0.77	7.30	1.29	5.64
75	0.74	8.20	1.43	5.72
100	0.71	9.00	1.52	5.93
125	0.68	9.70	1.59	6.15

The effect of changing the film thickness on the shift characteristics (change in peak properties upon changing the PCM state) is shown in Table 16, the thicker the PCM the larger the expected peak shift and reduction in peak transmittance.

Table 16: Effect of increasing PCM layer thickness on shift characteristics as seen in Figure 60 (left)

PCM *t* (nm)	Peak shift (μm)	Peak shift factor	Peak T reduction (%)
50	1.00	1.16	42.26
75	1.50	1.22	53.96
100	1.90	1.27	62.22
125	2.20	1.29	67.97

GST PCMs also tend to reduce in volume when crystallised, of the order of 5%, confirmed here by measuring film thicknesses before and after crystallisation. This is an important factor when attempting to characterise films for processes such as ellipsometry, but it only has a small effect on the optical characteristics

of tuneable filters. Simulations in Figure 61 show the peak transmission wavelength of various crystalline PCMs (GST-225, GST-326 and the Se-substituted composition $Ge_2Sb_2Se_4Te_1$, or GSST-2241), and that reducing a thickness by 5% (as compared to that of the amorphous phase) only marginally reduces the shift (< 2%) when compared to full-thickness films.

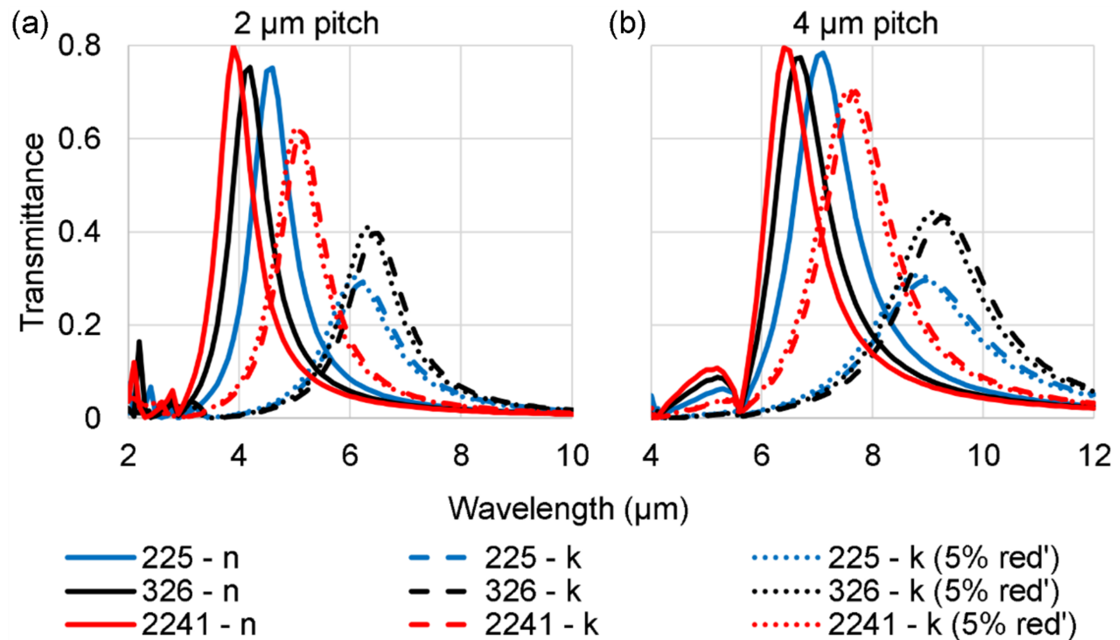

Figure 61: Simulated transmission spectra of (a) 2 μm and (b) 4 μm pitch EOT arrays in 40 nm Au film on CaF_2 substrates with 100 nm layers of amorphous (solid lines) and crystalline (dashed lines) PCM of different types (GST-225, GST-326 and GSST-2241). Plots of crystalline PCM with 5% thickness reductions are also shown (dotted lines).

5.4.3. PCM Layer Deposition Schemes

Several possible structure schemes for combining EOT arrays with phase-change material layers are shown in Figure 62, which could be realised by the manner and position of the PCM deposition within the fabrication process.

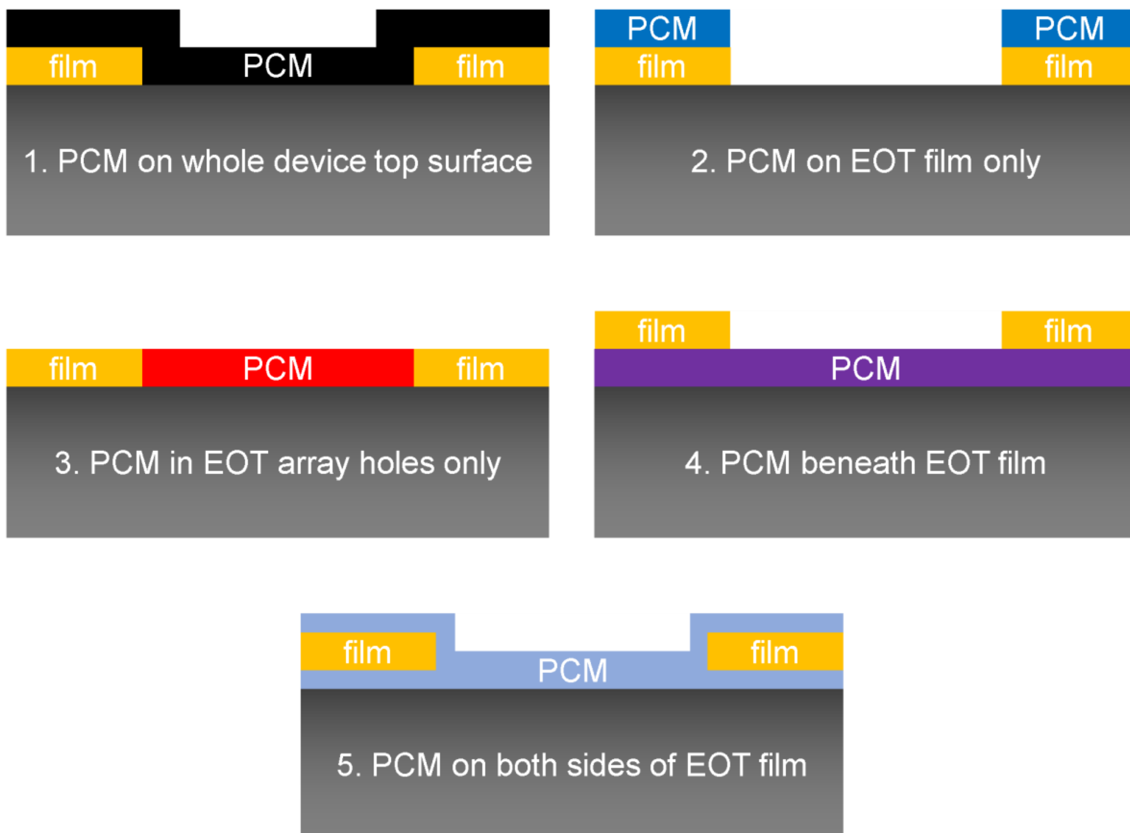

Figure 62: Schematics of different potential structures of combining PCM layers with EOT arrays. Note that option 5 has the same total PCM film thickness as the other cases but is split across the two layers.

1. Deposition is done after removing any lift-off/etching masks and is also compatible with direct patterning (FIB or laser ablation). This is the only scheme available if the EOT array needs to be characterised prior to PCM application, as the other approaches either require the mask to be left on to prevent PCM being deposited on unwanted areas or the EOT array being formed after the PCM has already been applied.

2. This would be the only scheme available if using lift-off and wanting to deposit the PCM immediately onto the metal film (also around hardened resist mask of pillars, to be removed and leaving array holes) to reduce the chance of contamination. This scheme was not tested here due to process issues using lift-off for EOT arrays and the scheme in any case not providing good shift characteristics in simulations.

3. This would be suitable only for processes that involve an etching mask, PCM deposited after the holes have been etched but the mask not yet removed. This option was considered but not tested, again because of the desire to characterise EOT arrays "blank", which would require mask removal. Other potential difficulties might include the ability to model accurately, as it is likely that PCM would build up on the vertical walls of the etching mask and reach sufficient thickness that they would remain in place after mask removal, making modelling of such structures more difficult.

4. An approach not even considered for fabrication, as it would prevent characterisation of a blank EOT array and also subject the PCM to any stresses involved with the following fabrication process steps (e.g. corrosive etchants, sonication or a patterning beam). If parameters could be sufficiently optimised it would be a potentially viable approach, if not using lift-off the PCM and metal layers could be deposited during the same session to avoid contamination between them.

5. Similar to approach 4, this method was not considered for fabrication as far more steps would be required than for other schemes, in particular two PCM depositions with the EOT array metal deposition and patterning in between with no tangible optical benefits.

Simulated transmittance spectra for otherwise identical devices using these five different structures are shown in Figure 63, demonstrating the relative similarity in optical performance of most cases, with the exception of scheme 2, where there is not only little difference between the plots for amorphous and crystalline PCMs, but with there being no PCM at all (see Figure 56).

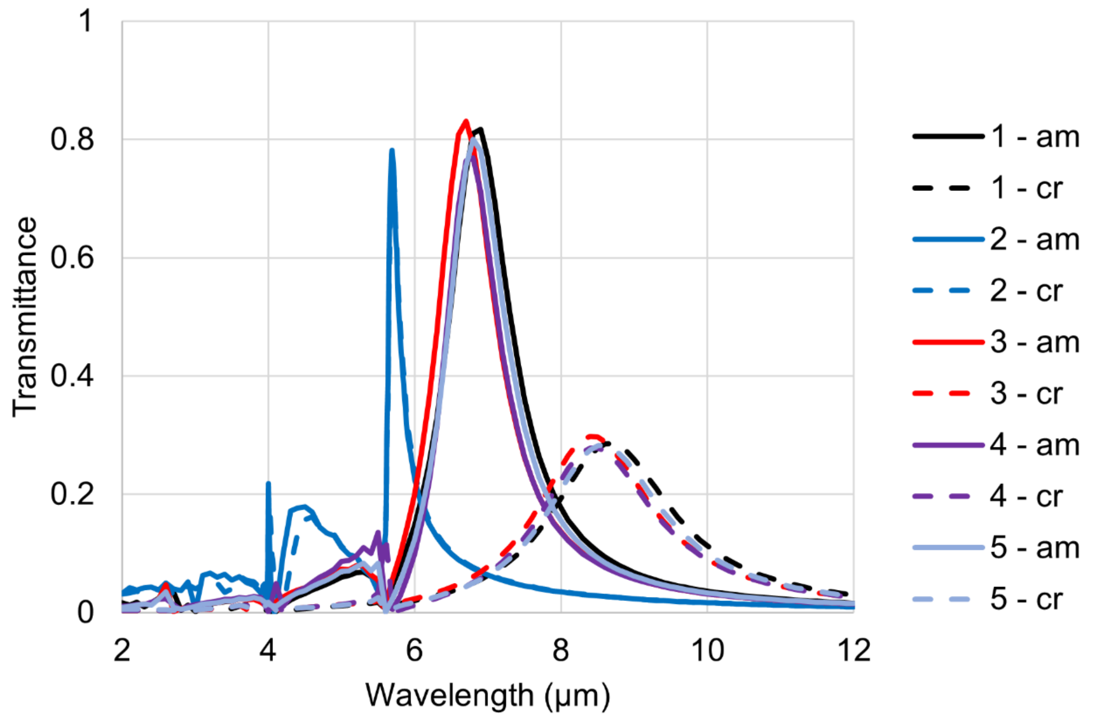

Figure 63: Simulated 4 μm pitch EOT arrays on CaF_2 substrate with fill-factor of 0.5 and 100 nm Au film, with 100 nm GST-225 PCM layers in the covering schemes shown in Figure 58 (50 nm each on top of and below the film for 5.)

Figure 64 shows a simulation plot of the electric field in the vicinity of the array holes in the case of scheme 3 (from Figure 62) at select wavelengths. It is clear that, at maximum transmission (and to an extent with the first "minor" peak), the concentration of the electric field strength is greatest within the array holes, thus requiring the placement of PCM inside to give any useful peak shifting (and explaining the lack of peak shifting seen when using scheme 2).

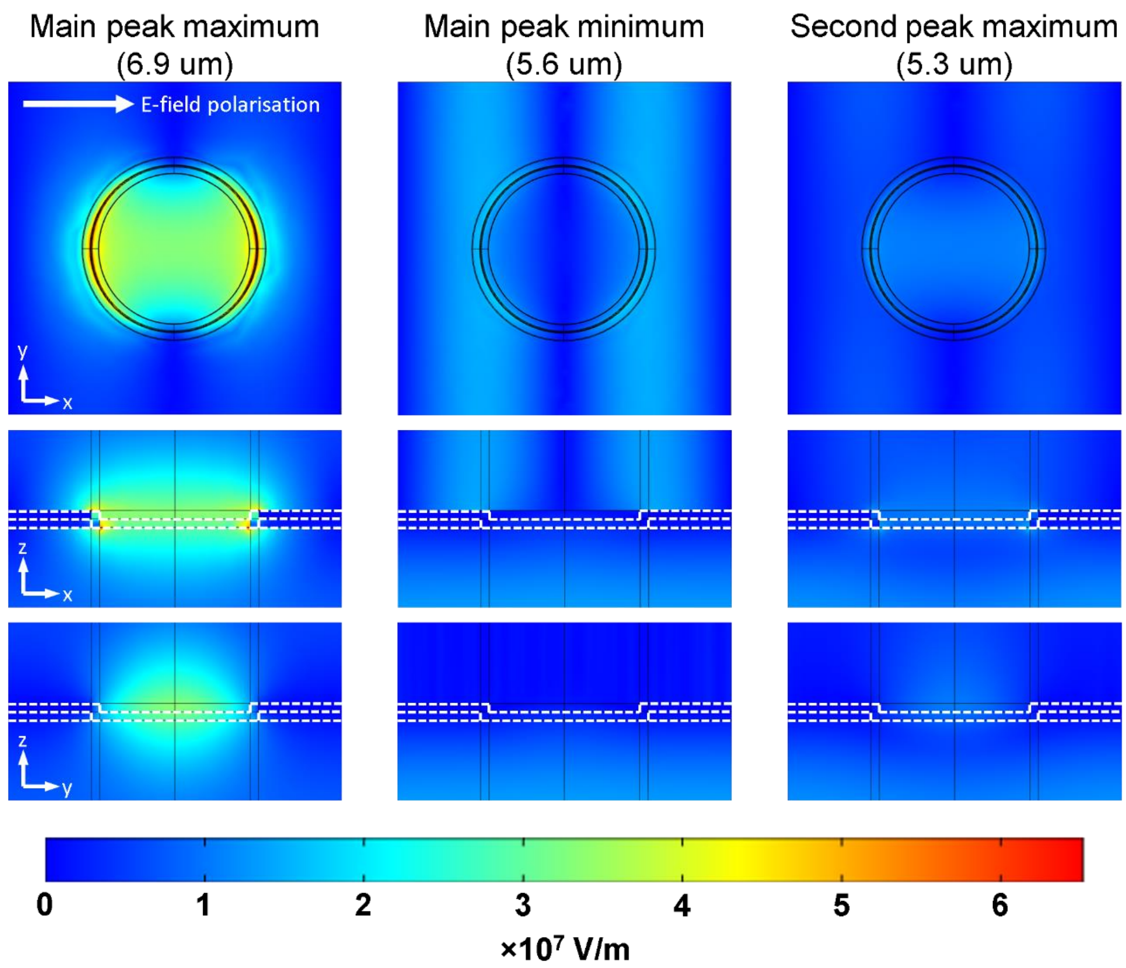

Figure 64: E-field plots of a simulated EOT array for deposition scheme 3 (as shown in Figure 63) for amorphous GST-225 PCM, z-plane in xy plots at the film (and PCM)/substrate interface, white-dashed lines on xz and yz plots marking out film and PCM layers

A similar set of plots is also shown in Figure 65 but for the magnetic field (H-field) with the same incident radiation configuration (E-field linearly polarised parallel to x-axis), demonstrating the perpendicular orientation of the fields.

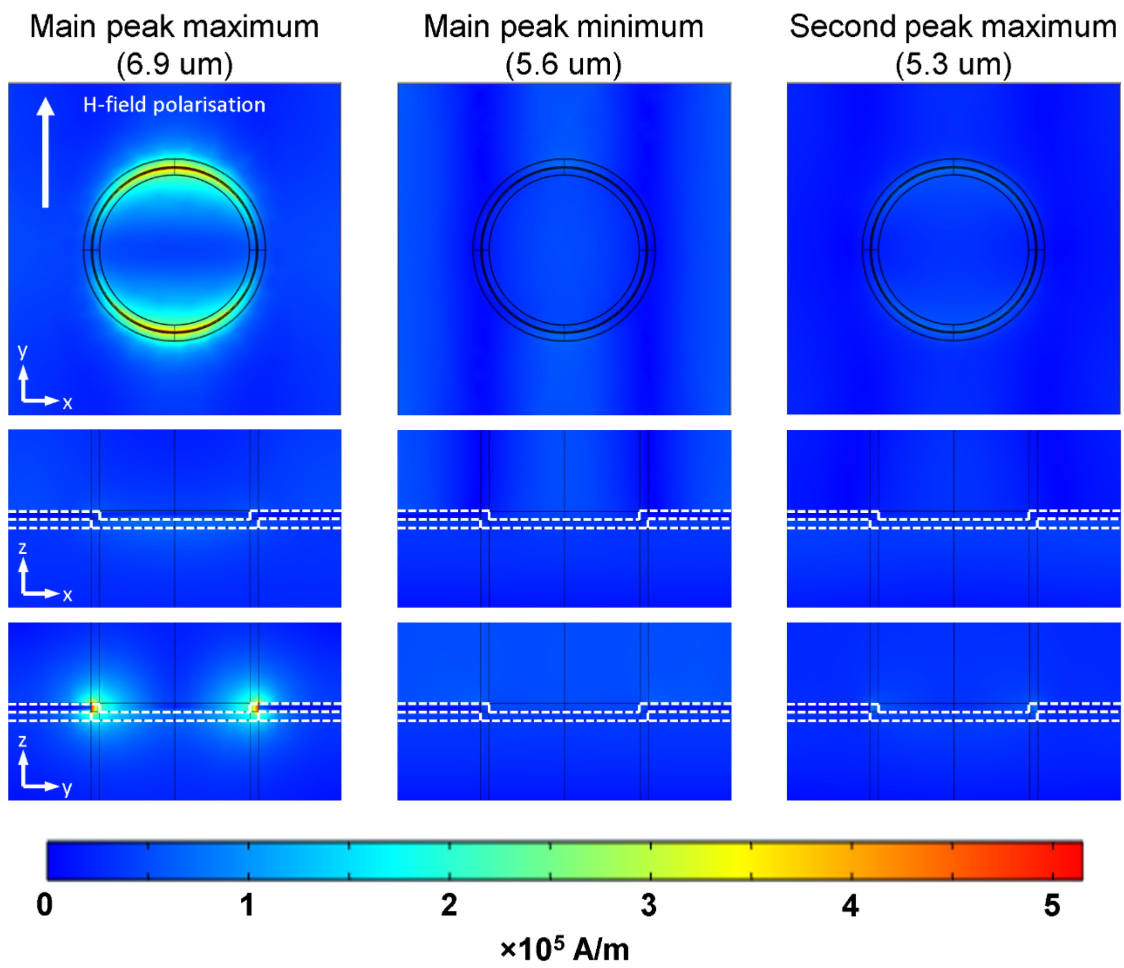

Figure 65: H-field plots of a simulated EOT array for deposition scheme 3 (as shown in Figure 63) for amorphous GST-225 PCM, z-plane in xy plots at the film (and PCM)/substrate interface, white-dashed lines on xz and yz plots marking out film and PCM layers.

5.4.3. Visible-NIR EOT-PCM arrays

For GST-225, GST-326 and GSST-2241, measured *n* & *k* data of samples deposited in-house were obtained for the visible to NIR range by ellipsometry measurements (reported in Figure 66), and could be utilised in the simulations.

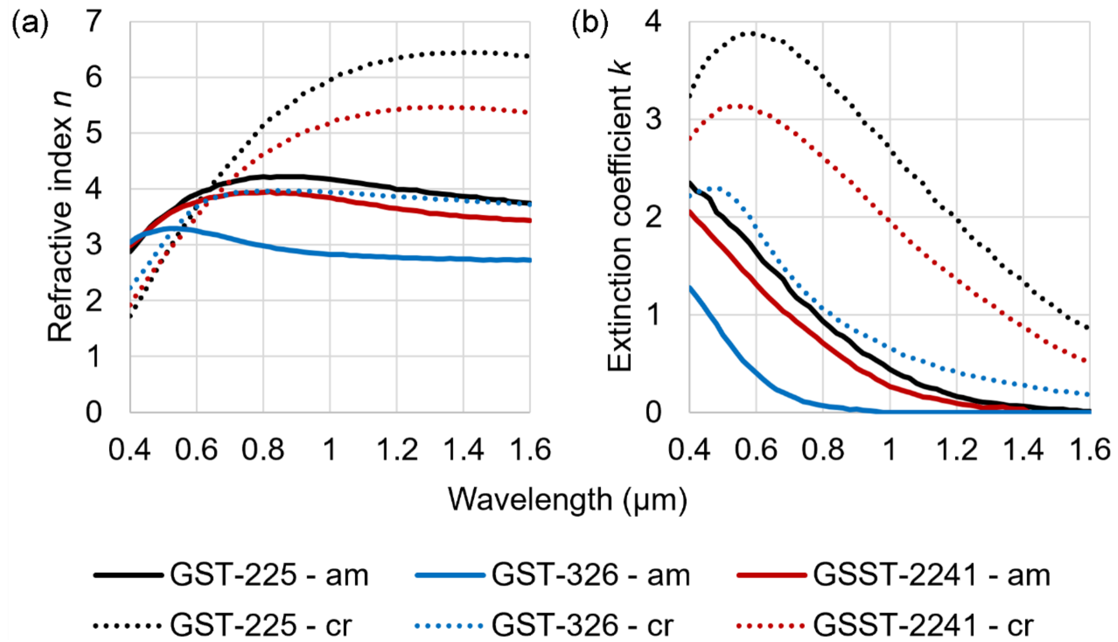

Figure 66: In-house ellipsometry-obtained optical data of GST-225, GST-326 and GSST-2241 PCMs (a) refractive index n (b) extinction coefficient k

Simulations were tried using this data for a range of PCM thicknesses (“deposited” uniformly on the entire surface, i.e. scheme 1 in Figure 62). In the cases of GST-225 (Figure 67) and GST-326 (Figure 68), a comparatively large separation between the peaks could be achieved (peak wavelength shifted by up to a factor of 40% in some cases) but with very poor Q-factor in the crystalline phase due to high *k*. Less loss was observed when simulating behaviour with GSST-2241 (Figure 69), but so was also less shift. As mentioned previously though, a large change in *k* can be utilised for signal modulation, with examples shown in Figure 70 of the contrast ratios/modulation depths (given in Equation (62)) for the devices shown in Figure 67 and Figure 69.

$$Modulation\ depth = \frac{T_{am}}{T_{cr}} \qquad (62)$$

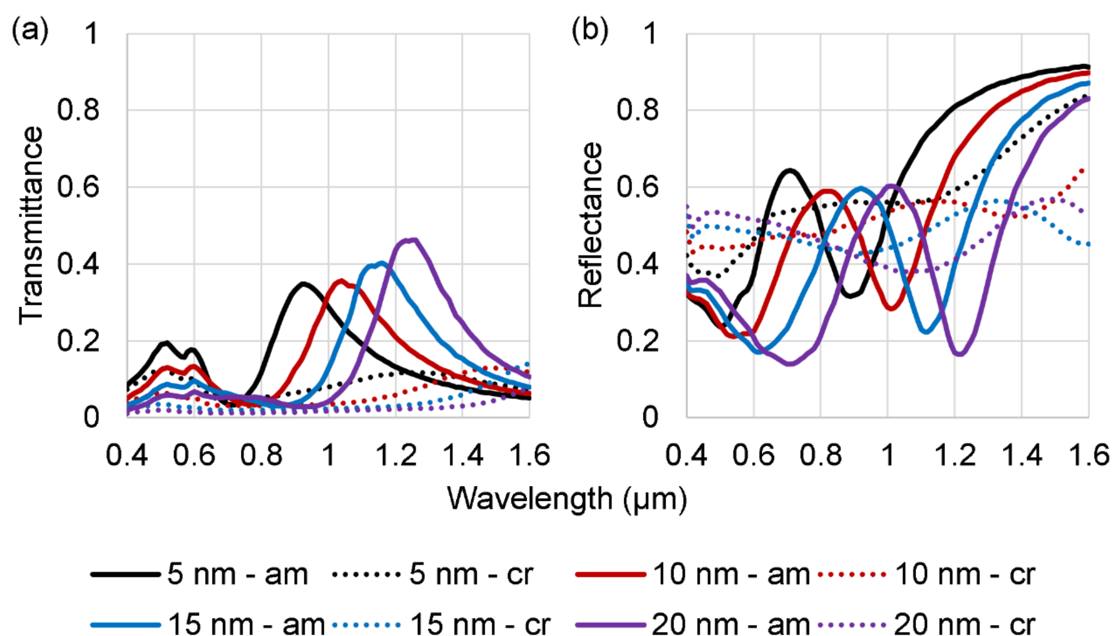

Figure 67: Simulated 400 nm pitch square arrays with ff=0.5 circular holes in 40 nm Au film on CaF_2, with GST-225 layers of varied thicknesses, (a) transmittance and (b) reflectance

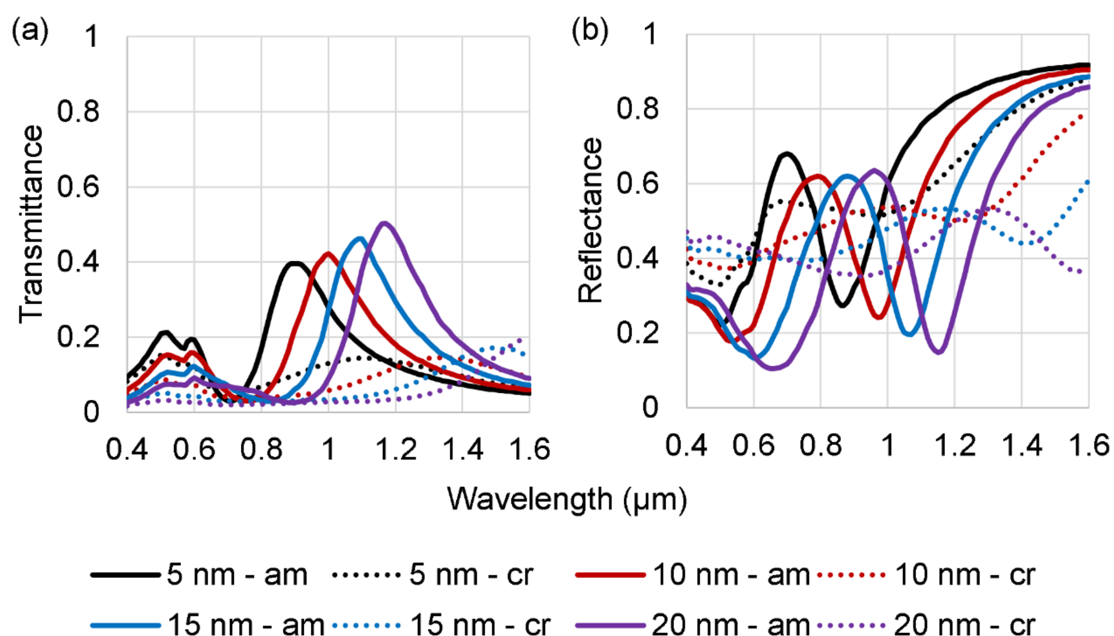

Figure 68: Simulated 400 nm pitch square arrays with ff=0.5 circular holes in 40 nm Au film on CaF_2, with GST-326 layers of varied thicknesses, (a) transmittance and (b) reflectance

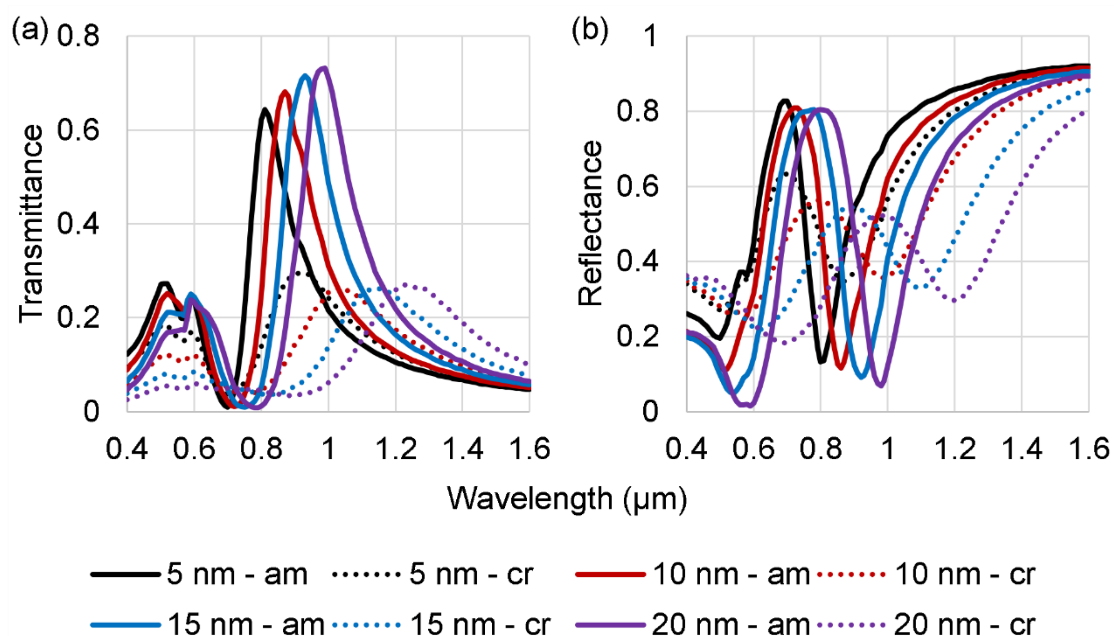

Figure 69: Simulated 400 nm pitch square arrays with ff=0.5 circular holes in 40 nm Au film on CaF_2, with GSST-2241 layers of varied thicknesses, (a) transmittance and (b) reflectance

GST-225 appeared to provide the best contrast ratio/modulation depth, with GSST-2241 providing slightly lower modulation depth but a higher Q-factor for a given PCM thickness, as shown in Table 17.

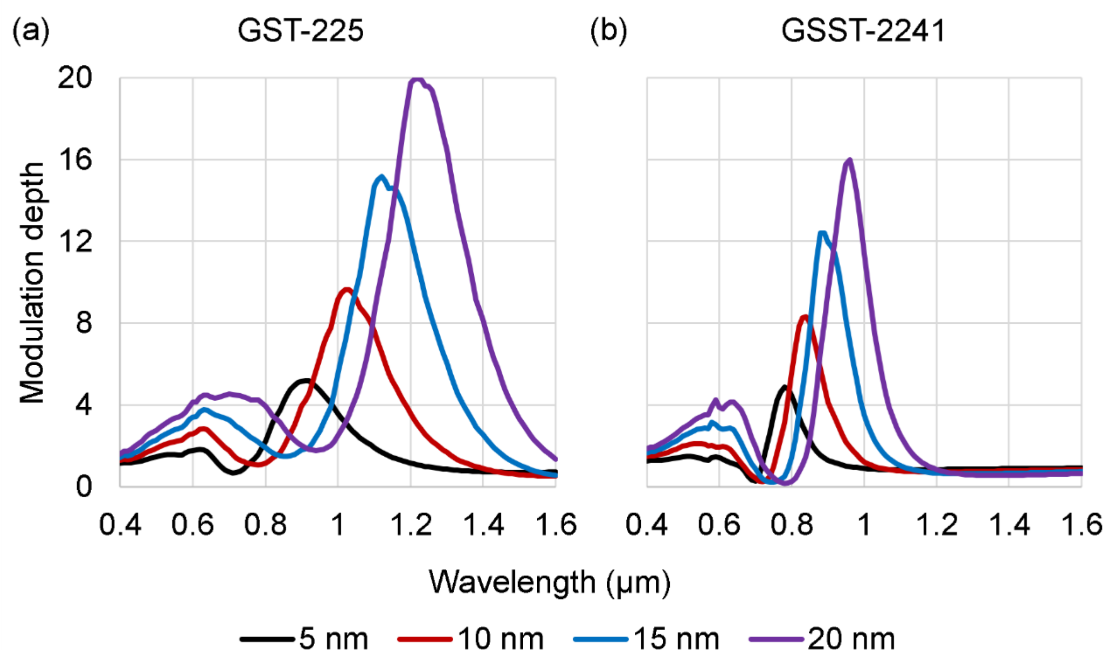

Figure 70: Modulation depths of simulated SWIR EOT arrays featuring (a) GST-225 and (b) GSST-2241 for PCM layers of various thicknesses

Table 17: Plot data from NIR EOT simulations shown in Figure 70

	PCM type	PCM thickness (nm)			
		5	10	15	20
Max mod' depth	225	5.18	9.65	15.17	19.96
	326	4.21	7.51	11.79	16.03
	2241	4.87	8.32	12.42	15.98
Q-factor	225	3.79	4.16	4.57	4.88
	326	4.14	4.62	5.35	5.45
	2241	7.22	7.64	6.85	6.58

Use of other PCMs to those shown above does open up the possibility of tuneable filters in the visible/NIR range, Sb_2S_3 and Sb_2Se_3 being two examples of such. As shown in Figure 71 with data from [97], these materials have generally much lower *k* values within the specified range, being negligible above 0.8 and 1 μm (for Sb_2S_3 and Sb_2Se_3 respectively) in the more-absorbing crystalline states.

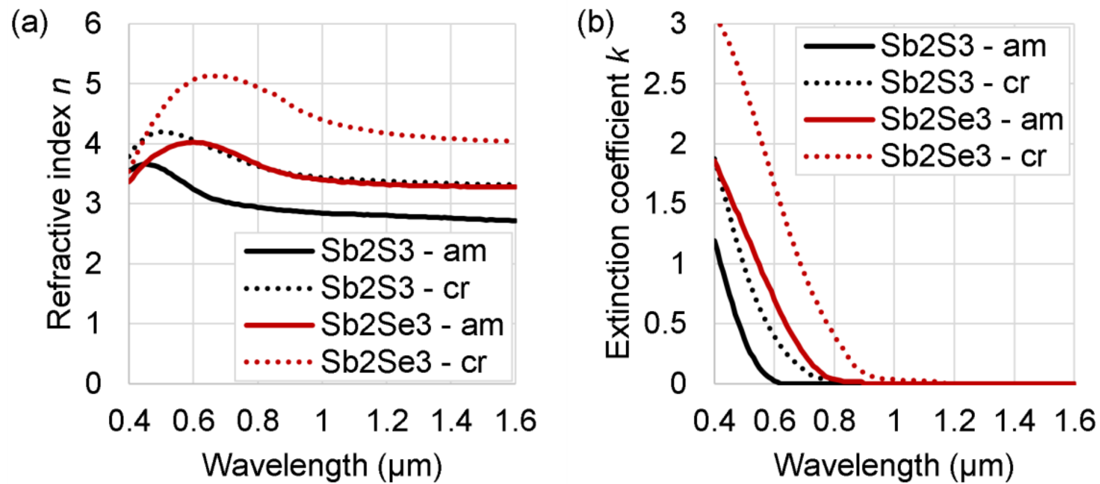

Figure 71: Optical data of Sb_2S_3 and Sb_2Se_3 PCMs, (a) refractive index n and (b) extinction coefficient k

Figure 72 and Figure 73 show transmission and reflection spectra of phase-change EOT devices modelled using these low-loss PCMs, with essential performance data in Table 18, demonstrating how the peaks retain much greater transmission in the crystalline PCM state. The *n* values of these materials in the amorphous state are similar to those of the GST and GSST material, but the smaller proportional changes in *n* mean than a thicker PCM layer is required to

obtain decent shifts (compare 20 nm layers for all materials), which may make switching more difficult.

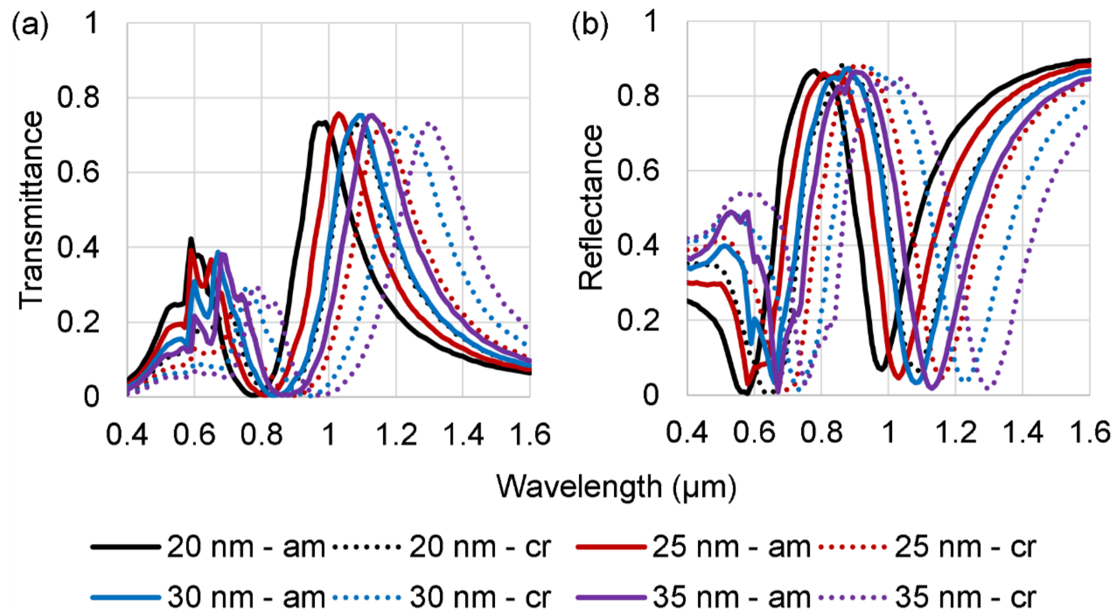

Figure 72: Simulated (a) transmitted and (b) reflectance spectra of a 400 nm pitch square array with coatings of Sb_2S_3 PCM

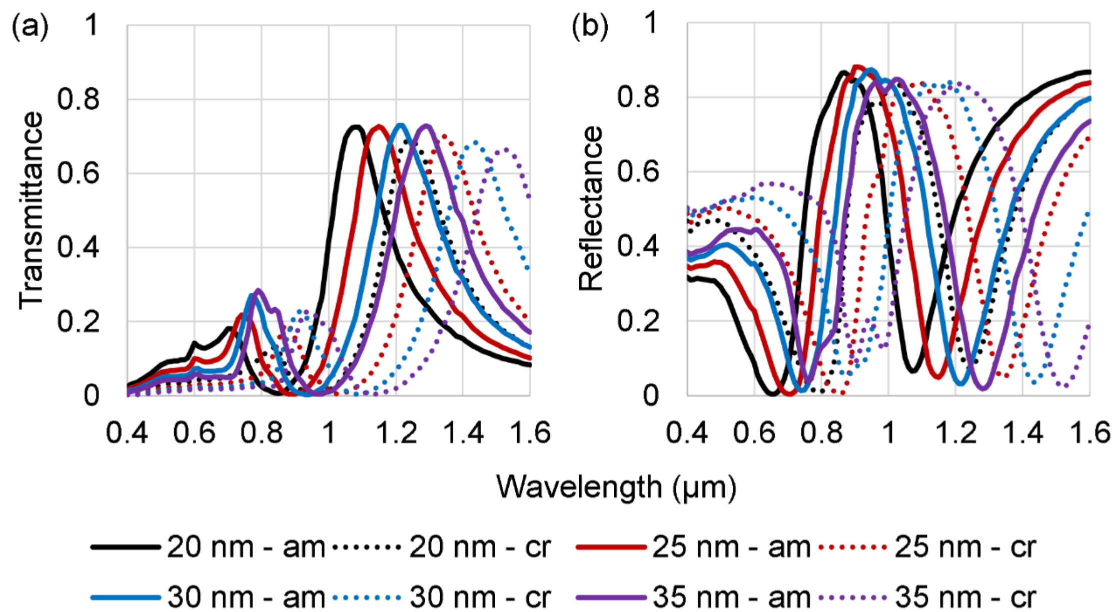

Figure 73: Simulated (a) transmitted and (b) reflectance spectra of a 400 nm pitch square array with coatings of Sb_2Se_3 PCM

Table 18: Visible-NIR EOT simulation data using low-loss (in this range) PCMs

	PCM type	PCM layer thickness (nm)			
		20	25	30	35
Peak T (am/cr)	Sb_2S_3	0.73/0.73	0.76/0.73	0.75/0.72	0.75/0.73
	Sb_2Se_3	0.73/0.69	0.73/0.70	0.73/0.68	0.73/0.67
Q-factor (am/cr)	Sb_2S_3	4.67/4.95	4.68/4.98	4.78/4.88	4.81/4.91
	Sb_2Se_3	4.95/5.10	4.79/5.36	4.73/5.42	4.78/NA
Peak shift (µm)	Sb_2S_3	0.11	0.14	0.12	0.17
	Sb_2Se_3	0.16	0.19	0.22	0.23

5.4.4. THz Modulator Arrays

While tuneable phase-change EOT filters made for multispectral imaging would benefit from universal reduction in the PCM layer's absorption coefficient *k*, devices made with the same structure but with a large contrast in *k* can act as effective signal modulators. GST-225 has such a large *k* contrast in the THz regime; indeed, as shown in Figure 74**,** within the 0.6-1.4 THz (500-214 µm) range *k* increases from ~0 to ~5 upon crystallisation.

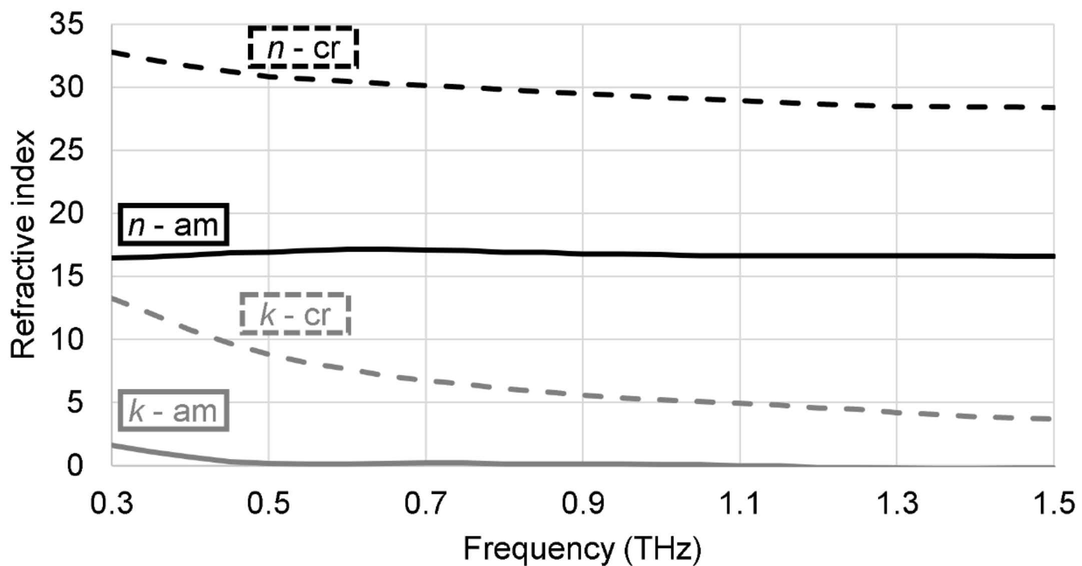

Figure 74: GST-225 n & k data in THz regime, crystallised at 300°C (from [98]*)*

This in turn means a much greater proportional reduction in transmission peak height is to be expected when switching devices from their amorphous to crystalline phase. This is confirmed by simulation results shown in Figure 75,

where devices had a 175 µm pitch to create peaks at around 1 THz (approximately 300 µm). From the results it would appear that PCM-EOT devices should act as effective modulators in the THz region of the spectrum. Increasing the device fill factor increases the peak transmittance as expected but at the expense of modulation depth and Q-factor (given here in Equation (63)).

$$Q - factor = \frac{F_{peak}}{\Delta F_{FWHM}} \tag{63}$$

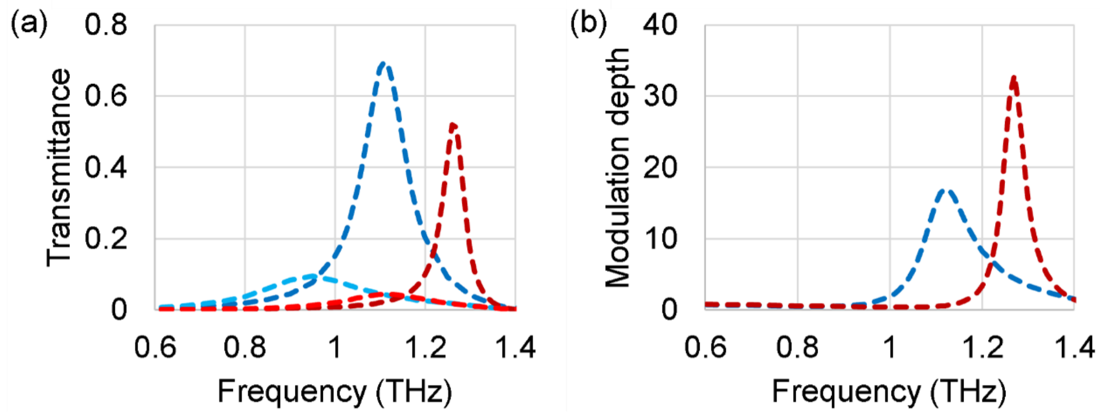

Figure 75: Simulated phase-change EOT modulator (a) transmittance and (b) modulation depths for fill factors of 0.3 and 0.4, using 100 nm Au film with 175 µm pitch, on quartz substrate with 100 nm GST-225

Table 19: Comparison of simulated modulator properties, "Peak T" given for filter as a whole in its most transmissive state

Fill factor	Peak T	Modulation depth	Modulation depth q-factor
0.3	0.52	32.9	22.3
0.4	0.7	16.99	8.77

5.5. Thermal Modelling

As pointed out previously (in Section 3.3.2), it might be possible to use the metallic film of the EOT array itself as a form of electrical heater to switch the PCM layer in PCM-EOT tuneable optical filter devices. Using the array film as a heating element for phase-change EOT devices has however certain challenges, in particular obtaining sufficiently high temperatures to melt the PCM (while not

melting the EOT film itself), and allowing it to cool down again fast enough for successful re-amorphisation. Simulations were therefore carried out to explore how altering different device factors contribute to the performance of the EOT-film as heater for switching, using a PCM melting temperature of 600°C and target cooling rates between 1-10 °C/ns at 200°C (a typical crystallising temperature).

5.5.1. Cooling Rates

The base device (shown in Figure 76) for thermal simulations consists of a 400 nm pitch array in a 40 nm gold film on a 500 μm MgF_2 substrate, using circular holes with a fill factor of 0.5. A 20 nm GSST-2241 covers the whole exposed surface, the material thermal properties used are show in Table 5. Unless stated otherwise, constant voltage pulse durations of 20 ns are used to drive current through the EOT metal film.

Table 20: Thermal properties of materials used in simulations, amorphous GSST-2241 from [63]*, gold from standard values used in the built-in COMSOL materials, MgF_2 from* [88]

Material	Thermal conductivity (W m^{-1} K^{-1})	Heat capacity (J K^{-1} m^{-3})
am GSST-2241	0.2	1.45×10^6
Gold	317	2.49×10^6
MgF_2	21	3.19×10^6

The thermal properties of GSST (and other PCMs) vary depending on the crystallisation state, but the variations are relatively minor and so, for simplicity, were ignored for the purposes of these simulations. Gold electrical resistivity however was set as a temperature-dependant variable, since it increases significantly with temperature (from ~2-8 $\times 10^8$ Ω.m between room temperature and 600°C) as shown in Section 4.1.2, Figure 15. Simulation runs were configured by setting the pulse voltage (across the unit cell) and duration, which were adjusted as needed to bring the PCM at the centre the EOT array holes up to the melting temperature of 600°C.

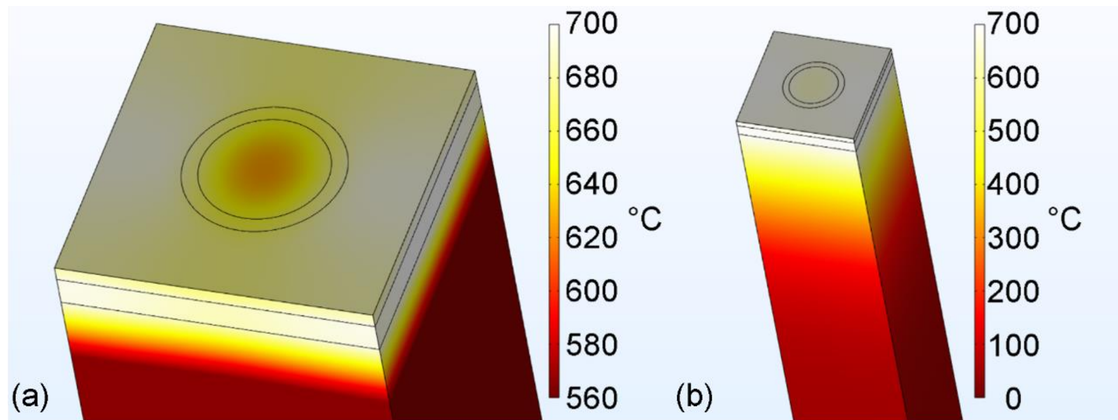

Figure 76: 3D temperature plot of 400 nm pitch Joule-heating device unit cell, showing (a) the centre of the hole being coolest and (b) temperature plot of larger section of device, including more of the substrate

A range of pulse lengths were trialled, from 5 to 50 ns, with the resulting temperature evolution at the centre of a PCM-filled hole in the EOT array being shown in in Figure 77. This required the voltage applied to be adjusted for each run to reach the desired temperature, the values are in Table 21 along with peak current. Peak current was always at the very start of the pulse, when temperature is lowest and gold electrical conductivity highest (see Section 4.1.2).

n.b. Bold values in Table 21-Table 28 are for the "base" device defined above, around which one parameter would be changed during each set of simulations

Also shown are the cooling rates after the peak temperature is reached, plotted against temperature to give a better idea if an adequate cooling rate can be achieved. It appears, as would be expected, that increasing the re-amorphisation pulse length decreases the cooling rate at any given temperature, with 1°C/ns being achieved at 200°C using a 20 ns or shorter pulse.

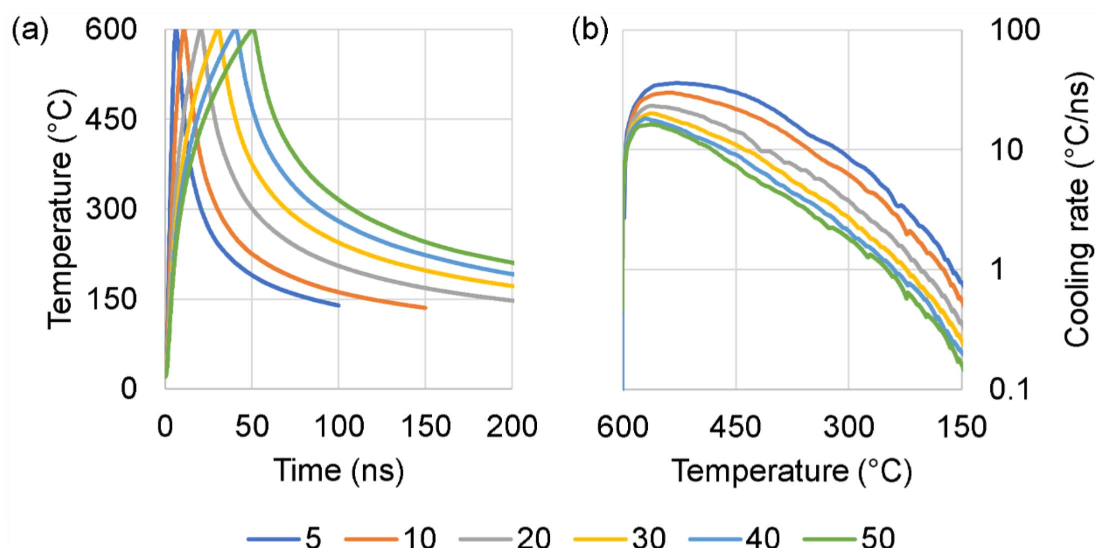

Figure 77: (a) Temperatures and (b) cooling rates at the centre of a PCM filled hole in the EOT array, while varying pulse duration (ns)

Table 21: Pulse voltage and peak current applied to devices in Figure 77

Pulse duration (ns)	**5**	**10**	**20**	**30**	**40**	**50**
Pulse voltage (V)	0.2320	00.1645	**0.1265**	0.1105	0.1005	0.0940
Peak current (A)	0.2801	0.1988	**0.1523**	0.1336	0.1215	0.1136

Other factors that might influence heating and cooling properties of the device include the thermal conductivities and heat capacities of the materials used. Generally speaking, when keeping the constant pulse duration of 20 ns (adjusting voltage only), simulations shown in Figure 78, Figure 79, Figure 80 and Figure 81 indicated that the higher the thermal conductivity and the lower the heat capacity, the higher the cooling rate that could be sustained. This would favour substrate materials such MgO (κ=42 W m^{-1} K^{-1}) [99] and Si (κ=163 W m^{-1} K^{-1}) [100] over something such as Al_2O_3 (κ=5 W m^{-1} K^{-1}) [101], but optical property suitability must also be considered in practical devices.

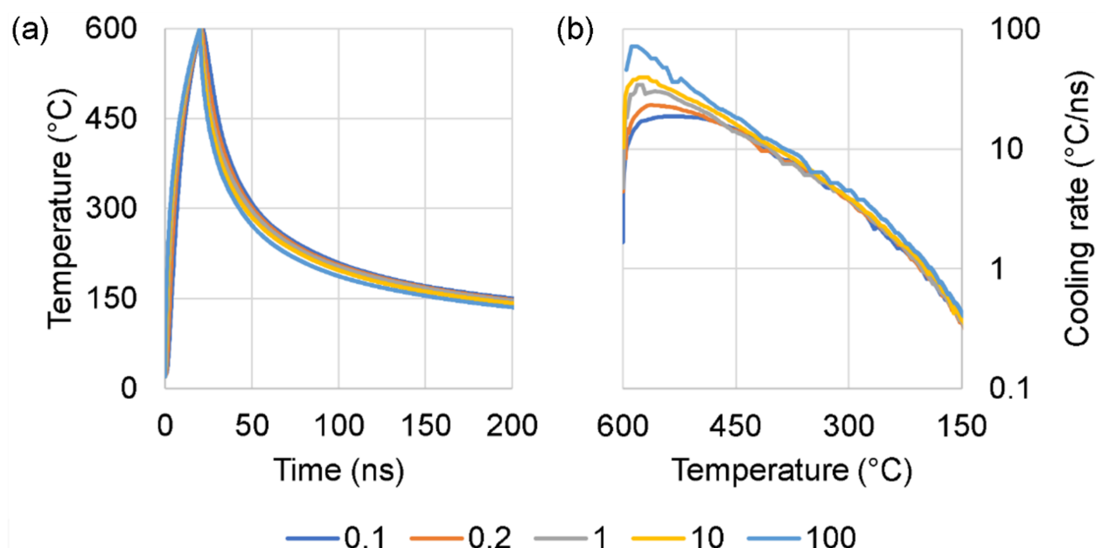

Figure 78: (a) Temperatures and (b) cooling rates at the centre of a PCM filled hole in the EOT array, while varying PCM thermal conductivity κ (W m^{-1} K^{-1})

Table 22: Pulse voltage and peak current applied to devices in Figure 78

PCM κ (W m^{-1} K^{-1})	0.1	0.2	1	10	100
Pulse voltage (V)	0.1285	**0.1265**	0.1250	0.1220	0.1150
Peak current (A)	0.1553	**0.1523**	0.1511	0.1475	0.1391

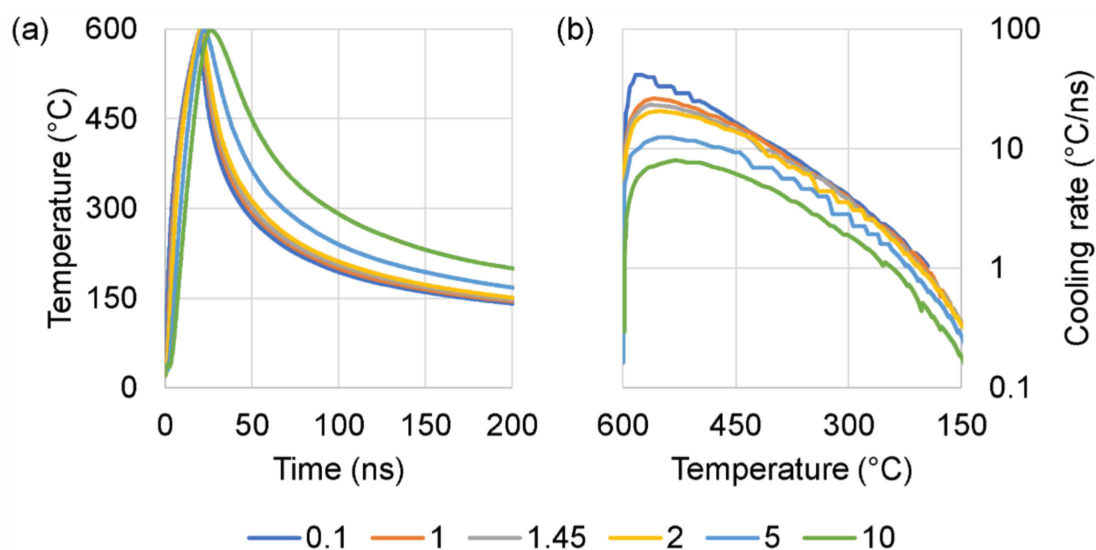

Figure 79: (a) Temperatures and (b) cooling rates at the centre of a PCM filled hole in the EOT array, while varying PCM heat capacity C (MJ kg^{-1} K^{-1})

Table 23: Pulse voltage and peak current applied to devices in Figure 79

PCM *C* (MJ kg^{-1} K^{-1})	**0.1**	**1**	**1.45**	**2**	**5**	**10**
Pulse voltage (V)	0.1225	0.1245	**0.1265**	0.1280	0.1395	0.1665
Peak current (A)	0.1481	0.1505	**0.1523**	0.1547	0.1683	0.1683

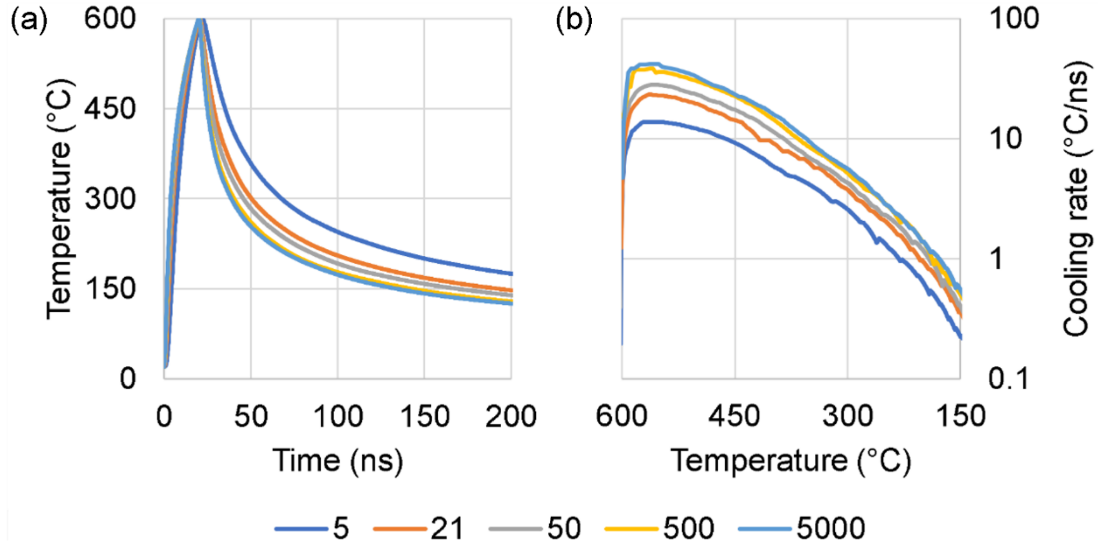

Figure 80: (a) Temperatures and (b) cooling rates at the centre of a PCM filled hole in the EOT array, while varying substrate thermal conductivity κ (W m^{-1} K^{-1})

Table 24: Pulse voltage and peak current applied to devices in Figure 80

Sub' *κ* (W m^{-1} K^{-1})	**5**	**21**	**50**	**500**	**5000**
Pulse voltage (V)	0.1030	**0.1265**	0.1500	0.2520	0.4445
Peak current (A)	0.1246	**0.1523**	0.1811	0.3018	0.5211

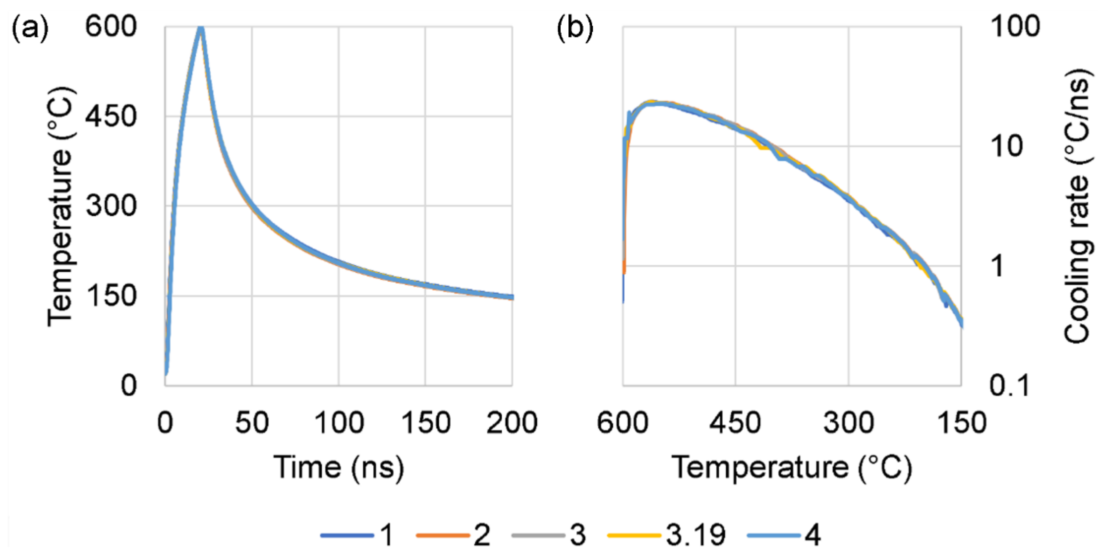

Figure 81: (a) Temperatures and (b) cooling rates at the centre of a PCM filled hole in the EOT array, while varying substrate heat capacity C (J kg^{-1} K^{-1})

Table 25: Pulse voltage and peak current applied to devices in Figure 81

Sub' *C* (MJ kg^{-1} K^{-1})	**1**	**2**	**3**	**3.19**	**4**
Pulse voltage (V)	0.0920	0.1100	0.1240	**0.1265**	0.1350
Peak current (A)	0.1114	0.1331	0.1499	**0.1523**	0.1631

It would be expected that the larger the hole size the greater the overall heating of the device is required and thus the lower the cooling rate. Figure 82 and Figure 83 respectively show simulations of the effect of altering the array pitch and fill factor, with slight changes in the predicted directions observed.

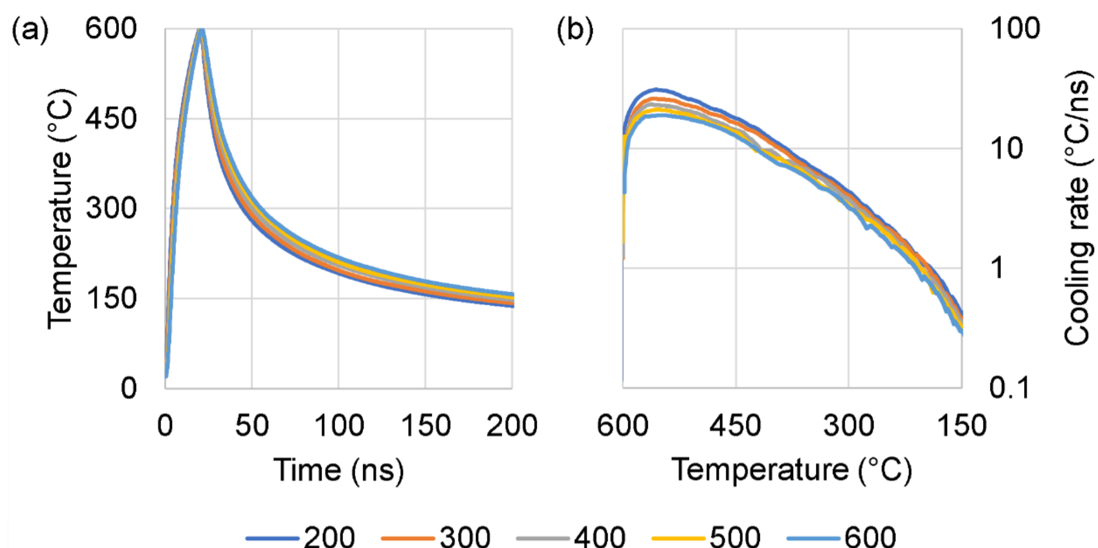

Figure 82: (a) Temperatures and (b) cooling rates at the centre of a PCM filled hole in the EOT array, while varying the array pitch (nm) and keeping a constant fill factor of 0.5

Table 26: Pulse voltage and peak current applied to devices in Figure 82

Array pitch (nm)	200	300	400	500	600
Pulse voltage (V)	0.0585	0.0910	**0.1265**	0.1645	0.2070
Peak current (A)	0.0708	0.1100	**0.1523**	0.1988	0.2489

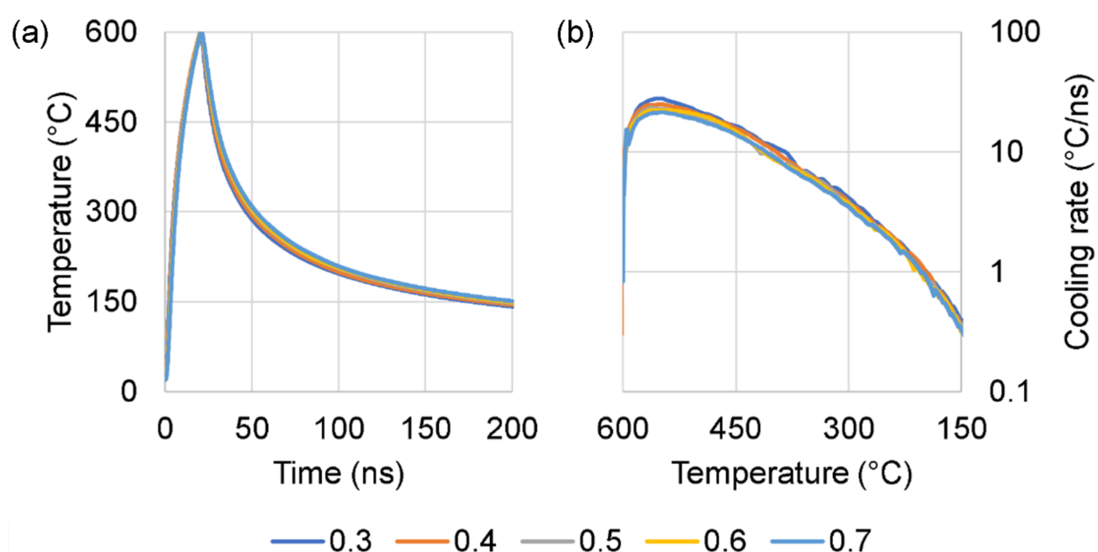

Figure 83: (a) Temperatures and (b) cooling rates at the centre of a PCM filled hole in the EOT array, while varying the array fill factor and keeping a constant pitch of 400 nm

Table 27: *Pulse voltage and peak current applied to devices in Figure 83*

Array fill factor	**0.3**	**0.4**	**0.5**	**0.6**	**0.7**
Pulse voltage (V)	0.1055	0.1140	**0.1265**	0.1430	0.1670
Peak current (A)	0.1650	0.1595	**0.1523**	0.1436	0.1323

The other geometric consideration is the thickness of the EOT film and PCM layers, Figure 84 and Figure 85 showing results of simulations with different PCM thicknesses for 40 nm and 100 nm Au films respectively. As might be expected, using thicker PCM layers reduces the cooling rates, but increasing the metal film thickness (comparing 40 nm vs 100 nm films) slightly increases them when using a thicker PCM layer (note 80 nm plots).

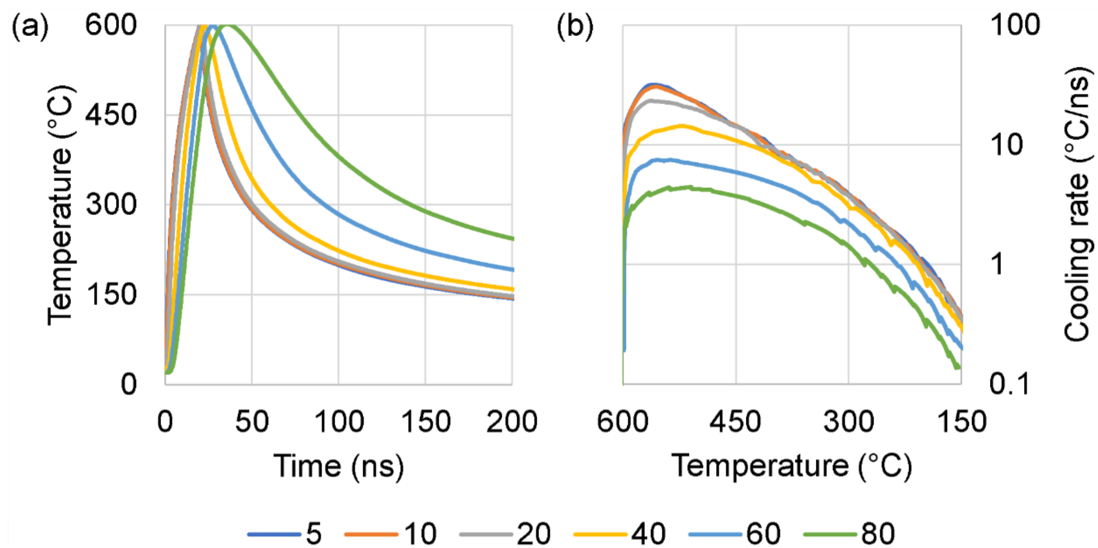

Figure 84: (a) Temperatures and (b) cooling rates at the centre of a PCM filled hole in the EOT array, while varying PCM thickness (nm), using 40 nm Au film

Table 28: Pulse voltage and peak current applied to devices in Figure 84

PCM thickness (nm)	**5**	**10**	**20**	**40**	**60**	**80**
Pulse voltage (V)	0.1250	0.1250	**0.1265**	0.1345	0.1655	0.2260
Peak current (A)	0.1511	0.1511	**0.1523**	0.1626	0.1992	0.2690

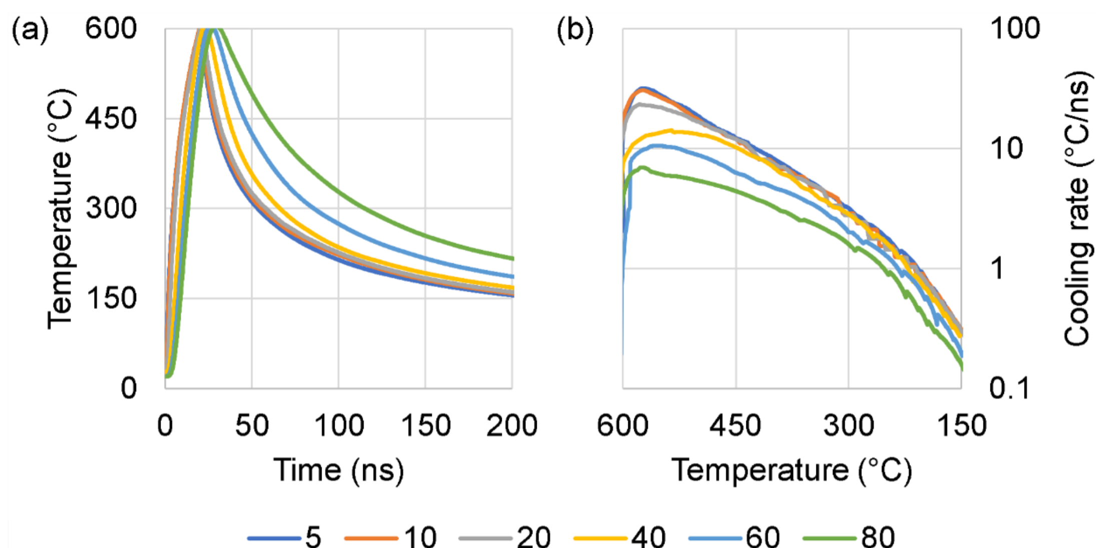

Figure 85: (a) Temperatures and (b) cooling rates at the centre of a PCM filled hole in the EOT array, while varying PCM thickness (nm), using 100 nm Au film

Table 29: Pulse voltage and peak current applied to devices in Figure 85

PCM thickness (nm)	**5**	**10**	**20**	**40**	**60**	**80**
Pulse voltage (V)	0.0815	0.0820	0.0825	0.0855	0.0955	0.1120
Peak current (A)	0.2467	0.2483	0.2498	0.2588	0.2886	0.33799

5.5.2. Peak Temperatures Reached

As well as achieving sufficiently high temperatures to melt the PCM layer in the holes of the EOT array, and achieving sufficiently high cooling rates for successful re-amorphisation, the hottest regions of the EOT metal film must not be allowed to reach temperatures at which they would undergo damage (or even melt) during heating. As shown in Figure 86, the hottest region in the EOT film itself lies between the holes and perpendicular to the flow of the current, This is to be expected since these regions have the smallest cross-section (to the current flow) and greatest resistance.

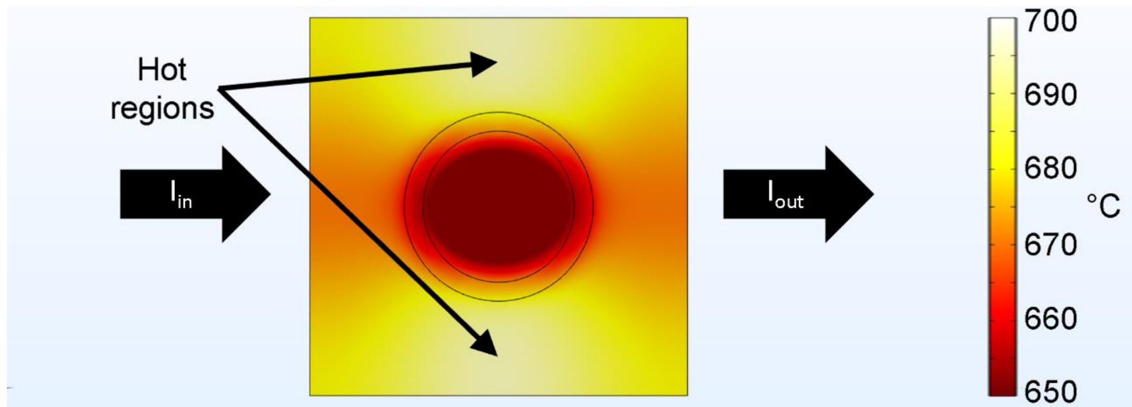

Figure 86: Schematic of temperature distribution across a unit cell during resistance/Joule heating, showing dependence on current flow direction

Using shorter pulses increases the maximum film temperature reached, Figure 87 showing the temperature profiles and peak temperatures in the EOT film (at the hottest points), with the 5 ns pulse resulting in temperatures very close to the gold melting point of 1064.18°C.

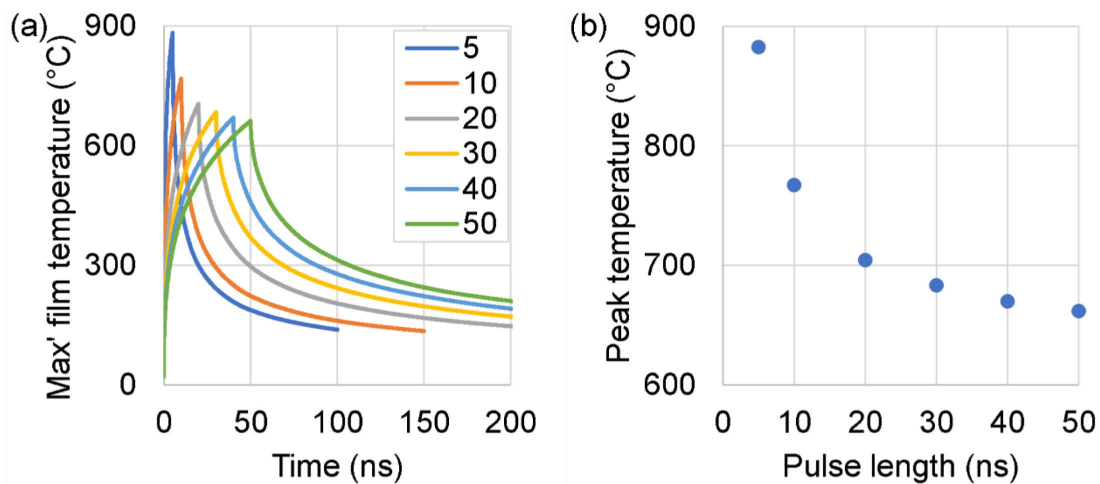

Figure 87: (a) Maximum film temperature against time and (b) peak temperatures reached in the EOT metal film for 5-50 ns re-amorphisation pulse durations

The other factors explored previously when examining the temperature reached in the PCM layer also contribute to the temperature reached in the EOT film. Figure 88 and Figure 89, for example, show how increasing thermal conductivity and heat capacity of both the PCM and substrate will respectively decrease or increases the peak temperatures reached in the EOT film.

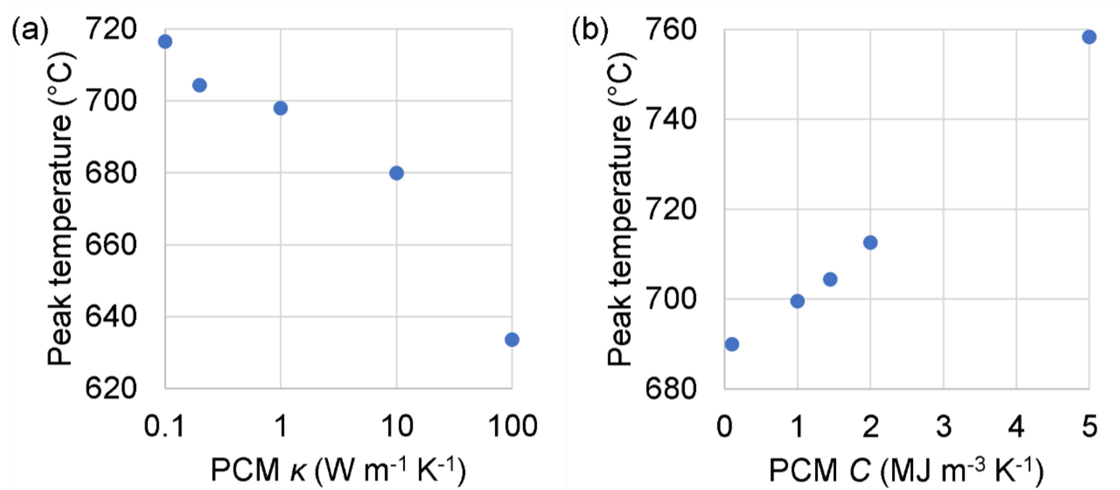

Figure 88: Peak temperatures reached in the EOT metal film when varying (a) PCM thermal conductivity and (b) heat capacity

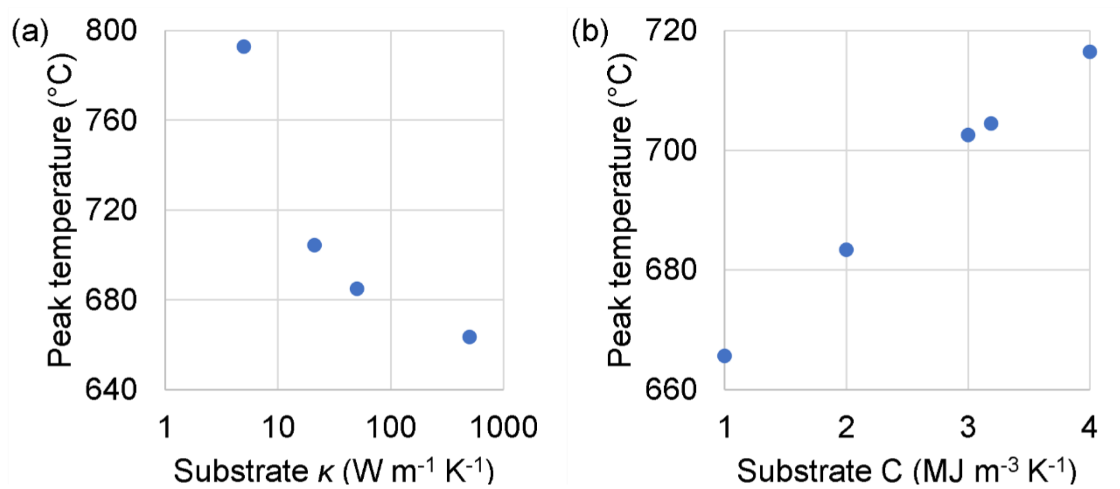

Figure 89: Peak temperatures reached in the EOT metal film when varying (a) substrate thermal conductivity and (b) heat capacity

Similarly, increasing hole size (whether by increasing the array pitch or fill factor) and PCM layer thickness also increases the peak temperatures reached in the EOT metal film, as shown in Figure 90 and Figure 91.

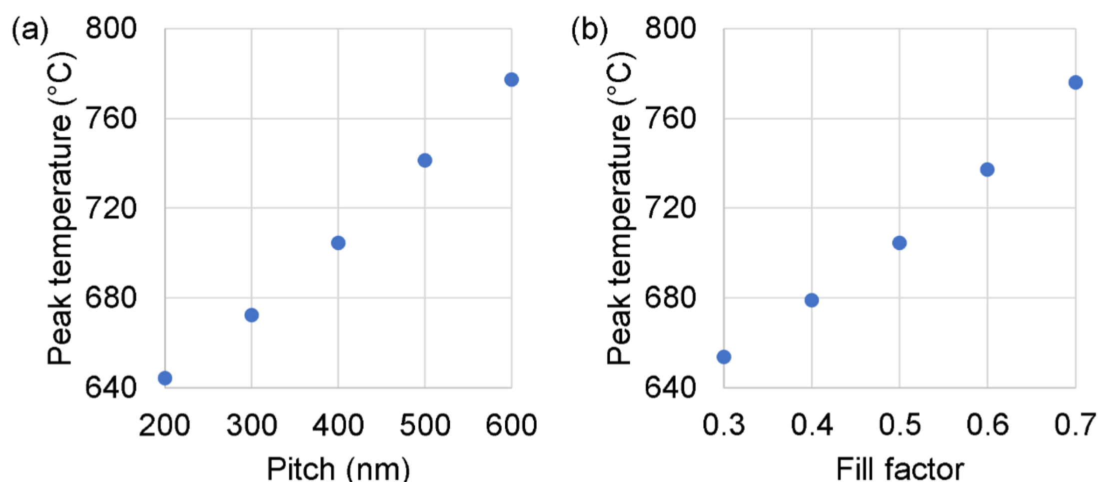

Figure 90: Peak temperatures reached in the EOT metal film when maintaining a constant fill factor of 0.5 and varying (a) array pitch and (b) keeping a 400 nm pitch while changing fill factor

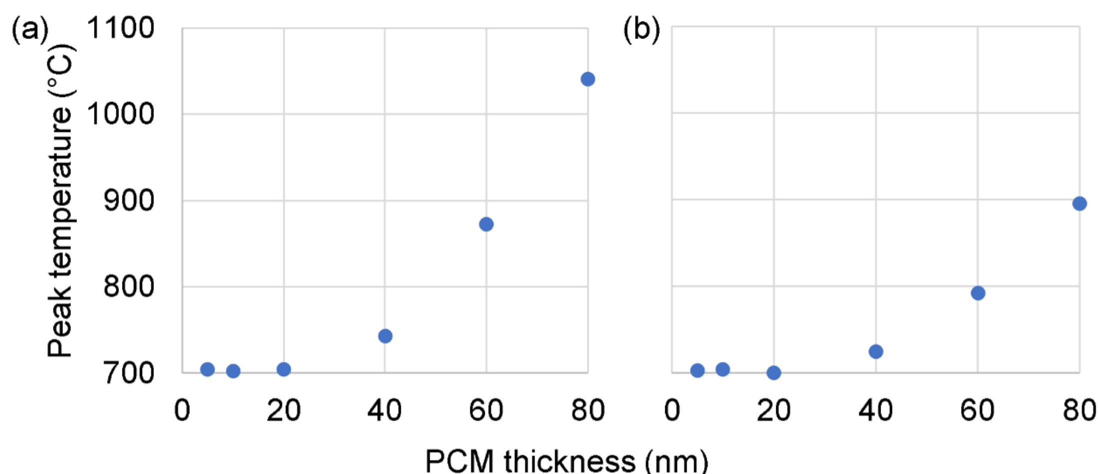

Figure 91: Peak temperatures reached in the EOT metal film when altering PCM thickness, with (a) 40 nm and (b) 100 nm Au films

The simulation data presented in Figure 90 and Figure 91 especially show the difficulties in applying this specific technique of using the EOT array film as a heating element. In addition to making achieving the required cooling rates to re-amorphise the PCM layer harder (as shown previously), increasing any dimensions (barring the EOT film thickness) increases the maximum temperature reached and this has potential to compromise device integrity. MWIR tuneable filters have array pitches an order of magnitude greater than those for visible-NIR devices, which would like compound such difficulties.

Further issues include the relatively high currents required, with examples of some devices modelled here shown in Figure 92 and Figure 93. Note also that the total switching energy of a practical device must take account of the total number of cells needed to cover the required surface area.

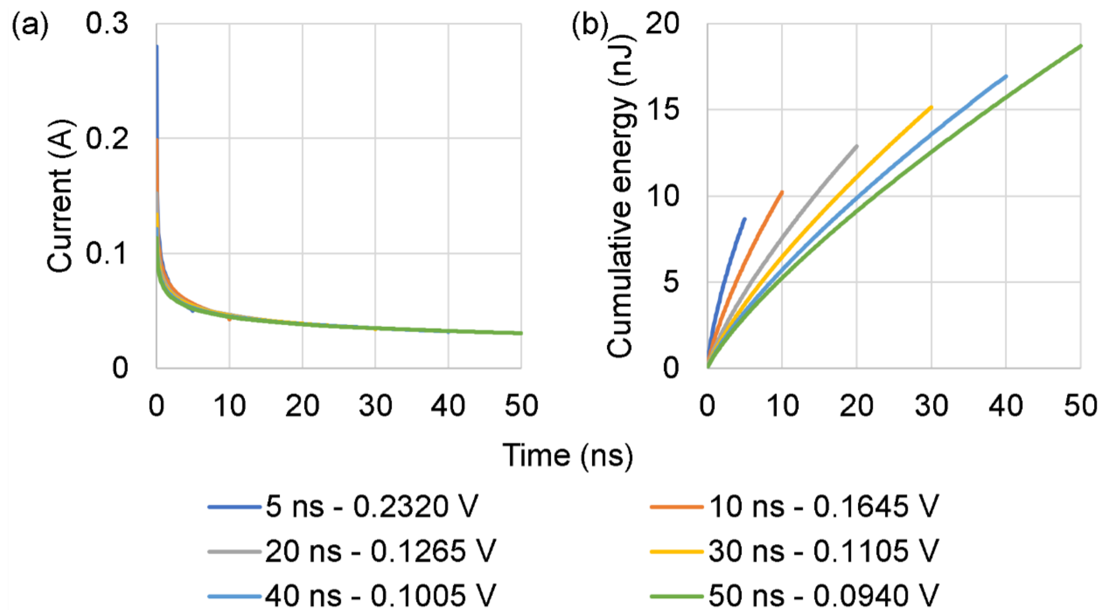

Figure 92: Plots of simulated (a) current and (b) cumulative energy expended of a single cell (400 nm array pitch, ff=0.5, 40 nm Au film and 20 nm PCM layer on 500 µm MgF_2 substrate) throughout pulses of 5-50 ns duration (runs shown in Figure 77/Table 21)

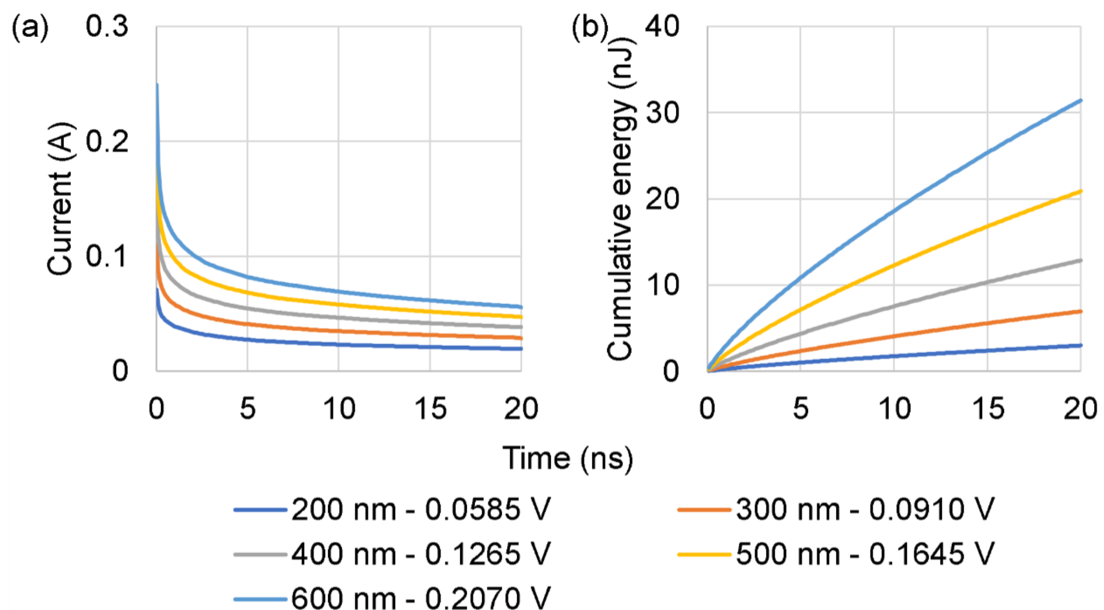

Figure 93: Plots of simulated (a) current and (b) cumulative energy expended of a single cell (200-600 nm array pitch, ff=0.5, 40 nm Au film and 20 nm PCM layer

on 500 µm MgF_2 substrate) throughout the 20 ns pulse, (runs shown in Figure 82/Table 26)

The issue of excessive temperature in the EOT film could be mitigated through several different methods:

- Using an EOT film with a higher melting point (e.g. tungsten at 3422°C, used as a separate heater layer for a reflective device in [102]), but this may compromise filter optical performance.

- Using a separate heating layer below the EOT metal layer, as shown in [63], [102], [103], potentially putting the heating element much closer to all regions of the PCM, regardless of hole size, but this would only work for devices operating in reflection unless the additional layers (heater, electrical insulator etc.) were suitably transmissive. A possible means of achieving this would be the use of PIN junction diodes, as shown in [104] for GST-coated photonic switches. A strip of pure/intrinsic (I) silicon is bookended by P-doped and N-doped strips, with Joule heating occurring in the I strip when current is passed between them. This could be applied to EOT devices by having the I strips positioned underneath the array holes, concentrating heating at the regions where the PCM must be shifted (see Section 5.4.3): this would require analysis to see if the design could be scaled to account for the relatively large percentage area of the surface covered by the holes (~30% for ff=0.6) compared to a photonic switch, and what effect the silicon layer (up to hundreds of nm thick) would have on the transmittance (poor in MIR compared to CaF_2, BaF_2 or MgF_2 [100]).

- Using PCMs with lower switching temperatures, reducing the required film heater maximum temperature.

- Not requiring PCMs to be fully switched, especially by allowing a region at the hole centre to remain crystalline. This would reduce the transmission peak shift seen in optical spectrum of devices when the PCM layer is switched (since not all of it would in fact switch), but would most likely reduce heater demands.

5.6. Chapter Summary

This chapter used extensive simulations to provide a detailed analysis of how altering the various design parameters of an EOT array (primarily designed for the mid-infrared regime) affects transmittance, both with and without the presence of PCM layers to introduce an element of tuneability. The general findings in this respect, for mid-infrared devices, are summarised in Table 30.

Table 30: Effects of changing device and material properties on phase-change EOT bandpass filter performance

Property change	Effect
Increasing array period *p*	Redshifts peak, increases peak width and decreases q-factor
Increasing array fill factor	Increases transmittance, increases peak width and decreases q-factor
Increasing EOT film thickness	Increases transmittance and q-factor, decreases peak width
Increasing substrate *n*	Redshifts peak
Increasing PCM *n*	Redshifts peak and increases width while reducing transmittance
Increasing PCM *k*	Lowers peak transmittance, increases width and decreases q-factor
Increasing PCM thickness	Lowers peak transmittance, increases peak width and decreases q-factor. Gives larger shift between crystallisation states but with bigger transmittance drop.

The effect of the structure of the PCM on the array was also investigated, and it was found that the key requirement is to ensure that the hole area is filled with PCM, otherwise the device acts almost as if there is no PCM present at all. Whether PCM is only in the holes; across the entire top of the EOT array film surface; between the substrate and the EOT array film or on both sides appeared to have little difference on transmission performance.

Rectangular EOT arrays may be useful for situations where polarisation sensitivity is needed (since the transmission spectra are different for light

polarised along the long and short axes of the array), though this comes at the expense of peak transmittance and yields a Q-factor disparity for the different polarisations. Square EOT arrays are ideal for devices that require polarisation independence (the equivalent hexagonal arrays showing some slight change in peak transmission with linear polarisation angle).

In the visible and NIR range, the same general characteristics of simulated arrays were observed as for the MWIR devices, both with and without PCM layers. The suitability of such arrays for different phase-change EOT applications varies with the choice of PCM, with "traditional" GST family materials (with relatively high extinction coefficient *k* in the crystalline state for this regime) seemingly working well for modulation applications and newer alloys (Sb_2S_3 and Sb_2Se_3, lower-loss) for tuneable bandpass filtering.

Using GST-225 for tuneable multispectral filtering in the infrared and signal modulation in THz regimes appears viable using the optical properties available in published sources, with array behaviour similar to that of those made for shorter wavelengths.

With regards to thermal performance, simulations performed here illustrate the possibility of using the EOT metal film itself as a heating element to switch the PCM layer. Maintaining a large enough cooling rate after the re-amorphisation pulse while not overheating the film favouring a thin PCM layer with small holes, as does having high thermal conductivity of the PCM layer and substrate, along with low heat capacities. Use of the EOT film as a heater does, however, require significant currents, with switching energies being in the region of several to 10s of nJ per array unit cell.

6. Phase-Change EOT Devices Experimental Results

This chapter concerns the experimental implementation of devices discussed and simulated previously. The reflection and transmission measurements of different EOT array designs (without PCM layers) are presented first. Next, the addition of GST PCMs to arrays to create tuneable devices is discussed. Mid-IR filter arrays were fabricated using both the established technique of e-beam lithography/wet-etching and the new method of laser-ablation; examples of both were optically characterised. Finally, additional experiments were conducted to investigate the effects of gold diffusion from the EOT metal layer in the PCM layer, and how this can be mitigated.

6.1. Gold EOT Arrays

6.1.1. Arrays Fabricated via E-beam Lithography

Using the general parameters established from simulations shown earlier, devices were fabricated to create EOT filters for the mid-IR regime, in this case defined as approximately 2-12 μm. Gold films (thickness of 40-100 nm) were deposited onto substrates via thermal evaporation with thin (3-5 nm) chromium layers laid down first to provide better adhesion.

The total film thickness was determined for each evaporation session using specially prepared test pieces; dots of 950K A6 PMMA were placed with a pipette on the corners of the polished side of oxidised silicon substrates, then baked on a hotplate for 10 minutes at 100°C. After the deposition, the test piece was sonicated in acetone to remove the PMMA, leaving behind the film on the substrate with sharp edges where the dots were, ready to be measured with a surface profiler.

The reason for using separate test pieces rather than putting PMMA dots on the samples made for optical measurements was to minimise the chance of contaminating the device surface. To ensure consistency between the thickness test samples and devices fabricated for optical characterisation, the sample stage in the evaporator that they were secured to was rotated during all depositions.

Samples should ideally be placed equidistant from the centre of the stage rotation to ensure even coverage, but this was not always possible, especially if depositing on a large sample (e.g. a 4” Si wafer for diffusion test pieces).

Calcium fluoride (CaF_2) was the main substrate material used for devices working in transmission, and EOT array pitches ranging from 2 μm to 6.6 μm were fabricated to create EOT transmission peaks within the required spectral range (whether uncoated or covered with a PCM layer).

E-beam lithography was used exclusively to create patterned masks either for lift-off or wet-etching but, as discussed in Section 4.2.3.3, the latter was used most of the time since it resulted in the highest quality devices and provided a robust and repeatable process. Another advantage to using wet-etching is the presence of the already-deposited gold film providing the conductive layer required for e-beam lithography, negating the requirement of a separate conductive polymer layer to be deposited on top of the PMMA thus removing spinning, baking and washing steps from the fabrication process, saving time and reducing complexity compared to lift-off. The surface area of the holes in the fabricated EOT arrays always covered less than half that of the total area of the array, so positive photoresist (written area of the resist being softened) was used to reduce writing time. 950K A4 PMMA was chosen, spun at 4,000 RPM to give a ~250 nm thick mask and baked on a hotplate for 2 minutes at 170°C to harden.

An example of an EOT array fabricated via wet-etching is shown in Figure 94. Examples of experimental EOT optical transmission spectra, measured using FTIR (as discussed in Section 4.2.4.7), are shown in Figure 95 for arrays of different pitches in Au films on CaF_2 substrates. Also shown in Figure 95 are COMSOL simulated spectra, with good correspondence seen between both the peak position (wavelength) and the absolute peak transmission.

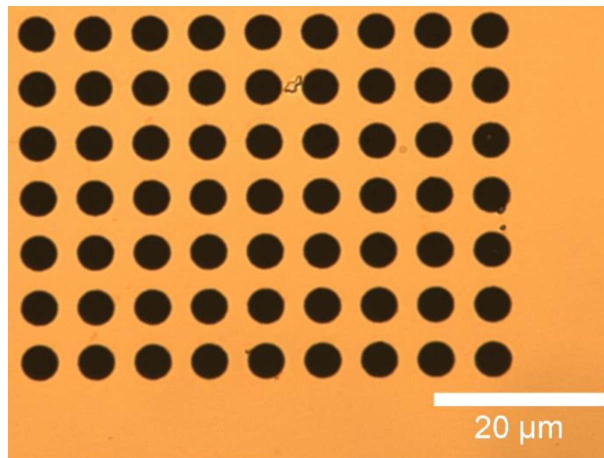

Figure 94: Optical microscope image of the corner of an EOT array in an Au film on a CaF2 substrate, wet-etched holes with a 6.6 µm pitch

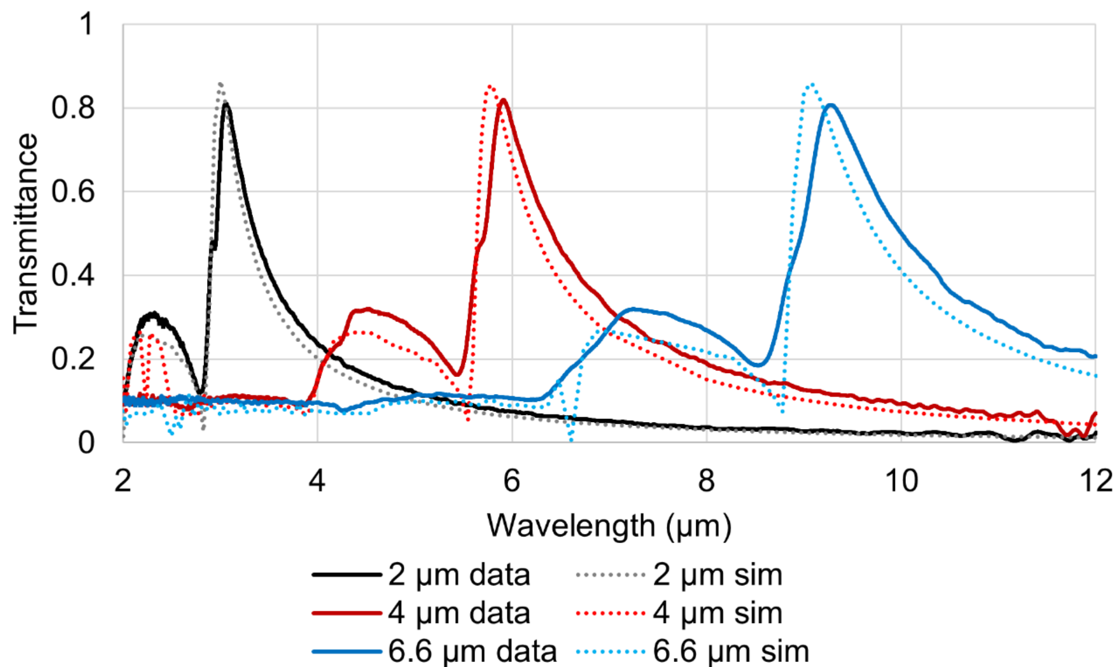

Figure 95: Transmission spectra for EOT arrays made in 3/40 nm Cr/Au film on calcium fluoride and with a constant fill-factor (hole diameter proportional to array period) of 0.6. Experimental (FTIR measured) results shown as solid lines, with COMSOL simulations as dotted lines

While the fabrication process described above was very successful in yielding high quality EOT arrays for use in the MWIR range, it proved considerably more difficult to fabricate devices with EOT arrays at a smaller geometric scale for measurement with a JASCO MSV-5300 microspectrometer (wavelength range of 200-1600 nm). Indeed, devices for this range fabricated using both wet-etching and lift-off approaches were of relatively poor quality (missing holes, poorly

defined holes, variable sized holes). It did prove possible, however, to fabricate good quality arrays for the visible-NIR range using an inverse-design approach, i.e. with patterns of discs/meta-atoms rather than holes, with one example of such an array being shown in Figure 96.

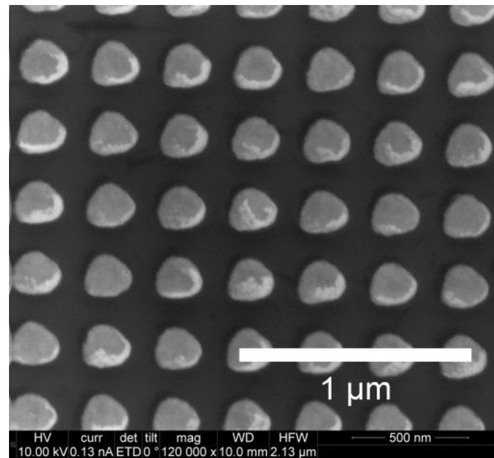

Figure 96: SEM image of a 300 nm pitch inverse-design disc/meta-atom array on an oxidised silicon substrate

Variations were made to examine the effect of altering geometric aspects of the inverse-design devices, with array pitches of 300, 350 and 400 nm (much smaller becoming increasingly difficult to make) and disc diameter/pitch ratio varied from 0.2 to 0.5. As shown in Figure 97, changing the array pitch has the same effect of shifting the reflectance peak position as was shown for the transmission peaks from the mid-infrared EOT arrays: increasing the relative disc diameter also increasing reflectance peak height and red-shifting the maxima position.

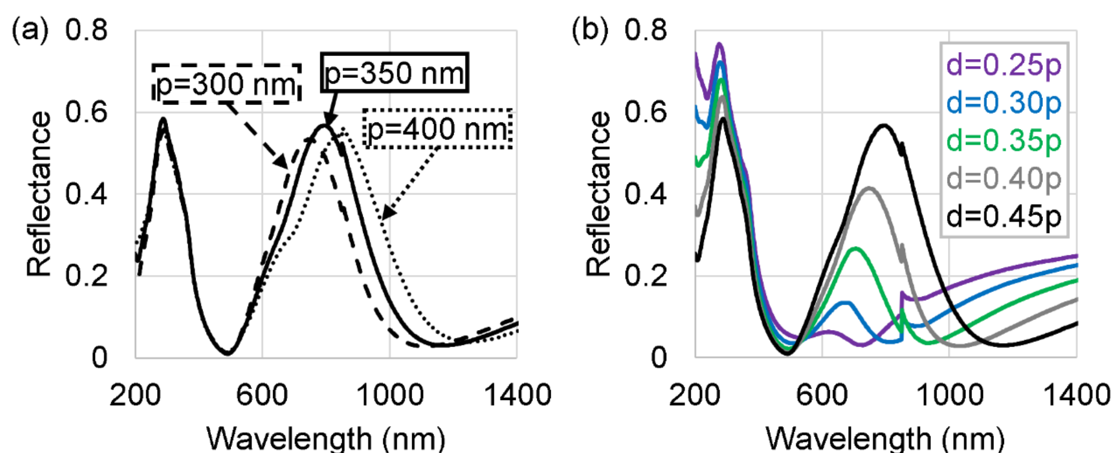

Figure 97: Example experimental reflectance spectra of disc arrays on oxidised silicon, (a) maintaining a constant designed relative disc diameter to array period of 0.45 and (b) with a constant array pitch of 350 nm

Additional disc arrays were also made on calcium fluoride substrates to obtain transmission spectra. Example results are shown in Figure 98, where transmission dips at wavelengths corresponding to reflection maxima are seen, with maximum depth achieved for a design pattern with disc diameter a quarter of the array pitch.

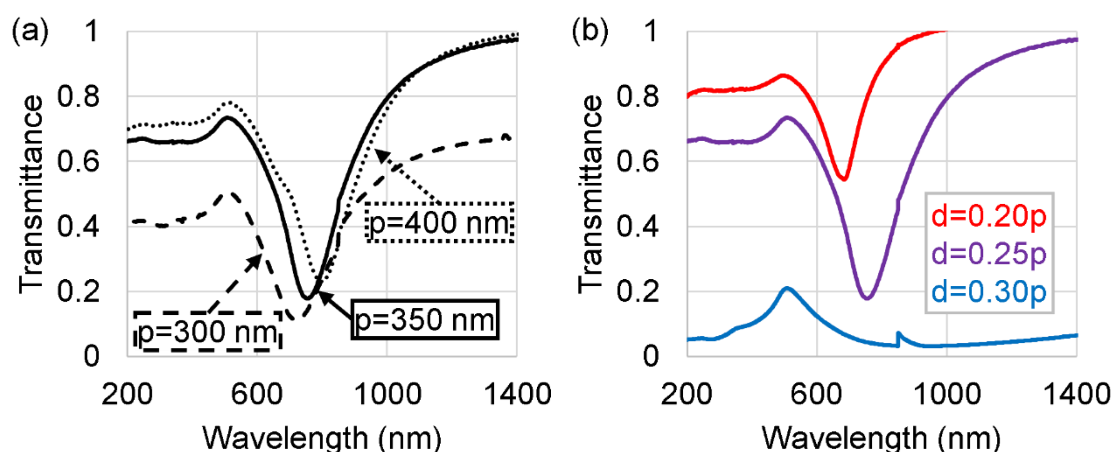

Figure 98: Example measured transmission spectra of disc arrays fabricated via lift-off on calcium fluoride (a) maintaining a constant relative disc diameter to array period of 0.25 and (b) with a constant array pitch of 350 nm

6.1.2. Mid-Infrared Arrays Fabricated via Laser Ablation

While the fabrication of EOT devices using conventional e-beam lithography combined with wet-etching was successful, it is a relatively slow process requiring multiple process steps, is not readily scaled-up to large sample sizes, requires costly equipment and is not particularly well-suited to real-world manufacture. So, as previously explained in Section 4.2.3.5, as part of the work of this thesis and with collaborators at IO-CSIC Madrid, a novel, single-step, ultra-fast laser patterning approach was also explored for the fabrication of EOT arrays.

6.1.2.1. Comparisons between Laser Ablation and Wet-Etching

Arrays were written using the laser ablation technique for a range of periods to create spectra with peaks across the mid-infrared regime. Figure 99 shows FTIR transmission spectra of various examples compared to equivalent devices (same materials, array periods, film thicknesses and hole fill-factors) made with e-beam/wet-etching, showing similar spectral responses.

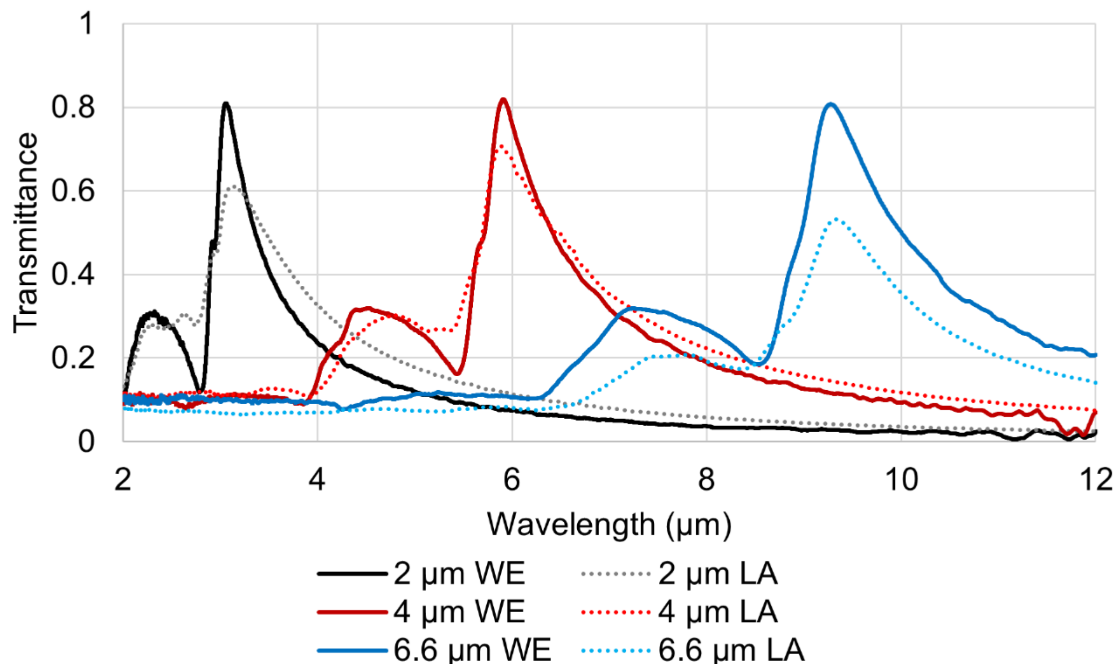

Figure 99: Transmission spectra of laser-ablated EOT (dotted lines) arrays vs wet-etched (solid lines), constant fill-factor of 0.6, 3/40 nm Cr/Au film on calcium fluoride, transmittance normalised to the substrate

It can be seen in Figure 99, however, that for comparable array specifications, the laser-ablated devices exhibited lower peak transmittance and Q-factors than the equivalent e-beam/wet-etched devices. Fabrication time for the laser-ablated devices was, however, of the order of minutes, compared to many hours for the e-beam fabricated devices. A comparison of key device performance and fabrication metrics for both the methods is given in Table 31.

Table 31: Comparison of peak properties for EOT arrays made with different fabrication methods, wet-etching (WE) and laser ablation (LA)

Period (μm)	Method	Peak T	Q-factor	Fabrication time	No. of steps
2	WE	0.81	4.99	Few hours	6
	LA	0.61	2.43	19 minutes	2
4	WE	0.82	5.66	Few hours	6
	LA	0.71	3.97	10 minutes	2
6.6	WE	0.81	6.08	Few hours	6
	LA	0.53	5.39	3 minutes	2

The reduced absolute transmission in the case of the laser fabricated devices is likely attributable to stitching errors as shown in Figure 100. “Stitching errors” is defined here as the hole position deviation from what was intended, giving non-perfect square lattices. This arose from the laser writer’s stage not resetting to the exact same *x* position after writing a row. Refinements to the scanning process to eradicate such errors have since been implemented by IO-CSIC.

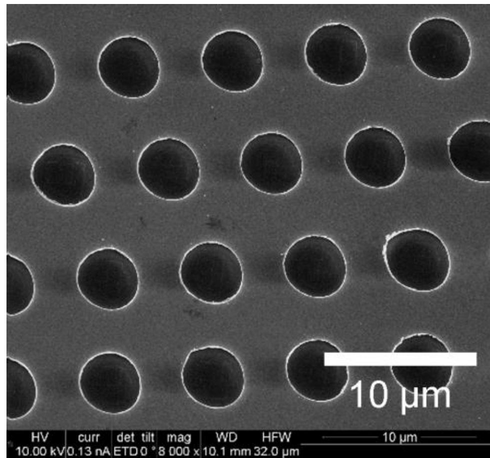

Figure 100: Scanning-electron microscope image of a typical laser fabricated EOT array, showing stitching errors between adjacent rows

6.1.2.2. Non-Square Arrays

The laser ablation method was also used to fabricate a range of non-square EOT arrays, with a view to exploring polarisation sensitivity in such arrays. Using 40 nm Au films with 3 nm Cr adhesive layers on 1 mm BaF_2 substrates (BaF_2 selected to allow transmission at longer wavelengths than CaF_2 permits), examples are shown of hexagonal arrays in Figure 101

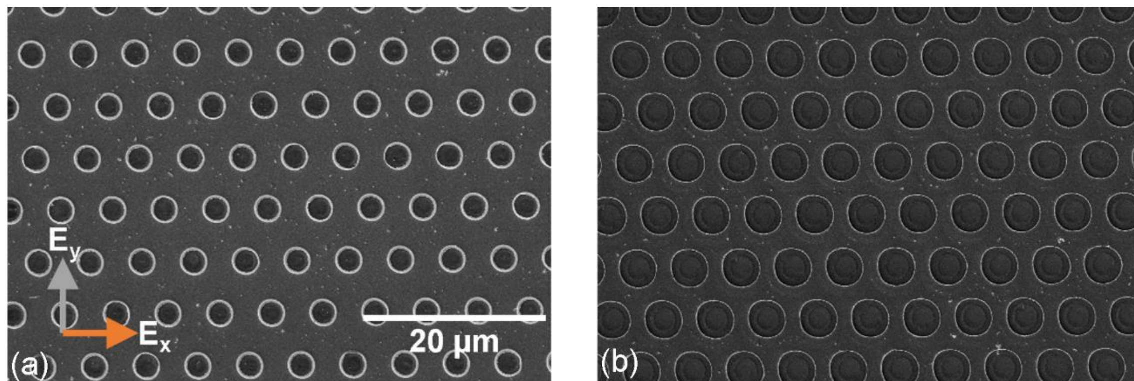

Figure 101: SEM images of hexagonal arrays fabricated via laser ablation, with low and high pulse intensities respectively giving (a) smaller and (b) larger holes

and of rectangular arrays in Figure 102.

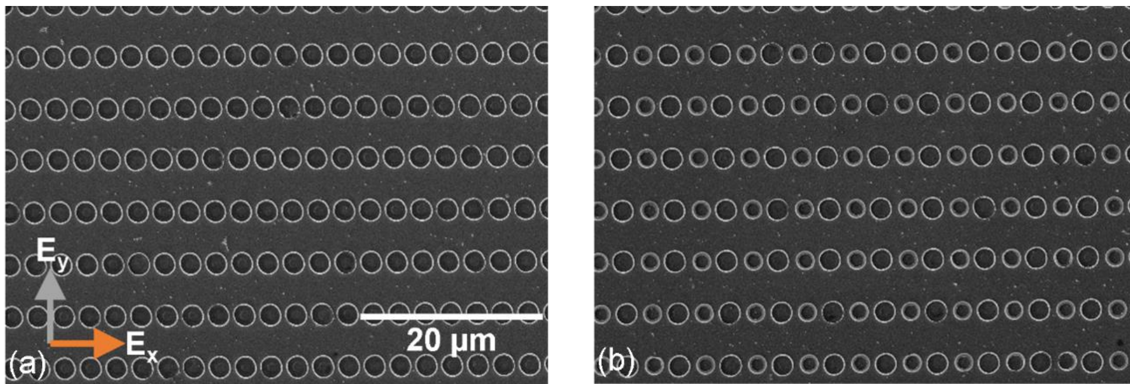

Figure 102: SEM images of rectangular arrays (with p_x=3 μm and p_y=6 μm) fabricated via laser ablation, with (a) identical holes and (b) alternating hole sizes along the rows. Note that issues of stitching errors had been resolved by the time these arrays had been fabricated.

FTIR spectra were taken of these devices, using a linear polariser to demonstrate the inherent polarisation dependence predicted in the simulations shown in Sections 5.2.1 and 5.2.2. Figure 103 shows this polarisation dependence for the hexagonal arrays shown in Figure 101, while Figure 104 shows it for the rectangular arrays of Figure 102. Each run has the array transmission normalised to all components but the array itself, negating their absorption. For non-polarised (no pol) runs this was just the substrate, for polarised (E_x and E_y) runs, this also included the polariser.

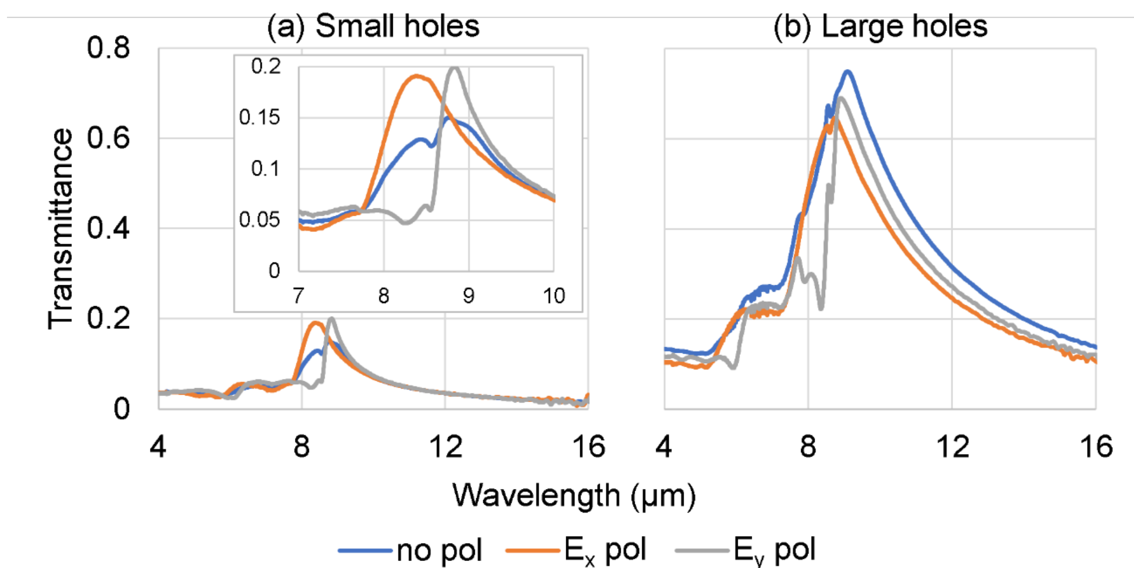

Figure 103: FTIR spectra of hexagonal arrays without linear polariser and under various incident polarisation conditions

With the small-hole hexagonal array, the no pol run clearly shows components of both the E_x and E_y polarisation main peaks, visible to a smaller extent in the large-hole array. While both cases differ from the simulations featured in Section 5.2.1 by showing main peak separation (though keeping the same general shape), secondary peak and minima features appear to have good overlap, which is consistent with the simulated examples of hexagonal arrays. This could potentially be attributed to manufacturing imperfections, such as slight deviations from exactly circular hole shape or hexagonal spacing.

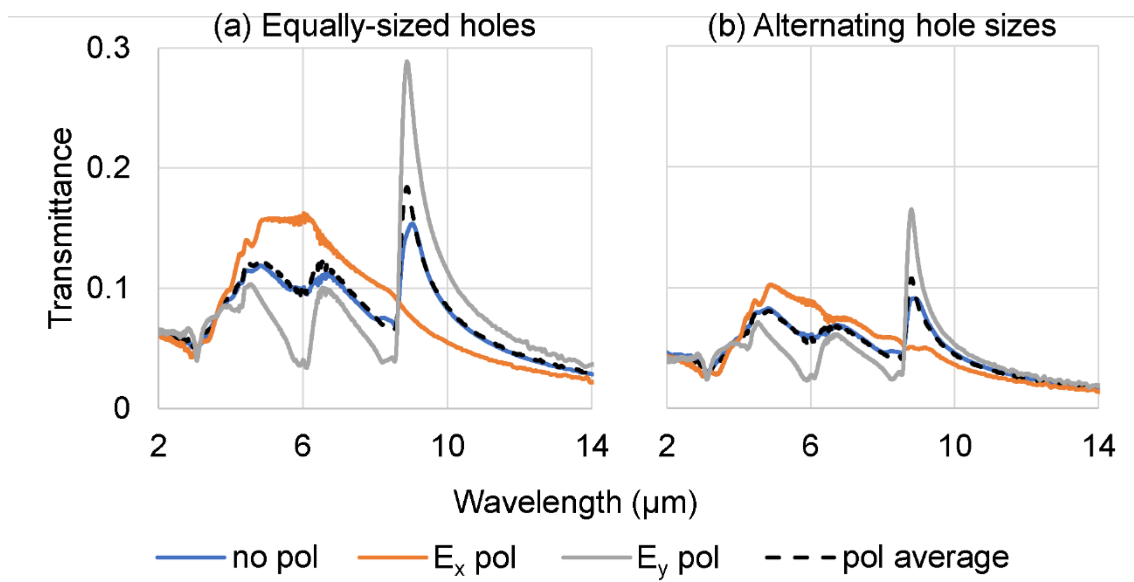

Figure 104: FTIR spectra of rectangular arrays without linear polariser and under various incident polarisation conditions (also including mean of E_x and E_y)

For the rectangular arrays, the features seen in Section 5.2.2 simulations are seen clearly, the E_x (parallel to short-pitch) polarisation giving a “bluer”, broader and shorter peak and the E_y (parallel to long-pitch) polarisation a “redder”, sharper and taller peak. As with the hexagonal arrays, the no pol run shows a combination of features of the spectra from both polarisations (notice coinciding minima and secondary peaks), with feature height almost an average of the two polarised runs’ spectra.

One point to consider is the absorption of the linear polariser, as shown in Figure 105 its transmittance being between around ~20-25% for the wavelength range.

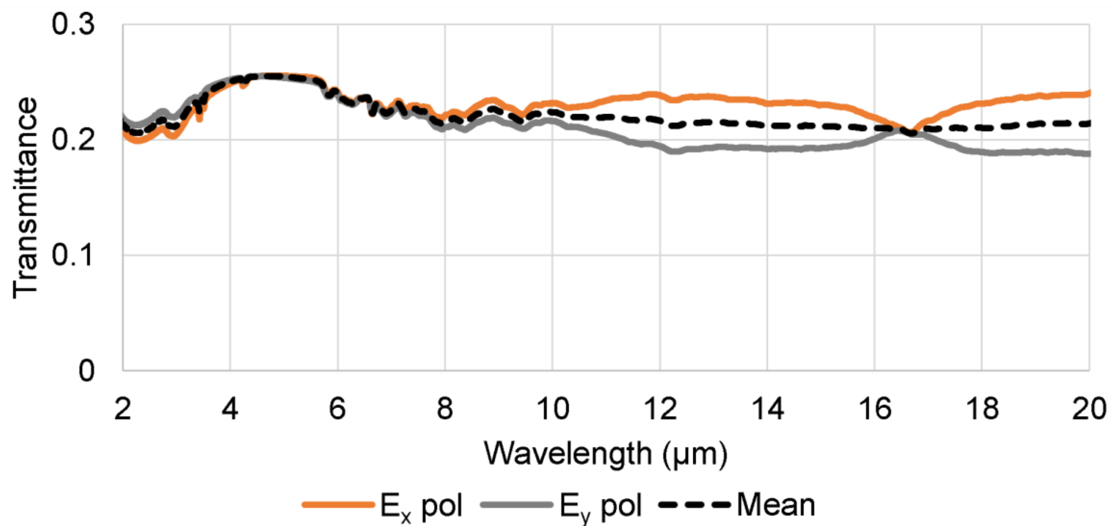

Figure 105: Transmittance of linear polariser used, orientations corresponding to those used for the array measurements

For comparative purposes, spectra for the measurements shown in Figure 103 and Figure 104 are also shown here in Figure 106 and Figure 107 respectively, but this time with all measurements normalised to the 1 mm BaF_2 substrate alone.

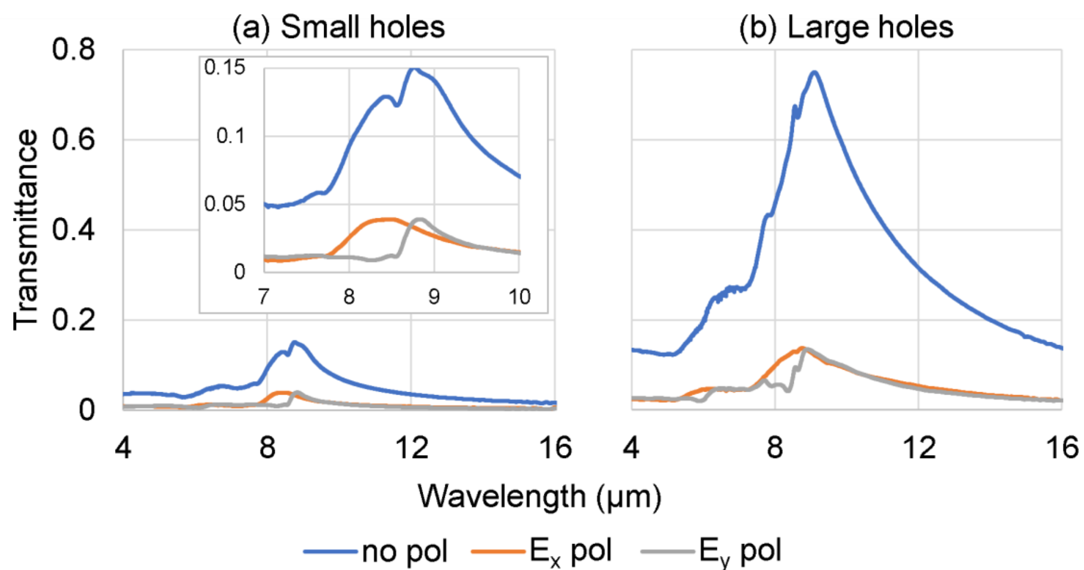

Figure 106: FTIR spectra of hexagonal arrays, all measurements normalised to the substrate alone

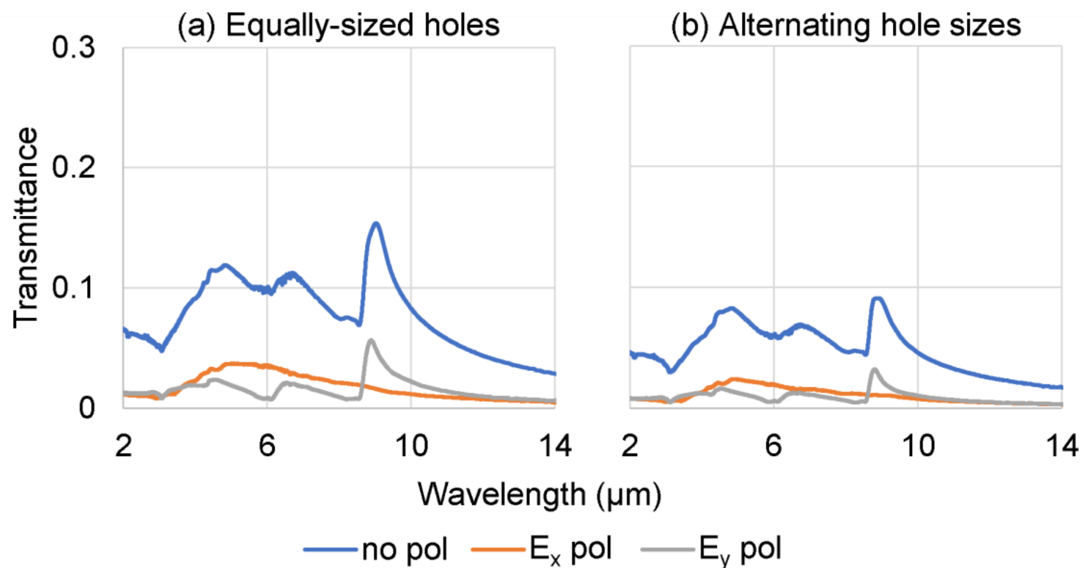

Figure 107: FTIR spectra of rectangular arrays, all measurements normalised to the substrate alone

6.2. Phase-Change EOT Devices

6.2.1. PCM Optical Data Obtained Through Ellipsometry

In order to properly design and optimise EOT-PCM based tunable filters, and to understand and analyse their experimental performance, it is important to know the optical properties (*n* and *k*) for the PCM used. To that end, the optical properties of the PCMs used here, GST-225 and GST-326, were obtained via ellipsometry for both the visible-NIR range and the MWIR range.

The vis-NIR measurement samples used 50 nm thick as-deposited layers on oxidised silicon substrates with an 8 nm Si_3N_4 capping layer. A 103 nm layer of Si_3N_4 was also deposited on a separate oxidised silicon substrate, it and a blank substrate provided reference data for measurements of the whole devices.

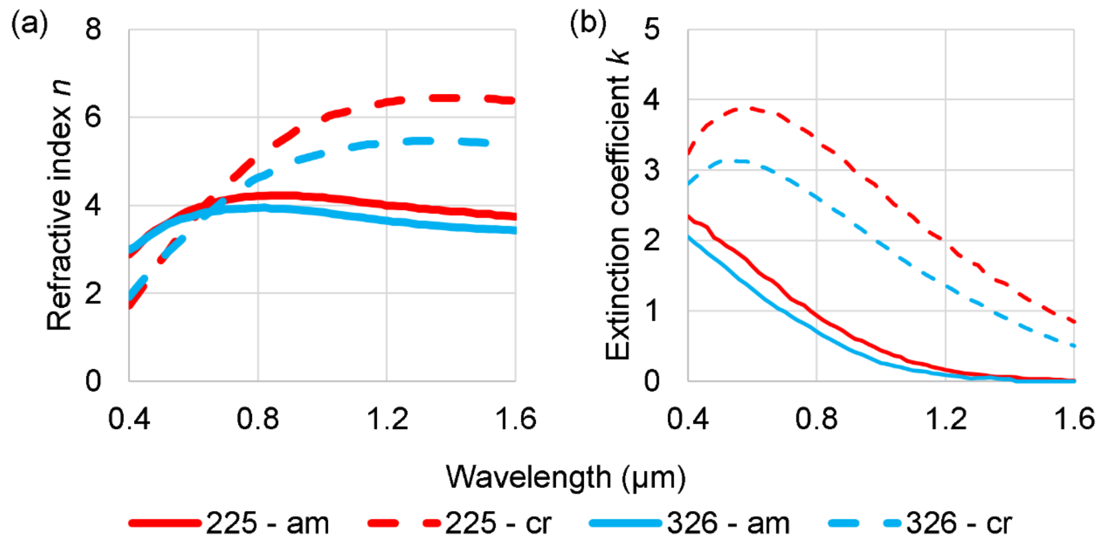

Figure 108: Measured GST PCM (a) n and (b) k in visible-NIR range

Figure 108 shows the resulting *n* and *k* values in the visible-NIR range. It can be seen that the GST-225 films show a slightly larger change in *n* between amorphous and crystalline states than for the GST-326 sample over most of the wavelength range shown here, while GST-326 shows a smaller extinction coefficient in both states. The values shown in Figure 108 are similar, though not identical, to previously published literature values (see example in Figure 109).

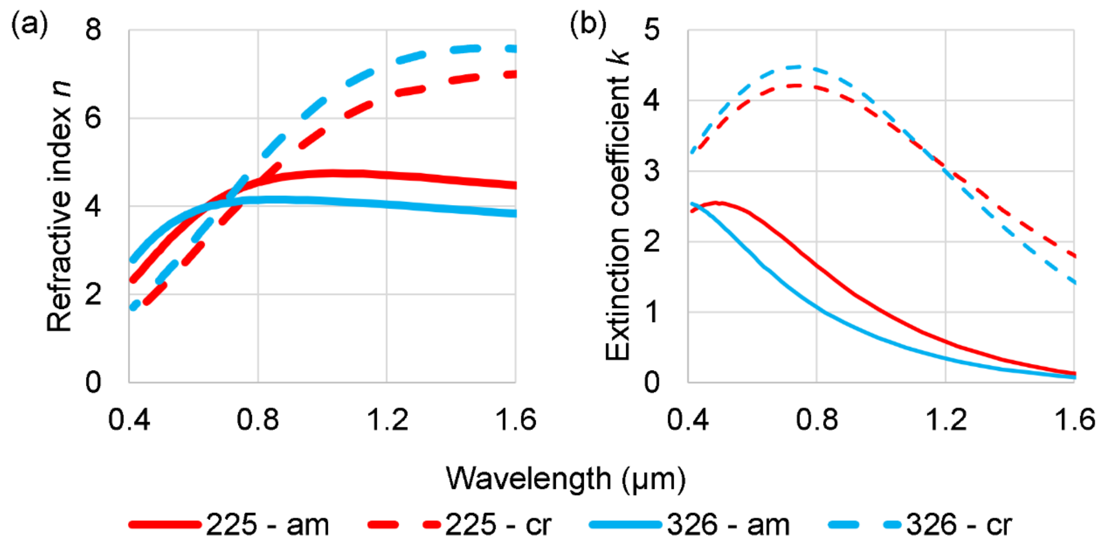

Figure 109: GST PCM (a) n and (b) k in visible-SWIR range, from [72]

As already pointed out in Section 3.3.1, variation in *n* and *k* data obtained by different groups for notionally the same PCM composition is common, due no

doubt to differences in deposition processes and/or slight variations in deposited compositions.

Figure 110 shows the MWIR psi and delta values (obtained as previously mentioned from ellipsometry measurements made by collaborators at UNCC in the USA). As-deposited (amorphous) PCM layer thicknesses were 355 nm for GST-225 and 387 nm for GST-326, deposited on single-surface-polished SiO_2 substrates with an 8 mm capping layer of Si_3N_4 to prevent oxidisation under heating. A 103 nm layer of Si_3N_4 was also deposited onto an oxidised silicon substrate to provide a reference for the barrier layer, with oxidised Si and SiO_2 substrates provided too for the same purpose.

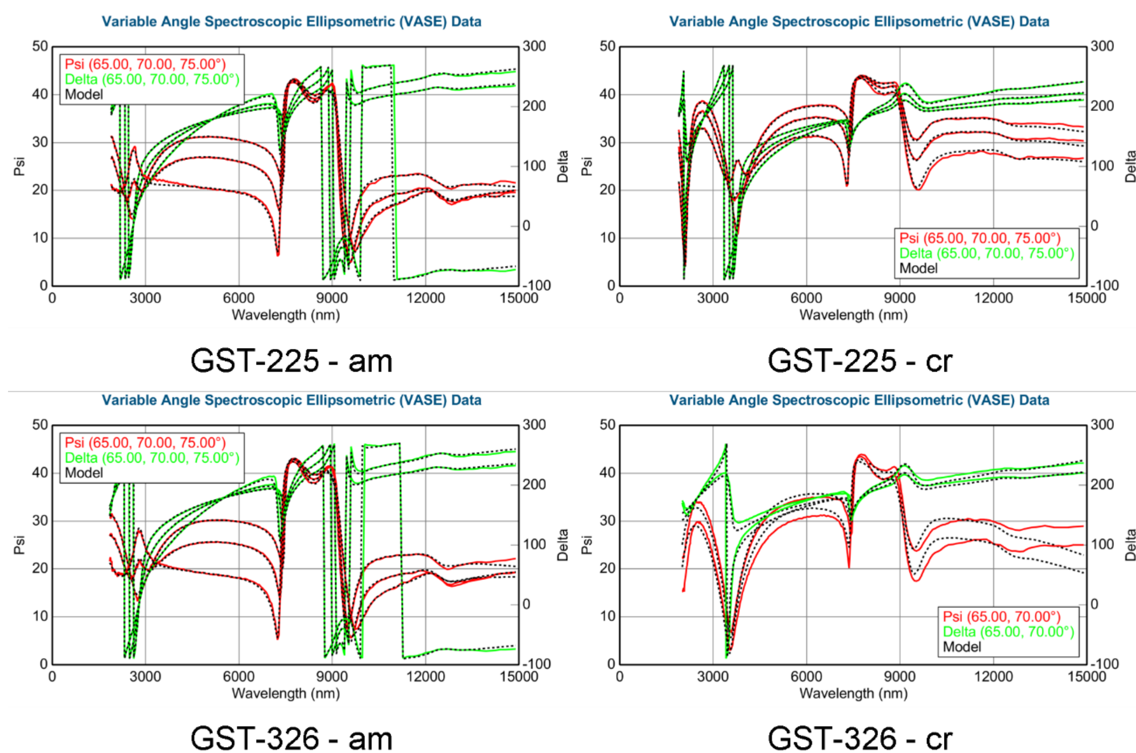

Figure 110: Psi and delta values obtained via mid-long infrared range ellipsometry of PCM samples, with example model fittings overlaid.

The *n* and *k* values derived from model fitting are shown in Figure 111, it is observed that the change in GST-225 refractive index *n* is significantly larger than that of GST-326 across the entire wavelength range, also with smaller extinction coefficient *k* values than for the GST-326 samples.

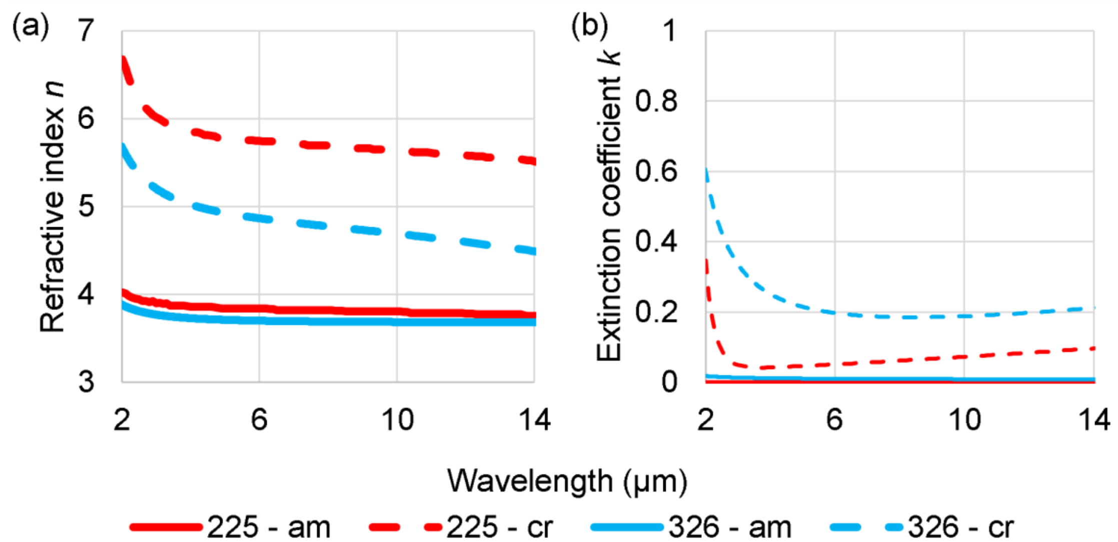

Figure 111: Measured GST PCM (a) n and (b) k in mid-long infrared range

This contrasts with values presented in [72] (shown in Figure 112), where GST-326 was observed to produce a greater change in *n* across the MWIR range with consistently lower *k*.

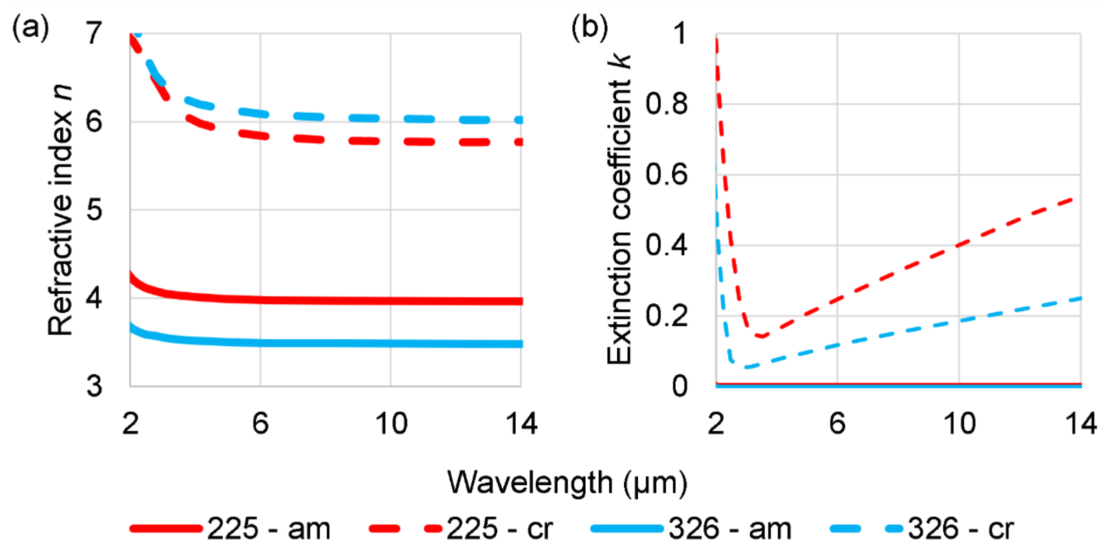

Figure 112: GST PCM (a) n and (b) k in mid-long infrared range, from [55]

As already mentioned, differences in reported *n* and *k* values for notionally identical PCMs most likely arise due to difference in deposition conditions (leading e.g. to different film densities) and/or differences in deposited film compositions. The compositions of films deposited here (and of the sputtering targets), was thus carried out to check for any deviation of composition from the

desired composition. The material compositions were measured via EDS analysis (as seen in **Error! Reference source not found.**) with a few measurements each taken of both the sputtering targets (approximately 5 nm thick) and 100 nm-thick films deposited on oxidised silicon substrates.

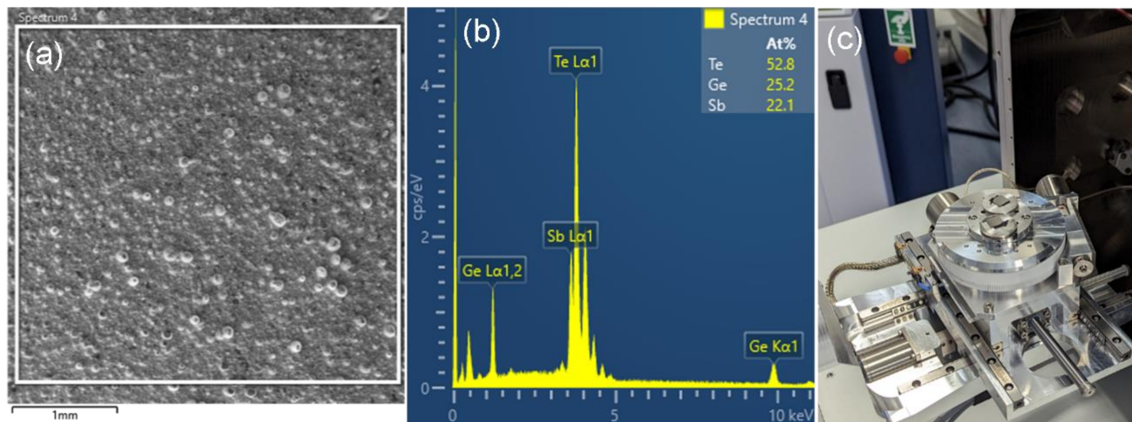

Figure 113: (a) SEM image of GST-225 target area measured via EDS, (b) EDS data plot and (c) samples mounted for EDS measurements in machine.

The visible peaks for the elements that make up GST PCMs are shown in Table 32. The Ge peaks are obviously isolated from any others, and while the Sb and Te peaks are quite close together (170 eV apart) they are still distinct, the 127 eV energy resolution sufficient to separate them.

Table 32: Positions of element emission peak observed for in-house EDS measurements of GST PCM samples [105].

Material	Peak	Peak position (keV)
Germanium	Ge Lα1/2	1.19
	Ge Kα1	9.89
Antimony	Sb Lα1	3.60
Tellurium	Te Lα1	3.77

The expected/desired target and film compositions are shown in Table 33**Error! Reference source not found.**, with the EDS measured values in Table 34**Error! Reference source not found.**.

Table 33: Expected compositions of GST PCMs

Element	Expected composition (%)	
	GST-225	GST-326
Ge	22.2	27.3
Sb	22.2	18.2
Te	55.5	54.6

Table 34: Calculated percentages of GST PCM elements in sputtering targets deposited films. Any elements not featured in the PCM (e.g. from substrate, barrier and capping layers) are not included in the total.

Element	Composition (%)			
	Targets		Deposited film	
	225	326	225	326
Ge	25.3	33.1	23.6	28.8
Sb	22.4	15.7	24.5	21.1
Te	52.3	51.2	51.9	50.0

The GST-225 target shows a very close match to the expected values, with the maximum variation being just over 2 atomic %, and probably within the uncertainty of the EDS measurement itself. The variation in quantities of elements between the measured and expected values for GST-326 target was larger, up to 5-6 atomic %.

n.b. Measured compositions are given to accuracy of 0.1 %, as displayed by software as shown in Figure 113 ***Error! Reference source not found.*** *(b).*

A similar story is seen with the deposited films, very similar quantities of Ge and Sb for GST-225 and relative quantities also very close to that expected. The relative quantities of Ge and Sb for the GST-326 sample are different however, with proportions very close to 3 and 2 parts respectively rather than 2 and 1, so that the film composition more closely resembles GST-325 than GST-326, Even taking into account the uncertainty of the EDS measurements (typically around 2 %), it would seem that our GST-326 samples do not in fact have exactly that

composition, and this could explain the differences seen in our *n* and *k* data for GST-326 as opposed to published values. Several factors could explain the differences, from target degradation and oxidisation (although all sputtering runs involve cleaning the target for a few minutes before depositions) and the possibility of the different elements in the target being deposited at different rates.

6.2.2. Mid/Long-IR Tuneable Filters

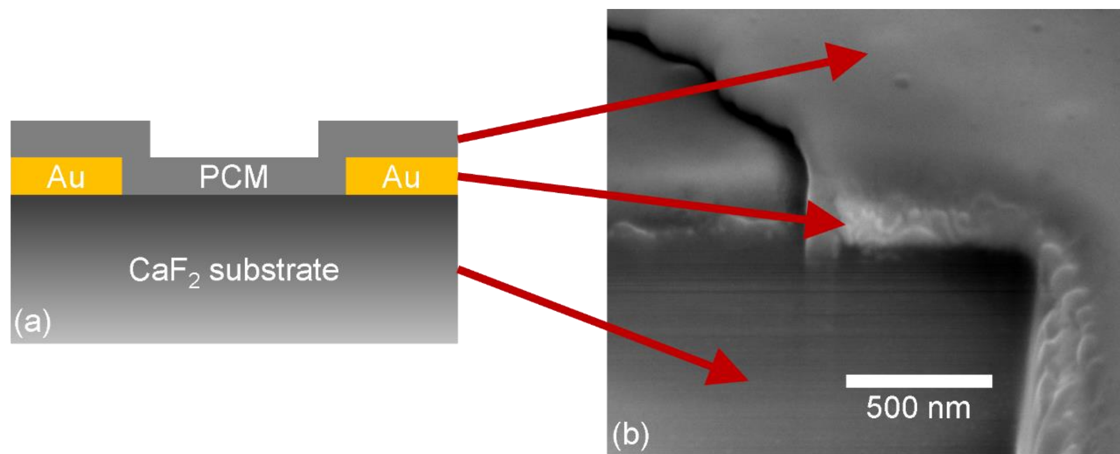

Figure 114: Schematic cross-section of a phase-change EOT device, showing (a) a schematic of how the PCM layer covers the metal film and fills the array holes and (b) a cross-section SEM image of a fabricated device, trench etched out with focused ion beam milling.

The basic structure used to realise EOT-based tuneable bandpass optical filters is shown in Figure 114. To prevent inter-diffusion of GST and gold, devices with an 8 nm Si_3N_4 barrier between the gold and PCM layer were also fabricated. All devices were also capped with 8 nm Si_3N_4 layers to prevent degradation upon heating (Si_3N_4 layers not shown in Figure 114).

The as-deposited PCM layers were always in the amorphous phase. Crystallisation, to induce shifting of the optical transmission peak, was achieved by heating devices on a hotplate for a range of temperatures and times.

Exemplar results are given in Figure 115, where measured and simulated transmission spectra for two devices having EOT arrays with 4 µm pitches and different PCM types (GST-225 and GST-326) are shown. The devices were

fabricated using e-beam lithography and wet-etching, and PCM layers crystallised by heating on hot plates until no further wavelength shift of the peak was observed. Plots are normalised to the peak transmittance in the amorphous state, to give better comparisons of the changes in transmittance between the difference devices and types of runs.

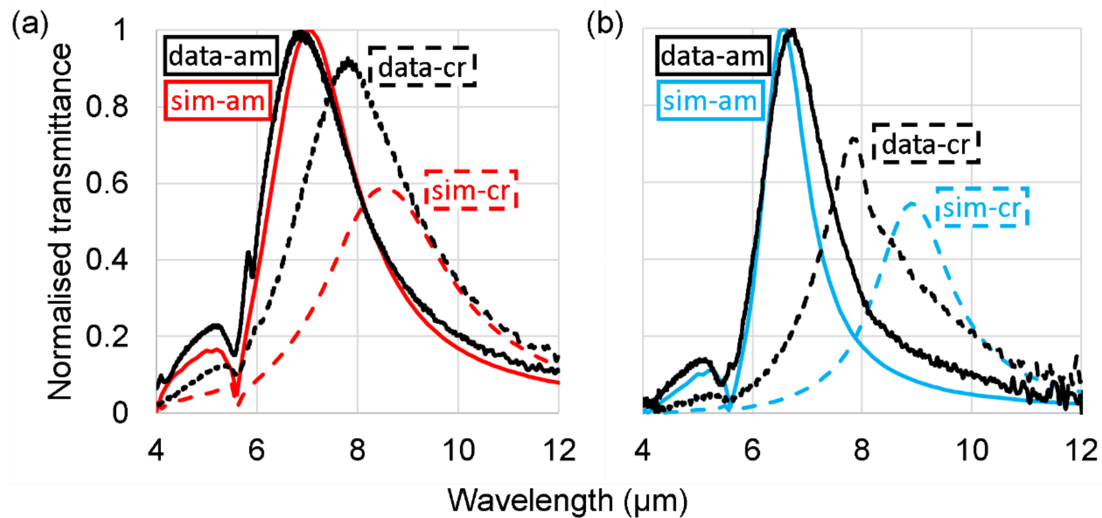

Figure 115: Transmission spectra of measurements vs simulations (using optical data from [55]*) of wet-etched phase-change EOT devices in 40 nm Au films on* CaF_2*, with (a) 70 nm GST-225 (crystallised by heating for 3 minutes on 150°C hotplate, using 1 minute intervals) and (b) 100 nm GST-326 (crystallised by heating for 5 minutes on 300°C hotplate, shortest time tested and no change observed after further heating)*

The simulated results shown in Figure 115 use published *n* and *k* values taken from Michel et al. [55] (see Figure 112). Good agreement between simulation and experiment is seen with the GST (both 225 and 326) in the amorphous state, but the simulated results show a larger than experimentally observed transmission peak shift upon crystallisation, in addition to a greater drop in absolute transmittance.

Figure 116 shows the same experimental results as Figure 115, but with the simulations using the experimentally obtained *n* and *k* data for both GST-225 and GST-326. Better agreement between experiment and simulation is now apparent, in particular in relation to the absolute transmittance value for the crystalline case, but also in the wavelength shift (though for the GST-225 case

the simulated data still overestimates the amount of shift obtained). Note that the narrower peaks (thus smaller peak transmittances and higher Q-factors) of the GST-326 devices is a result of them having a smaller fill-factors of 0.48 rather than the 0.64 of the GST-225 device.

Key performance metrics (transmittance, Q-factor, peak-shift etc.) for the results shown in Figure 115 and Figure 116 are given in Tables 24, 25, 26 and 27.

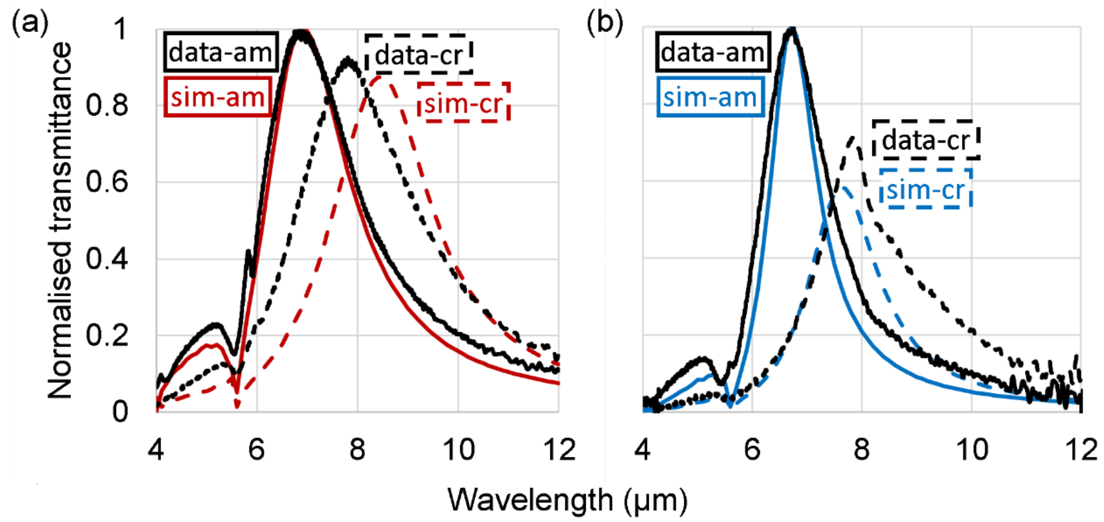

Figure 116: Transmission spectra of measurements vs simulations (using optical data obtained by ellipsometry) of wet-etched phase-change EOT devices in 40 nm Au films on CaF_2, with (a) 70 nm GST-225 and (b) 100 nm GST-326

Table 35: Performance metrics of wet-etched phase-change EOT device with 70 nm GST-225 layer shown in Figure 115 and Figure 116

Plot	Peak T	Peak WL (μm)	Peak width (μm)	Q-factor
measured – am	**0.92**	**6.90**	**2.19**	**3.15**
measured – cr	0.85	7.81	2.80	2.78
source data – am	**0.89**	**7.00**	**2.06**	**3.40**
source data – cr	0.52	8.50	2.99	2.84
own data – am	**0.89**	**6.90**	**1.99**	**3.46**
own data – cr	0.78	8.50	2.42	3.52

Table 36: Peak shift properties of wet-etched phase-change EOT device with 70 nm GST-225 layer shown in Figure 115 and Figure 116

Plot	Shift (μm)	Shift factor	T reduction (%)
measured	0.91	1.13	7.61
source data	1.50	1.21	41.57
own data	1.60	1.23	12.36

Table 37: Performance metrics of wet-etched phase-change EOT device with 100 nm GST-326 layer shown in Figure 115 and Figure 116

Plot	Peak T	Peak WL (μm)	Peak width (μm)	Q-factor
measured – am	**0.55**	**6.74**	**1.44**	**4.67**
measured – cr	0.39	7.83	1.80	4.35
source data - am	**0.74**	**6.60**	**1.01**	**6.53**
source data – cr	0.40	8.90	1.72	5.17
own data – am	**0.73**	**6.70**	**1.06**	**6.30**
own data – cr	0.43	7.60	1.56	4.88

Table 38: Peak shift properties of wet-etched phase-change EOT device with 100 nm GST-326 layer shown in Figure 115 and Figure 116

Plot	Shift (μm)	Shift factor	T reduction (%)
measured	1.09	1.25	29.09
source data	2.30	1.70	45.95
own data	0.90	1.47	41.10

6.2.3. Visible-NIR Tuneable Filters

For the realisation of visible-NIR tuneable filters, thin layers of GST-225 were deposited onto the silicon based and calcium fluoride-based disc arrays (of the type shown previously in Figure 91). An 8 nm thick S_3iN_4 barrier layer to prevent inter-diffusion between GST layer and the metal disc array was also deposited (the issue of inter-diffusion is discussed in detail in Section 6.3). The resulting experimental reflectance spectra, shown in Figure 117 (a), indicate that the peak

position is effectively shifted by the application of a 15 nm later of amorphous GST-225, but (unlike the simulations in Section 5.4.3) there is little change in wavelength upon PCM crystallisation (for 1 hour on a 300°C hotplate) and peak definition is largely lost. Similar effects were observed with the device made for working in transmission (Figure 117 (b)). The reasons for the lack of shift of the transmission peak and the general loss of optical performance upon crystallisation of the GST layer are not clear, and further work in this would be needed to ascertain such reasons.

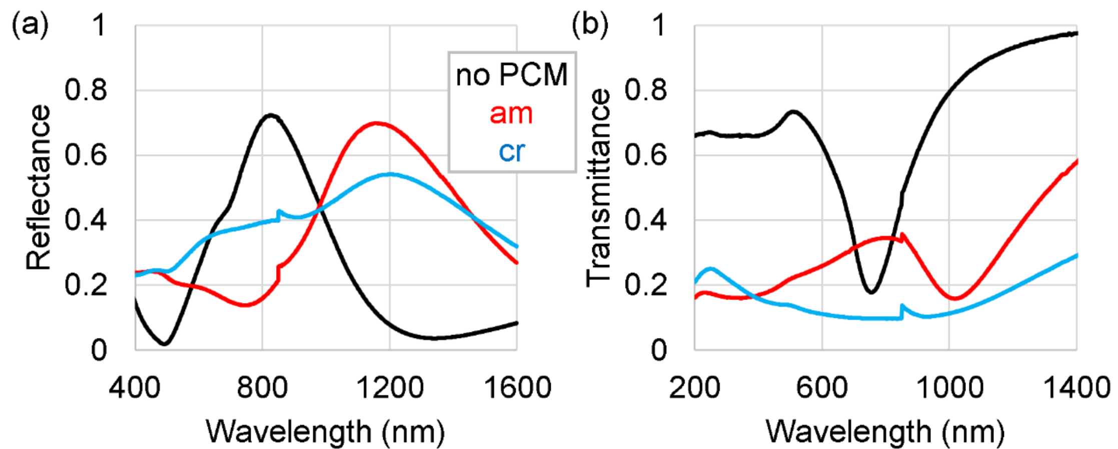

Figure 117: Exemplar reflection and transmission spectra for 'inverse-design' visible-NIR disc arrays with 15 nm of GST-225 PCM and 8 nm barrier and capping layers. (a) Reflectance spectra of a 400 nm pitch disc array with d=0.5p on oxidised silicon and (b) transmittance spectra of 350 nm pitch disc array with d=0.25p on calcium fluoride

6.2.4. Laser-Processed Devices

An example of the measured transmission spectrum of an EOT array made via layer ablation and then coated with 100 nm layer of GST-326 is shown in Figure 118, where it is also compared to simulations made assuming a "perfect" hole array with equivalent 3.95 μm pitch and fill factor of 0.61 (measured by AFM). Crystallisation was done by heating the device for 2 minutes on a 300°C hotplate.

The differences in experimental and simulated peak transmittance values (shown in Table 39 and Table 40) can likely be at least partly attributed to the stitching errors present at the time using this fabrication method. It can also be seen in

Figure 118 that (in contrast to the wet-etched devices) a larger shift in peak position is measured than was simulated. Interestingly, there is evidence of secondary peak in the measured spectrum, that does coincide in position more closely with the simulated results. It is possible, therefore, that there are variations in the regularity of the laser-written hole pattern, and this in turn leads to differences between simulated and measured spectra.

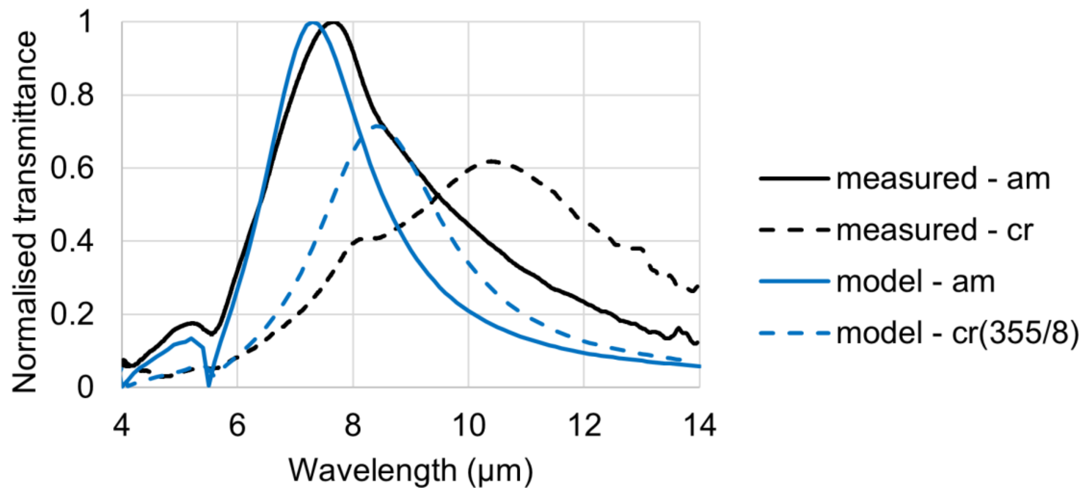

Figure 118: Measured and simulated transmission spectra (simulated using optical data obtained by ellipsometry) of laser-ablated phase-change EOT device in 40 nm Au film on CaF_2, with 100 nm GST-326 layer, simulated fill factor of 0.61

Table 39: Key performance metrics of laser-ablated phase-change EOT device with 100 nm GST-326 layer, extracted from Figure 118

Plot	Peak T	Peak WL (μm)	Peak width (μm)	Q-factor
measured – am	**0.60**	**7.66**	**3.24**	**2.36**
measured – cr	0.37	10.40	5.66	1.84
model – am	**0.88**	**7.70**	**3.25**	**2.37**
model – cr	0.68	8.90	3.74	2.38

Table 40: Peak shift properties of laser-ablated phase-change EOT device with 100 nm GST-326 layer, extracted from Figure 118

Plot	Shift (μm)	Shift factor	T reduction (%)
measured	2.73	1.36	38.2
own data	1.20	1.16	23.2

6.3. Investigation of Au/PCM Diffusion Effects

6.3.1. Investigation of Diffusion in Phase-Change EOT Devices

A persistent issue with combining phase-change materials and EOT arrays is that commonly used plasmonic metals can readily diffuse into PCMs upon heating [106]. In practice, this means that an EOT array in a gold film will continue showing a well-defined transmission peak when a layer of GST-225 has been initially applied (assuming deposited at non-elevated temperatures), unless mitigation processes (e.g. the application of a barrier layer) are applied the spectral features (peaks) degrade as the sample is heated to crystallised it. This is most likely due, as reported in [106], to inter-diffusion of the Au and GST layers and the formation of gold-tellurides.

A typical example of the degradation induced by such diffusion in EOT filter devices is shown in Figure 119: they were heated for 1-minute intervals with temperatures increased if no change was observed, total of 4 mins at 150°C, 2 mins at 175°C, 3 mins at 200°C and 5 mins at 225°C. The start and end results are shown in Figure 119**,** with such degradation being irreversible. Evidence of gold diffusion can be seen in the optical microscope images shown in Figure 120, the annealed version of the sample having a definite gold colour.

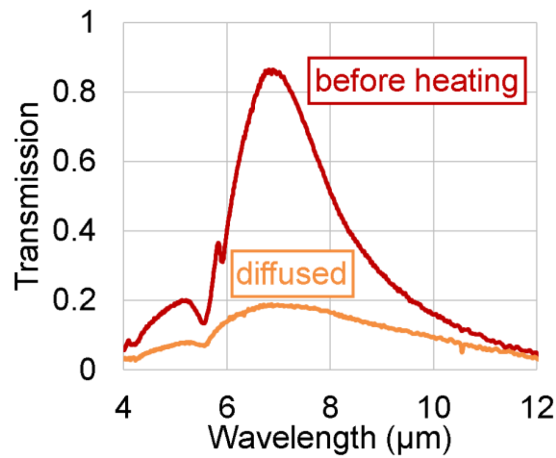

Figure 119: Transmission spectrum of 4 um-pitch EOT array in 3/40 nm Cr/Au film with a 70 nm GST-225 layer. There was no barrier layer between the gold and the GST (though there was an 8 nm Si_3N_4 capping layer). The transmission peak almost completely degraded upon heating.

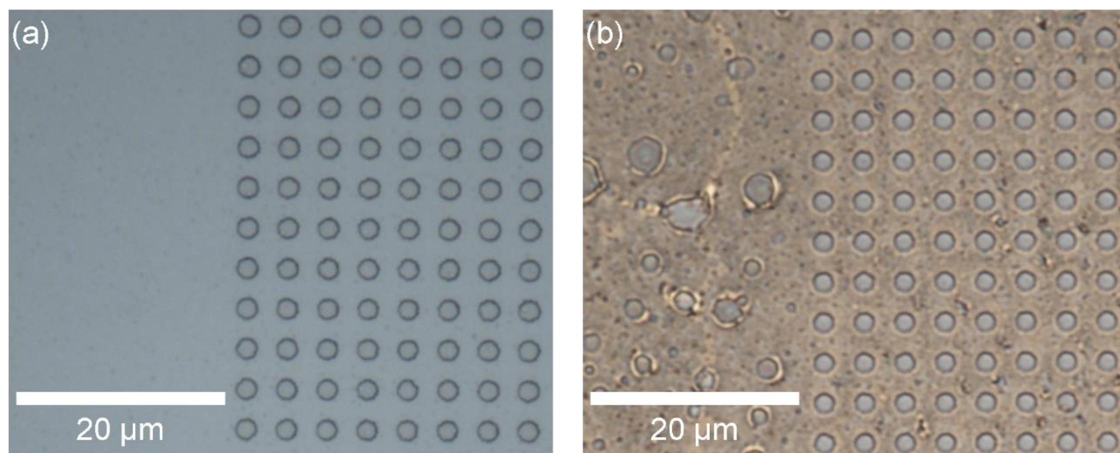

Figure 120: Optical microscope images of phase-change EOT arrays (a) before and (b) after heating, showing evidence of gold diffusion

The use of alternative, less diffusion-prone, materials for the EOT film is one possible approach to alleviate the above described diffusion issues (e.g. titanium nitride having been demonstrated to work in plasmonic devices [107], [108]). However, a simpler solution is to instead implement the use of a barrier layer between the metal and PCM layers.

A thin layer of silicon nitride (Si_3N_4, the same material used here for capping PCM layers to prevent oxidisation) is known to provide useful barrier properties [106], the use of an 8 nm S_3iN_4 layer in the EOT devices of this thesis was explored. It

is not expected this layer would have any detrimental effects on the transmission spectrum of the basic EOT array. This was confirmed by measuring the spectrum of a gold EOT array both before and after the barrier layer deposition, as shown in Figure 121.

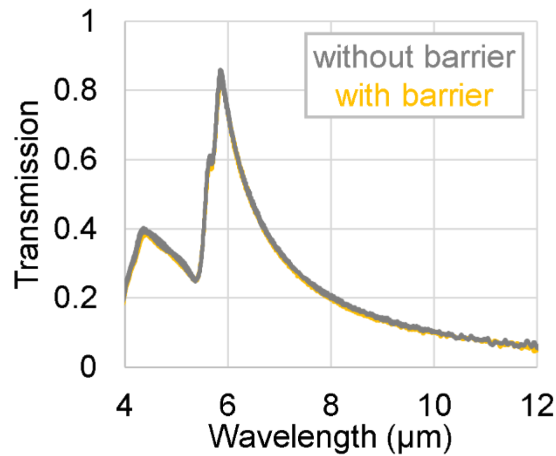

Figure 121: Transmission spectra of 4 um-pitch EOT device in 5/90 nm Cr/Au film on CaF_2 substrate both before (grey line) and after (yellow) line the deposition of an 8 nm Si_3N_4 layer on top of the gold layer.

In practice, the barrier layers were added during the same PVD session as the PCM and capping layers were deposited, maximising cleanliness (no chance for contaminants to be introduced between layers) and reducing fabrication time: film thicknesses were measured by fabrication of separate test samples (PMMA dots on blank silicon substrates) to also reduce the risk of contaminating the EOT devices. These factors make determining the individual layer thicknesses difficult (can only measure total thickness with an AFM or profiler), necessitating accurate calibration runs of the individual material and careful monitoring of the run parameters during deposition sessions.

6.3.2. TEM imaging of Diffusing Layers in Reflection Cavities

To explore the issue of inter-diffusion of gold and PCMs in more detail, samples for cross-sectional analysis by TEM were also fabricated. These were not EOT devices, but simple reflection cavities that were easy to fabricate (requiring no lithographic patterning) while at the same time having specific optical resonances that might be expected to be adversely affected by gold-PCM inter-diffusion.

n.b. All TEM imaging and analysis was carried out by Dr. Geoff West at the Warwick Manufacturing Group in the University of Warwick.

Specifically, the devices prepared for TEM imaging were unpatterned films on oxidised silicon substrates, a 3/40 nm Cr/Au metal film deposited via thermal evaporation and layers of GST-225 and 8 nm silicon nitride via physical vapour deposition. The starting thickness of GST-225 used was 20 nm, in the region of what would be suitable for devices working in the UV-NIR regime (see sections above regarding disc arrays).

After deposition, some of the samples were heated on a 300°C hotplate for 1 hour, after which they looked vastly different to the naked eye (between with barrier/no barrier), similar to Figure 120. TEM cross-sectional imaging was carried out on samples before and after heating, and revealed stark differences, as shown in Figure 122. The sample without the S_3iN_4 barrier layer has no perceptible separation between the regions that were originally gold and GST-225, the former having been completely assimilated into the latter. The sample with the barrier layer, on the other hand, does show a clear distinction between the two regions, separated by the barrier layer.

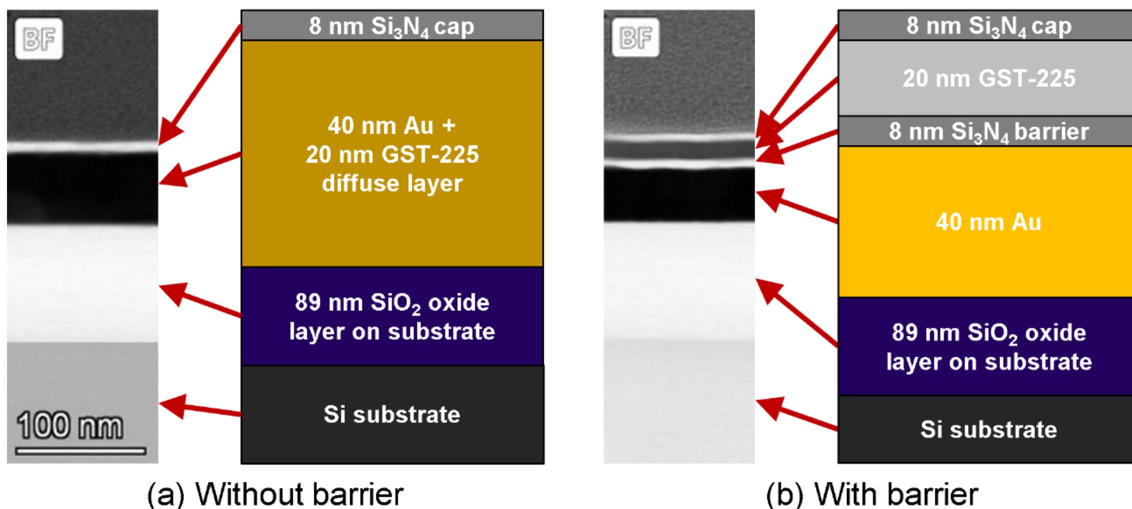

Figure 122: Cross-section TEM images of diffusion test samples using 20 nm GST-225 PCM both (a) without and (b) with S_3iN_4 barrier layers, alongside schematic diagrams illustrating the layer structure

This analysis is supported by energy-dispersive x-ray spectroscopy (EDS) chemical linescan measurements, Figure 123 showing the combined EDS maps of the cavities with 20 nm GST layers, with the position of the EDS linescans in the slice superimposed.

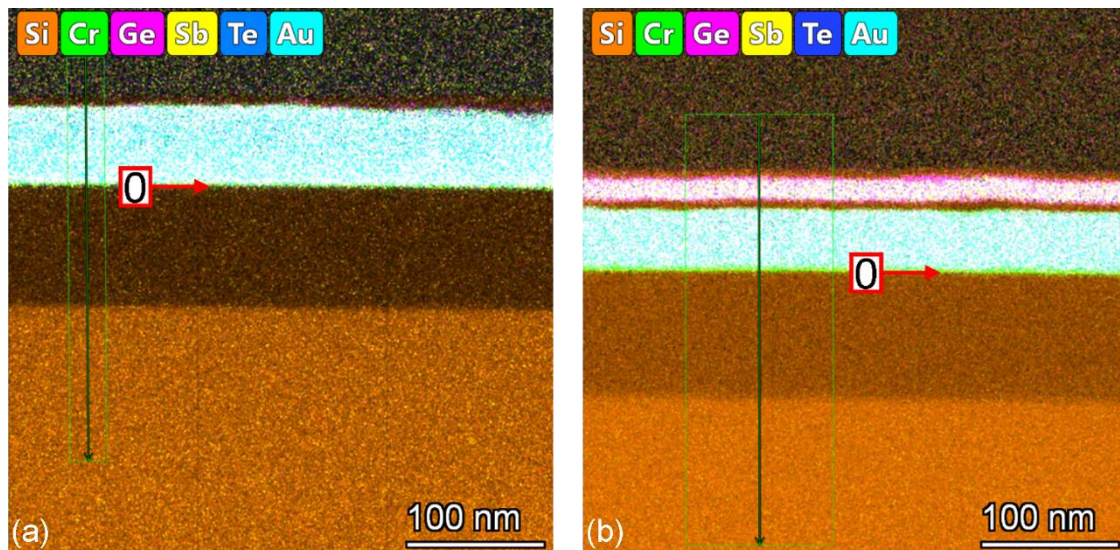

Figure 123: EDS maps of 20 nm-thick GST diffusion test samples, with (a) no barrier layer and (b) 8 nm Si_3N_4 barrier, with position "zero" points (where the deposited layers meet the substrate) indicated

The EDS linescan plots (showing elemental composition against position in slice) are shown in Figure 124 and Figure 125, respectively without and with the barrier layers. As indicated by Figure 122**,** the sample without the barrier layer (in Figure 124) shows that there is significant overlap of the gold/chromium layer with the components of the GST layer, the tellurium component in particular showing strong affinity for assimilation.

Figure 125 shows the linescans for the sample with a barrier layer, confirming that the presence of said barrier layer keeps the materials concerned isolated in their respective layers.

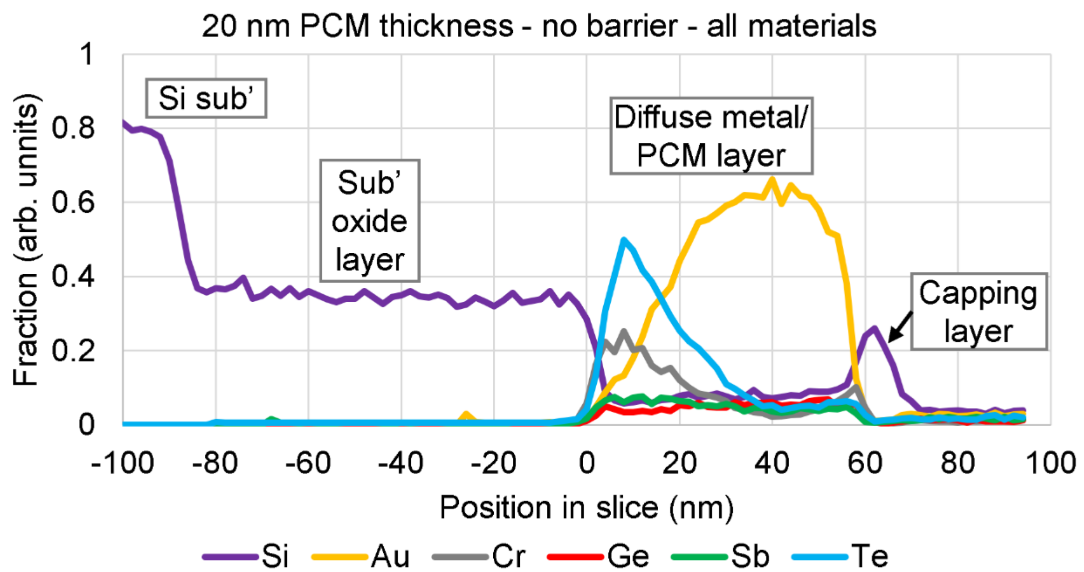

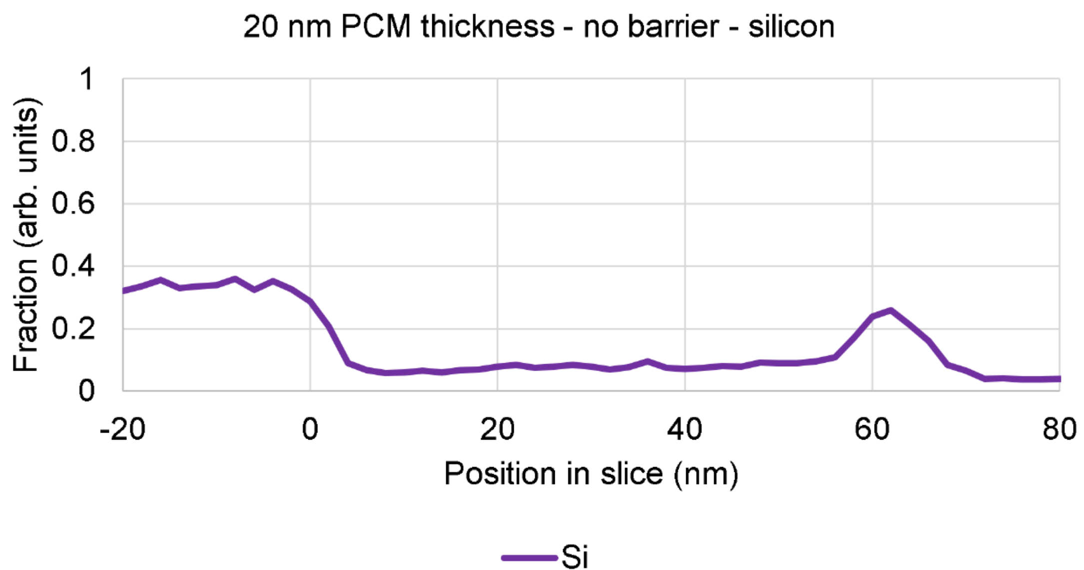

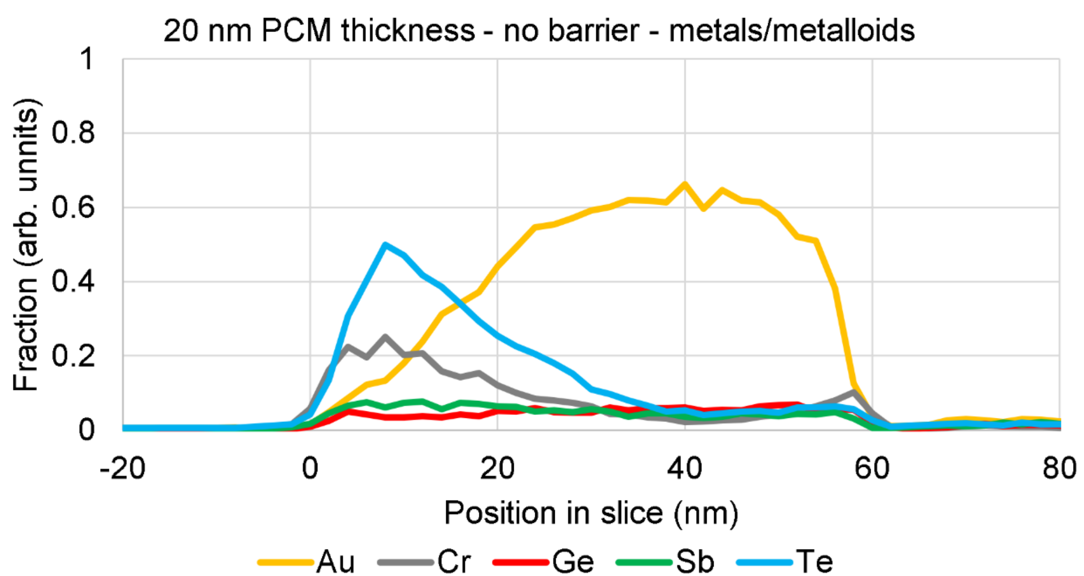

Figure 124: EDS scans of 20 nm PCM diffusion sample without a barrier layer

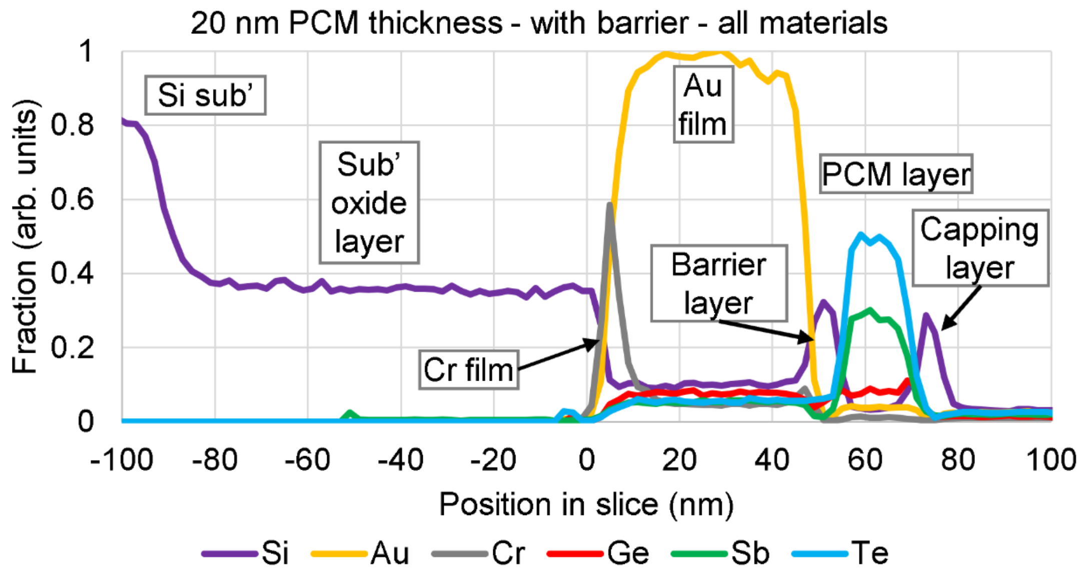

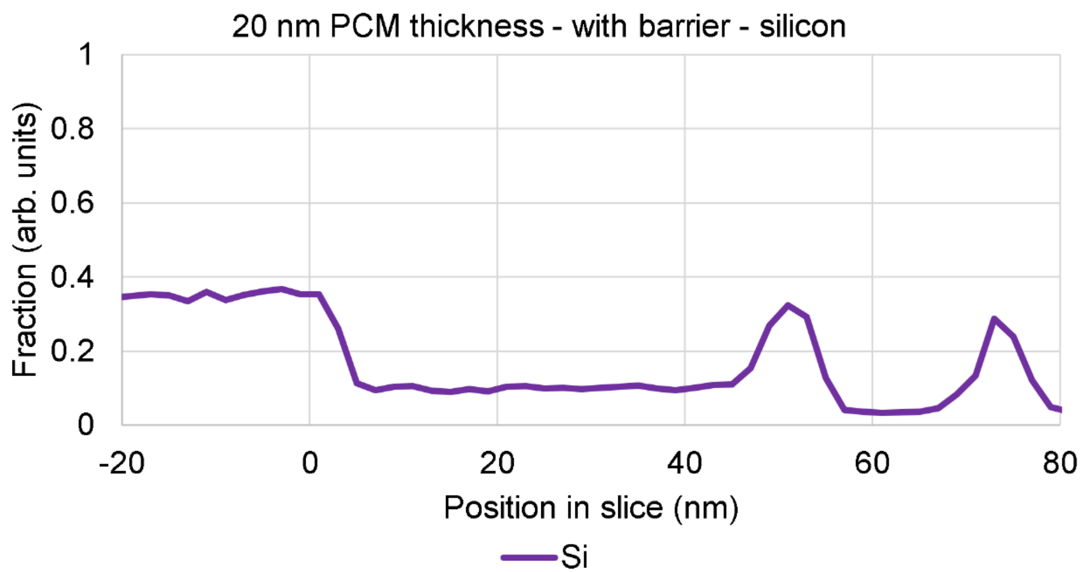

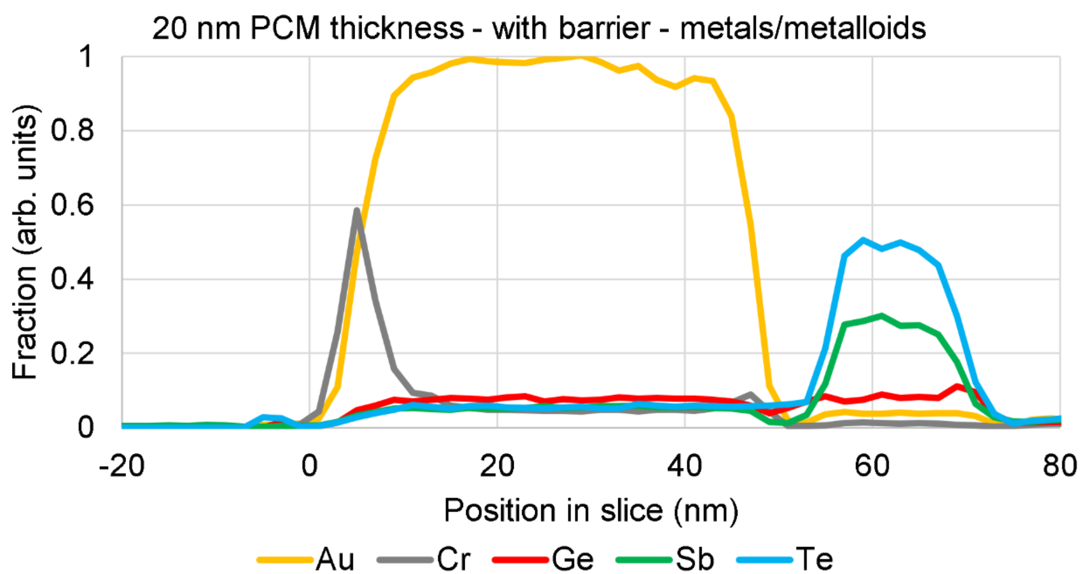

Figure 125: EDS scans of 20 nm PCM diffusion sample with a barrier layer

It was also desired to investigate whether diffusion would persist as a problem when the film thickness was substantially increased. Test samples were therefore made with identical specifications as previously, but for a 220 nm GST-225 layer in lieu of 20 nm. Cross-section TEM imaging as shown in Figure 126 shows that the metal and PCM layers remain visually distinct after heating (again at 300°C for 1 hour), even without the barriers. A thin layer is, however, visible between the metal and GST film, indicating that diffusion is still occurring but with proportionally limited penetration into this much thicker PCM layer.

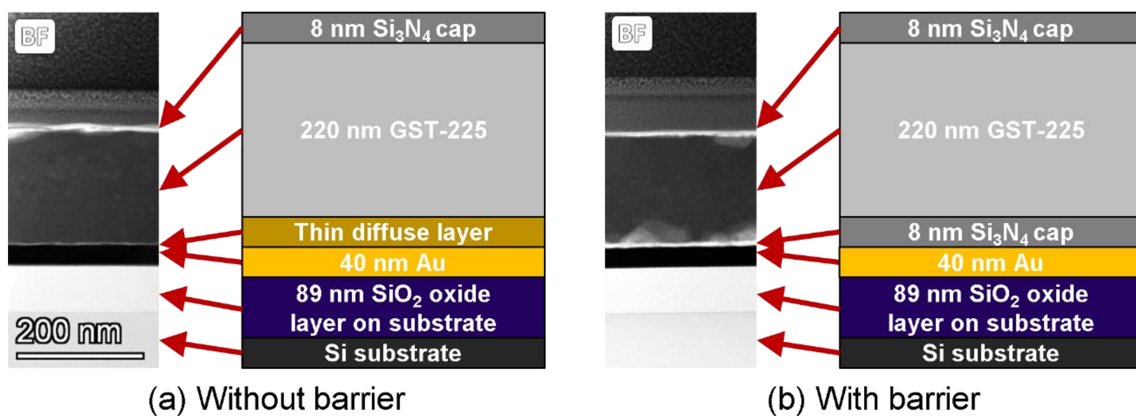

Figure 126: Cross-sectional TEM images of diffusion test samples using 220 nm GST-225 PCM both (a) without and (b) with barrier layers, alongside schematic diagrams illustrating layer composition

Figure 127 shows the combined EDS maps of the thicker-PCM samples, with the different elements coloured-in and the profile of the EDS linescans indicated.

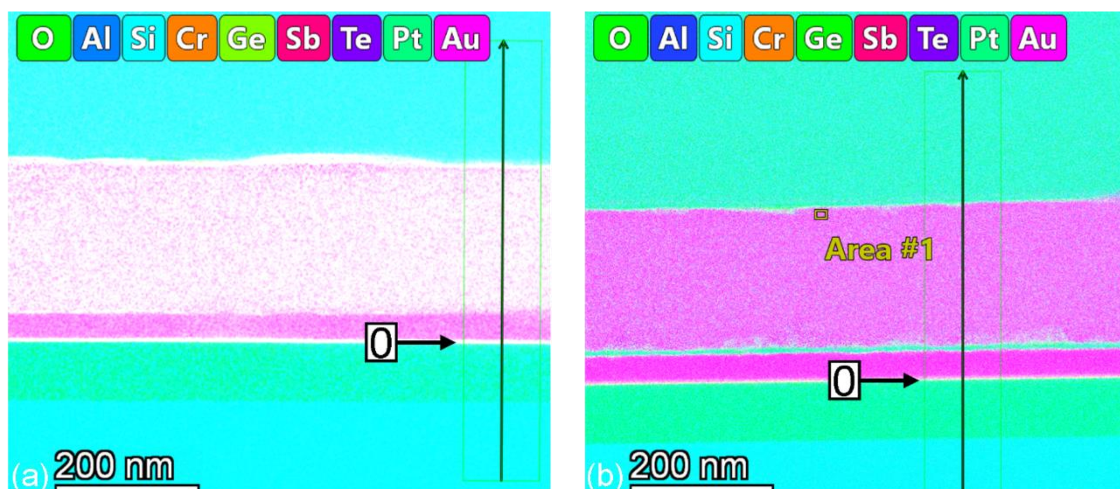

Figure 127: EDS maps of 220 nm-thick PCM diffusion test samples, with (a) no barrier layer and (b) 8 nm Si_3N_4 barrier, with position "zero" points (where the deposited layers meet the substrate) indicated

Figure 128 and Figure 129 plot the EDS results for the samples without and with a barrier respectively. When without, there is overlap between regions where gold and GST components are detected, indicating mixing in the same manner as shown for the 20 nm thickness samples seen in Figure 124, with gold being detected in significant concentration well beyond 20 nm past the metal/PCM interface. As shown in Figure 125, elements of the barrier layer show up as sharp spikes separating the film and PCM elements.

More elements are shown in the 220 nm PCM devices, these include:

- Nitrogen, from the Si_3N_4 barrier and capping layers
- Aluminium, likely background from the instrument chamber
- Platinum, from the conductive coating applied for FIB milling
- Oxygen, in the oxide layer of the Si substrates but also apparently in the Si_3N_4 barrier/capping layers, possibly a result of cross-contamination

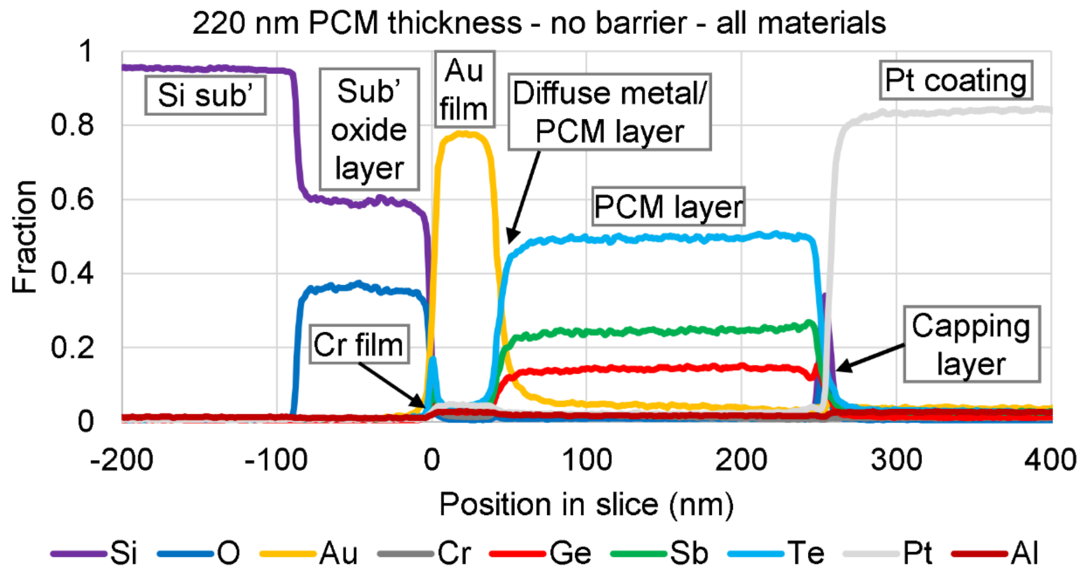

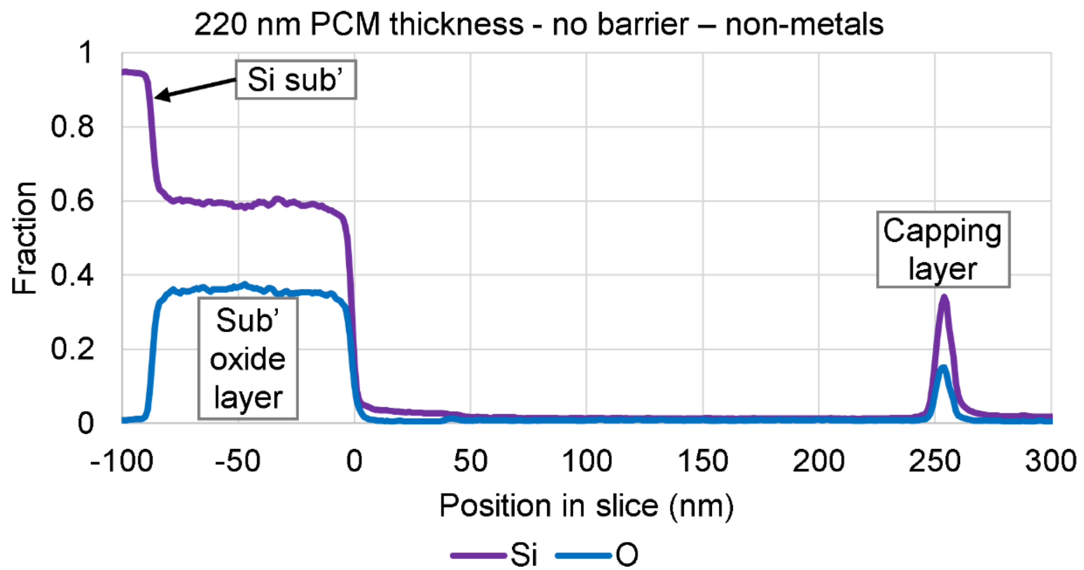

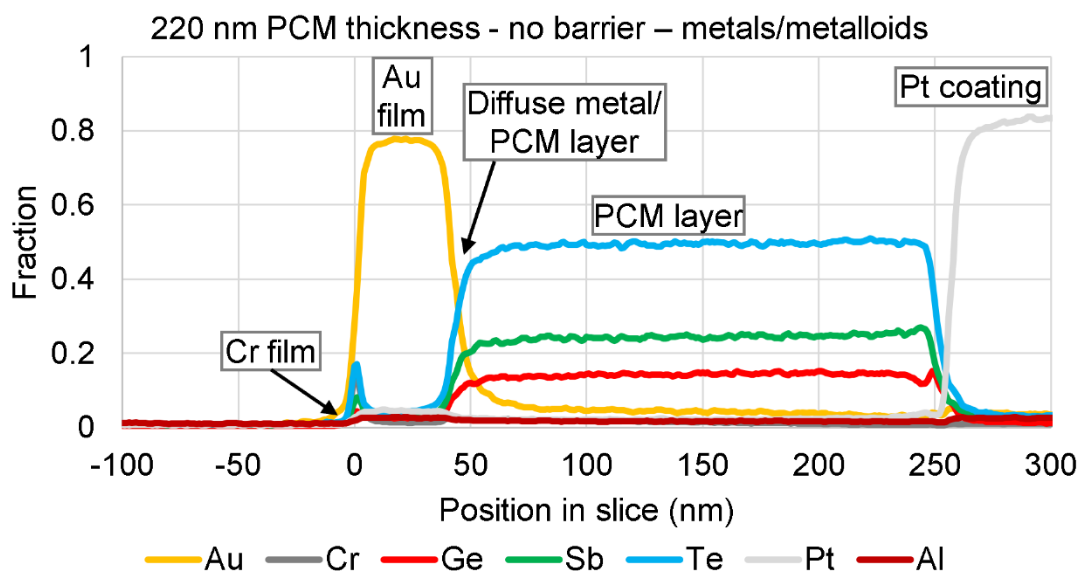

Figure 128: EDS scans of 220 nm PCM diffusion sample without a barrier layer

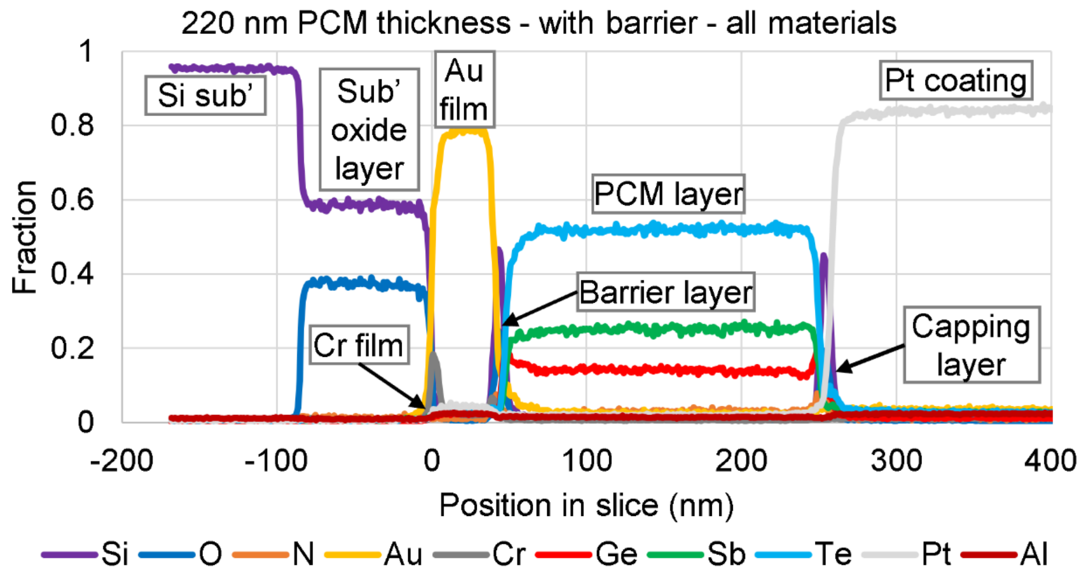

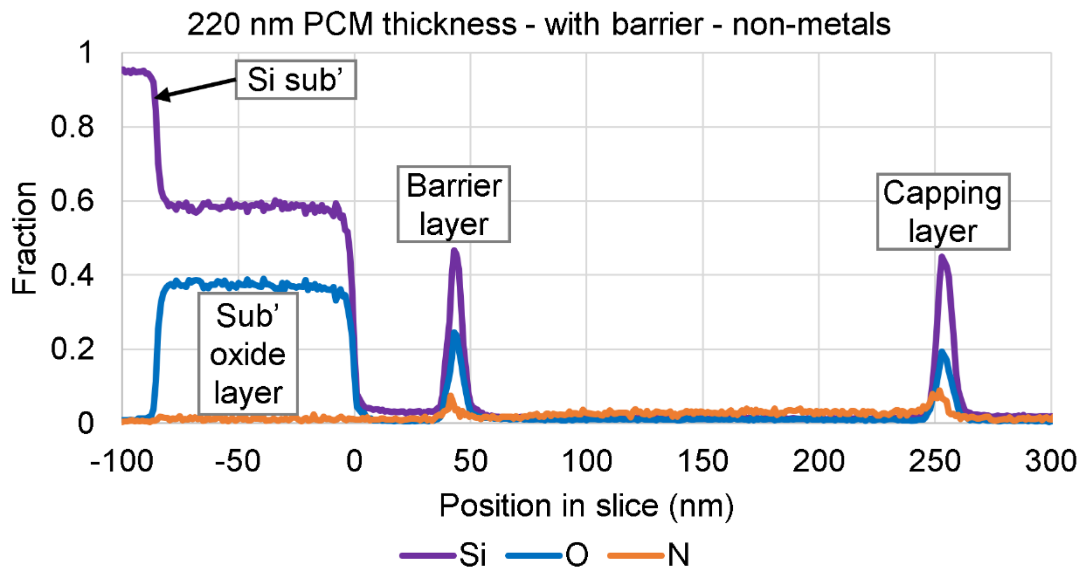

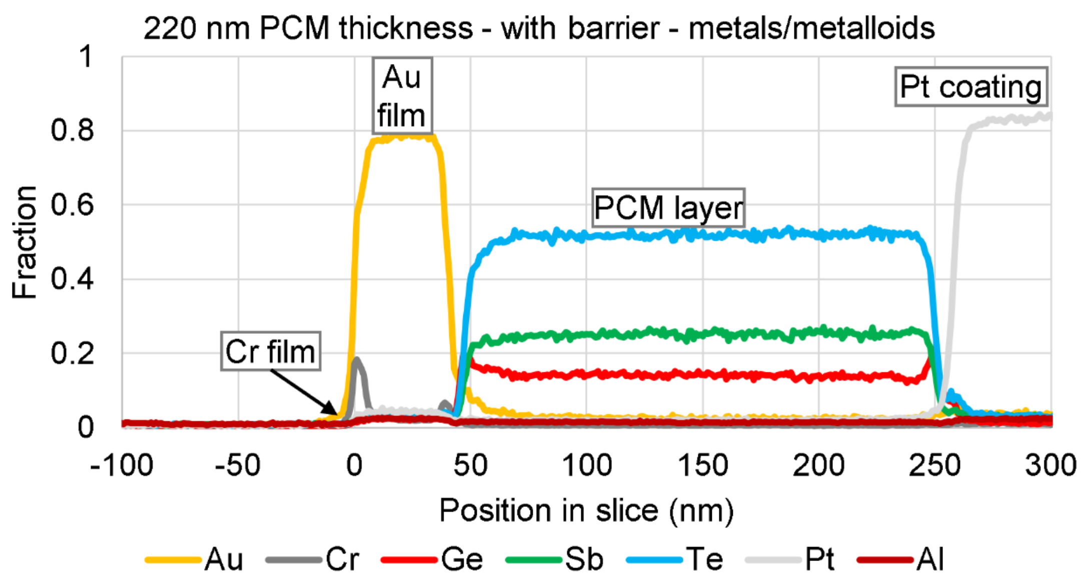

Figure 129: EDS scans of 220 nm PCM diffusion sample with a barrier layer

6.3.3. Optical Response of Reflection Cavities

The same devices prepared for the TEM analysis also served as reflection cavities for optical measurements, the positions of dips in the reflectance spectra dependant of the PCM refractive index and layer thickness of material on top of the metal film. Calculations and COMSOL simulations were used to determine the suitable PCM thicknesses to enable spectral measurements within the capabilities of the available optical test equipment, with a 20 nm GST-225 layer providing resonance features (in both the amorphous and crystalline states) within the 200-1600 nm wavelength range of the JASCO MSV-5300 and the 220 nm PCM layer samples within the range of the Bruker Vertex 80v FTIR.

Measurements were taken of the devices as-deposited with an amorphous PCM layer, after half an hour of heating at 300°C and then another half-hour (also at 300°C) to observe if the spectra had changed (and if the devices had reached their end-states). After optical measurements were concluded these same samples were processed for TEM imaging.

The samples with 20 nm thick GST-225 layers show a definite redshift in position of the reflection dip for the amorphous state upon application of the barrier layer, likely due to the increase in thickness of material above the gold film. Upon crystallisation the dip is preserved for the sample with the barrier layer, but completely disappears for the sample without a barrier, as shown in Figure 130.

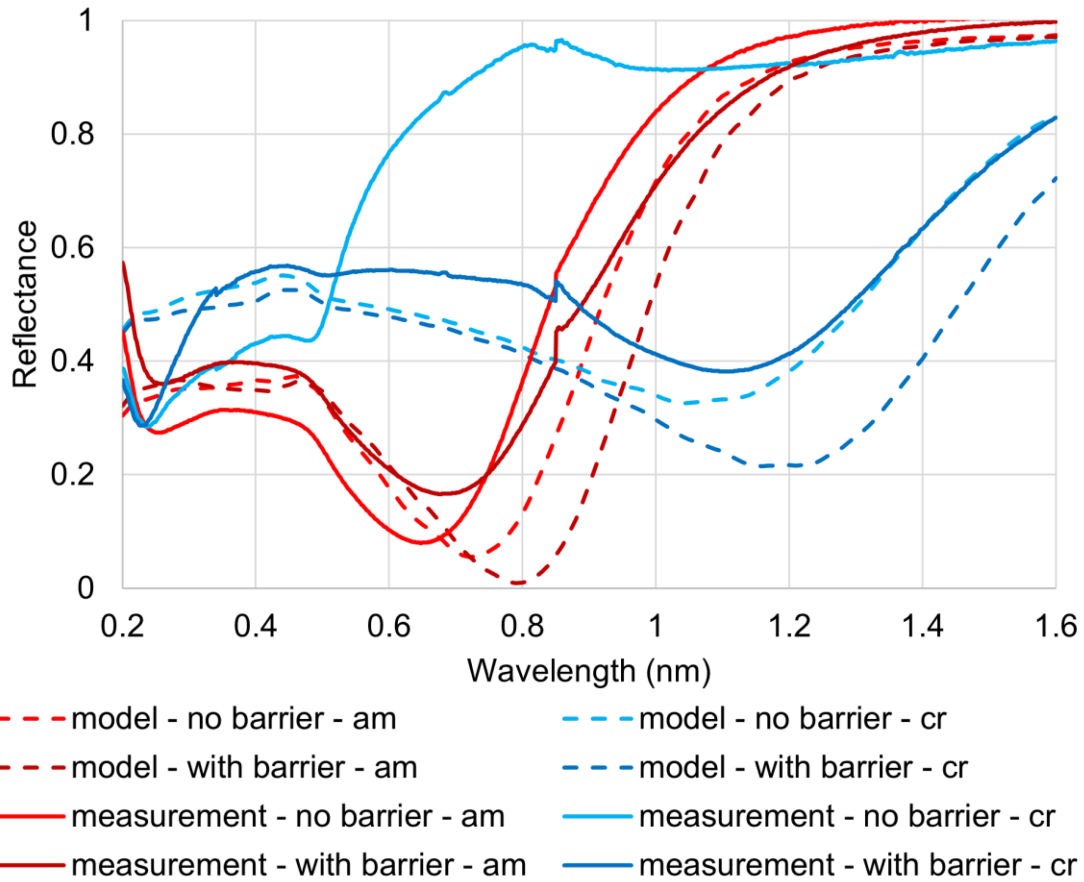

Figure 130: Microspectrometer measurements of reflection cavities with 20 nm GST-225 PCM layers (solid lines) and simulations of equivalent devices (without factoring in PCM diffusion for no-barrier structure) in COMSOL (dashed lines)

The spectra of the samples with 220 nm thick GST-225 layers seen in Figure 131 also show a redshift with the application of a barrier layer, but in this case the reflection dips are preserved even after the heating. The difference in peak position, with and without barrier layers, could be as a result of the PCM layer effectively becoming thinner in the latter case, as the material closest to the gold layer has been contaminated by the diffusing metal.

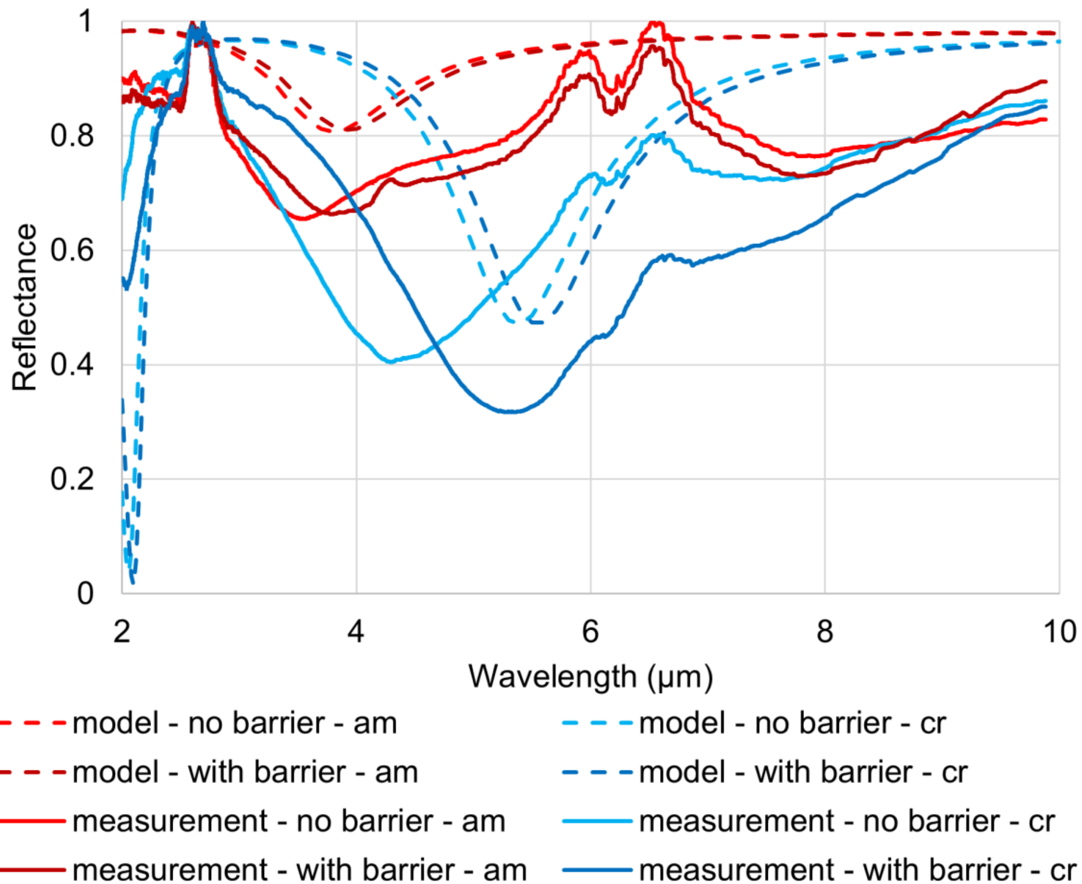

Figure 131: FTIR reflectance measurements of reflection cavities with 220 nm GST-225 PCM layers (solid lines) and simulations of equivalent devices (without factoring in PCM diffusion for no-barrier structure) in COMSOL (dashed lines)

6.4. Chapter Summary

In this chapter, actively-tunable phase-change EOT metasurface bandpass filters working in the mid-wave infrared range were successfully designed, modelled, fabricated and tested, using both GST-225 and GST-326 PCMs. The PCM optical properties differed from those expected from the literature, but using optical data gathered from films deposited in-house resulted in good agreement between simulated and measured device transmittance spectra. Tuneable filters of this type may well find application in areas such as multispectral sensing and imaging, potentially providing much-reduced size and complexity compared to conventional multispectral sensing approaches. Brief tests were made of a form of inverse-design EOT arrays (disks as opposed to holes) for operation in the visible-NIR regime, and while the application of GST-225 PCM layers demonstrated visible peak shifting, further experimentation is required to deliver

proper tuneable filter operation in this case. It must be noted that although the devices featured here were switched from amorphous to crystalline states by heating on a hotplate with no provision for resetting back to amorphous states. Other recent work, carried out contemporaneously with the work of this thesis, has demonstrated the switching of similar EOT devices to those reported here across multiple switching cycles [32], using 1.8 μm pitch hex arrays coated with GST-225 that was shifted between states (as-deposited amorphous to crystalline and back to amorphous) via laser heating.

As an alternative to the slow process of e-beam lithography and wet-etching, a viable method for scaling-up of the fabrication of EOT arrays using a “single-step” ultrafast laser-ablation process was also demonstrated. Comparable transmission spectra to wet-etched arrays of the same dimensions were achieved, and the technique was demonstrated to be capable of creating not only square but also hexagonal and rectangular arrays, which allowed for demonstration of polarisation-dependent transmittance behaviour.

Finally, the importance of a protective barrier layer between the gold and GST-225 layers was demonstrated, without which the heating of the device will result in the inter-diffusion of these two materials in areas where they are in direct contact. This was shown by both an example phase-change EOT array device and multiple unpatterned reflection cavities made specifically for testing this effect, which were TEM-imaged, EDS-scanned and also measured for reflectance with FTIR spectroscopy.

7. Conclusions and Future Work

Phase-change materials have opened up a wide variety of novel approaches to address new technological requirements, ranging from display solutions to computer memory, with room-temperature non-volatility and fast, dependable switching repeatability making them attractive solutions.

This thesis has showed, in both theory and practice, how PCMs can be combined with EOT arrays to make phase-change EOT metasurface devices which can be used for tuneable filter systems, with applications including multispectral imaging and signal modulation. A particular focus was made on the mid to long-wave infrared region (most often here around 2 to 12 μm), but EOT arrays for use in the near-infrared and even the visible region were also explored. For the latter, an inverse-design approach was used, i.e. the EOT device using arrays sub-wavelength diameter metal discs rather than sub-wavelength holes in a continuous metal film.

The EOT effect was thoroughly examined via finite element simulation, to explore the impact of various array properties on the spectral transmission properties of devices: these included both geometric parameters (pitch, fill factor, film thicknesses etc.) and the materials used for the different components. Changing a single parameter would generally affect multiple spectral properties, e.g. increasing array fill-factor would generally increase both the peak broadness and maximum transmittance, showing that array designs must be tailored to their specified applications to get the optimum balance of characteristics.

Further simulations investigated the effect of adding of PCM layers in various deposition schemes, showing how the material must at the least cover the array holes to have any shifting effect. Experimenting with the optical properties and dimensions of the PCM components showed how peak properties are affected by said changes, e.g. increasing the PCM thickness to get a larger wavelength shift would necessarily result in greater absorption.

EOT arrays were fabricated in gold films using a variety of methods, specifically e-beam lithography and wet-etching, e-beam lithography and lift-off and a novel

“single-step” approach using laser ablation. The transmission (and in appropriate cases reflection) spectra of the as-fabricated EOT arrays were measured using FTIR spectroscopy (and in some cases microspectrophotometry) and results compared to simulation, with very good agreement being obtained between the two in terms of key spectral features (absolute peak transmission, peak transmission wavelengths, peak Q-factors). This demonstrates the high degree of accuracy achievable with simulation and the ability to fabricate devices that compare well with the “perfect” models. The converse was also demonstrated, with imperfections resultant of moveable stage misalignments during some laser-ablation tests being theorised as the reason for reduced transmission a model was made that attempted to replicate it. While not as an accurate comparison as other simulations (only able to model a small section of an imperfect array), the hole mispositioning produced a similar effect to that with the measured devices.

Having successfully designed and fabricated ‘bare’ EOT arrays, PCM layers, specifically GST-225 and GST-326, were deposited onto such arrays and successful control of spectral transmission peak wavelength was demonstrated by switching the phase-state of the PCM layer. Specifically, tuneable bandpass filters for the MWIR regime were demonstrated using micron-scale array pitches (from 2-6.6 μm) in thin (40-100 nm) gold films coated with (70-100 nm thick) GST-225 or GST-326 layers on transparent (up to ~13 μm) calcium/barium fluoride substrates. Degrees of tuneability were obtained by application of 70-100 nm layers of GST-255 or GST-326 phase-change materials. The effect of using the different PCMs (GST-225 and GST-326) on device transmission spectra was explored, with the degree of peak wavelength shifting and change in absolute transmission being shown, as expected, to be dependent on the differences between phase-states of the refractive index n and extinction coefficient k. Decent agreement with simulated device spectra was obtained, in particular when using PCM n and k data obtained for the actual films deposited in this work, rather than relying on literature values.

Extending the concept of EOT-PCM-based devices to the THz region was also explored (in simulation) and showed that such devices might provide very useful modulation capabilities in this waveband, at least for GST-225 which, according to literature values, has a large extinction coefficient in its crystalline phase in this

region of the spectrum. Spectral properties are affected in the same ways as the shorter wavelength devices when altering array geometry or material optical properties, of most interest is that increasing the PCM layer thickness also increases modulation depth/contrast ratio at the expense of absolute transmission efficiency. Such modulators could, due to their relatively large feature sizes, be relatively inexpensive and easy to produce using the laser ablation method for fabrication of the EOT arrays.

Finally, the work of the thesis confirmed the (often overlooked) potentially destructive effect of gold-PCM inter-diffusion on the performance of devices where such layers are in intimate contact. Specifically, it was found that the EOT transmission peaks were almost completely suppressed, and tuneable filter functionality lost, on extended heating of the PCM layer. It was also shown, as previously reported [106] that a thin protective barrier, in this case 8 nm of silicon nitride, can effectively prevent the inter-diffusion issues, so leading to retention of device transmission and spectral tuning properties on switching/heating of the PCM layer. Detailed TEM analysis (on specially designed reflection cavity test samples) confirmed the high degree of inter-diffusion than occurs between the gold and PCM (specifically GST-225) layers, with samples showing complete merging of thin 20 nm GST layers with adjacent 40 nm thick gold layers after heating on a hotplate.

The optical resonances in such samples were also demonstrated to be severely degraded after such heating: in contrast, cavity samples having much larger PCM film thicknesses (here 220 nm) largely retained their optical resonance properties, even after extended heating. In such samples, TEM analysis showed that there was still substantial gold-PCM inter-diffusion, but it was limited in spatial extent such that a large portion of the PCM layer remained uncontaminated. TEM cross-sectional analysis also confirmed the effectiveness of a Si_3N_4 barrier layer in preventing inter-diffusion of the gold and PCM materials.

In terms of recommended future work, this could involve:

- Investigation of the effects of partial crystallisation of the PCM layers of phase-change EOT devices, allowing for tuneable filters having multiple

peak transmission wavelengths within the extremes of those provided by fully amorphous and fully crystalline states. This is in fact essential for multispectral sensing/imaging applications, which depend on having a significant "set" of filter configurations in order to work most effectively.

- The development of a practicable in-situ heating method for switching of the PCM layers in an EOT device, the key desired property being compatibility with a device working in transmission. Various in-situ heating methods using embedded electrical micro-heaters have already been demonstrated for various PCM-based devices [62], [63], [109], such concepts (whether plain metal layer or PIN-junction diode type heaters) could be extended to EOT-based devices.

  Plasmonic EOT devices have the inherent advantage of a metal layer being intrinsic to their structure, and this could be used to provide some kind of embedded heater, with exploratory simulations carried out in this thesis showing that such heaters should be able to provide the necessary heating and cooling requirements for successful PCM switching (though with rather high powers).

  Test devices were fabricated to investigate the electrical properties of thin films, one such shown in Figure 132 having five "strips" etched into a 40 nm Au film on an oxidised silicon substrate, the design made to fit into an existing electrical testing setup. While heating tests with this setup were not gotten around to, tests of a strip's resistance with a multimeter produced the same ~1 Ω as predicted by COMSOL simulations.

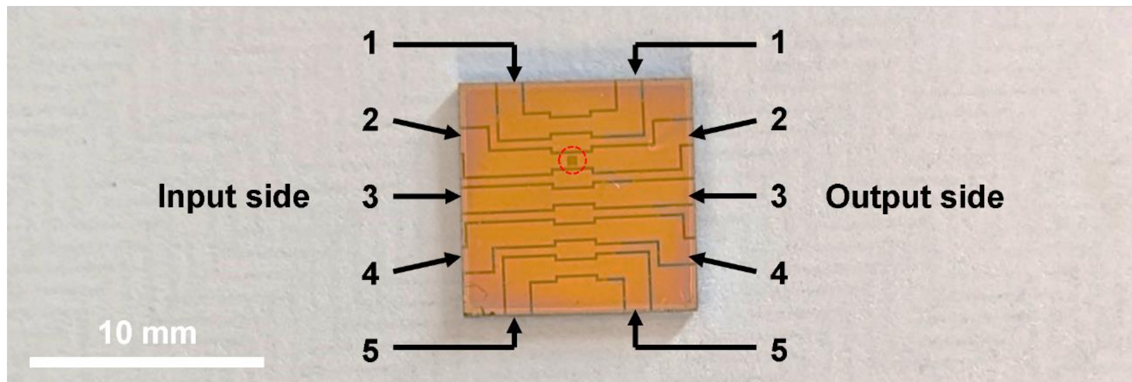

Figure 132: Device fabricated to test electrical properties, red circle in the centre of strip 2 marking out an array.

- Continued refinement of laser ablation as a method of array fabrication for large areas in short timescales. While promising results were shown, the precision available with using electron beam-based techniques consistently produced larger peak transmission efficiencies and higher quality factor for equivalent devices, not to mention the ability to pattern smaller hole sizes than those using the laser ablation approach. Improvements in motorised stage positioning to make more "perfect" arrays would help on the former front, the latter could be tackled by using a system that can create laser beams with smaller spots.

- Further exploration of the use of EOT-PCM based devices for modulator application in the THz region. As discussed above, EOT-based devices might provide for simple, cost-effective to produce THz modulators, but further work in the characterisation of the optical properties of phase-change materials in the THz range needs to be carried out, since currently very few compositions have been explored in this spectral range.

8. Appendices

8.1. Simulation Mesh Configuration

Increasing the fineness of the COMSOL mesh produces geometry closer to the real devices and should produce more accurate simulations, but this is at the expense of processing time as seen in Figure 133. All the electromagnetic simulations in this thesis used swept meshes, a face at the top of the cell is extruded down and split into "slices": while the fineness of the slices is significant (especially at the interfaces between materials) the example given here alters only the extruded face.

Only the "Coarse" setting shown in this example produces a main peak of noticeably different height than the finer settings, and as fineness increases the unwanted oscillation seen in the secondary peak (4-5.5 µm) reduces, with very little difference between the "Fine" and "Finer" settings showing that the nearly-doubled runtime doesn't provide much benefit in this case.

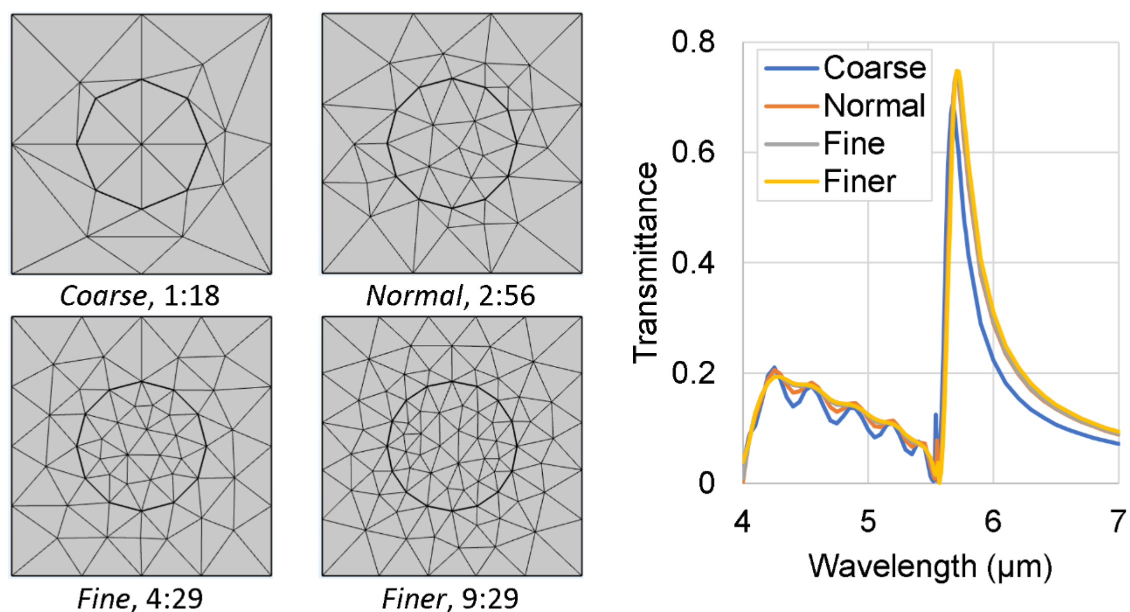

Figure 133: COMSOL swept mesh cross sections with fineness settings (4 µm array pitch with ff=0.5 in 40 nm Au on CaF_2) with comparative run durations, alongside the models' corresponding simulated transmittance spectra.

Another point to consider is the height of the cell, if the ports are too close to the device surface artefacts can become visible. Figure 134 shows example EOT spectra where the only variable is the effective thickness of the air above and substrate below the array, the larger sizes split into more slices to keep the mesh fineness of these sections constant. When the height is very small a peak with maximum transmittance greater than 1 is seen at ~4 µm, obviously an artefact, this diminishes as cell height increases until a shape is convereged upon. A height of six array periods was used consistently for modelling, while this didn't produce a significant difference in runtime compared to taller examples it helped prevent the geometry from becoming unweildy, making assigment of materials, ports and boundary conditions easier.

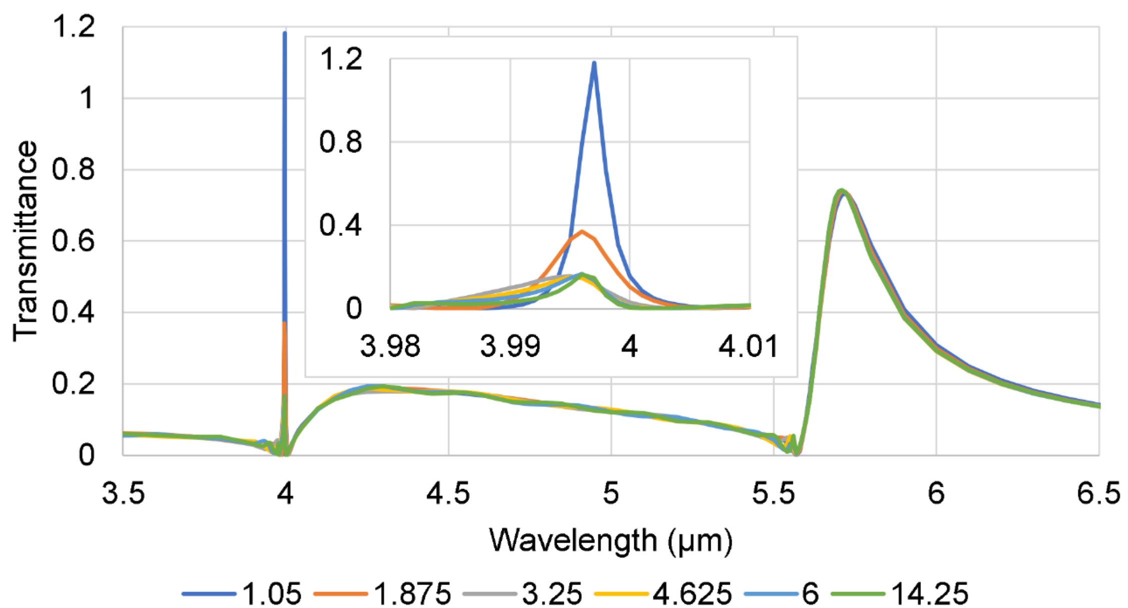

Figure 134: Transmission spectra for COMSOL simulations of same basic model shown in Figure 133 (with "Fine" mesh setting) altering the height of the cell between transmitting and receiving ports (given as a multiple of the array period), small range inset to show anomalous peak at 4 µm in more detail).

8.2. Fabrication Process Notes

8.2.1. Metal Deposition with HHV Auto 306 Thermal Evaporator

1. Remove any debris from evaporator chamber with vacuum cleaner and brush over all walls with acetone-soaked cleanroom wipe

2. Attach substrates to mounting block with Kapton™ tape, then load block into chamber
3. Load chromium pellet for adhesive layer (if needed) and gold wire for main layer (~2 mm for every 10 nm, ~1 mm extra for safety and to allow for "cleaning") into their respective boats, ensuring that the boat stage is positioned for the gold boat is to be heated
4. Pump chamber down to base pressure of 2×10^{-6} Torr
5. Ensure that shutter covering samples is closed, then turn on LT power and slowly increase voltage applied to gold boat to melt the pieces of wire (process is visible through the evaporator's viewport in the door) then reduce voltage and turn off power
6. Wait a few minutes to allow melted gold to be guaranteed solidified
7. Rotate boat stage to position for heating chromium pellet boat
8. Set the machine program to chromium, in order to give an accurate thickness readout
9. Enable rotation of the sample block to ensure even coverage of metal on the devices
10. Turn on LT power and slowly adjust voltage until a stable deposition rate between 0.5-1 Å s^{-1} is achieved
11. Allow a few nm thickness of chromium to show on the thickness readout prior to opening the shutter, cleaning the source metal before depositing on the sample
12. Simultaneously open the shutter and zero the thickness readout
13. Monitor the thickness readout, adjusting voltage if necessary to maintain a deposition rate between 0.5-1 Å s^{-1} as the figure is prone to fluctuation
14. When the desired thickness (typically 3-5 nm) is reached, close the shutter then slowly reduce the voltage before turning off LT power
15. Rotate boat stage to position for heating gold boat
16. Set the machine program to gold, in order to ensure an accurate thickness readout
17. Repeat steps 9-13 but for gold of the necessary thickness (typically 40-100 nm)
18. Disable rotation of the sample block
19. Allow the machine to cool for ~10 minutes before venting
20. Vent and unload samples

8.2.2. Thickness-Check Sample Preparation

1. Set a hotplate to 100°C
2. Gently sonicate substrate in beaker of acetone for 10 minutes (80 kHz at lowest power with sweep enabled), then sonicate for further 10 minutes in beaker of isopropyl alcohol (IPA) at same settings
3. Blow substrate dry with nitrogen gun
4. Apply dots of 950K A6 PMMA to corners of substrate with a pipette
5. Bake substrates on 100°C hotplate for 10 minutes

8.2.3. Lithography and Wet-Etching

1. Set a hotplate to 170°C
2. Gently sonicate device (metalled substrate) in beaker of acetone for 10 minutes (80 kHz at lowest power with sweep enabled), then sonicate for further 10 minutes in beaker of IPA at same settings
3. Blow device dry with nitrogen gun
4. Mount device on spinner stage and apply the vacuum to fix it in place
5. Apply a few drops of 950K A4 PMMA to metalled surface of device, enough that it will be covered once spun
6. Spin-coat the PMMA onto the device at 4,000 RPM until evenly distributed (~45 second program)
7. Remove device from spinner and bake on 170°C hotplate for 2 minutes

8. “Paint” 4 silver dots on edges of device (to aid focusing with e-beam) with toothpick-type stick
9. Mount device on e-beam chuck with carbon tape and obtain positions of silver dots with computerised stage
10. Insert chuck into its cassette and the cassette into e-beam loading chamber
11. Pump down e-beam chamber to base pressure of 2.4×10^{-6} mbar or below
12. Load chuck into writing chamber
13. Fine-focus on silver dots

14. Write pattern with 10 nA beam current with appropriate dosage for feature size and PMMA layer thickness (dose of 10 for system used), increasing either factor giving larger feature sizes in a given time so less shape precision
15. Unload chuck from writing chamber and vent machine

16. Develop written pattern by submerging device for 30 seconds in 15:5:1 solution of isopropyl alcohol (IPA), 4-methyl-2-pentanone (MKI) and methyl-ethyl ketone (MEK), keeping device as still as possible
17. Stop developing by submerging device for 1 minute in IPA
18. Blow device dry with nitrogen gun

19. Fill 3 glass beakers with deionised water (DI water)
20. Half-fill 1 glass beaker with diluted gold etchant [110] (1 part to 7 parts DI water) that has been chilled in fridge (set to 3-5°C)
21. Submerge device in etchant beaker and hold still for 15 seconds (for 40 nm Au film) to etch pattern, then quickly dip device into the 2 of the DI water beakers and leave it for 1 minute in the 3rd to stop the etching process
22. Remove device from last DI water beaker and blow dry with nitrogen gun
23. Wash out beakers with DI water, disposing of used etchant in appropriate vessel
24. Repeat steps 19-23, but with device submerged in undiluted room-temperature chromium etchant [111] for 10 seconds to etch the adhesive layer

25. Soak device in warm acetone for at least 10 minutes to remove PMMA mask
26. Wash device with IPA to remove any acetone residue
27. Blow device dry with nitrogen gun

8.2.4. Laser-Ablation

1. Configure set up (as seen in Figure 24) using appropriate details as shown in Table 41
2. Load device (metalled substrate) onto moveable stage
3. Focus on device
4. Write pattern

Table 41: Laser-ablation setup configuration details

Setting	Array		
	2 µm	4 µm	6.6 µm
Laser	Satsuma – 1030 nm		
Pulse length (fs)	340		330
Repetition rate (kHz)	1		
Aperture (mm)	5		
Aspheric lens NA	0.47	0.25	
Metallic filter optical density	1		
Camera focus distance (µm)	5	60	60
CCD-AL distance (cm)	93		
Power (500 kHz) (W)	0.008	0.03	0.081

8.2.5. Sputtering with NanoPVD

1. Vent chamber with argon gas
2. Attach devices to sample plate
3. Load 2” targets onto their respective guns and secure with metal rings
4. Cover targets on guns with metal cowls
5. Check resistance of cowls and rings with multimeter (grounded to chamber shell), former should be very low and latter very high (~0.1 Ω and ~1 MΩ respectively)
6. Load sample plate onto rotating shaft on lid of chamber
7. Pump down chamber to base pressure of 2×10^{-6} mbar
8. Ensure that shutter is covering samples
9. Enable argon gas flow

Controlled variable is flow rate, normal working pressure of 5×10^{-3} mbar required typically ~1 sccm but higher rates (up to 30 sccm sometimes) often needed to strike plasma before reducing

10. Select target and strike plasma (check visually with chamber window and readings on display) by setting the power

Testbourne™ GST-225 and GST-326 targets struck plasma at 15% RF power (22.5 W), which would then immediately be reduced to 10% (15 W). Si_3N_4 target struck plasma at 50% RF power (75 W), deposited at this power also.

11. Clean target for 3 minutes, keeping shutter closed, ensuring that plasma power and chamber pressure is stable at ~5×10^{-3} mbar
12. Shut off power and then disable gas flow
13. Let chamber be pumped for 15 minutes to cool and clear
14. Enable sample plate rotation (10-20 RPM)
15. Repeat steps 9-10 to produce stable plasma at ~5×10^{-3} mbar chamber pressure
16. Open shutter for required deposition time (calculated by measuring rate with thickness check samples beforehand)

Typically 2-2.5 nm per minute for GST targets at given powers (varied over time), consistently 1 nm per minute for Si3N4

17. Close shutter
18. Let chamber be pumped for 15 minutes to cool and clear
19. Repeat steps 15-17 for each material deposition, changing to the necessary targets
20. Disable sample plate rotation
21. Vent chamber with argon
22. Unload samples and targets

9. References

[1] E. Humphreys, J. Bertolotti, and C. D. Wright, "Phase-Change Extraordinary Optical Transmission Metasurfaces for Active Filtering from the Visible to the THz Regimes," in *12th International Conference on Metamaterials, Photonic Crystals and Plasmonics (META 2022 Torremolinos - Spain)*, 2022, pp. 949–950.

[2] E. Humphreys, J. Bertolotti, and C. D. Wright, "Filtering and Modulation from Visible to Terahertz using Phase-Change Extraordinary Optical Transmission Metasurfaces," in *European Phase-Change and Ovonic Symposium (E\PCOS 2022)*, 2022, pp. 4–5.

[3] C. Ruiz de Galarreta *et al.*, "Tunable optical metasurfaces enabled by chalcogenide phase-change materials: From the visible to the THz," *J. Opt. (United Kingdom)*, vol. 22, no. 11, 2020.

[4] C. Ruiz de Galarreta *et al.*, "Single-Step Fabrication of High-Performance Extraordinary Transmission Plasmonic Metasurfaces Employing Ultrafast Lasers," *ACS Appl. Mater. Interfaces*, vol. 14, no. 2, pp. 3446–3454, 2022.

[5] E. Humphreys, J. Bertolotti, C. R. de Galarreta, N. Casquero, J. Siegel, and C. D. Wright, "Filtering and Modulation from the Infrared to the Terahertz using Phase-Change Extraordinary Optical Transmission Metasurfaces," *Phys. Status Solidi - Rapid Res. Lett.*, vol. 2200474, pp. 1–7, 2023.

[6] P. Gutruf, C. Zou, W. Withayachumnankul, M. Bhaskaran, S. Sriram, and C. Fumeaux, "Mechanically tunable dielectric resonator metasurfaces at visible frequencies," *ACS Nano*, vol. 10, no. 1, pp. 133–141, 2016.

[7] T. Matsui *et al.*, "Reconfigurable THz and microwave metamaterials based on π-conjugated polymers." pp. 1–4, 2016.

[8] E. Arbabi, A. Arbabi, S. M. Kamali, Y. Horie, M. S. Faraji-Dana, and A. Faraon, "MEMS-tunable dielectric metasurface lens," *Nat. Commun.*, vol. 9, no. 1, 2018.

[9] J. Wen, Q. Ren, R. Peng, and Q. Zhao, "Multi-functional tunable ultra-broadband water-based metasurface absorber with high reconfigurability."

[10] P. Kapitanova, M. Odit, D. Dobrykh, A. Andryieuski, A. V. Lavrinenko, and P. Belov, "Tunable water-based microwave metasurface," *2017 11th Eur. Conf. Antennas Propagation, EUCAP 2017*, pp. 2599–2602, 2017.

[11] S. Foo, "Liquid-crystal-tunable metasurface antennas," *2017 11th Eur.*

Conf. Antennas Propagation, EUCAP 2017, pp. 3026–3030, 2017.

[12] A. Couch and A. Grbic, “A phase-tunable, liquid crystal-based metasurface,” *2016 10th Int. Congr. Adv. Electromagn. Mater. Microwaves Opt. METAMATERIALS 2016*, no. September, pp. 94–96, 2016.

[13] V. Sorathiya and S. Patel, “Graphene metasurface based tunable double split-ring resonator for far infrared frequency region,” *2019 IEEE Int. Symp. Antennas Propag. Usn. Radio Sci. Meet. APSURSI 2019 - Proc.*, pp. 1625–1626, 2019.

[14] C. Argyropoulos, “Enhanced transmission modulation based on dielectric metasurfaces loaded with graphene,” *Opt. Express*, vol. 23, no. 18, p. 23787, 2015.

[15] S. Yoshida, T. Yamaguchi, and A. Kinbara, “Optical properties of aggregated silver films,” *JOSA*, vol. 61, no. 1, pp. 62–69, 1971.

[16] S. G.-C. Carrillo, “Reconfigurable Phase-Change Metasurface Absorbers for Optoelectronic Device Applications,” University of Exeter, 2019.

[17] A. Arbabi and A. Faraon, “Advances in optical metalenses,” *Nat. Photonics*, vol. 17, no. 1, pp. 16–25, 2023.

[18] P. Berini, “Optical Beam Steering Using Tunable Metasurfaces,” *ACS Photonics*, vol. 9, no. 7, pp. 2204–2218, 2022.

[19] Carlota RUIZ DE GALARRETA, “Reconfigurable phase-change optical metasurfaces : novel design concepts to practicable devices,” University of Exeter, 2019.

[20] S. B. Glybovski, S. A. Tretyakov, P. A. Belov, Y. S. Kivshar, and C. R. Simovski, “Metasurfaces: From microwaves to visible,” *Phys. Rep.*, vol. 634, pp. 1–72, 2016.

[21] B. Shen, P. Wang, R. Polson, and R. Menon, “Ultra-high-efficiency metamaterial polarizer,” *Optica*, vol. 1, no. 5, p. 356, 2014.

[22] H. A. Bethe, “Theory of diffraction by small holes,” *Phys. Rev.*, vol. 66, no. 7–8, pp. 163–182, 1944.

[23] T. W. Ebbesen *et al.*, “Extraordinary optical transmission through sub-wavelength hole arrays,” *Nature*, vol. 86, no. 6, pp. 1114–7, 1998.

[24] F. Przybilla, A. Degiron, J. Y. Laluet, C. Genet, and T. W. Ebbesen, “Optical transmission in perforated noble and transition metal films,” *J. Opt. A Pure Appl. Opt.*, vol. 8, no. 5, pp. 458–463, 2006.

[25] Y. Ekinci, H. H. Solak, and C. David, “Extraordinary optical transmission in

the ultraviolet region through aluminum hole arrays," *Opt. Lett.*, vol. 32, no. 2, pp. 172–174, Jan. 2007.

[26] R. Gordon, M. Hughes, B. Leathem, K. L. Kavanagh, and A. G. Brolo, "Basis and lattice polarization mechanisms for light transmission through nanohole arrays in a metal film," *Nano Lett.*, vol. 5, no. 7, pp. 1243–1246, 2005.

[27] M. Rudé *et al.*, "Ultrafast and Broadband Tuning of Resonant Optical Nanostructures Using Phase-Change Materials," *Adv. Opt. Mater.*, vol. 4, no. 7, pp. 1060–1066, 2016.

[28] J. G. Rivas, C. Schotsch, P. H. Bolivar, and H. Kurz, "Enhanced transmission of THz radiation through subwavelength holes," *Phys. Rev. B - Condens. Matter Mater. Phys.*, vol. 68, no. 20, pp. 68–71, 2003.

[29] D. Hu and B. Chen, "Extraordinary terahertz transmission through a copper film perforated with circular and rectangular apertures," *J. Mod. Opt.*, vol. 62, no. 19, pp. 1623–1629, 2015.

[30] F. Van Beijnum, C. Rétif, C. B. Smiet, H. Liu, P. Lalanne, and M. P. Van Exter, "Quasi-cylindrical wave contribution in experiments on extraordinary optical transmission," *Nature*, vol. 492, no. 7429, pp. 411–414, 2012.

[31] J. A. Hutchison, D. M. O'Carroll, T. Schwartz, C. Genet, and T. W. Ebbesen, "Absorption-induced transparency," *Angew. Chemie - Int. Ed.*, vol. 50, no. 9, pp. 2085–2089, 2011.

[32] M. Julian, C. Williams, S. Borg, S. Bartram, and H. J. Kim, "Reversible optical tuning of GeSbTe phase-change metasurface spectral filters for mid-wave infrared imaging," *Optica*, vol. 7, no. 7, pp. 28–30, 2020.

[33] F. J. Garcia-Vidal, E. Moreno, J. A. Porto, and L. Martin-Moreno, "Transmission of light through a single rectangular hole," vol. 103901, no. September, pp. 1–4, 2005.

[34] F. J. García-Vidal, H. J. Lezec, T. W. Ebbesen, and L. Martín-Moreno, "Multiple Paths to Enhance Optical Transmission through a Single Subwavelength Slit," *Phys. Rev. Lett.*, vol. 90, no. 21, p. 4, 2003.

[35] D. E. Grupp, H. J. Lezec, T. Thio, and T. W. Ebbesen, "Beyond the Bethe limit: Tunable enhanced light transmission through a single sub-wavelength aperture," *Adv. Mater.*, vol. 11, no. 10, pp. 860–862, 1999.

[36] A. Degiron, H. J. Lezec, N. Yamamoto, and T. W. Ebbesen, "Optical transmission properties of a single subwavelength aperture in a real metal,"

Opt. Commun., vol. 239, no. 1–3, pp. 61–66, 2004.

[37] F. Przybilla, C. Genet, and T. W. Ebbesen, “Long vs short-range orders in random subwavelength hole arrays,” *Opt. Express*, vol. 20, no. 4, p. 4697, 2012.

[38] I. V Bykov, A. V Dorofeenko, A. S. Ilyin, I. A. Ryzhikov, M. V Sedova, and A. P. Vinogradov, “Extraordinary optical transmission through a random array of subwavelength holes,” *Phys. Rev. B - Condens. Matter Mater. Phys.*, vol. 78, no. 5, pp. 1–5, 2008.

[39] J. Bravo-Abad, A. I. Fernández-Domínguez, F. J. García-Vidal, and L. Martín-Moreno, “Theory of extraordinary transmission of light through quasiperiodic arrays of subwavelength holes,” *Phys. Rev. Lett.*, vol. 99, no. 20, pp. 14–17, 2007.

[40] W. L. Barnes, A. Dereux, and T. W. Ebbesen, “Surface plasmon subwavelength optics,” *Nature*, vol. 424, no. 6950, pp. 824–830, 2003.

[41] L. Martín-Moreno *et al.*, “Theory of extraordinary optical transmission through subwavelength hole arrays,” *Phys. Rev. Lett.*, vol. 86, no. 6, pp. 1114–1117, 2001.

[42] C. Genet, M. P. Van Exter, and J. P. Woerdman, “Fano-type interpretation of red shifts and red tails in hole array transmission spectra,” *Opt. Commun.*, vol. 225, no. 4–6, pp. 331–336, 2003.

[43] H. Ghaemi, T. Thio, D. Grupp, and T. Ebbesen, “Surface plasmons enhance optical transmission through subwavelength holes,” *Phys. Rev. B - Condens. Matter Mater. Phys.*, vol. 58, no. 11, pp. 6779–6782, 1998.

[44] S. G. Rodrigo, F. de León-Pérez, and L. Martín-Moreno, “Extraordinary Optical Transmission: Fundamentals and Applications,” *Proc. IEEE*, vol. 104, no. 12, pp. 2288–2306, 2016.

[45] A. Krishnan *et al.*, “Evanescently coupled resonance in surface plasmon enhanced transmission,” *Opt. Commun.*, vol. 200, no. 1–6, pp. 1–7, 2001.

[46] F. J. G. . de Abajo *et al.*, “Light transmission through a single cylindrical hole in a metallic film,” *Opt. Express*, vol. 10, no. 25, p. 1475, 2002.

[47] S. G. Rodrigo, F. J. García-Vidal, and L. Martín-Moreno, “Theory of absorption-induced transparency,” *Phys. Rev. B - Condens. Matter Mater. Phys.*, vol. 88, no. 15, pp. 1–6, 2013.

[48] S.-H. Chang, S. K. Gray, and G. C. Schatz, “Surface plasmon generation and light transmission by isolated nanoholes and arrays of nanoholes in

thin metal films," *Opt. Express*, vol. 13, no. 8, p. 3150, 2005.

[49] A. E. Cetin, M. Dršata, Y. Ekşioğlu, and J. Petráček, "Extraordinary Transmission Characteristics of Subwavelength Nanoholes with Rectangular Lattice," *Plasmonics*, vol. 12, no. 3, pp. 655–661, 2017.

[50] A. Degiron and T. W. Ebbesen, "The role of localized surface plasmon modes in the enhanced transmission of periodic subwavelength apertures," *J. Opt. A Pure Appl. Opt.*, vol. 7, no. 2, 2005.

[51] K. J. K. Koerkamp, S. Enoch, F. B. Segerink, N. F. Van Hulst, and L. Kuipers, "Strong influence of hole shape on extraordinary transmission through periodic arrays of subwavelength holes," *Phys. Rev. Lett.*, vol. 92, no. 18, pp. 18–21, 2004.

[52] R. Gordon, A. G. Brolo, A. McKinnon, A. Rajora, B. Leathem, and K. L. Kavanagh, "Strong Polarization in the Optical Transmission through Elliptical Nanohole Arrays," *Phys. Rev. Lett.*, vol. 92, no. 3, p. 4, 2004.

[53] S. R. Ovshinsky, "Reversible electrical switching phenomena in disordered structures," *Phys. Rev. Lett.*, vol. 21, no. 20, pp. 1450–1453, 1968.

[54] P. Nestler and C. A. Helm, "Determination of refractive index and layer thickness of nm-thin films via ellipsometry," *Opt. Express*, vol. 25, no. 22, p. 27077, 2017.

[55] A. K. U. Michel, M. Wuttig, and T. Taubner, "Design Parameters for Phase-Change Materials for Nanostructure Resonance Tuning," *Adv. Opt. Mater.*, vol. 5, no. 18, pp. 1–8, 2017.

[56] Y. Zhang *et al.*, "Broadband transparent optical phase change materials for high-performance nonvolatile photonics," *Nat. Commun.*, pp. 1–9, 2019.

[57] J. Orava, A. L. Greer, B. Gholipour, D. W. Hewak, and C. E. Smith, "Characterization of supercooled liquid Ge2Sb2Te 5 and its crystallization by ultrafast-heating calorimetry," *Nat. Mater.*, vol. 11, no. 4, pp. 279–283, 2012.

[58] L. Trimby, A. Baldycheva, and C. D. Wright, "Phase-change band-pass filters for multispectral imaging," *SPIE Proc.*, vol. 10541, no. February, pp. 105412B-10541–8, 2018.

[59] A. V. Kolobov, P. Fons, A. I. Frenkel, A. L. Ankudinov, J. Tominaga, and T. Uruga, "Understanding the phase-change mechanism of rewritable optical media," *Nat. Mater.*, vol. 3, no. 10, pp. 703–708, 2004.

[60] J. A. Kalb, M. Wuttig, and F. Spaepen, "Calorimetric measurements of

structural relaxation and glass transition temperatures in sputtered films of amorphous Te alloys used for phase change recording,” *J. Mater. Res.*, vol. 22, no. 3, pp. 748–754, 2007.

[61] M. Wuttig and N. Yamada, “Phase-change materials for rewriteable data storage,” *Nat. Mater.*, vol. 6, no. 11, pp. 824–832, 2007.

[62] N. Farmakidis *et al.*, “Electronically Reconfigurable Photonic Switches Incorporating Plasmonic Structures and Phase Change Materials,” *Adv. Sci.*, vol. 9, no. 20, pp. 1–8, 2022.

[63] Y. Zhang *et al.*, “Electrically reconfigurable non-volatile metasurface using low-loss optical phase-change material,” *Nat. Nanotechnol.*, vol. 16, no. 6, pp. 661–666, 2021.

[64] R. Lasaponara and N. Masini, “Detection of archaeological crop marks by using satellite QuickBird multispectral imagery,” *J. Archaeol. Sci.*, vol. 34, no. 2, pp. 214–221, 2007.

[65] H. Liang, “Advances in multispectral and hyperspectral imaging for archaeology and art conservation,” *Appl. Phys. A Mater. Sci. Process.*, vol. 106, no. 2, pp. 309–323, 2012.

[66] Y. Huang, S. J. Thomson, Y. Lan, and S. J. Maas, “Multispectral imaging systems for airborne remote sensing to support agricultural production management,” *Int. J. Agric. Biol. Eng.*, vol. 3, no. 1, pp. 50–62, 2010.

[67] Y. Huang, K. N. Reddy, R. S. Fletcher, and D. Pennington, “UAV Low-Altitude Remote Sensing for Precision Weed Management,” *Weed Technol.*, vol. 32, no. 1, pp. 2–6, 2018.

[68] L. Deng, Z. Mao, X. Li, Z. Hu, F. Duan, and Y. Yan, “UAV-based multispectral remote sensing for precision agriculture: A comparison between different cameras,” *ISPRS J. Photogramm. Remote Sens.*, vol. 146, no. September, pp. 124–136, 2018.

[69] D. W. Lamb, “The use of qualitative airborne multispectral imaging for managing agricultural crops-a case study in south-eastern Australia,” *Aust. J. Exp. Agric.*, vol. 40, no. 5, pp. 725–738, 2000.

[70] N. Gat, “Imaging spectroscopy using tunable filters: a review,” *Wavelet Appl. VII*, vol. 4056, no. April 2000, pp. 50–64, 2000.

[71] Y. Zheng, “An overview of night vision colorization techniques using multispectral images: From color fusion to color mapping,” *ICALIP 2012 - 2012 Int. Conf. Audio, Lang. Image Process. Proc.*, no. July, pp. 134–143,

2012.

[72] S. Serranti, A. Gargiulo, and G. Bonifazi, “Application of NIR hyperspectral imaging for post-consumer polyolefins recycling,” *Adv. Environ. Chem. Biol. Sens. Technol. IX*, vol. 8366, no. May 2012, p. 83660G, 2012.

[73] S. Serranti, R. Palmieri, and G. Bonifazi, “Hyperspectral imaging applied to demolition waste recycling: innovative approach for product quality control,” *J. Electron. Imaging*, vol. 24, no. 4, p. 043003, 2015.

[74] C. Schweitzer, K. Stein, and N. Wendelstein, “Evaluation of appropriate sensor specifications for space based ballistic missile detection,” *Electro-Optical Infrared Syst. Technol. Appl. IX*, vol. 8541, no. October, p. 85410M, 2012.

[75] J. A. Shenson, G. S. Liu, J. Farrell, and N. H. Blevins, “Multispectral Imaging for Automated Tissue Identification of Normal Human Surgical Specimens,” *Otolaryngol. - Head Neck Surg. (United States)*, vol. 164, no. 2, pp. 328–335, 2021.

[76] “Multispectral Imaging Camera Drones In Farming Yield Big Benefits.” [Online]. Available: https://www.dronezon.com/learn-about-drones-quadcopters/multispectral-sensor-drones-in-farming-yield-big-benefits/. [Accessed: 20-Apr-2023].

[77] “Sentera 6X Sensors.” [Online]. Available: https://sentera.com/products/fieldcapture/sensors/6x/. [Accessed: 20-Apr-2023].

[78] “Salvo Technologies SpectroCam.” [Online]. Available: https://salvotechnologies.com/product/spectrocam/. [Accessed: 20-Apr-2023].

[79] D. Sarid and W. A. Challener, *Modern introduction to Surface Plasmons: Theory, Mathematica Modeling, and Applications*. Cambridge University Press, 2010.

[80] R. A. Matula, “Electrical resistivity of copper, gold, palladium, and silver,” *J. Phys. Chem. Ref. Data*, vol. 8, no. 4, pp. 1147–1298, 1979.

[81] “Barium Fluoride (BaF2).” [Online]. Available: https://www.crystran.co.uk/optical-materials/barium-fluoride-baf2. [Accessed: 20-Apr-2023].

[82] “Calcium Fluoride (CaF2).” [Online]. Available: https://www.crystran.co.uk/optical-materials/calcium-fluoride-caf2.

[Accessed: 20-Apr-2023].
[83] P. A. Thomas, K. S. Menghrajani, and W. L. Barnes, “All-optical control of phase singularities using strong light-matter coupling,” *Nat. Commun.*, vol. 13, no. 1, 2022.
[84] “TESPA-V2.” [Online]. Available: https://www.brukerafmprobes.com/p-3844-tespa-v2.aspx. [Accessed: 20-Apr-2023].
[85] P. T. Pinard, A. Protheroe, J. Holland, S. Burgess, and P. J. Statham, “Development and validation of standardless and standards-based X-ray microanalysis,” *IOP Conf. Ser. Mater. Sci. Eng.*, vol. 891, no. 1, 2020.
[86] “Introduction to Fourier Transform Infrared Spectroscopy Introduction,” *ThermoFisher Scientific*. 2022.
[87] D. H. Kim, F. Merget, M. Laurenzis, P. H. Bolivar, and H. Kurz, “Electrical percolation characteristics of Ge 2Sb 2Te 5 and Sn doped Ge 2Sb 2Te 5 thin films during the amorphous to crystalline phase transition,” *J. Appl. Phys.*, vol. 97, no. 8, 2005.
[88] “Magnesium Fluoride (MgF2).” [Online]. Available: https://www.crystran.co.uk/optical-materials/magnesium-fluoride-mgf2. [Accessed: 20-Apr-2023].
[89] H. H. Li, “Refractive index of alkaline earth halides and its wavelength and temperature derivatives,” *J. Phys. Chem. Ref. Data*, vol. 9, pp. 161–290, Jan. 1980.
[90] A. D. Rakić, “Algorithm for the determination of intrinsic optical constants of metal films: application to aluminum,” *Appl. Opt.*, vol. 34, no. 22, pp. 4755–4767, Aug. 1995.
[91] A. Ciesielski, L. Skowronski, M. Trzcinski, and T. Szoplik, “Controlling the optical parameters of self-assembled silver films with wetting layers and annealing,” *Appl. Surf. Sci.*, vol. 421, pp. 349–356, 2017.
[92] R. L. Olmon *et al.*, “Optical dielectric function of gold,” *Phys. Rev. B*, vol. 86, no. 23, p. 235147, Dec. 2012.
[93] S. G. Rodrigo, *Optical Properties of Nanostructured Metallic Systems*. 2012.
[94] M. A. Ordal, R. J. Bell, R. W. Alexander, L. A. Newquist, and M. R. Querry, “Optical properties of Al, Fe, Ti, Ta, W, and Mo at submillimeter wavelengths,” *Appl. Opt.*, vol. 27, no. 6, pp. 1203–1209, Mar. 1988.
[95] A. D. Rakić, A. B. Djurišić, J. M. Elazar, and M. L. Majewski, “Optical

properties of metallic films for vertical-cavity optoelectronic devices," *Appl. Opt.*, vol. 37, no. 22, pp. 5271–5283, Aug. 1998.

[96] M. R. Querry, "Optical Constants, Report No. AD-A158 623," *Crdc*, vol. CR-85034, pp. 1–413, 1985.

[97] M. Delaney, I. Zeimpekis, D. Lawson, D. W. Hewak, and O. L. Muskens, "A New Family of Ultralow Loss Reversible Phase-Change Materials for Photonic Integrated Circuits: Sb2S3 and Sb2Se3," *Adv. Funct. Mater.*, vol. 30, no. 36, pp. 1–10, 2020.

[98] K. Makino *et al.*, "Terahertz spectroscopic characterization of Ge2Sb2Te5 phase change materials for photonics applications," *J. Mater. Chem. C*, vol. 7, no. 27, pp. 8209–8215, 2019.

[99] "Magnesium Oxide (MgO)." [Online]. Available: https://www.crystran.co.uk/optical-materials/magnesium-oxide-mgo. [Accessed: 20-Apr-2023].

[100] "Silicon (Si)." [Online]. Available: https://www.crystran.co.uk/optical-materials/silicon-si. [Accessed: 20-Apr-2023].

[101] "Sapphire (Al2O3)." [Online]. Available: https://www.crystran.co.uk/optical-materials/sapphire-al2o3. [Accessed: 20-Apr-2023].

[102] S. Abdollahramezani *et al.*, "Electrically driven programmable phase-change meta-switch reaching 80% efficiency," pp. 1–11.

[103] K. V. Sreekanth *et al.*, "Electrically Tunable All-PCM Visible Plasmonics," *Nano Lett.*, vol. 21, no. 9, pp. 4044–4050, 2021.

[104] J. Zheng *et al.*, "Nonvolatile electrically reconfigurable integrated photonic switch," *ArXiV Prepr.*, no. December, p. arXiv:1912.07680, 2019.

[105] R. D. Deslattes, E. G. Kassler, P. Indelicato, L. De Billy, E. Lindroth, and J. Anton, "X-ray transition energies: New approach to a comprehensive evaluation," *Rev. Mod. Phys.*, vol. 75, no. 1, pp. 35–99, 2003.

[106] L. Lu, W. Dong, J. K. Behera, L. Chew, and R. E. Simpson, "Inter-diffusion of plasmonic metals and phase change materials," *J. Mater. Sci.*, vol. 54, no. 4, pp. 2814–2823, 2018.

[107] A. Shabani, M. R. Roknabadi, M. Behdani, M. K. Nezhad, and N. Rahmani, "Extraordinary optical transmission of periodic array of subwavelength holes within titanium nitride thin film," *J. Nanophotonics*, vol. 11, no. 4, pp. 1–10, 2017.

[108] S. Murai, K. Fujita, Y. Daido, R. Yasuhara, R. Kamakura, and K. Tanaka,

"Plasmonic arrays of titanium nitride nanoparticles fabricated from epitaxial thin films," *Opt. Express*, vol. 24, no. 2, p. 1143, 2016.

[109] S. G.-C. Carrillo, A. M. Alexeev, Y.-Y. Au, and C. D. Wright, "Reconfigurable phase-change meta-absorbers with on-demand quality factor control," *Opt. Express*, vol. 26, no. 20, p. 25567, 2018.

[110] Merck, "Gold etchant, standard." [Online]. Available: https://www.sigmaaldrich.com/GB/en/product/aldrich/651818. [Accessed: 13-Aug-2023].

[111] Merck, "Chromium etchant." [Online]. Available: https://www.sigmaaldrich.com/GB/en/product/aldrich/651826. [Accessed: 13-Aug-2023].